

**PHOTOPHYSICOCHEMICAL STUDIES OF  $d^{10}$   
METALLOPHTHALOCYANINES AND THEIR  
INTERACTION WITH NANOPARTICLES**

**A thesis submitted in fulfillment of the requirements for the degree of**

**DOCTOR OF PHILOSOPHY**

**Of**

**RHODES UNIVERSITY**

**By**

**WADZANAI JANET UPENYU CHIDAWANYIKA**

**January 2010**

## **DEDICATION**

**To my parents, Anna and Alban Chidawanyika**

*“Victory is always possible for the person who refuses  
to stop fighting”*

**-Napoleon Hill**

# ACKNOWLEDGEMENTS

*“Put God in the centre and everything will come together”*

To Him I give thanks for making all things possible!

To my supervisor, Prof. Tebello Nyokong, thank you for believing in my ability and giving me the opportunity to work under your guidance and for numerous other opportunities that challenged me to achieve my highest potential.

Thanks also to Prof. Nagao Kobayashi, Dr. Soji Shimizu, and the entire research group at Tohoku University, Japan for their generosity and support during my stay there.

I would also like to acknowledge Dr. Abimbola Ogunsipe, Dr. Edith Antunes, Dr. Christian Litwinski and Dr. John Mack for their invaluable contribution to this work.

To my family; Mom and Dad I cannot express my gratitude for your constant love, support, encouragement, and of course persuasion to continue to study and understand the true value of education and the rewards of perseverance. To my brother, Tanaka (“Dude”) thanks for the direction, “Just go straight”! To my entire extended family, I appreciate your prayers and encouragement. This is only the beginning! Many thanks to ALL my friends, particularly Sanel (“Chickie”) and Jerry for your understanding and patience.

I thank all my ‘peops’ in the S22 research group (for the Good Times!) and the Rhodes University Chemistry Department staff and postgraduate students. Tea time will never be the same anywhere else.

Financial support from Rhodes University in association with the Andrew Mellon Foundation and the National Research Foundation (NRF) of South Africa are gratefully acknowledged.

## ABSTRACT

The syntheses, extensive spectroscopic characterization, photophysical and photochemical studies have been conducted for a variation of  $d^{10}$  metallophthalocyanines (MPcs). Comparisons have been made taking into consideration the influence of the central metal ion, solvent properties, substituent type and position. Coordination to heavy central metals i.e. Hg gives enhanced triplet state properties.

Low symmetry metallophthalocyanine complexes were similarly characterized and the influence of interactions with nanoparticles on their photophysical and photochemical properties determined. The MPcs have been linked and adsorbed or mixed with nanoparticles i.e. chemically functionalized single-walled carbon nanotubes (SWCNT) and mercaptocarboxylic acid capped CdTe quantum dots (QDs) and changes in the spectra accounted for with respect to the proposed conjugate structures. Distinct differences occur for linked and adsorbed or mixed conjugates in the absorption, infrared (IR) and Raman spectra and for thermal gravimetric decay profiles, suggesting successful formation of covalent bonds (linked) and point to structurally different materials.

SWCNT quench MPc fluorescence by a photoinduced electron transfer mediated process to give low fluorescence quantum yields.

The QDs were used as energy transfer donors and facilitate energy transfer, through Förster resonance energy transfer (FRET) from the QDs to the MPcs. Improved FRET efficiencies were found for linked MPc-QD conjugates relative to the mixed species.

Photophysicochemical properties of MPcs were, in general, improved as a result of interactions with nanoparticles.

# CONTENTS

<b>Title Page</b>	<b>i</b>
<b>Dedication</b>	<b>ii</b>
<b>Acknowledgements</b>	<b>iii</b>
<b>Abstract</b>	<b>iv</b>
<b>Contents</b>	<b>v</b>
<b>List of Abbreviations</b>	<b>xi</b>
<b>List of Symbols</b>	<b>xv</b>
<b>List of Figures</b>	<b>xvii</b>
<b>List of Schemes</b>	<b>xxii</b>
<b>List of Tables</b>	<b>xxiii</b>
<b>1. Introduction</b>	<b>1</b>
<b>1.1 Nanoscience</b>	<b>2</b>
<b>1.1.1 Single-walled carbon nanotubes</b>	<b>2</b>
<b>1.1.2 Quantum dots</b>	<b>7</b>
<b>1.1.2.1 Aqueous synthesis of QDs</b>	<b>8</b>
<b>1.1.2.2 Absorption and fluorescence spectra of QDs</b>	<b>11</b>
<b>1.1.3 Methods of characterizing nanoparticles</b>	<b>14</b>
<b>1.2 Metallophthalocyanine (MPc) Chemistry</b>	<b>18</b>
<b>1.2.1. Phthalocyanine syntheses</b>	<b>19</b>
<b>1.2.1.1 Symmetrically ring-substituted phthalocyanines</b>	<b>21</b>
<b>1.2.1.2 Low-symmetry A<sub>3</sub>B type phthalocyanines</b>	<b>22</b>

1.2.1.3 Phthalocyanines synthesized in this work	25
1.2.1.4 Synthesis of phthalocyanine-nanoparticle conjugates	29
1.2.2 Ground state electronic absorption spectra of phthalocyanines	35
1.2.2.1 Origins of spectra	35
1.2.2.2 Phthalocyanine aggregation	39
1.2.3 Magnetic circular dichroism (MCD) spectroscopy	41
1.2.4 Molecular orbital (MO) theoretical calculations	44
1.3 Photophysical Properties	45
1.3.1 Fluorescence	46
1.3.1.1 Fluorescence spectra	46
1.3.1.2 Fluorescence quantum yields and lifetimes	48
1.3.1.3 Förster resonance energy transfer (FRET)	50
1.3.2 Triplet quantum yields and lifetimes	53
1.4 Photochemical Properties	57
1.4.1 Singlet oxygen	57
1.4.2 Photodegradation	63
1.5 Summary of Aims of Thesis	66
2. Experimental	68
2.1 Materials	69
2.1.1 Solvents	69
2.1.2 Synthesis and photophysicochemical reagents	69
2.2 Instrumentation	70

<b>2.3</b>	<b>Methods</b>	<b>76</b>
2.3.1	Absorption studies	76
2.3.2	Magnetic circular dichroism (MCD) spectra	77
2.3.3	Fluorescence spectra and quantum yields	77
2.3.4	Fluorescence lifetimes	77
2.3.5	Triplet quantum yields and lifetimes	78
2.3.6	Singlet oxygen and photodegradation quantum yields	78
<b>2.4</b>	<b>Synthesis</b>	<b>79</b>
2.4.1	Functionalization of single-walled carbon nanotubes	79
2.4.2	Synthesis of quantum dots	80
2.4.3	Synthesis of unsubstituted MPcs	82
2.4.4	Synthesis of mono-substituted phthalonitriles	83
2.4.5	Synthesis of symmetrical aryloxy tetra-substituted MPcs	87
2.4.6	Synthesis of symmetrical <i>tert</i> -butyl and alkanethio tetra-substituted MPcs	92
2.4.7	Synthesis of low-symmetry (A <sub>3</sub> B type) tetra-substituted MPcs	93
2.4.8	Synthesis of MPc-SWCNT conjugates	95
2.4.9	Synthesis of MPc-QD conjugates	97
	<b>Results and Discussion</b>	<b>99</b>
	<b>Publications</b>	<b>100</b>
<b>3.</b>	<b>Synthesis and Spectroscopic Characterization</b>	<b>102</b>

<b>3.1</b>	<b>Functionalization, Synthesis and Characterization of Nanoparticles</b>	<b>103</b>
3.1.1	Chemical functionalization of SWCNT	103
3.1.2	Mercaptocarboxylic acid capped CdTe QDs	108
<b>3.2</b>	<b>Metallophthalocyanines</b>	<b>111</b>
3.2.1	Unsubstituted MPcs	113
3.2.2	Symmetrically tetra-substituted metallophthalocyanine derivatives	115
3.2.2.1	Mono-substituted phthalonitriles	115
3.2.2.2	Symmetrical aryloxy tetra-substituted MPc derivatives	117
3.2.2.3	Symmetrical <i>tert</i> -butyl and alkanethio tetra-substituted MPcs	131
3.2.3	Low-symmetry (A <sub>3</sub> B type) tetra-substituted MPcs	136
<b>3.3</b>	<b>Conclusions</b>	<b>148</b>
<b>4.</b>	<b>Photophysical and Photochemical Properties</b>	<b>149</b>
<b>4.1</b>	<b>Fluorescence Spectra</b>	<b>150</b>
4.1.1	Nanoparticles	150
4.1.2	Metallophthalocyanines	152
4.1.2.1	Symmetrically substituted metallophthalocyanines	152
4.1.2.2	Low-symmetry metallophthalocyanines	155
<b>4.2</b>	<b>Fluorescence Quantum Yields and Lifetimes</b>	<b>161</b>
4.2.1	Nanoparticles (QDs)	161
4.2.2	Metallophthalocyanines	163



<b>4.3</b>	<b>Triplet State Quantum Yields and Lifetimes of MPc Complexes</b>	<b>165</b>
<b>4.4</b>	<b>Singlet Oxygen and Photodegradation Quantum Yields of MPc Complexes</b>	<b>174</b>
<b>4.4.1</b>	<b>Singlet oxygen quantum yields (<math>\Phi_{\Delta}</math>)</b>	<b>174</b>
<b>4.4.2</b>	<b>Photodegradation quantum yields</b>	<b>182</b>
<b>4.5</b>	<b>Conclusions</b>	<b>185</b>
<b>5.</b>	<b>Interaction of Metallophthalocyanines with Nanoparticles</b>	<b>187</b>
<b>5.1</b>	<b>Interaction of Metallophthalocyanines with Single-Walled Carbon Nanotubes</b>	<b>188</b>
<b>5.1.1</b>	<b>Synthesis and spectroscopic characterization of MPc-SWCNT conjugates</b>	<b>189</b>
<b>5.1.2</b>	<b>Fluorescence spectra, quantum yields and lifetimes</b>	<b>203</b>
<b>5.2</b>	<b>Interaction of Metallophthalocyanines with Quantum Dots</b>	<b>207</b>
<b>5.2.1</b>	<b>Synthesis and spectroscopic characterization of MPc-QD conjugates</b>	<b>208</b>
<b>5.2.2</b>	<b>Fluorescence quantum yields and lifetimes</b>	<b>212</b>
<b>5.2.3</b>	<b>Förster resonance energy transfer (FRET)</b>	<b>214</b>
<b>5.2.4</b>	<b>Triplet quantum yields and lifetimes</b>	<b>219</b>
<b>5.2.5</b>	<b>Singlet oxygen quantum yields</b>	<b>221</b>
<b>5.3</b>	<b>Conclusions</b>	<b>222</b>
<b>6.</b>	<b>General Conclusions and Future Prospects</b>	<b>224</b>

<b>6.1 General Conclusions</b>	<b>225</b>
<b>6.2 Future Prospects</b>	<b>226</b>
<b>References</b>	<b>228</b>

## LIST OF ABBREVIATIONS

<b>Abs</b>	=	Absorbance
<b>ADMA</b>	=	Tetrasodium $\alpha,\alpha$ -(anthracene-9,10-diyl) dimethylmalonate
<b>AE</b>	=	Acceptor emission
<b>AFM</b>	=	Atomic force microscopy
<b>ASE</b>	=	Acceptor sensitized emission
<b>CD</b>	=	Circular dichroism
<b>CD-RW</b>	=	Rewritable optical media (compact disc)
<b>CHCl<sub>3</sub></b>	=	Chloroform
<b>CR</b>	=	Charge recombination
<b>DA</b>	=	Donor absorption
<b>DABCO</b>	=	1,4-Diazabicyclo-octane
<b>DBN</b>	=	1,5-Diazabicyclo[4.3.0]non-5-ene
<b>DBU</b>	=	1,8-Diazabicyclo[5.4.0]undec-7-ene
<b>DCC</b>	=	Dicyclohexylcarbodiimide
<b>DCM</b>	=	Dichloromethane
<b>DE</b>	=	Donor emission
<b>DFT</b>	=	Density functional theory
<b>DMAE</b>	=	<i>N,N</i> -dimethylaminoethanol
<b>DMF</b>	=	<i>N,N</i> -dimethylformamide
<b>DMSO</b>	=	Dimethylsulfoxide
<b>DOS</b>	=	Density of states
<b>DPBF</b>	=	1,3-Diphenylisobenzofuran

<b>DSC</b>	=	Differential scanning calorimetry
<b>EDC</b>	=	1-Ethyl-3-(3-dimethylaminopropyl) carbodiimide
<i>Eff</i>	=	Efficiency of energy transfer
<i>Eff<sub>ss</sub></i>	=	Efficiency of energy transfer from steady state fluorescence
<i>Eff<sub>tr</sub></i>	=	Efficiency of energy transfer from time resolved fluorescence
<b>ET</b>	=	Energy transfer
<b>EtOH</b>	=	Ethanol
<b>F</b>	=	Fluorescence intensity
<b>FRET</b>	=	Förster resonance energy transfer
<b>FWHM</b>	=	Full width at half maximum
<b>FT-IR</b>	=	Fourier transform-infrared
<b>H<sub>2</sub>Pc</b>	=	Metal free phthalocyanine
<b>HOMO</b>	=	Highest occupied molecular orbital
<b>HPLC</b>	=	High performance liquid chromatography
<b>IC</b>	=	Internal conversion
<b>IR</b>	=	Infrared
<b>ISC</b>	=	Intersystem crossing
<b>lcp</b>	=	Left circularly polarized
<b>L-cys</b>	=	L-cysteine
<b>LED</b>	=	Light emitting diode
<b>LUMO</b>	=	Lowest unoccupied molecular orbital
<b>MCD</b>	=	Magnetic circular dichroism
<b>ME</b>	=	Mercaptoethanol

<b>MeOH</b>	=	Methanol
<b>MO</b>	=	Molecular orbital
<b>MPA</b>	=	Mercaptopropionic acid
<b>MPc</b>	=	Metallophthalocyanine
<b>NHS</b>	=	N-hydroxysuccinimide
<b>NIR</b>	=	Near infrared
<b>NMR</b>	=	Nuclear magnetic resonance
<b>NR</b>	=	Non-radiative
<b>NRDR</b>	=	Non-radiative donor relaxation
<b>OD</b>	=	Optical density
<b>P</b>	=	Phosphorescence
<b>Pc</b>	=	Phthalocyanine
<b>PDT</b>	=	Photodynamic therapy
<b>PHT</b>	=	Photohyperthermia therapy
<b>PL</b>	=	Photoluminescence
<b>PMT</b>	=	Photomultiplier tube
<b>QD</b>	=	Quantum dot
<b>RBM</b>	=	Radial breathing modes
<b>rcp</b>	=	Right circularly polarized
<b>SEM</b>	=	Scanning electron microscopy
<b>SOC</b>	=	Spin orbit coupling
<b>S-S</b>	=	Singlet-singlet
<b>STM</b>	=	Scanning tunneling microscopy

<b>SWCNT</b>	=	Single-walled carbon nanotubes
<b>TBPO</b>	=	Tributylphosphine oxide
<b>TCSPC</b>	=	Time correlated single photon counting
<b>TD-DFT</b>	=	Time dependent-density functional theory
<b>TEM</b>	=	Transmission electron microscopy
<b>TFA</b>	=	Trifluoroacetic acid
<b>TGA</b>	=	Thermal gravimetric analysis
<b>TGA</b>	=	Thioglycolic acid
<b>THF</b>	=	Tetrahydrofuran
<b>TLC</b>	=	Thin layer chromatography
<b>TOP</b>	=	Trioctylphosphine
<b>TOPO</b>	=	Trioctylphosphine oxide
<b>T-T</b>	=	Triplet-triplet
<b>UV</b>	=	Ultraviolet
<b>UV-Vis</b>	=	Ultraviolet-Visible
<b>VR</b>	=	Vibrational relaxation
<b>XPS</b>	=	X-ray photoelectron spectroscopy
<b>XRD</b>	=	X-ray diffraction

## LIST OF SYMBOLS

$\alpha$	=	Fraction of light absorbed
$\beta$	=	Full width at half maximum
$B$	=	Field strength
$C_h$	=	Roll-up vector
$e^-$	=	Electron
$\epsilon$	=	Molar extinction coefficient
$\epsilon_S$	=	Singlet state extinction coefficient
$\epsilon_T$	=	Triplet state extinction coefficient
$g_L$	=	Landé factor
$h\nu$	=	Light
$I$	=	Intensity of light
$I_{abs}$	=	Intensity of light absorbed
$J$	=	Degree of spectral overlap of donor emission and acceptor absorbance spectra
$\kappa^2$	=	Dipole orientation factor
$\lambda_{Em}$	=	Wavelength of emission spectrum maximum
$\lambda_{Exc}$	=	Wavelength of excitation spectrum maximum
$\lambda_{exc}$	=	Excitation wavelength of phthalocyanines
$\lambda_{max}$	=	Wavelength maximum
$m$	=	Electric dipole moment
$\mu$	=	Magnetic dipole moment

$\mu_B$	=	Bohr magneton
$n$	=	Refractive index
$^1O_2 (^1\Delta_g)$	=	Singlet molecular oxygen
$O_2 (^3\Sigma_g^-)$	=	Ground state molecular oxygen
$\Phi_\Delta$	=	Singlet oxygen quantum yield
$\Phi_F$	=	Fluorescence quantum yield
$\Phi_{IC}$	=	Internal conversion quantum yield
$\Phi_{Pd}$	=	Photodegradation quantum yield
$\Phi_T$	=	Triplet quantum yield
$r$	=	Centre to centre separation distance between donor and acceptor
$R_0$	=	Critical distance at which efficiency of energy transfer is 50 %
$\tau_D$	=	Singlet oxygen lifetime
$\tau_F$	=	Fluorescence lifetime
$\tau_T$	=	Triplet state lifetime
$S_0$	=	Ground singlet state
$S_1$	=	Excited singlet state
$S_n$	=	$n^{\text{th}}$ singlet state
$T$	=	Temperature
$T_1$	=	First excited triplet state
$T_2$	=	Second excited triplet state
$T_n$	=	$n^{\text{th}}$ triplet state



# LIST OF FIGURES

1.1	Quantum confinement structural features and density of states	3
1.2	Schematic representation of a 2-dimensional graphite layer and the resultant SWCNT tubular structure	4
1.3	Schematic diagram of carbon nanotubes modified with biomolecules	5
1.4	Carbon nanotube chemical modification	6
1.5	Schematic illustration of QD nanocrystal coated with thiol solubilizing ligands	9
1.6	Illustration of the synthetic route to obtain thiol-capped CdTe QDs	11
1.7	Discrete energy levels of a QD	12
1.8	Size dependent fluorescence emission spectra of QDs	13
1.9	Absorption and fluorescence emission spectra of high quality QDs	14
1.10	Simplified diagram illustrating typical X-ray diffractogram of QDs	15
1.11	Basic structure of the nanoparticles used in this work	17
1.12	Molecular structure of metallophthalocyanines	18
1.13	Statistical condensation of two phthalonitriles	24
1.14	Structural representation of MPcs studied	27
1.15	Typical ground state electronic absorption spectra of symmetrical and low-symmetry MPcs	36
1.16	Electronic transitions in symmetrical and symmetry lowered MPcs	37
1.17	Exciton coupling in co-facial dimers and co-planar dimers	40
1.18	The origin of the Faraday $A_1$ , $B_0$ and $C_0$ terms in MCD spectra	42
1.19	A modified Jablonski diagram	46

<b>1.20</b>	Typical absorption and fluorescence emission spectra of an MPc	<b>48</b>
<b>1.21</b>	Typical fluorescence decay curve of QDs	<b>49</b>
<b>1.22</b>	Simplified Förster resonance energy transfer (FRET) Jablonski diagram	<b>51</b>
<b>1.23</b>	Typical triplet decay curve of MPcs	<b>54</b>
<b>1.24</b>	Typical singlet oxygen decay signal for MPcs	<b>62</b>
<b>2.1</b>	Schematic diagram of the TCSPC set-up	<b>73</b>
<b>2.2</b>	Schematic diagram of a laser flash photolysis set-up	<b>74</b>
<b>2.3</b>	Schematic diagram of a photochemical set-up	<b>75</b>
<b>2.4</b>	Schematic diagram of the singlet oxygen detection set-up	<b>76</b>
<b>3.1</b>	FT-IR spectra of SWCNT-COOH ( <b>1a</b> ) and SWCNT-NH <sub>2</sub> ( <b>1b</b> )	<b>105</b>
<b>3.2</b>	Raman spectra of SWCNT, <b>1a</b> and <b>1b</b>	<b>106</b>
<b>3.3</b>	TGA profiles of SWCNT, <b>1a</b> and <b>1b</b>	<b>108</b>
<b>3.4</b>	Electronic absorption spectra of MPA capped CdTe QDs ( <b>2</b> ) in aqueous media	<b>109</b>
<b>3.5</b>	Normalized electronic absorption and emission spectra of <b>2</b>	<b>110</b>
<b>3.6</b>	X-ray diffractogram of MPA capped CdTe QDs ( <b>2</b> )	<b>111</b>
<b>3.7</b>	Ground state electronic absorption spectra of ZnPc ( <b>22</b> ), CdPc ( <b>23</b> ) and HgPc ( <b>24</b> ) in DMSO	<b>114</b>
<b>3.8</b>	FT-IR spectrum of $\alpha$ -CdTtBuPhPc ( <b>28d</b> )	<b>119</b>
<b>3.9</b>	Electronic absorption spectra of Zn(II), Cd(II) and Hg(II) tetrapyridyloxy substituted complexes <b>25a</b> , <b>26a</b> and <b>27a</b> in (i) DMF and (ii) DMSO	<b>120</b>
<b>3.10</b>	Electronic absorption spectra of Cd(II) tetra (a) pyridyloxy, (b) phenoxy,	

	(c) <i>tert</i> -butylphenoxy and (d) benzyloxyphenoxy $\alpha$ -substituted ( <b>28a-d</b> ) and $\beta$ -substituted ( <b>26b-d</b> ) Pc complexes in (i) DMF and (ii) DMSO	121
<b>3.11</b>	Disaggregation absorption spectra of $\beta$ -CdTPyPc ( <b>26a</b> ) in CHCl <sub>3</sub>	126
<b>3.12</b>	Electronic absorption spectrum of $\beta$ -HgTPyPc ( <b>27a</b> ) in CHCl <sub>3</sub>	126
<b>3.13</b>	Electronic absorption spectra of $\beta$ -CdTBzPhPc ( <b>26b</b> )	127
<b>3.14</b>	Electronic absorption spectra of <b>26b</b> in THF, DMSO and CHCl <sub>3</sub>	129
<b>3.15</b>	Protonation of $\beta$ -CdTPhPc ( <b>26c</b> ) in CHCl <sub>3</sub> using TFA	131
<b>3.16</b>	Electronic absorption spectra of $\beta$ -ZnttbPc ( <b>29</b> ) and $\beta$ -ZnTMPyPc ( <b>30</b> )	134
<b>3.17</b>	Electronic absorption spectra of <b>22</b> , <b>30</b> and ZnPc-COOH ( <b>32</b> ) in CHCl <sub>3</sub>	139
<b>3.18</b>	Electronic absorption spectrum of <b>32</b> in DCM and Triton X-100	140
<b>3.19</b>	Electronic absorption and MCD spectra of ZnttbIPc ( <b>31</b> ) in CHCl <sub>3</sub>	141
<b>3.20</b>	Experimental and TD-DFT absorption spectra of <b>22</b> and ZnIPc	143
<b>3.21</b>	MO energy diagrams for <b>22</b> and ZnIPc	147
<b>4.1</b>	Normalized fluorescence emission spectra of ( <b>2</b> ) in aqueous media	150
<b>4.2</b>	Comparison of fluorescence emission spectra of <b>2</b> in (i) 0.1 M NaOH and (ii) DMF:water (4:1) solvent mixture	151
<b>4.3</b>	Absorption, fluorescence emission and excitation spectra of <b>30</b> in THF	152
<b>4.4</b>	Absorption, fluorescence emission and excitation spectra of <b>27a</b> , <b>28d</b> and <b>26b</b>	154
<b>4.5</b>	Absorption, fluorescence emission and excitation spectra of <b>31</b> in CHCl <sub>3</sub>	156
<b>4.6</b>	Absorption, fluorescence emission and excitation spectra of <b>32</b> in THF	157
<b>4.7</b>	Photoluminescence decay curves of <b>2</b> in (i) 0.1 M NaOH and (ii) DMF:water (4:1) solvent mixture	163

<b>4.8</b>	Transient absorption spectra of <b>31</b> and <b>26d</b> in toluene	<b>169</b>
<b>4.9</b>	Absorption spectra of <b>26a</b> in DMSO, before and after laser photolysis	<b>173</b>
<b>4.10</b>	Typical photodegradation of DPBF in the presence of MPc	<b>175</b>
<b>4.11</b>	Photodegradation spectral changes of <b>32</b> in CHCl <sub>3</sub>	<b>183</b>
<b>4.12</b>	Changes in absorption spectra of <b>28a</b> in DMF on photolysis	<b>185</b>
<b>5.1</b>	FT-IR spectra of <b>1a</b> , ZnPc( <b>31</b> )-SWCNT-linked ( <b>49</b> ) and <b>31</b>	<b>191</b>
<b>5.2</b>	FT-IR spectra of <b>1b</b> , <b>32</b> and ZnPc( <b>32</b> )-SWCNT-linked ( <b>50</b> )	<b>192</b>
<b>5.3</b>	FT-IR spectra of ZnPc( <b>31</b> ):SWCNT-adsorbed ( <b>51</b> ) and ZnPc( <b>32</b> ): SWCNT-adsorbed ( <b>52</b> )	<b>193</b>
<b>5.4</b>	Electronic absorption spectra of <b>31</b> , SWCNT, <b>1a</b> , <b>49</b> , <b>51</b> and ZnttbIPc+ SWCNT mixed composite (1:9 w/w) in DMF	<b>195</b>
<b>5.5</b>	Electronic absorption spectra of <b>32</b> , <b>1b</b> , <b>50</b> and <b>52</b> in DMF	<b>197</b>
<b>5.6</b>	Raman spectra of SWCNT, <b>1a</b> , <b>49</b> and <b>51</b>	<b>198</b>
<b>5.7</b>	Raman spectra of SWCNT, <b>1b</b> , <b>50</b> and <b>52</b>	<b>199</b>
<b>5.8</b>	TGA profiles of <b>1a</b> , <b>49</b> , <b>51</b> and <b>31</b>	<b>200</b>
<b>5.9</b>	TGA profiles of SWCNT, <b>1b</b> , <b>50</b> , <b>52</b> and <b>32</b>	<b>202</b>
<b>5.10</b>	Fluorescence emission spectra of <b>31</b> , <b>49</b> and <b>51</b> in DMF	<b>204</b>
<b>5.11</b>	Fluorescence emission spectra of <b>32</b> , <b>50</b> and <b>52</b> in DMF	<b>205</b>
<b>5.12</b>	Possible deactivation pathways of <b>31</b> or <b>32</b> upon photoexcitation	<b>206</b>
<b>5.13</b>	Fluorescence decay profile for <b>49</b> in DMF	<b>207</b>
<b>5.14</b>	FT-IR spectra of <b>2</b> , <b>31</b> , ZnPc ( <b>31</b> )-QD-linked ( <b>53</b> ) and ZnPc( <b>31</b> ):QD-mixed ( <b>54</b> )	<b>209</b>
<b>5.15</b>	Raman spectra of <b>2</b> , <b>31</b> , <b>54</b> and <b>53</b>	<b>210</b>

<b>5.16</b>	Electronic absorption spectra of <b>2</b> , <b>31</b> , <b>53</b> and <b>54</b>	<b>211</b>
<b>5.17</b>	Electronic absorption of <b>31</b> and fluorescence emission spectra of <b>2</b>	<b>215</b>
<b>5.18</b>	Fluorescence emission spectra of <b>2</b> , <b>53</b> and <b>31</b> in DMF:water	<b>216</b>
<b>5.19</b>	Fluorescence emission spectra of <b>2</b> , <b>54</b> and <b>31</b> in DMF:water	<b>216</b>
<b>5.20</b>	Normalized transient absorption spectra of <b>31</b> and <b>54</b> in DMF	<b>220</b>
<b>5.21</b>	$^1\text{O}_2$ decay curve for <b>31</b> in DMF-water	<b>222</b>

# LIST OF SCHEMES

<b>1.1</b>	Synthetic routes to obtain MPcs from different precursors	<b>20</b>
<b>1.2</b>	Synthesis of non-peripheral and peripheral tetra substituted MPcs	<b>22</b>
<b>1.3</b>	Synthesis of A <sub>3</sub> B type MPcs	<b>25</b>
<b>1.4</b>	Type I and Type II photochemical mechanisms	<b>58</b>
<b>1.5</b>	Reactions leading to the decay of singlet oxygen in solution	<b>60</b>
<b>1.6</b>	[4+2] cycloaddition reaction of MPc with singlet oxygen	<b>64</b>
<b>3.1</b>	Covalent functionalization of SWCNT	<b>104</b>
<b>3.2</b>	Synthesis of mercaptocarboxylic acid CdTe QDs	<b>109</b>
<b>3.3</b>	Synthetic routes to Zn(II), Cd(II) and Hg(II) tetra-aryloxy $\alpha$ - and $\beta$ -substituted Pc complexes	<b>116</b>
<b>3.4</b>	Syntheses of mono-substituted phthalonitriles, <b>46</b> and <b>47</b>	<b>117</b>
<b>3.5</b>	Synthetic route to $\beta$ -ZnttbPc, ( <b>29</b> ) and $\beta$ -ZnTMPyPc, ( <b>30</b> )	<b>132</b>
<b>3.6</b>	Syntheses of low-symmetry ZnttbIPc ( <b>31</b> ) and ZnPc-COOH ( <b>32</b> )	<b>137</b>
<b>5.1</b>	Synthesis routes to ZnPc( <b>31</b> )-SWCNT-linked ( <b>49</b> ) and ZnPc( <b>32</b> )-SWCNT-linked ( <b>50</b> )	<b>189</b>
<b>5.2</b>	Synthesis routes to ZnPc( <b>32</b> ):SWCNT-adsorbed ( <b>51</b> ) and ZnPc( <b>32</b> ):SWCNT-adsorbed ( <b>52</b> )	<b>190</b>
<b>5.3</b>	Synthetic route to ZnPc( <b>31</b> )-QD-linked conjugate ( <b>53</b> )	<b>208</b>

## LIST OF TABLES

<b>1.1</b>	List and structures of MPcs adsorbed on or linked to SWCNT	<b>31</b>
<b>1.2</b>	List and structures of MPcs adsorbed on or linked to QDs	<b>33</b>
<b>1.3</b>	Photophysical properties of some MPcs	<b>50</b>
<b>1.4</b>	The photochemical properties associated with some ZnPc derivatives	<b>63</b>
<b>3.1</b>	List of functionalized or synthesized nanoparticles	<b>103</b>
<b>3.2</b>	List of synthesized symmetrically and unsymmetrically tetra-substituted MPcs	<b>112</b>
<b>3.3</b>	Spectral properties of unsubstituted MPc complexes <b>22</b> , <b>23</b> and <b>24</b>	<b>115</b>
<b>3.4</b>	Spectral properties of Zn(II), Cd(II) and Hg(II) tetra-aryloxy substituted MPc complexes	<b>122</b>
<b>3.5</b>	Spectral data of zinc(II) phthalocyanine complexes, <b>29</b> , <b>30</b> , <b>31</b> and <b>32</b>	<b>135</b>
<b>3.6</b>	TD-DFT calculated spectra of <b>22</b> , Zn3B1N and ZnIPc	<b>145</b>
<b>4.1</b>	Spectral properties, fluorescence quantum yields and lifetimes of <b>2</b>	<b>151</b>
<b>4.2</b>	Fluorescence data of all complexes studied in various organic solvents	<b>158</b>
<b>4.3</b>	Triplet state quantum yields and lifetimes of the MPcs studied	<b>166</b>
<b>4.4</b>	Singlet oxygen and photodegradation quantum yields of MPcs studied	<b>176</b>
<b>5.1</b>	Absorption and fluorescence properties of linked and adsorbed MPc-SWCNT conjugates	<b>196</b>
<b>5.2</b>	Photophysical parameters of <b>31</b> in the presence of QDs in DMF:water	<b>213</b>
<b>5.3</b>	Time resolved fluorescence data for <b>2</b> in conjugates <b>53</b> and <b>54</b>	<b>214</b>
<b>5.4</b>	Energy transfer parameters for <b>53</b> and <b>54</b> in DMF:water	<b>217</b>

## **1. Introduction**

**This chapter gives a general overview of nanoparticles and metallophthalocyanines, including basic properties, nomenclature and associated characteristics. The characterization techniques used in this thesis have also been summarized.**



## 1.1 Nanoscience

Nanomaterials can be defined as aggregates of atoms within the nanometer (nm) size range. They are considered as a subdivision of a bulk material but possess properties that differ from those of pure bulk materials, as a result of their unique crystal structures [1,2]. In this work, nanomaterials i.e. single-walled carbon nanotubes (SWCNT) and quantum dots (QDs) will be linked to phthalocyanines, hence they are discussed.

### 1.1.1 Single-walled carbon nanotubes (SWCNT)

Since their discovery, by Iijima and Ichihashi [3,4] in 1991, carbon nanotubes have become the focal point of widespread scientific research owing to their outstanding chemical, mechanical and physical properties. Single-walled carbon nanotubes (SWCNT) are defined as quasi-1-dimensional (1-D) quantum structures or pseudo-quantum wires due to the spatial confinement of electrons in 2-dimensions (Figure 1.1) [1,2].

SWCNT consist entirely of elemental carbon in the  $sp^2$  hybridization; their structure is essentially a single graphite sheet rolled into a seamless hollow tube (Figure 1.2) with diameters ranging from 0.4-2 nm and lengths of several microns [5-8]. The orientation of the graphite plane relative to the tube axis and the tube diameter are pivotal in determining the unique physical properties associated with these structures which include high electrical conductivity, surface area, tensile strength, resilience, thermal stability and metallic to semiconducting current carrying capacity [6,9-14].

SWCNT have been known to absorb up to 100 times their own volume of hydrogen atoms, which makes them of particular use for storage of hydrogen for fuel cells [15]. In vitro medical studies have shown that these carbonaceous tubules are useful molecular

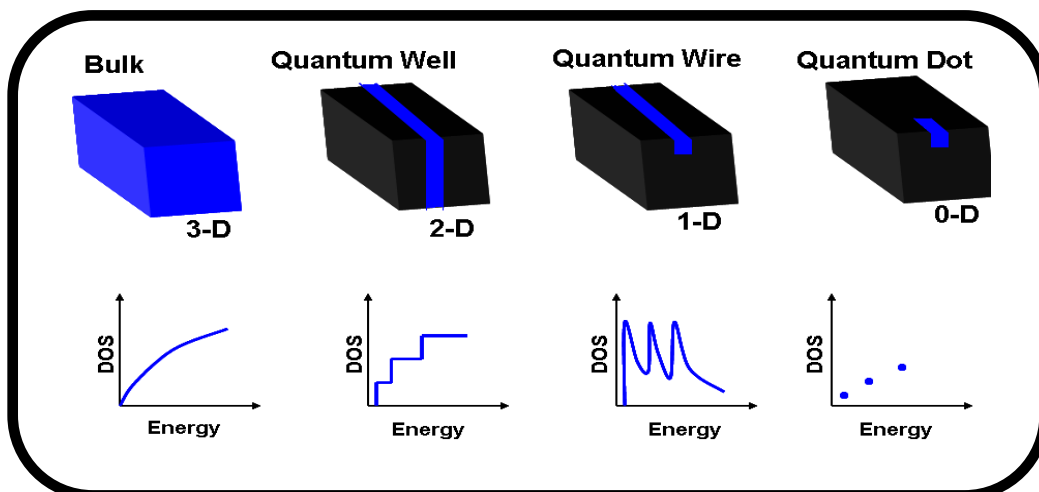


**Figure 1.1:** Quantum confinement structural features and density of states (DOS) effects [2].

transporters and can thus be used to deliver therapeutic drugs and diagnostic molecules into cells [16-19]. The ability of SWCNT to absorb light in the near-infrared (NIR) region and initiate cell death *via* a photothermal or photohyperthermia (PHT) effect [16] is of particular interest. Death of cancerous tissue is initiated since such tissue is sensitive to heat, while normal cells are often unaffected by application of high temperatures [20]. PHT is also known to improve the effectiveness of other cancer therapies such as chemotherapy, radiotherapy and photodynamic therapy (PDT). PDT is a cancer treatment that uses light, a photosensitizer and singlet oxygen to initiate cancer cell death.

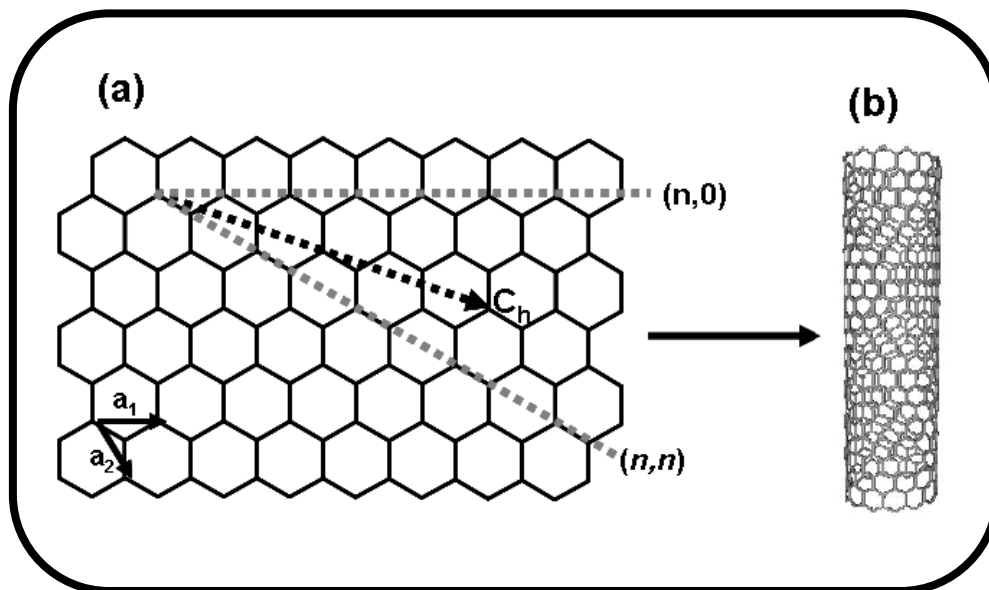


**Figure 1.2:** Schematic representation of (a) a 2-dimensional graphite layer with the lattice vectors  $a_1$  and  $a_2$  and the roll-up vector  $C_h = na_1 + ma_2 \equiv (n,m)$  and (b) the resultant SWCNT tubular structure [5].

The application of SWCNT in chemical, biochemical and biomedical applications is often limited by a lack of solubility [9,18,21,22]. End and side-wall functionalization is often necessary to enable solubilization, dispersion, dissolution and enhance the chemical compatibility of SWCNT with other molecules. Literature comments on two main modification pathways to functionalize SWCNT i.e. by covalent (Figure 1.3a and Figure 1.4) and non-covalent (adsorptive) (Figure 1.3b) means. Biomedical applications, in particular, make reference to an additional method; the hybrid approach whereby a small ‘anchor’ molecule is initially adsorbed onto the nanotube surface, following which covalent linkage occurs to the molecule of interest (Figure 1.3c) [18].

Covalent functionalization alters the conjugated  $sp^2$ -hybridized system to  $sp^3$ ; which is seldom a desired characteristic as many of the optical, electrical and thermal properties are dependent on the extended  $\pi$ -conjugated system.

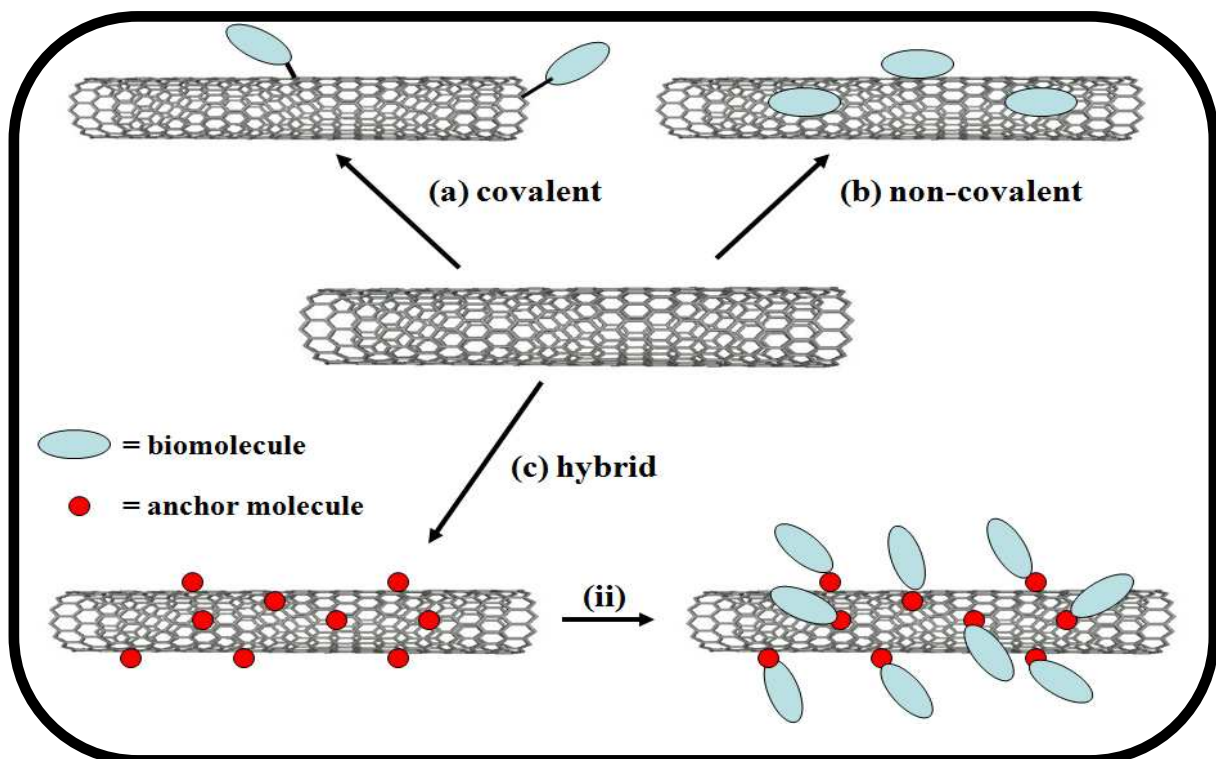


**Figure 1.3:** Schematic diagram showing the 3 main approaches to obtain modified carbon nanotubes with biomolecules (a) the covalent approach, (b) non-covalent approach and (c) hybrid approach (i) a small anchor molecule is attached non-covalently to the nanotube surface and then (ii) a chemical reaction links the biomolecule of interest to the anchor [18].

The introduction of carboxylic acid groups on carbon nanotubes is the most common method for covalent functionalization. This can be readily achieved by reaction under oxidative conditions using strong acids, such as  $\text{HNO}_3$  and or  $\text{H}_2\text{SO}_4$  which form carboxyl terminated groups primarily at the open ends or defect sides of SWCNT (Figure

1.4a) [6,9,10]. Such acid treatment generates dangling bonds that impart reactivity to the nanotubes [10]. Nitrene cycloaddition (Figure 1.4b), arylation, using diazonium salts (Figure 1.4c) or 1,3-dipolar cycloadditions (Figure 1.4d) can be employed for direct side-wall functionalization [7,23].

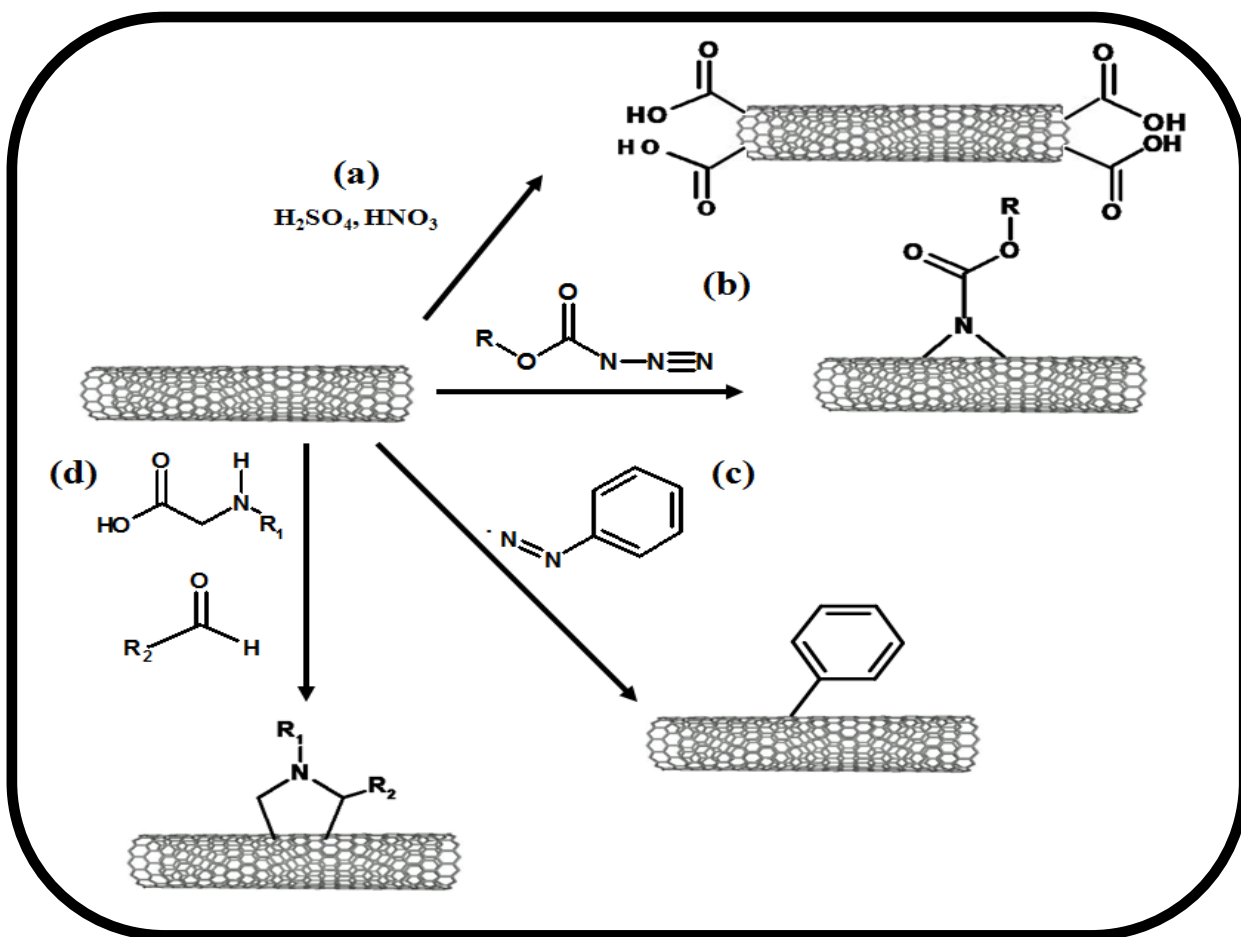


**Figure 1.4:** Carbon nanotube chemical modification by (a) oxidation using strong acids, (b) nitrene cycloaddition, (c) arylation using diazonium salts and (d) 1,3-dipolar cycloaddition [18].

Non-covalent surface modification is the result of intermolecular bonding processes, which preserve the  $\pi$ -conjugated backbone of the nanotubes and thus their intrinsic electronic and catalytic properties [1,22,24,25]. This functionalization is best served by

planar molecules that are capable of adsorbing onto the carbon nanotube surface *via*  $\pi$ - $\pi$  interactions [26,27]. The resulting strong interactions between carbon nanotubes and other aromatic molecules can serve as a platform for further functionalization, particularly with biomolecules [18].

In this work, acid and amine functionalized SWCNT will be used for the attachment of phthalocyanine (Pc) units. Development of such a bifunctional agent may be used in bimodal cancer therapy, combining PDT and PHT, for improved treatment of cancers. The SWCNT bound to Pc are thus characterized by fourier transform infrared (FT-IR), ultraviolet-visible (UV-Vis) electronic absorption and Raman spectroscopies [28-37].

### **1.1.2 Quantum dots**

Quantum dots (QDs) are defined as 0-dimensional semiconductor materials (Figure 1.1) as a result of quantum confinement of electrons in all 3 physical dimensions [1,2]. They are often synthesized from elements that belong to groups 12-14 or 13-15 with physical dimensions smaller than the exciton Bohr radius; usually less than 10 nm [2,38-40]. QDs have quantized energy which gives way to their unique optical properties, which lie between those of bulk and atomic materials [2,38-41]. Of particular interest is their broad absorption spectrum, which allows excitation over a broad range of wavelengths and their size tunable narrow emission spanning the ultraviolet (UV) to infrared region [39,42], which makes them well suited for imaging applications [43,44]. They also show great promise due to their excellent photostability [42].

Due to their size dependent properties, QDs have also found application in various fields including high-density data storage, chemical sensing, optics, telecommunications,

computing and more extensively in biomedicine [2,39,41,45]. Recently QDs have found focus as a new generation of photosensitizers in photodynamic therapy (PDT) [41,45-47]. QDs are capable of transferring energy to ground state molecular oxygen to generate cytotoxic singlet oxygen and thus enhance the efficacy of PDT [46,48,50]. The singlet oxygen generating capabilities of QDs are limited [46], therefore conjugation of QDs to a mediating PDT photosensitizer e.g. a metallophthalocyanine, facilitates the probability of increased PDT efficiency through energy transfer (ET).

Therefore, the aim in this work is to synthesize mercaptopropionic acid (MPA) capped CdTe QDs. The terminal –COOH groups of the MPA capping agent will facilitate conjugation to mono-substituted phthalocyanines *via* the formation of an amide bond. Such biomolecules are of particular use for the imaging and therapeutic treatment of cancers.

#### **1.1.2.1 Aqueous synthesis of QDs**

QD synthesis is often tailored to specific requirements. Biomedical applications often require water-soluble systems to enable biological compatibility. For high quality QDs with narrow size distribution within 2 % [51], attention must be focused on the core, shell and coating characteristics, all of which may influence the photophysical properties i.e. photoluminescence (PL) quantum yields and luminescence lifetimes. Several methods exist for the surface modification of QDs [47,52,53] but currently two synthetic strategies are used to prepare QDs; non-aqueous and aqueous synthesis. The former, more common method produces QDs by pyrolysis of organometallic precursors in high boiling point organic solvents such as trioctylphosphine (TOP) or trioctylphosphine oxide (TOPO) to

give hydrophobic QDs [54-56]. Further modification is necessary to transfer the hydrophobic QDs to the aqueous phase; steps which often result in decreased photoluminescence [57-59]. Alternatively, the aqueous synthetic route is cheaper and more reproducible and produces water-soluble biocompatible QDs directly without the need for further modification [60].

Therefore organic cappings that produce water-soluble QDs are frequently used for functionalization. Thiol moieties such as MPA are commonly used for surface attachment (Figure 1.5), while terminal carboxyl groups facilitate hydrophilic interactions and

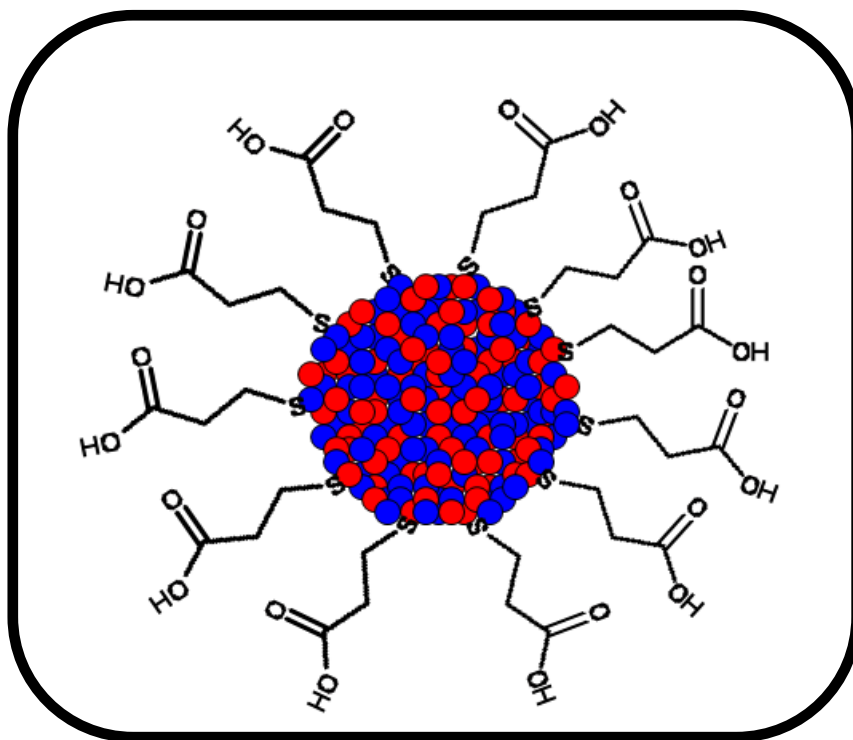


**Figure 1.5:** Schematic illustration of a QD nanocrystal coated with thiol solubilizing ligands.

bioconjugation to other molecules [57,61]. Thiol groups are also useful in suppressing intermittence of emission (blinking) [62]. Following surface functionalization, further



molecular interactions can be achieved *via* covalent attachment, electrostatic forces, adsorption, hydrogen bonding and silanization [38,63].

The most common aqueous synthetic procedure is the hydrothermal method (Figure 1.6) [60,64,65]. It has been used for the synthesis of a variety of nanocrystals i.e. CdS, CdSe, CdTe, ZnS, ZnSe and HgTe. The focus of this work has been on CdTe. The method involves dissolution of the salt of interest e.g. Cd, in water followed by the addition of a stabilizer e.g. MPA, thioglycolic acid (TGA) under an inert, oxygen free, atmosphere, to form the Cd precursor solution. NaOH is added to adjust the solution pH to alkaline conditions. Rapid injection of a freshly prepared NaHTe (for CdTe QDs) solution [66-68], follows, which reacts with  $\text{Cd}^{2+}$  and thus affords an aqueous colloidal CdTe solution. The introduction of heat ( $\sim 100^\circ\text{C}$ ) progresses QD growth *via* the Ostwald ripening process [69], which is subsequently terminated once the desired emission properties are attained. Under the basic pH conditions used for the reaction, the stabilizer binds to the QD surface and the carboxylic end is deprotonated into carboxylate and thus renders the QD water-soluble [70]. During growth, the stabilizer is responsible for control of the size and shape distribution, crystal structure and stability [71].

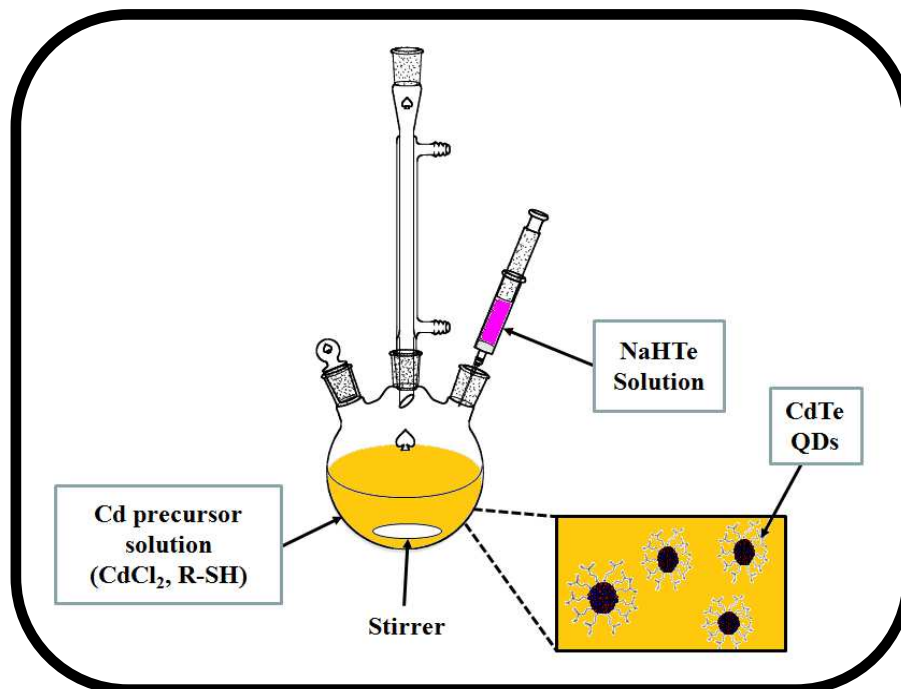


**Figure 1.6:** Diagram illustrating the synthetic route to obtain thiol-capped CdTe QDs.

### 1.1.2.2 Absorption and fluorescence spectra of QDs

The properties of bulk semiconductors are dependent on the energy bandgap between its valence and conduction band. A progression from bulk material to QDs results in discreteness and the density of states ceases to be continuous. As a result, there are a specific number of well-separated states for the electrons to occupy at a given energy (Figure 1.7) [72,73].

Any alteration in the crystal size alters the size of the bandgap, where a decrease in size results in a larger bandgap identified by a shift in the absorption spectra from the infrared to the visible region. This allows one to tune the electronic and optical characteristics of the nanomaterial. Figure 1.8 shows the influence of size changes on the emission properties of QDs.

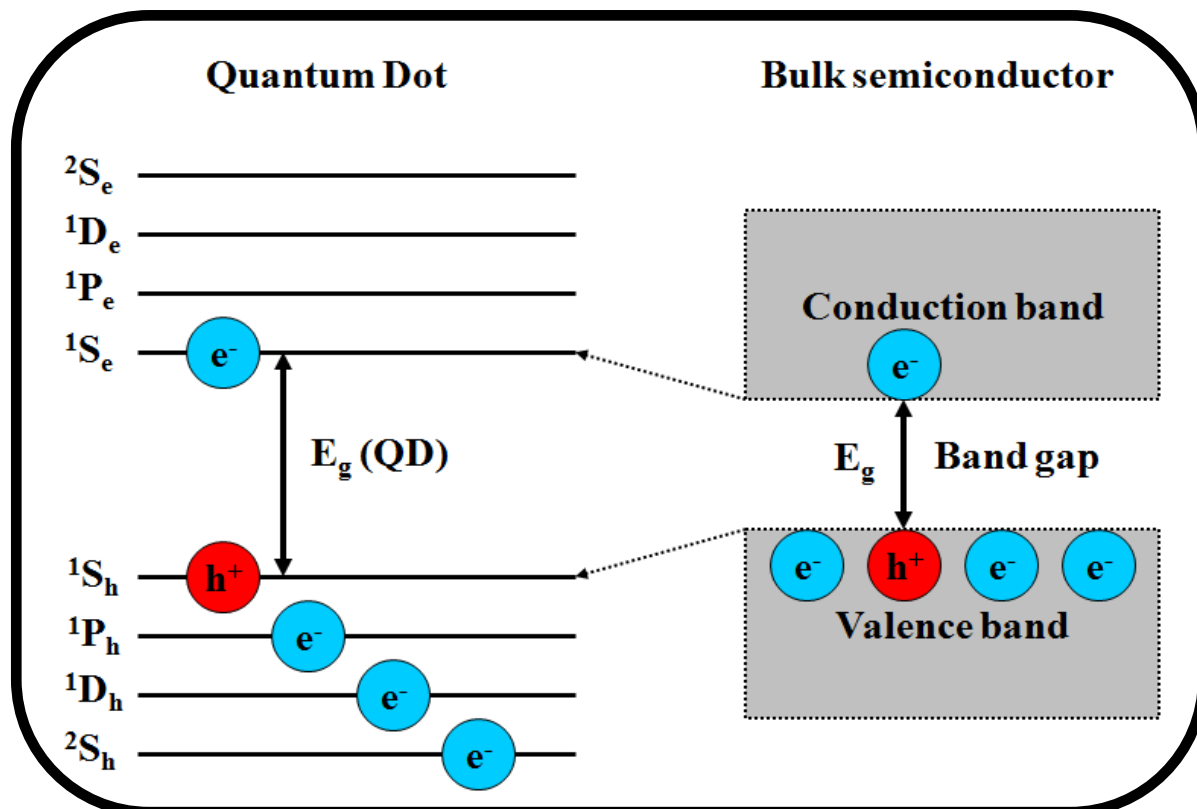
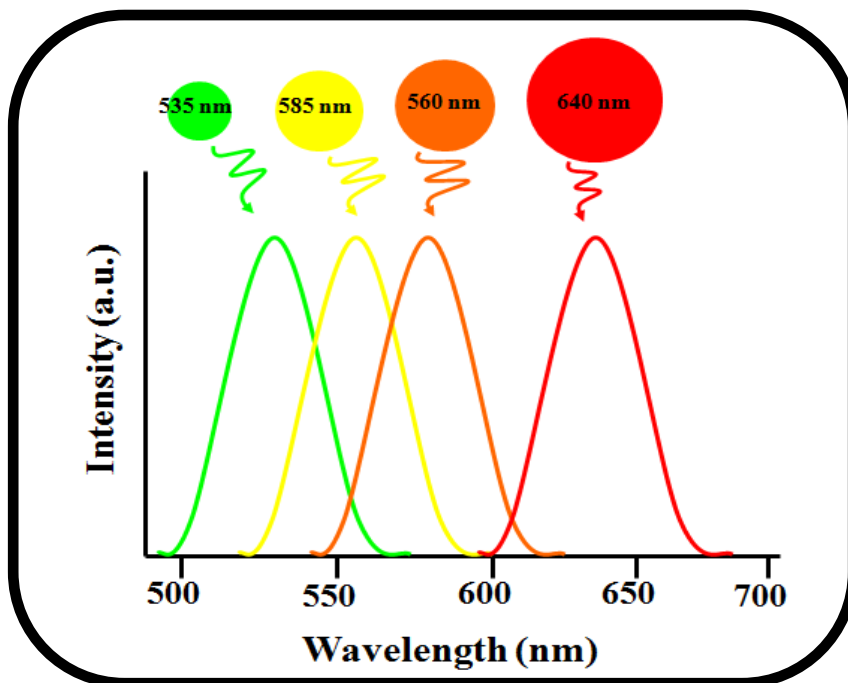


Figure 1.7: Simplified diagram illustrating discrete energy levels of a QD compared to the continuous levels in a corresponding bulk semiconductor crystal [72].

The typical absorption spectra of QDs are characterized by sharp well resolved features (Figure 1.9). Broadening is often a consequence of dispersion in size and shape distribution. The lack of well resolved features may also be influenced by growth conditions i.e. temperature, pH and solvent properties, presence of defects and solution concentrations used for the spectra. Band flattening in CdTe QDs has been attributed to more pronounced confinement [40].



**Figure 1.8:** Size dependent fluorescence emission spectra of QDs. QDs have been drawn to scale.

The radiative recombination [74] of excitons or free carriers in QDs leads to narrow distinctive photoluminescence or fluorescence emission spectra (Figure 1.9).

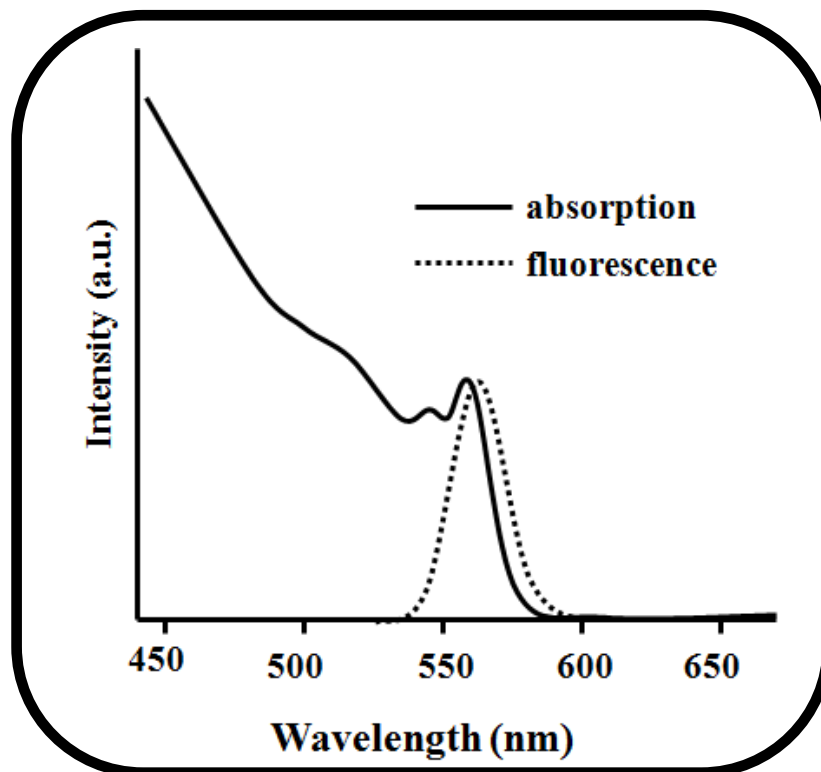


**Figure 1.9:** Classic absorption and fluorescence emission spectra of high quality QDs [55].

### 1.1.3 Methods of characterizing nanoparticles

A broad inventory of characterization and analytical techniques, other than those discussed, applies to nanostructure materials. In general two fundamental techniques exist for characterization of nanomaterials: imaging by microscopy and analysis by spectroscopy [75].

X-ray diffraction (XRD) is a spectroscopic technique used for elucidation of structural information relating to the crystal lattice, Figure 1.10 [66,76,77]. The mean particle size can be determined using the Scherrer equation [78].

$$d(\text{\AA}) = \frac{k\lambda}{\beta \cos\theta} \quad (1.1)$$

where  $k$  is an empirical constant (0.9),  $\lambda$  is the X-ray source wavelength (1.5405 Å for Cu),  $\beta$  is the full width at half maximum (FWHM) of the diffraction peak, and  $\theta$  is the angle of the peak (Figure 1.10).

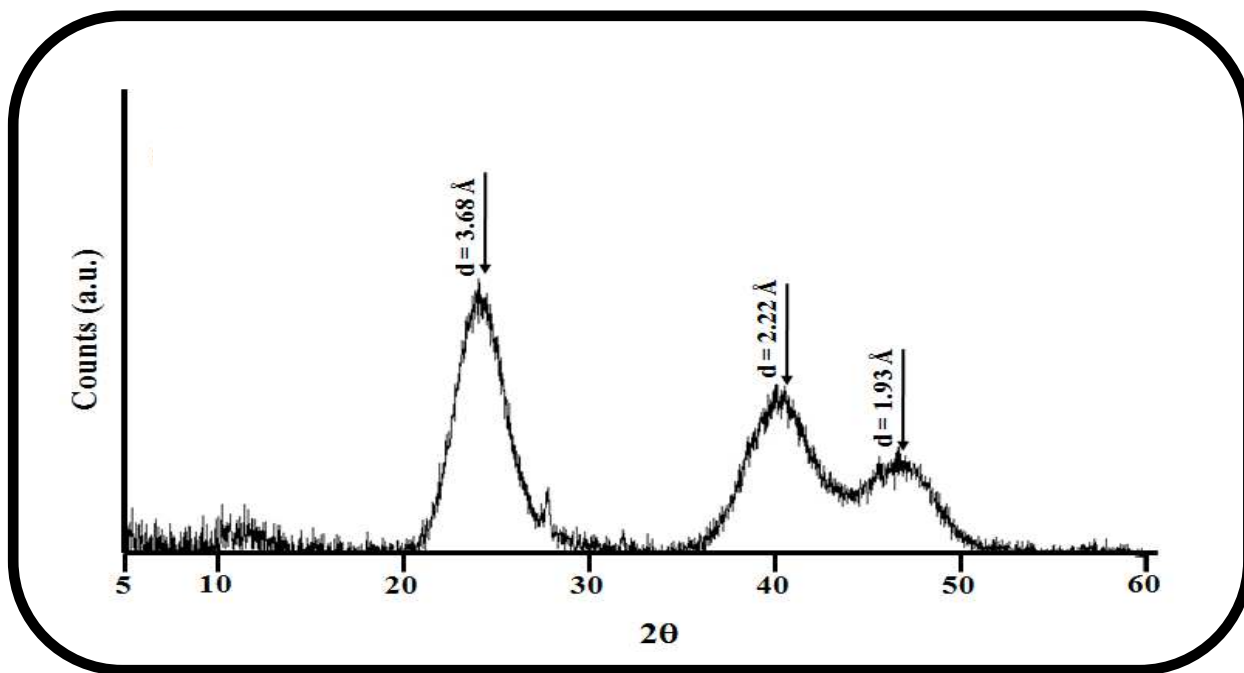


**Figure 1.10: Simplified diagram illustrating typical X-ray diffractogram of QDs [76,77].**

Fourier transform infrared spectroscopy (FT-IR) can be used for asymmetrical vibration analysis. It is particularly useful for the characterization of chemically functionalized CNT. Raman spectroscopy similarly is often used for characterization of SWCNT. Raman spectra of SWCNT are distinguished from other forms of carbon by 2 dominant Raman signatures i.e. the radial breathing modes (RBM) between  $100 - 300 \text{ cm}^{-1}$  and the G band, typically found around  $1590 \text{ cm}^{-1}$ . UV-Vis electronic absorption spectroscopy is often employed for analysis of the optical properties that accompany nanoparticles such as SWCNT and QDs. Thermal gravimetric analysis (TGA) is a thermodynamic

characterization method that records the mass loss or gain from a sample versus temperature. The technique may be considered spectroscopic, where different decay profiles point to structurally different materials and provides information related to phase changes, thermal stability and composition.

X-ray photoelectron spectroscopy (XPS) is used for surface analysis and depth profiling. Scanning electron microscopy (SEM) gives high-resolution images of the sample surface and transmission electron microscopy (TEM) is used to probe the internal surface structure and give access to morphological fine structural details. Atomic force microscopy (AFM) and scanning tunneling microscopy (STM) are scanning probe methods, both of which provide surface topological information, and imaging of the surface structure. Other commonly employed techniques include solid-state nuclear magnetic resonance spectroscopy (NMR) and differential scanning calorimetry (DSC) [19,36].

In this thesis, XRD, FT-IR, UV-Vis and Raman spectroscopies and TGA have been used to elucidate the structural properties of SWCNT functionalized with carboxylic acid groups (-COOH, **1a**) or ethylamine units (**1b**) and MPA capped CdTe QDs (**2**) (Figure 1.11) and the interaction of these materials with metallophthalocyanines.

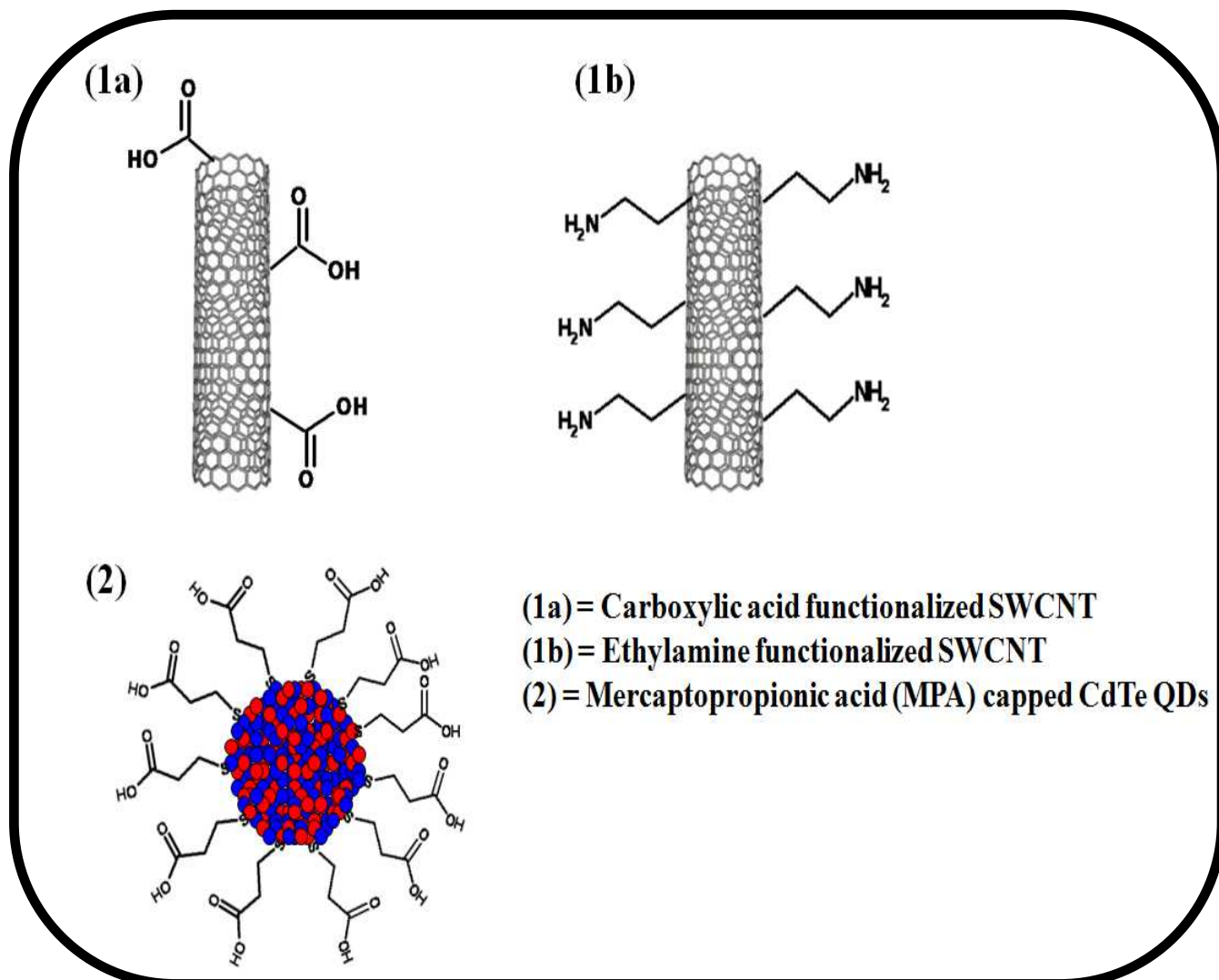
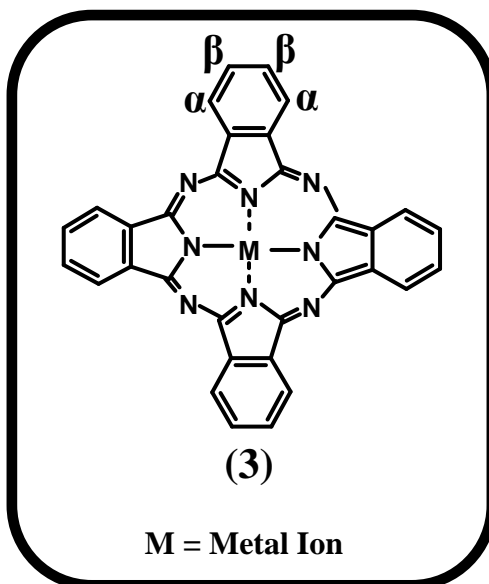


Figure 1.11: Basic structure of the nanoparticles used in this work.



## 1.2 Metallophthalocyanine (MPc) Chemistry

Since their discovery in the early 1900s, the chemistry of phthalocyanines (Pcs) has been studied extensively owing to their high chemical and thermal stability, high degree of aromaticity, synthetic flexibility and ability to adapt to a wide range of applications. The term, ‘phthalocyanine’ was initially conceived by Linstead as a result of its structural origin from a phthalic acid precursor and ‘cyanine’ which refers to their blue colour [79-82]. Metallophthalocyanines (MPcs, **3**) are planar, tetrapyrrolic macrocyclic aromatic compounds which absorb strongly in the red end region of the visible spectrum due to their highly conjugated 18- $\pi$  electron system (Figure 1.12). Variation in the central metal, type, number and position of substituents (either  $\alpha$ -non-peripheral substitution,  $\beta$ -peripheral substitution or axial substitution), attached to the MPc macrocycle, greatly influence the robust chemical properties that make them applicable in a diverse range of fields [83,84].



**Figure 1.12:** Molecular structure of metallophthalocyanines (MPcs).

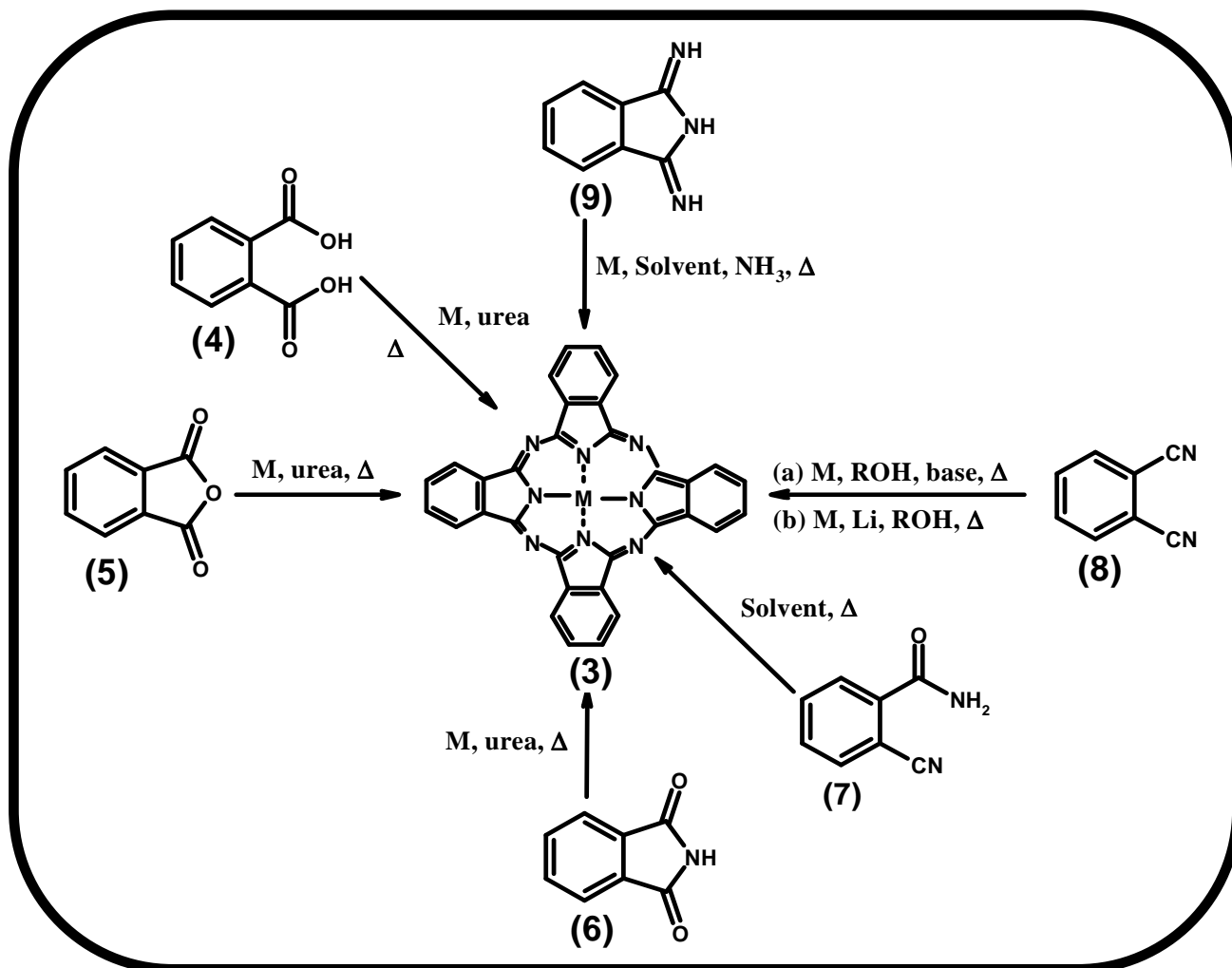
Commercial applications, in which MPcs are mostly used as dyes, rely on their characteristic intense blue-green colour, chemical stability and their exceptional fastness to light [85]. They have also found application in high-technology industrial applications; as photoconductors in laser printing devices, for optical data storage in the form of rewritable optical media (CD-RW) [86], in photochemical and photovoltaic cells for energy conversion [87], non-linear optics [88,89], Langmuir-Blodgett thin films [90,91], field effect transistors [92], chemical sensors [93], liquid crystals [94-96], as catalysts for degradation of pollutants [97] and in medicine, particularly as photosensitizers in PDT [98-101] and as photocatalysts [102-104].

Extensive research has gone into the use of MPc photosensitizing properties for therapeutic cancer treatment i.e. PDT which combines the selectivity of fibre optic directed light with the cell destruction properties of singlet oxygen. For ease of administration *via* injection into the blood stream and transport across lipid membranes, water soluble, lipophilic derivatives have often been considered for PDT [98-100,105,106]. The covalent or non-covalent conjugation of MPcs to site specific molecules, such as proteins, for targeted drug delivery, has also been reported [107].

### **1.2.1 Phthalocyanine syntheses**

Success of the synthetic approach is dependent on several factors namely choice of: precursor, metal salt (metals, metal salts, oxides, sulphates and halides), solvent (high boiling point solvents), temperature (to facilitate melting of the precursor and rapid cyclotetramerization), base and catalyst.

The most common routes involve the use of different phthalyl groups (Scheme 1.1) i.e. phthalic acid (**4**) [108], phthalic anhydride (**5**) [109], phthalimide (**6**) [110], *o*-cyanobenzamide (**7**), phthalonitrile (**8**) [111] or 1,3-diminoisoindoline (**9**). The use of phthalonitrile precursors is considered the simplest approach and generally gives highly pure products.



**Scheme 1.1:** Synthetic routes to obtain MPcs from different precursors.

Phthalonitriles are often reacted at high temperature in the presence of a metal salt and a basic solvent, such as *N,N*-dimethylaminoethanol (DMAE) to afford cyclization of the Pc macrocycle. Alcoholic solvents e.g. 1-pentanol in combination with bases such as 1,8-

diazabicyclo[5.4.0]undec-7-ene (DBU), 1,5-diazabicyclo[4.3.0]non-5-ene (DBN), piperidine or cyclohexylamine can be used as an alternative route which facilitates mild and efficient cyclotetramerization of the phthalonitrile to the Pc [112].

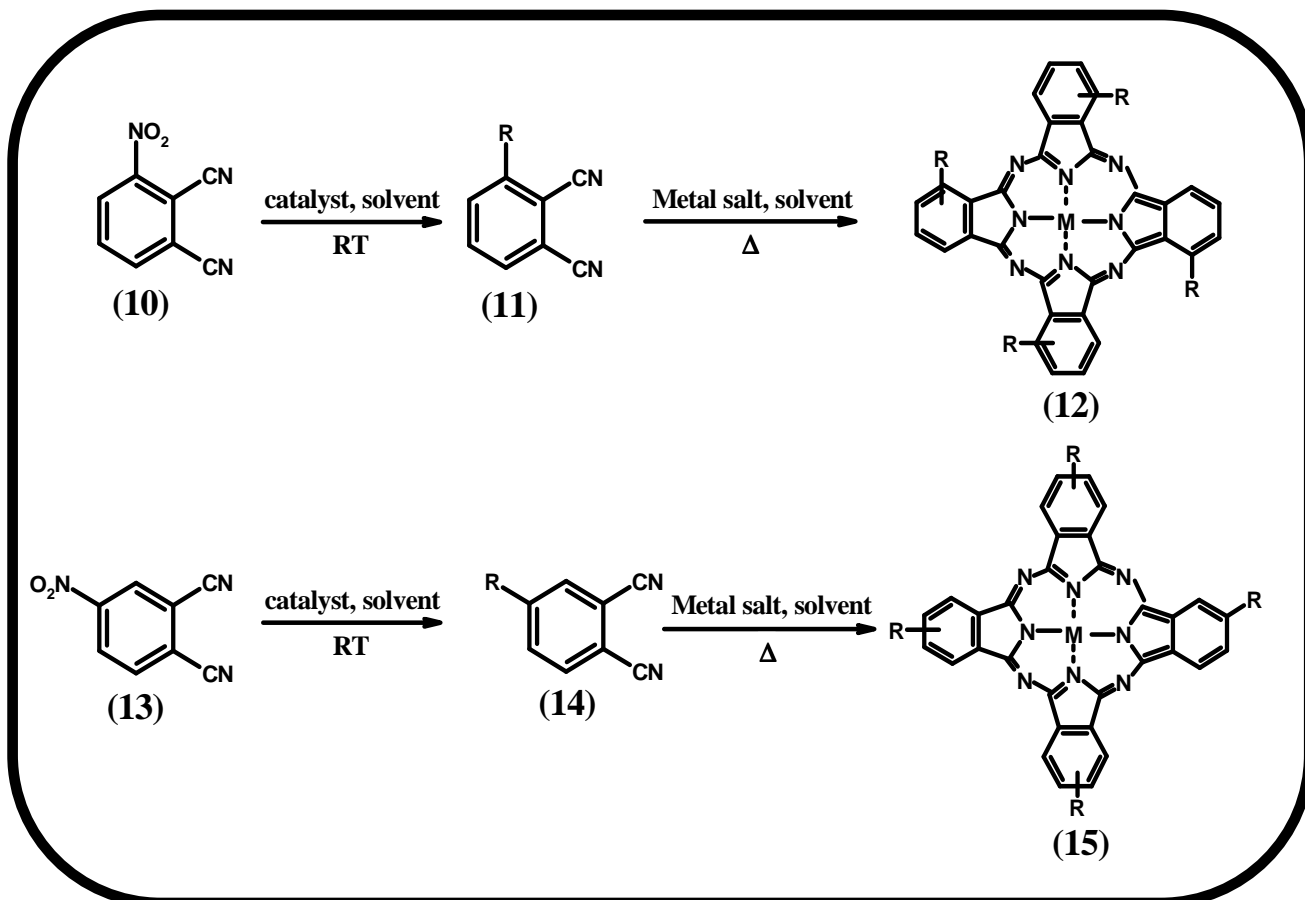
Labile metals such as lithium or sodium may be used for synthesis of Pcs with large central metals. Labile metal ions can be easily exchanged within the reaction vessel to form the desired MPc [113]. The presence of urea, which acts a source of nitrogen, and catalysts such as ammonium molybdate or boric acid, may also promote cyclization to form the Pc ring when using phthalic anhydride and phthalimide precursors [114].

### 1.2.1.1 Symmetrically ring-substituted phthalocyanines

Substitution at either the  $\alpha$  (non-peripheral),  $\beta$  (peripheral) or axial positions of the MPc is known to enhance their solubility. Variation in the number of substituents attached to the Pc ring is achieved by the condensation of mono-, di- or tetra-substituted phthalonitriles, to produce the corresponding symmetrical tetra-, octa- or 16-substituted Pcs [115,116].

The condensation of phthalonitrile (**8**) monosubstituted at either the 3 or 4-position [117,118] gives tetra substituted Pcs (Scheme 1.2), usually as a mixture of positional isomers with  $C_{4h}$ ,  $D_{2h}$ ,  $C_{2v}$ , and  $C_s$  symmetries, with a relative allocation of 12.5 %, 12.5 %, 25 % and 50 % respectively [119,120] for the  $\beta$ -substituted (Figure 1.12) complexes. Allocation in  $\alpha$ -substituted (Figure 1.12) Pc complexes depends on the central metal ion and structure of the substituents. Isolation to give a single isomer can be achieved using specifically designed high performance liquid chromatography (HPLC) separation techniques, which are very difficult and often time consuming [121]. However, it has

been found that the enhanced solubility that often accompanies tetra substituted Pcs is a result of the presence of such isomers in addition to the use of bulky substituents, which prevent aggregation. The use of a mixture containing such isomers may be more useful than a single isomer, therefore purification steps to give a single isomeric compound have been omitted in this work.



**Scheme 1.2:** Synthesis of non-peripheral (12) and peripheral (15) tetra substituted MPcs from monosubstituted phthalonitriles (10) and (13).

### 1.2.1.2 Low-symmetry $\text{A}_3\text{B}$ type phthalocyanines

In recent years, research focus has shifted to studies on unsymmetrical Pc systems. The intrinsic symmetry of the Pc molecule at times presents limitations for various purposes;

therefore lowering the symmetry allows the co-existence of different functionalities and the fine tuning of their physical properties for various applications [122-126].

A<sub>3</sub>B type phthalocyanines consist of one different and three identical isoindole subunits. There are 3 main synthetic approaches that can be employed to obtain these Pcs: the statistical condensation route [127-129], the polymer support route [130,131] and the subphthalocyanine (SubPc) route [132]. Owing to its simplicity, the statistical condensation approach is the most widely applied method to obtain these molecules. It is a non-selective method based on the reaction of two differently substituted phthalonitriles or 1,3-diiminoisoindolines (A and B) to afford in principle, a mixture of six compounds as indicated in Figure 1.13 [133,134]. The desired product can be isolated from the statistical mixture of compounds using chromatographic separation techniques.

Increased solubility, less tendency to aggregate and reduced number of products can be attained by adding, at least one bulky or rigid group to the Pc macrocycle [135,136].

In the quest to obtain optimum yields of the desired A<sub>3</sub>B derivative, particular consideration must be given to the stoichiometry of the reactants. Often a 3:1 ratio for two precursors of similar reactivity affords a mixture of products in the following predicted percentages: A<sub>4</sub> (33 %), A<sub>3</sub>B (44 %) and 23 % for other cross-condensation products. Therefore a 3:1 ratio is commonly administered for favourable formation of the A<sub>3</sub>B type Pc [137-139]. Modification of the stoichiometry, to higher ratios, may be necessary upon consideration of the relative reactivity of the precursors involved, for example, A:B molar ratios of up to 9:1 may be used when the reactivity of B exceeds that of A [140,141].

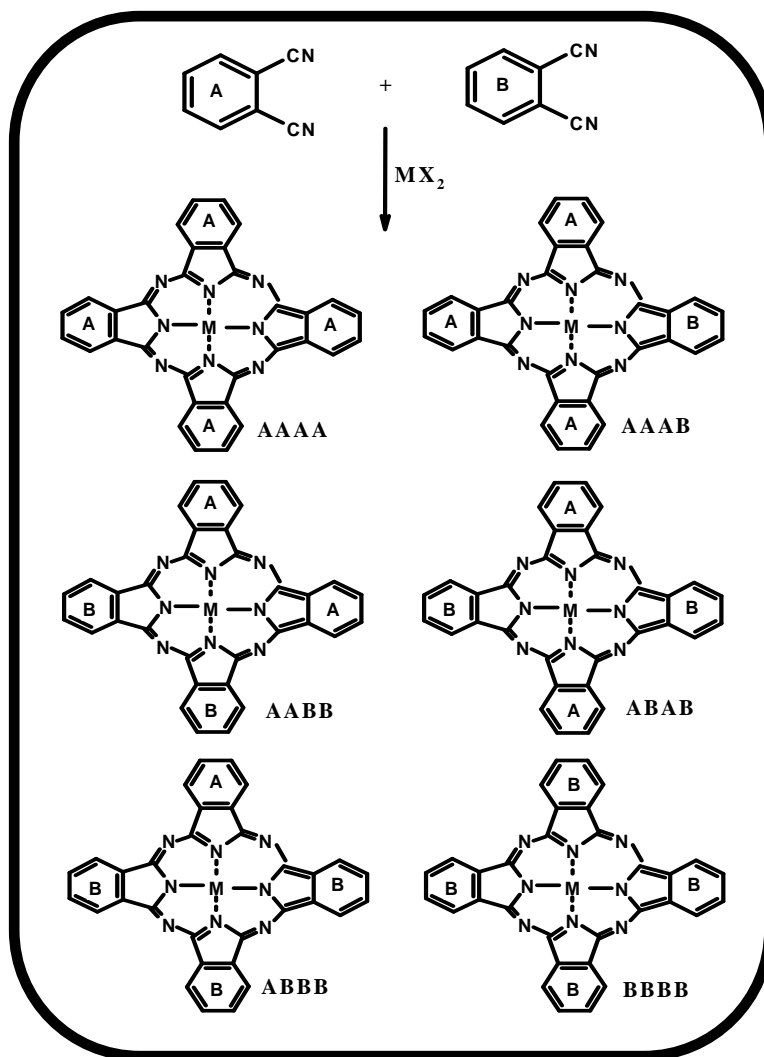
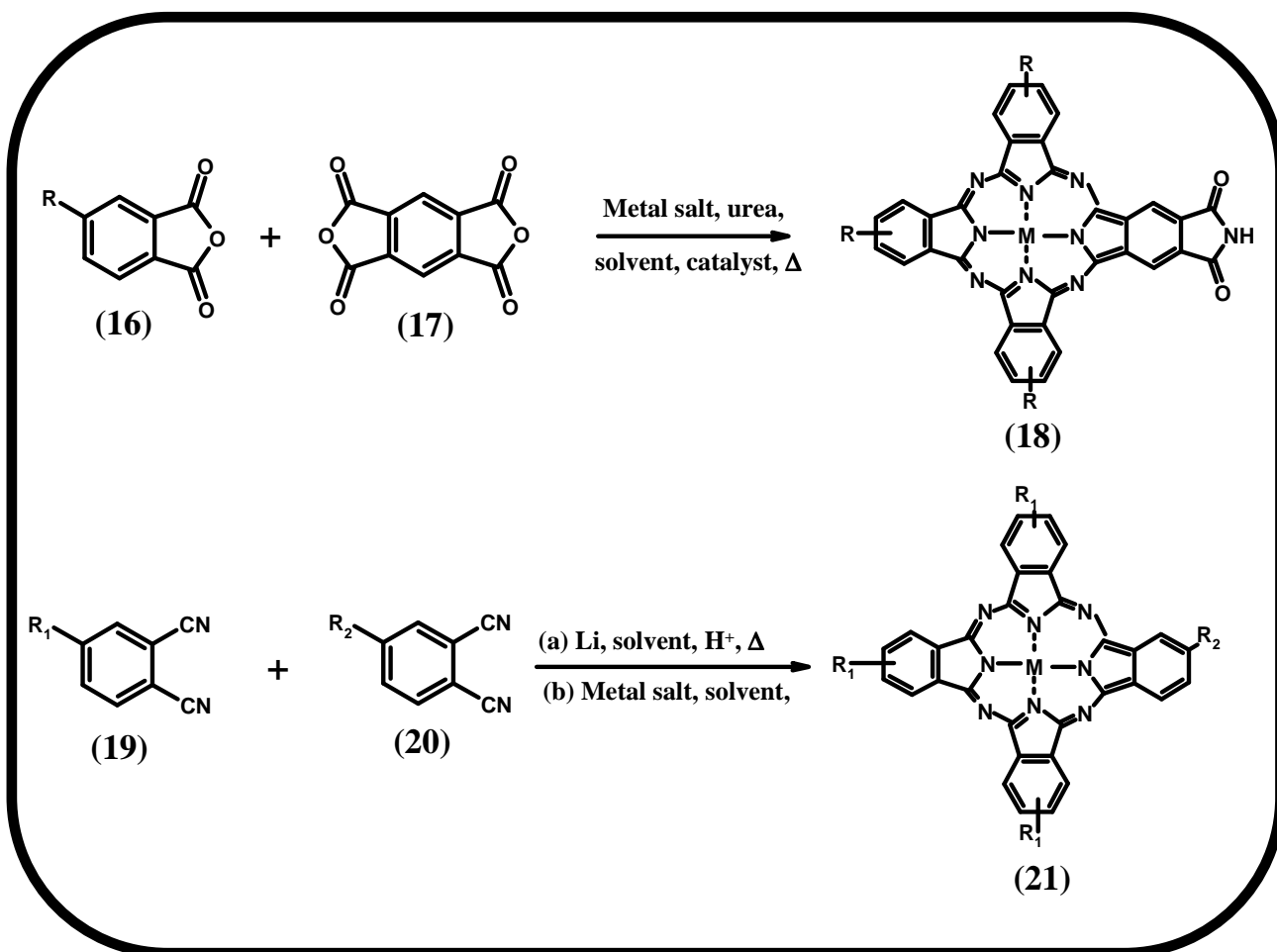


**Figure 1.13: Statistical condensation of two phthalonitriles to give 6 possible products [133,134].**

In this work, the desired low-symmetry derivatives have been prepared using conventional methods and involve either reaction between a substituted phthalic anhydride (**16**) and a phthalic dianhydride (**17**) precursor or reaction of two differently substituted phthalonitrile derivatives (**19** and **20**) (Scheme 1.3).



Scheme 1.3: Synthesis of A<sub>3</sub>B type MPcs.

### 1.2.1.3 Phthalocyanines synthesized in this work

The structures of the phthalocyanines that have been synthesized and studied in this work are shown in Figure 1.14. The synthetic routes used to obtain unsubstituted MPc derivatives of zinc (22), cadmium (23) and mercury (24) are well documented in literature [142-144]. Photophysical studies have indicated the excellent photosensitizing ability of ZnPc (22) [145,146] and its substituted derivatives, such as tetrakis{2,(3)-pyridyloxyphthalocyaninato}zinc(II) (ZnTPyPc, 25a), which has been reported, but containing a 3-pyridyloxy substituent [147] instead of 2-pyridyloxy which is

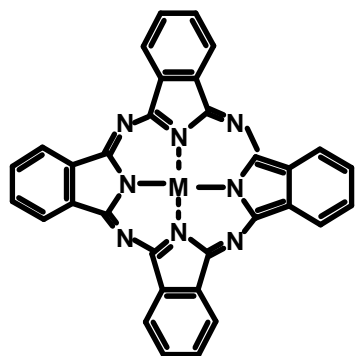


used in this work. However, the photophysical properties associated with ZnTPyPc (**25a**) was not reported. Similarly the synthesis of substituted tetrakis{2,(3)-pyridyloxyphthalocyaninato}cadmium(II) (**CdTPyPc, 26a**) and tetrakis{2,(3)-pyridyloxyphthalocyaninato}mercury(II) (**HgTPyPc, 27a**) derivatives is reported here for the first time. In general, there have been inadequate studies on CdPc and HgPc derivatives.

A few reports have described the synthesis and spectroscopic properties of octa-alkyl substituted CdPc derivatives [148,149]. However, there is no literature on tetra-substituted CdPc derivatives. CdPc complexes are expected to show enhanced triplet state properties; a characteristic that may be exploited in photocatalytic applications. It is for this purpose that aryloxy substituted CdPc derivatives (**26a-d** and **28a-d**) will be synthesized and their photophysical properties studied. The choice of the substituents is based on their bulkiness, often known to prevent aggregation and enhance solubility.

Mystery surrounds the spectroscopic behaviour of HgPcs. Although some records make mention of HgPc complexes [150,151], not much is known about their photosensitizing tendencies. They have been used for the catalytic degradation of hydrogen peroxide [152], but there are no other reports on their triplet state yields and singlet oxygen producing capabilities to determine their efficacy in photocatalysis. In this work we report the photophysics and photochemistry associated with unsubstituted HgPc (**HgPc, 24**) and a new pyridyloxy-substituted derivative (**HgTPyPc, 27a**).

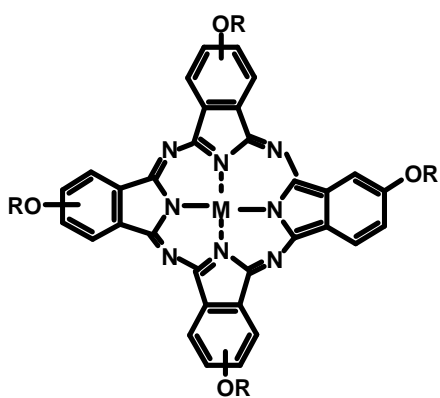
The synthesis of numerous symmetrical zinc phthalocyanine analogues, such as tetrakis{2,(3)-*tert*-butylphthalocyaninato}zinc(II) ( **$\beta$ -ZnttbPc, 29**) [153] and



(22) ZnPc : M = Zn

(23) CdPc : M = Cd

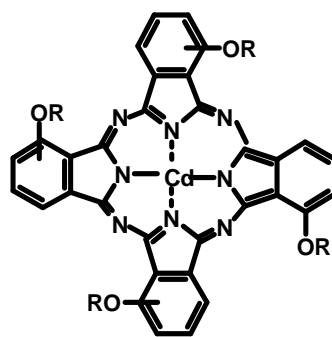
(24) HgPc : M = Hg



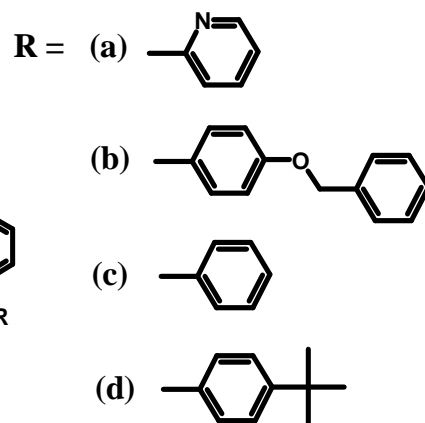
(25) M = Zn

(26) M = Cd

(27) M = Hg



(28)



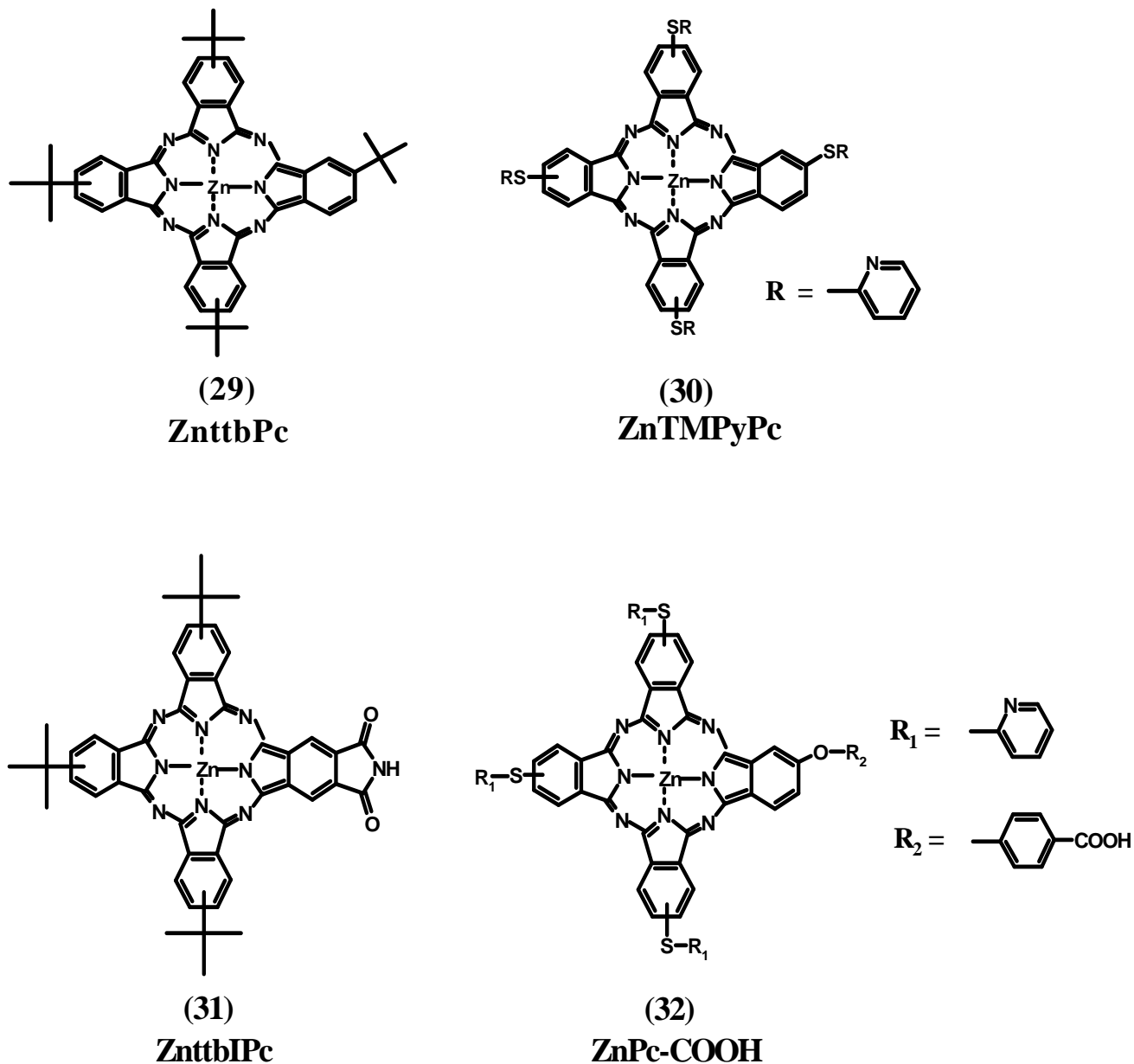


**Figure 1.14:** Structural representation of MPcs studied.

tetrakis{2,(3)-mercaptopyridinephthalocyaninato}zinc(II) ( $\beta$ -ZnTMPyPc, **30**) [154], have been investigated, however synthesis of their low-symmetry counterparts has not been reported. Unsymmetrically substituted MPcs present interesting spectroscopic chemistry but there are limited accounts of their photophysicochemistry [155,156].

Reported in this work, is the development of new low-symmetry ZnPc derivatives, tris{9 (10), 16 (17), 23 (24)-(tert-butyl)imidophthalocyaninato}zinc(II) (**ZnttbIPc, 31**) and tris{9 (10), 16 (17), 23 (24)-(4-2-mercaptopyridine)-2-(4-carboxyphenoxy)phthalocyaninato}zinc(II) (**ZnPc-COOH, 32**), with the aim of studying their photophysical and photochemical performance.

This work thus reports on the spectroscopic and photophysicochemical properties of various MPc complexes, investigating the influence of the nature and position of substituents and symmetry reduction.

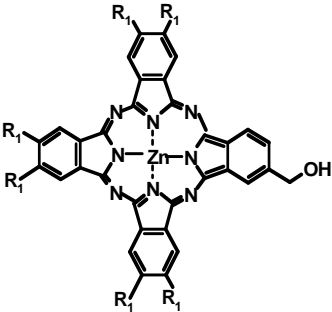
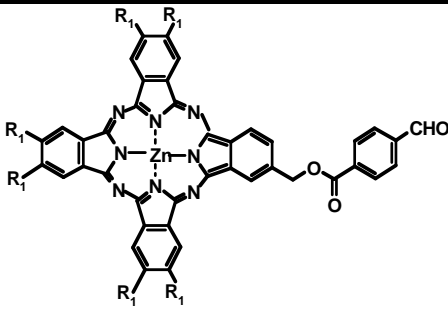
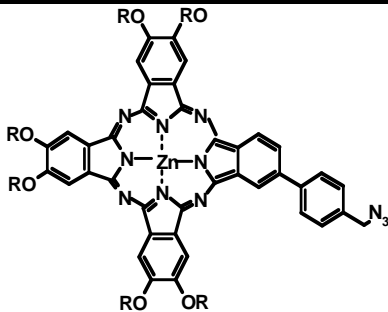
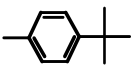
#### 1.2.1.4 Synthesis of phthalocyanine-nanoparticle conjugates

Nanoparticles may enhance the photosensitizing properties associated with Pcs. The synthesis of low-symmetry ZnPc derivatives thus paves the way for conjugation to nanoparticles such as SWCNT and QDs and an investigation into the photophysical consequences of the interaction between them carried out to determine their potential as photocatalysts. The adsorptive interaction of single-walled carbon nanostructures with symmetrical phthalocyanines for application in PDT has been reported [16].

There have been a few reports on the synthesis of SWCNT-low symmetry ZnPc conjugates (Table 1.1) [33,157,158]. In both cases, however, the ZnPcs were substituted at 7, of the 8,  $\beta$ -positions to give hexa-(tert-butylphenoxy-2-hydroxymethyl)phthalocyanine zinc(II) (**33**), hexa-(tert-butylphenoxy-4-formylbenzoyloxymethyl)phthalocyaninato Zn(II) (**34**) and Zn(II) azidophthalocyanine (**35**). In the reported studies, the conjugates are formed by different reaction methods i.e. direct reaction between the functional groups attached to the carbon nanotubes and the

phthalocyanine unit without the use of coupling or activating agents. Also, the SWCNT were modified with complexes which are not readily available. The aim of this work is to form a direct chemical (amide) linkage between the ZnPc molecules and the functionalized SWCNT with the aid of commercially available complexes. As yet there have been no such studies with low-symmetry ZnPc complexes. Similarly, work using low-symmetry ZnPc complexes adsorbed onto SWCNT is reported here for the first time.

Table 1.1: List and structures of MPcs adsorbed on or linked to SWCNT.

MPc	<sup>a</sup> Structure	<sup>b</sup> SWCNT	Ref
ZnPc (22)	See Figure 1.14	SWCNT-COOH	[16]
ZnPc (33)	 <p style="text-align: center;"><math>R_1 = p\text{-}(t\text{-Bu})(C_6H_4)O</math></p>	SWCNT-COOH SWCNT-HiPco	[33]
ZnPc (34)	 <p style="text-align: center;"><math>R_1 = p\text{-}(t\text{-Bu})(C_6H_4)O</math></p>	SWCNT-COOH SWCNT-HiPco	[33]
ZnPc (35)	 <p style="text-align: center;"><math>R = </math> </p>	SWCNT	[157]

<sup>a</sup>*t*-Bu = *tert*-butyl; <sup>b</sup>HiPco= High-pressure carbon monoxide.

There have been numerous reports on the interaction of QDs and MPcs [154,158-166]. Passivation of the QD surface is known to facilitate interaction with other molecules, such as MPcs, *via* electrostatic forces, hydrophobic interactions, hydrogen bonding, adsorption or covalent attachment [38,47,63]. Adsorptive interactions between CdSe and CdTe QDs, capped with various carboxylic acid thiol groups i.e. L-cysteine (L-cys), 2-mercaptoethanol (2-ME), MPA and TGA, and various symmetrically substituted MPc derivatives (including zinc (II) tetracarboxyphthalocyanine (**ZnTCPc**, **36**) and aluminium (**AlTSPc**, **37**) and zinc (**ZnTSPc**, **38**) tetra-sulfonated phthalocyanines) (Table 1.2) are commonly reported [154,164,165]. However, the chemical coordination of MPcs to QDs has received little attention. Burda's group has reported extensively on the synthesis of linked conjugates of SiPc [**SiPc4** (**39**), **SiPc117** (**40**), **SiPc123** (**41**), **SiPc158** (**42**)] with CdSe QDs, formed through axial ligation [46,47,158-163]. Recently the synthesis of a chemically coordinated CdTe MPA QD-ZnPc conjugate has been reported. The ZnPc is tetra-substituted with amino groups (**ZnTAPc**, **43**) that can be attached to the QD surface ligands through an amide bond [166]. The presence of numerous amino groups presents a problem in identifying the number of ZnPc units coordinated to the QD-surface; one Pc unit may interact with several QD clusters. To date, there have been no reports on the covalent attachment of low-symmetry ZnPcs such as **ZnttbIPc** (**31**); thus the aim is to synthesize new conjugates of CdTe QDs and this molecule. The presence of a single imido-group allows specific attachment to the QDs through one point on the Pc ring.

Table 1.2: List and structures of MPcs adsorbed on or linked to QDs.

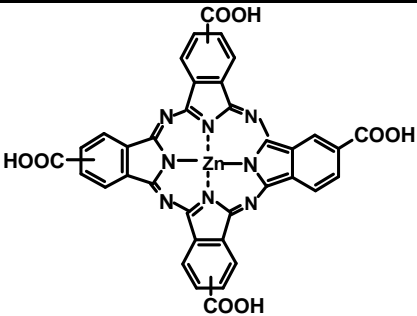
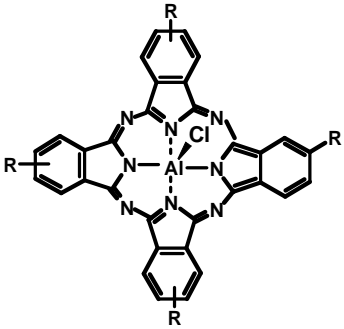
<sup>a</sup> MPc	<sup>b</sup> Structure	<sup>c</sup> QD	Ref
ZnTPyPc (25a)	See Figure 1.14	CdTe MPA CdTe TGA	[154]
ZnTMPyPc (30)	See Figure 1.14	CdTe MPA CdTe TGA	[154]
ZnTCPc (36)		CdTe 2-ME CdTe TGA	[165]
AITSPc (37)	 <p><math>R = \text{SO}_3^- \text{Na}^+</math></p>	CdTe MPA CdTe TGA CdTe L-cys	[164]



Table 1.2 contd.

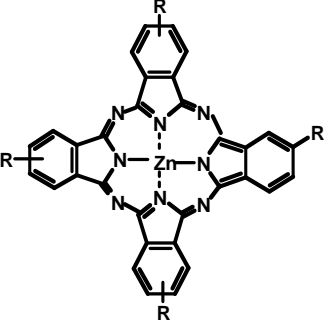
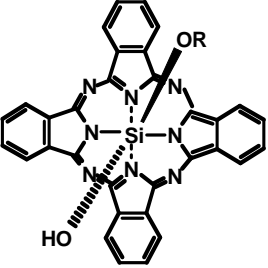
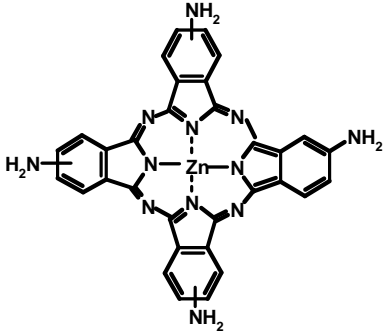
<sup>a</sup> MPc	<sup>b</sup> Structure	<sup>c</sup> QD	Ref
ZnTSPc (38)	 <p style="text-align: center;"><math>R = SO_3^- Na^+</math></p>	CdTe TGA CdTe 2-ME	[165]
SiPc	 <p>(39) SiPc4 : <math>R = Si(CH_3)_2(CH_2)_3N(CH_3)_2</math></p> <p>(40) SiPc117 : <math>R = Si(CH_3)_2(CH_2)_{11}N(CH_3)_2</math></p> <p>(41) SiPc123 : <math>R = Si(CH_3)_2(CH_2)_3N(CH_2CH_2)_2</math></p> <p>(42) SiPc158 : <math>R = Si(CH_3)_2(CH_2)_3NH_2</math></p>	CdSe TOPO CdSe TBPO	[46,47,158-163]

Table 1.2 contd.

<sup>a</sup> MPc	<sup>b</sup> Structure	<sup>c</sup> QD	Ref
ZnTAPc (43)		CdTe MPA	[166]

<sup>a</sup>AITSPc = aluminium (III) tetrasulfophthalocyanine; ZnTSPc = zinc (II) tetrasulfophthalocyanine; ZnTAPc = zinc (II) tetraaminophthalocyanine; <sup>b</sup>SiPc4 = HOSiPcOSi(CH<sub>3</sub>)<sub>2</sub>(CH<sub>2</sub>)<sub>3</sub>N(CH<sub>3</sub>)<sub>2</sub>; SiPc117 = HOSiPcOSi(CH<sub>3</sub>)<sub>2</sub>(CH<sub>2</sub>)<sub>5</sub>N(CH<sub>3</sub>)<sub>2</sub>; SiPc123 = HOSiPcOSi(CH<sub>3</sub>)<sub>2</sub>(CH<sub>2</sub>)<sub>3</sub>N(C<sub>6</sub>H<sub>13</sub>)<sub>2</sub>; SiPc158 = HOSiPcOSi(CH<sub>3</sub>)<sub>2</sub>(CH<sub>2</sub>)<sub>3</sub>NH<sub>2</sub>; <sup>c</sup>TBPO = tributylphosphine oxide.

## 1.2.2 Ground state electronic absorption spectra of phthalocyanines

### 1.2.2.1 Origins of spectra

The absorption spectra of monomeric MPcs are characterized by intense electronic absorptions between 600-750 nm, to give the characteristic Q band (Q<sub>00</sub>), with a molar absorptivity often exceeding 10<sup>5</sup> L mol<sup>-1</sup> cm<sup>-1</sup> [167,168]. The less intense broad band at ~ 350 nm is the Soret or B band [167-169]. The B band consists of two bands, the B<sub>1</sub> and B<sub>2</sub> bands. The Q band is also accompanied by one or two weak vibronic bands (Q<sub>vib</sub>) with an absorbance of less than 10 % of the main Q<sub>00</sub> band (Figure 1.15).

The origin of these bands can be explained using Gouterman's four-orbital model [170], which considers four frontier molecular orbitals: Highest occupied molecular orbital-1

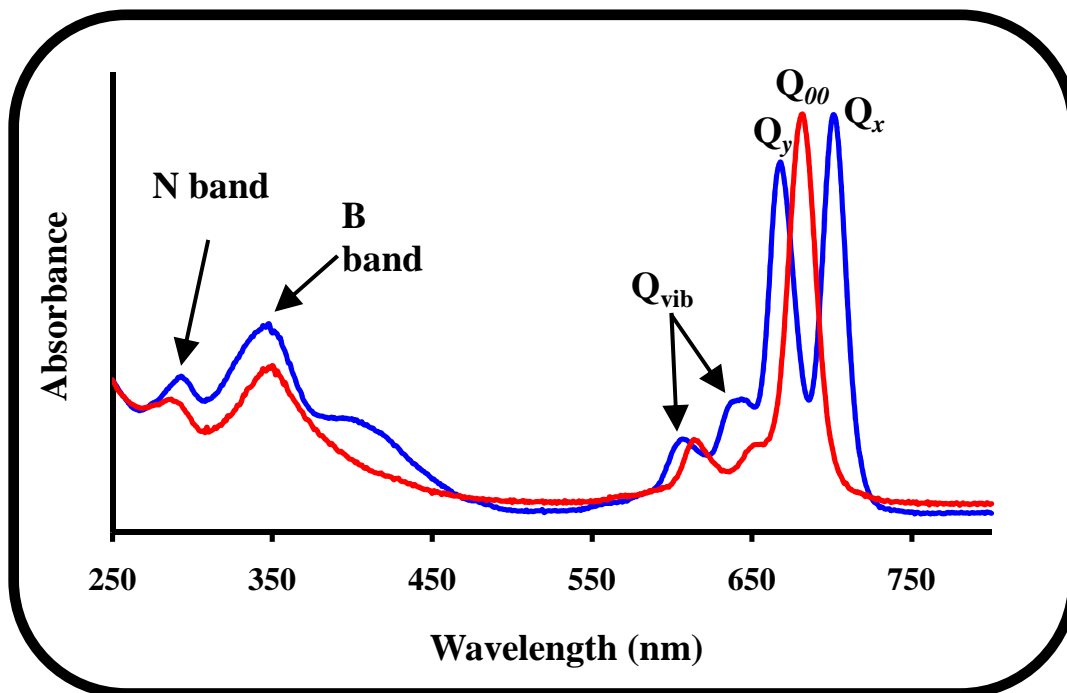


**Figure 1.15:** Typical ground state electronic absorption spectra of symmetrical (red) and low-symmetry (blue) MPcs.

(HOMO-1), HOMO, lowest unoccupied molecular orbital (LUMO) and LUMO+1 account for transitions that give rise to the first two allowed transitions in the UV-visible spectrum (Figure 1.16). These transitions are generally  $\pi$ - $\pi^*$  ( $x/y$  polarized), where the Pc Q band ( $Q_{00}$ ) is the result of a transition from the  $a_{1u}$  (HOMO) to the degenerate  $e_g$  (LUMO) orbital while the transition from  $a_{2u}$  and  $b_{2u}$  to  $e_g$  results in the B band absorptions ( $B_1$  and  $B_2$ ). Additional bands referred to as N, L and C, in terms of ascending energy, are accessible below 300 nm in UV-transparent solvents such as dichloromethane (DCM) [171,172]. Significant energy separation between the  $a_{1u}$  and  $a_{2u}$  orbitals results in less configuration interaction and thus accounts for the greater intensity of the Q band versus the B band.

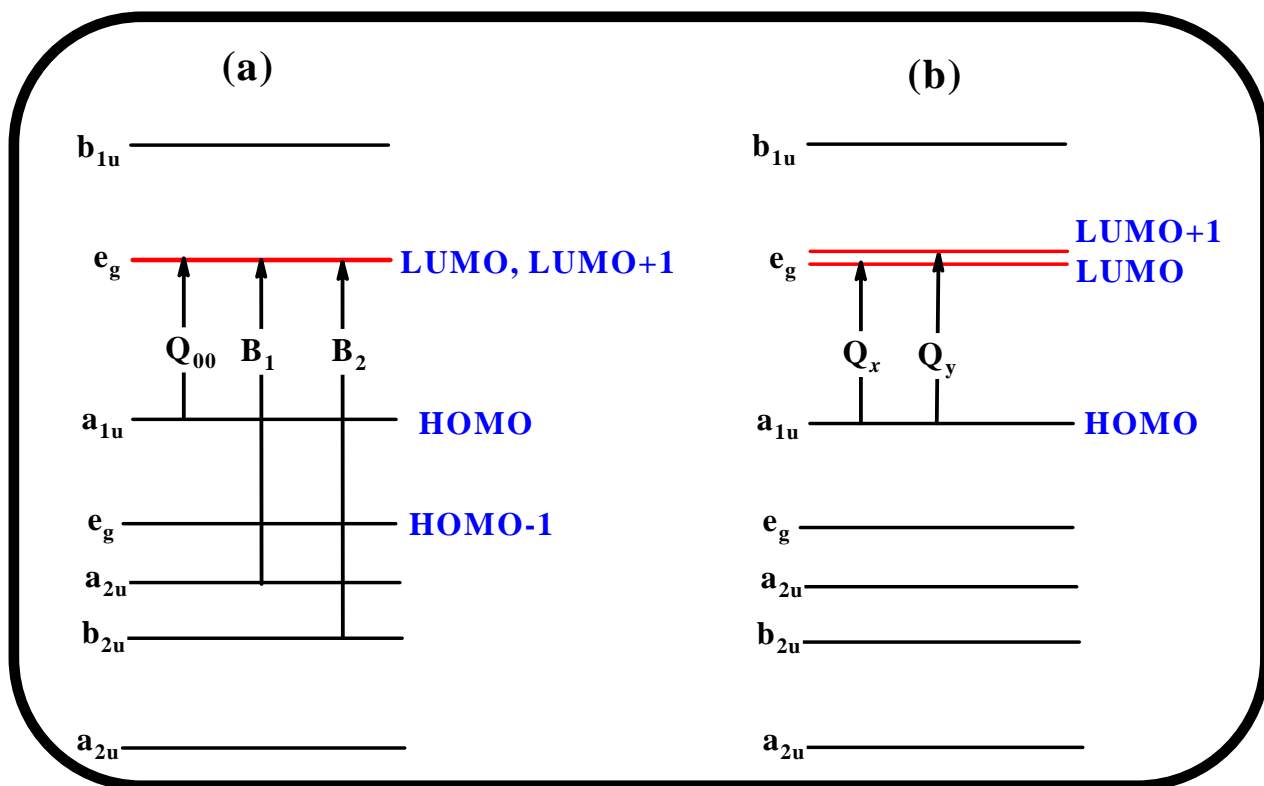


**Figure 1.16:** Electronic transitions (a) in symmetrical MPcs showing the origin of the  $Q_{(00)}$  band and  $B_1$  and  $B_2$  absorption bands [176] and (b) in symmetry lowered MPcs showing the origin of the  $Q_x$  and  $Q_y$  bands.

The absorption spectra of Pcs are sensitive to changes in central metal, solvent, substitution pattern and tendency to aggregate [173,174]. These will be considered in turn below.

Metal free Pcs are characterized by  $D_{2h}$  symmetry. Introduction of a metal that fits into the Pc cavity (3.96 Å) [175,176] maintains the planarity of the molecule and results in increased symmetry to  $D_{4h}$  and an accompanied reduction in number of allowed electronic transitions. Further symmetry perturbations can occur on the introduction of large metals ions i.e.  $Zn^{2+}$ ,  $Sn^{2+}$ ,  $Pb^{2+}$ , which often do not fit into the Pc cavity and thus lower the symmetry to  $C_{4v}$ . Zinc is displaced 0.45 Å from the plane of the aromatic ring

to form a domed shape [171,177] and  $\text{Pb}^{2+}$  ions force the Pc to adopt a shuttlecock configuration [178].

Absorption spectra, in solvents of different polarity, affect the shape, position and intensity of absorption bands. In general, with increasing polarity, the Q band becomes red shifted [179]. The use of coordinating solvents such as *N,N*-dimethylformamide (DMF), dimethylsulfoxide (DMSO) and pyridine results in interactions which stabilizes the LUMO to give Pcs with red-shifted Q bands [180]. Conjugated and aromatic solvents have a similar effect [181]. Acidic solvents such as DCM and chloroform can effect ring oxidation, at times resulting in demetallation [145,173,182] or protonation [146] and their non coordinating nature favours the formation of Pc aggregates [180,183].

Non-peripheral ( $\alpha$ ) substitution results in a larger destabilization effect on the HOMO and thus red shifted spectra relative to peripherally ( $\beta$ ) substituted complexes when coordinated with electron donating groups, while the situation is reversed on attachment of electron-withdrawing groups [184,185]. This effect is in relation to the magnitude of atomic orbital coefficients at the  $\alpha$ - or  $\beta$ -position; molecular orbital (MO) calculations have found that coefficients at the  $\alpha$ -carbon atoms tend to be larger than those at the  $\beta$ -position. Symmetry reductions by reaction of differently substituted precursor units may alter the shape of the absorption spectra, often resulting in a split Q band (Figure 1.15) as a result of a transition from the HOMO to orbitally non-degenerate split LUMO and LUMO+1 levels (Figure 1.16).

### 1.2.2.2 Phthalocyanine aggregation

In polar solvents such as water and methanol (MeOH), Pcs are particularly prone to aggregation due to their large  $\pi$ -system [186]. This intrinsic property alters their absorption features giving an indication of the presence of additional electronic levels of the aggregates (Figure 1.17). By definition, aggregation is referred to as a coplanar association of Pc rings progressing from monomer to dimer and higher-order complexes often driven by non-covalent interactions i.e.  $\pi$ - $\pi$  interactions between the conjugated Pc rings or hydrophobic interactions in polar solvents that arise as a function of their lipophilicity [186-188]. The molecular arrangement of the Pcs in the aggregate can result in broadening and splitting of the main absorption Q band with the loss of resolution of the vibrational components and a hypsochromic (blue) or bathochromic (red) shift [189,190].

According to the exciton coupling model [191,192], interactions between molecules that have sufficient overlap, gives rise to a splitting of the degenerate excited state (E) to generate two new exciton states E' and E''. For parallel transition dipoles, an out of phase dipole arrangement corresponds to a lowering in energy (E''), while an in-phase interaction causes repulsion and thus an increase in energy (E'). The sum of the individual transition dipole moments for a transition to E'' is zero and thus forbidden while transitions to E' are highly allowed resulting in a blue-shifted absorption spectrum (Figure 1.17a). This is the case for cofacial dimers and these arrangements are commonly referred to as H-aggregates. For a co-planar Pc arrangement, with in-line transition dipoles, transitions to the lower energy (E') become allowed, while a transition to the higher energy (E'') is forbidden owing to a transition moment of zero. This gives rise to

red-shifted absorption (Figure 1.17b) characteristic of J-aggregates, which are observed in some molecules, usually under certain conditions such as the nature of the solvent and substituents attached to Pc ring periphery [193].

The tendency for Pcs to aggregate is dependent on the central metal, position and type of substituents on the Pc periphery as well as the solvent properties such as polarity [188,194-196] and coordinating power [184]. Introduction of bulky substituents, particularly at the  $\alpha$ -position of the Pc ring, are predominantly helpful in reducing the tendency to aggregate as a consequence of their ability to impose steric repulsion [197,198]. Bulky substituents can also distort the Pc ring from planarity to give a significant reduction in aggregation [199].

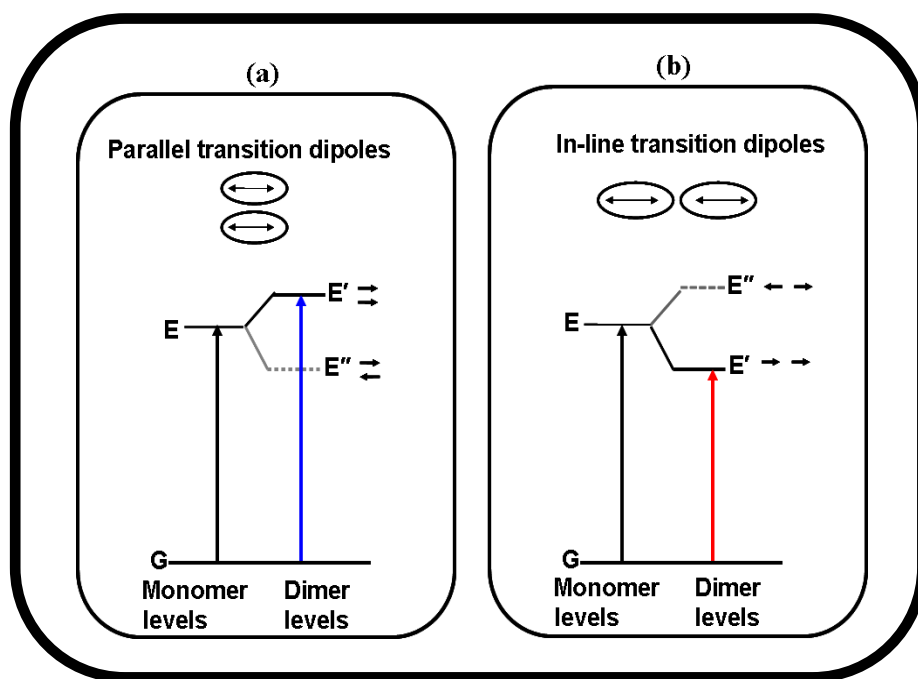


**Figure 1.17:** Exciton coupling in (a) co-facial dimers that gives rise to blue-shifted spectra and (b) co-planar dimers that gives characteristic red-shifted spectra [192].

### 1.2.3 Magnetic circular dichroism (MCD) spectroscopy

This spectroscopic technique has been applied to metallocomplexes since 1970 to explicate their electronic structures [167,176,200-203]. MCD is based on the wavelength dependent differential absorption of left (lcp) and right (rcp) circularly polarized light in the presence of a magnetic field to form excited electronic states. The signal that arises is due to similar transitions as those seen in the electronic absorption spectrum, but with a variation in the selection rules. Intensity in the UV-Vis absorption spectrum is dominated by the electric dipole moment ( $m$ ), however, the MCD intensity is dependent on the coupling of the ground and excited states through the electric ( $m$ ) and magnetic dipole moments ( $\mu$ ) [204,205]. The MCD intensity equation, modified from a previous form adopted by Piepho and Schatz [204], is given in terms of  $\Delta A_{l-r}$  for the difference in absorption of lcp and rcp by Equation 1.2:

$$\frac{\Delta A_{l-r}}{E} = 152.5Bcl \cdot \left[ \mathcal{A}_1 \left( \frac{df}{dE} \right) + \left( \mathcal{B}_0 + \frac{C_0}{kT} \right) f \right] \quad (1.2)$$

where  $B$  is the field strength (in Tesla),  $cl$  is the product of the concentration in  $\text{mol L}^{-1}$  and path length in  $\text{cm}^{-1}$ ,  $E$  represents the energy coordinate in  $\text{cm}^{-1}$ ,  $f$  refers to the normalized band shape function (normally assumed to be a Gaussian shaped curve). The expression takes into account the rigid-shift, Born-Oppenheimer and Franck-Condon approximations [201,206]. Analysis of the MCD spectra is thus a function of an estimation of the magnitudes of the three Faraday terms  $\mathcal{A}_1$ ,  $\mathcal{B}_0$  and  $C_0$  based on the Zeeman splitting of the absorption bands for lcp and rcp, the field-induced mixing of zero-field states and the Zeeman splitting based ground state population adjustment, respectively (Figure 1.18).



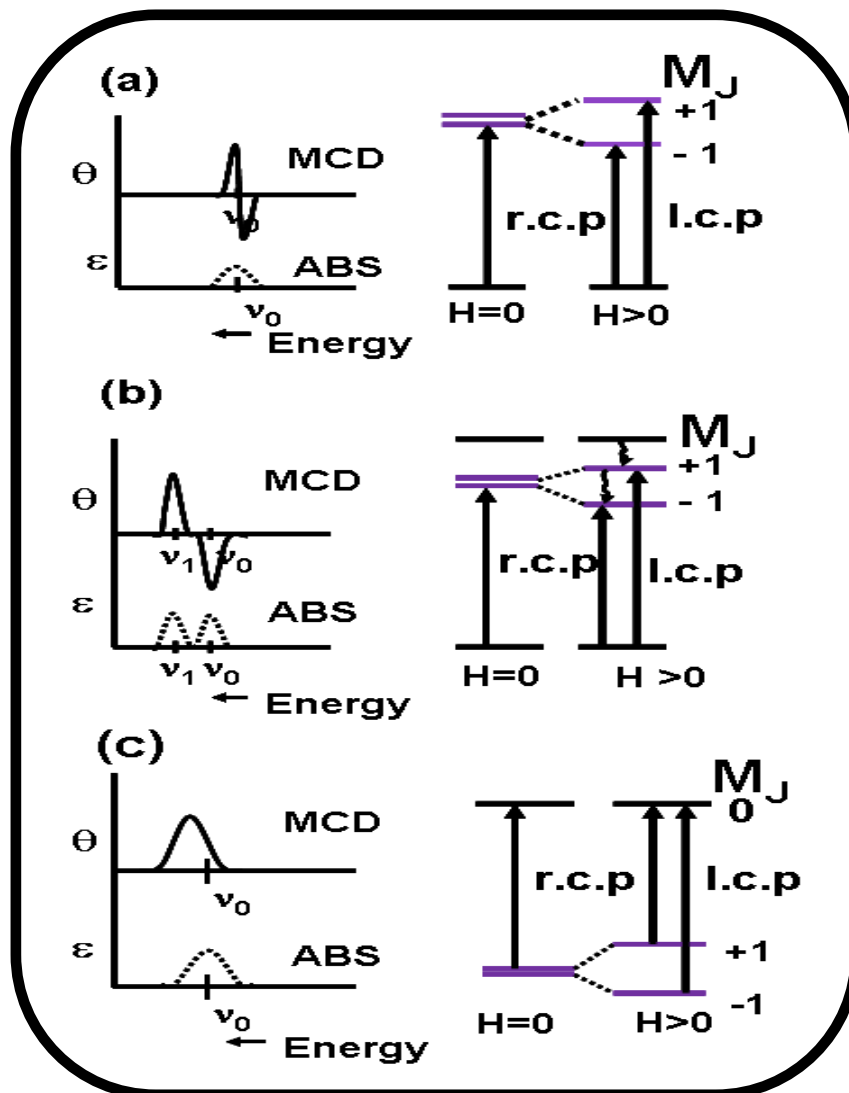


Figure 1.18: The origin of the Faraday (a)  $\mathcal{A}_1$  (b)  $\mathcal{B}_0$  and (c)  $\mathcal{C}_0$  terms in MCD spectra [176].

The Faraday  $\mathcal{A}_1$  term is a temperature independent term that arises from the presence of orbitally degenerate excited states that become split by application of the magnetic field. The Zeeman splitting of the band centers of the lcp ( $\Delta M_J = +1$ ) and rcp ( $\Delta M_J = -1$ ) absorption bands is given by Equation 1.3:

$$\Delta E = 2g_L\mu_B M_J B \quad (1.3)$$

where  $g_L$  = Landé factor (g-factor),  $\mu_B$  = Bohr magneton,  $B$  = field strength. The Zeeman splitting is responsible for the characteristic derivative shape (Figure 1.18a). The  $\mathcal{A}_1$  term is generally anticipated for molecules that possess at least a 3-fold symmetry axis, therefore the MCD spectra of planar  $D_{4h}$ , MPC complexes are typically dominated by derivative-shaped  $x/y$ -polarized  $\mathcal{A}_1$  terms [206].

The Gaussian shaped, temperature independent  $\mathcal{B}_0$  term arises from mixing of the excited states with nearby transitions *via* magnetic dipole transition moments. A lowering in molecular symmetry, below  $D_{4h}$ , results in MCD spectra that are completely dominated by coupled oppositely-signed, Gaussian-shaped  $x$ - and  $y$ -polarized Faraday  $\mathcal{B}_0$  terms (Figure 1.18b) [207,208]. Pseudo- $\mathcal{A}_1$  terms often occur as a result of small splitting of the  $x/y$ -polarized transitions.

The  $\mathcal{C}_0$  term gives Gaussian shaped bands that show strong ( $1/kT$ ) temperature dependence (Figure 1.18c) used to identify an orbitally degenerate ground state. The temperature dependence is a function of the Boltzmann population distribution across the split orbital components of the degenerate ground state [209,210]. PCs lack ground state degeneracy, therefore the  $\mathcal{C}_0$  term can be excluded when considering the MCD spectra of MPCs.

MCD spectroscopy provides the ground and excited state degeneracy information required to fully understand the electronic structure of high symmetry complexes based on the orbital angular momentum properties of the frontier molecular orbitals (MOs) [204,206]. MCD is also utilized to accurately assign absorption bands. A combination of UV-Vis electronic absorption and MCD spectral data allows for spectral deconvolution

that provides good estimates of the band energies, polarizations and intensities which can be used to test the validity of theoretical calculations [176,201,206,209,210].

#### **1.2.4 Molecular orbital (MO) theoretical calculations**

The application of theoretical models is of particular use for correlation with experimental spectral data. Calculations allow determination of the MOs involved in transitions responsible for the optical spectra, the energies of these orbitals and the intensities of the resultant transitions. The earliest orbital assignments made for the porphyrins to give a straight-forward molecular orbital picture of the porphyrin  $\pi$ -ring was described by Simpson [211] and was based essentially on the 18- $\pi$  MO arrangement in a cyclic polyene. This method is applicable today as an introduction to the spectral properties of porphyrins and Pcs. Later, calculations specific for Pcs were introduced and today several revised techniques, based on similar theoretical models, exist [170,212-215]. Modern computational techniques such as density functional theory (DFT) [216] and more common time-dependent DFT (TD-DFT) [217,218] can provide a significantly more accurate description of the ground state geometry than the semi-empirical techniques used by Gouterman and Michl [170,211-215]. TD-DFT based UV-Vis and circular dichroism (CD) predictions using the electric and magnetic dipole based properties enables determination of the expected ground state electronic absorption and MCD spectra of radially symmetric and low symmetry porphyrinoids using the Gaussian 03W software package [219-221].

Calculations based on mono-substituted low symmetry Pc derivatives are of particular interest [181,204,219,222]. The MO calculations reveal several characteristic features:

(1) a characteristic split Q band to give  $Q_x$ ,  $Q_y$  peaks can be assigned to transitions from the HOMO to the LUMO ( $Q_x$ ) and HOMO to the LUMO+1 ( $Q_y$ ), the lower energy transition ( $Q_x$ ) often being of weaker intensity. However the presence of extra nitrogens at the meso positions of Pcs is known to shift the Q band to longer wavelengths with a concomitant increase in intensity compared to porphyrins. Therefore, the condition with respect to intensity may be reversed in such cases for the  $Q_x$  and  $Q_y$  bands; (2) Soret band splitting is also possible but is often difficult to distinguish as a result of a superimposition of several transitions [172]; (3) the oscillator strength ( $f$ ) is a function of the size of fused molecules, with larger magnitudes for the attachment of larger molecules; (4) ring expansion destabilizes the HOMO considerably while there is minimal effect with respect to the HOMO-1 and LUMO [181,222].

In this work, molecular orbital calculations were performed with the aid of the G03W software package [221] to analyze the electronic structure of a low symmetry Pc molecule. The molecular geometries were first optimized at the DFT level using the B3LYP functional with 6-31G(d) basis sets, followed by TD-DFT calculations.

### 1.3 Photophysical Properties

The photophysical properties of Pcs are of particular importance in PDT, optical data storage systems as red or near-infrared (NIR) light absorbers, photoconductors and in solar cells. The Jablonski diagram [223-225] (Figure 1.19) explains the origin of the radiative (fluorescence (F), phosphorescence (P)) and non-radiative (internal conversion (IC), vibrational relaxation (VR), intersystem crossing (ISC)) photophysical properties [224].

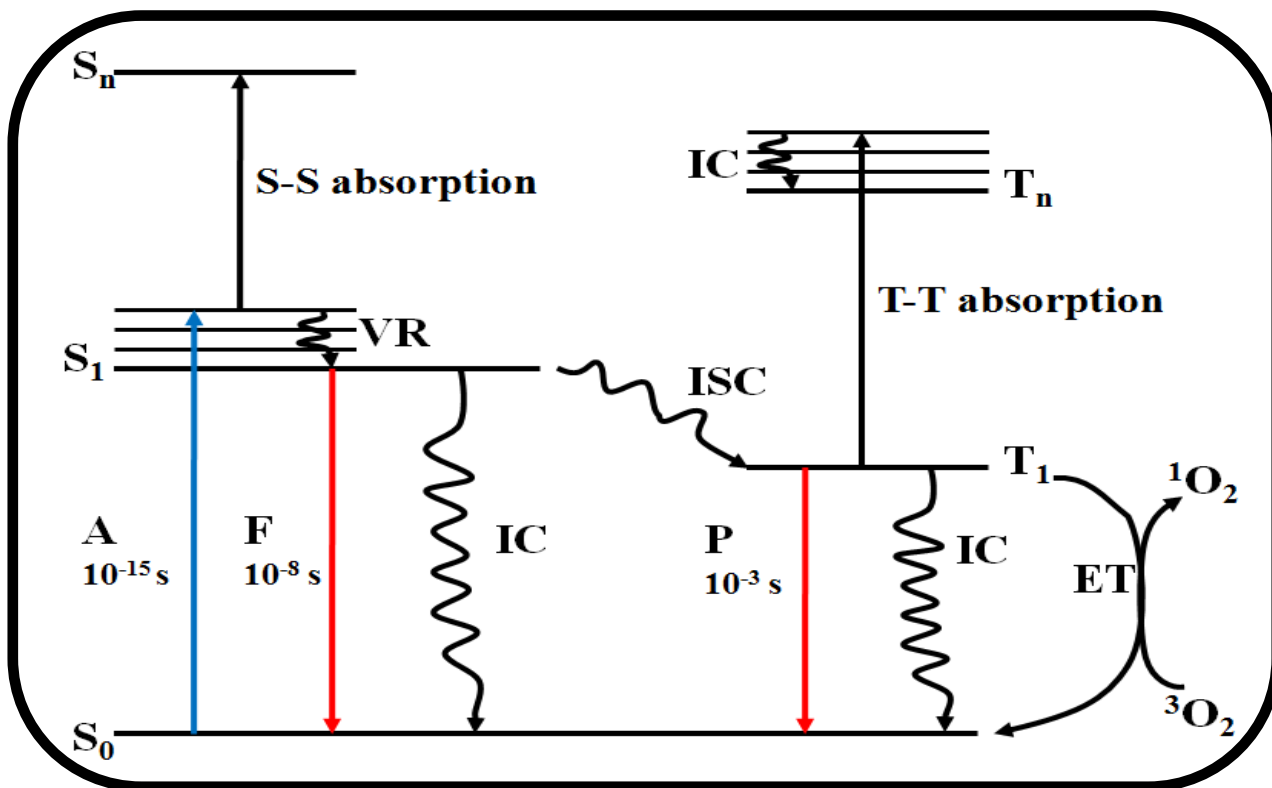


Figure 1.19: A modified Jablonski diagram showing the transition between the singlet ground state ( $S_0$ ) and electronic excited states ( $S_1$  and  $T_1$ ). A = absorption, F = fluorescence, VR = vibrational relaxation, IC = internal conversion, ISC = intersystem crossing, P = phosphorescence.  $S_1$  = singlet excited state and  $T_1$  = triplet excited state.

### 1.3.1 Fluorescence

#### 1.3.1.1 Fluorescence spectra

Fluorescence in MPCs is usually short lived, of the order  $10^{-8}$  s. MPC fluorescence properties such as fluorescence intensity, fluorescence quantum yield ( $\Phi_F$ ) and fluorescence lifetimes ( $\tau_F$ ) are influenced by several factors which include but are not limited to, aggregation, solvent properties, concentration (quenching), nature of the

central metal atom, substituent type (particularly halogenation) and photo-induced energy transfer [101]. Fluorescence is reduced substantially in the presence of paramagnetic metals and metals of high atomic number, an effect in response to the heavy atom effect. These types of compounds encourage ISC, a spin-forbidden process, but which occurs as a consequence of spin-orbit coupling (SOC).

As a result of the lower energy emitted photon, Pc fluorescence emission spectra are at longer wavelengths than the absorption spectra (Figure 1.20), where the difference in spectral position is known as the Stokes shift. Minimal rearrangement of the atomic coordinates of normal Pcs on photoexcitation results in small Stokes shifts [210].

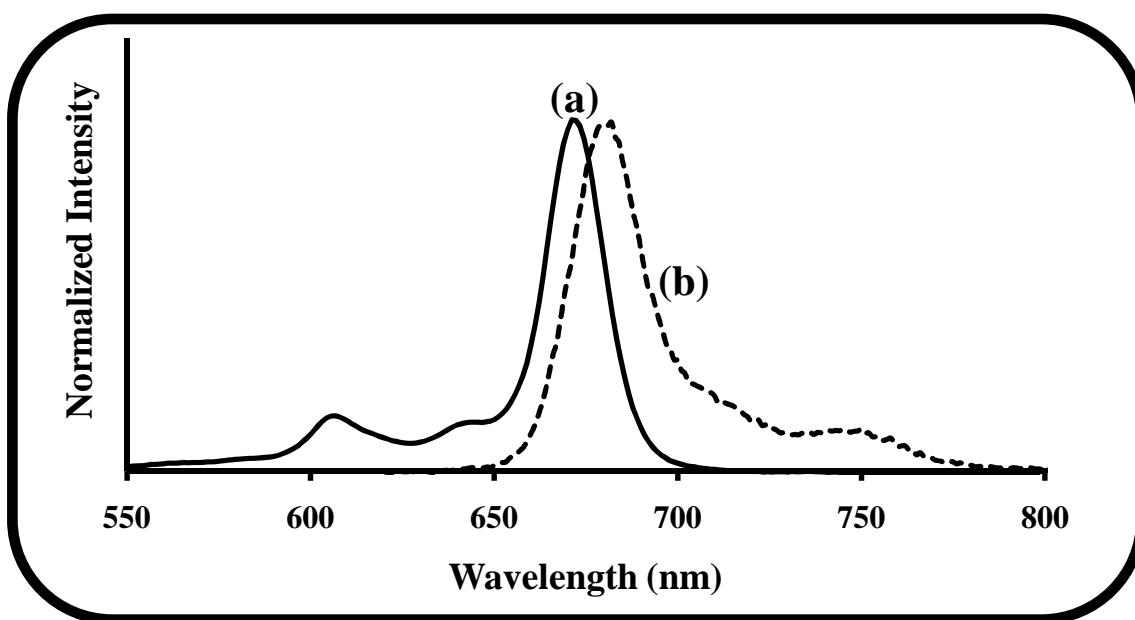


**Figure 1.20:** Typical (a) absorption and (b) fluorescence emission spectra of a symmetrical  $D_{4h}$  type MPc [165].

In general, the excitation spectra are similar to the corresponding absorption spectra; however conformational reorganization on excitation may influence alteration in the shape of the spectra. Such a change reflects a difference in the nuclear arrangement of the

ground and excited states as a result of changes in the structure of the absorbing molecule. This is typical of MPcs with reduced symmetry as a result of protonation or the presence of large central metals prone to demetallation [146,226].

### 1.3.1.2 Fluorescence quantum yields and lifetimes

Quantum yields ( $\Phi$ ) are used to give a measure of the efficiency of a photophysical or photochemical process. Fluorescence quantum yields ( $\Phi_F$ ) are determined by steady-state fluorescence measurements and give a measure of the efficiency of an emission process.  $\Phi_F$  is defined by a ratio of the number of fluorescing molecules to the number of photons absorbed. Relative  $\Phi_F$  can be determined by a comparative method using a standard reference [227,228], whereby the  $\Phi_F$  of an unknown substance is related to that of a sample with a known  $\Phi_F$  value (standard) using Equation 1.4:

$$\Phi_F = \Phi_F^{\text{Std}} \frac{F \cdot A_{\text{Std}} \cdot n^2}{F_{\text{Std}} \cdot A \cdot n_{\text{Std}}^2} \quad (1.4)$$

where  $\Phi_F^{\text{Std}}$  is the fluorescence quantum yield of the standard;  $F$  and  $F_{\text{Std}}$  refer to the areas under the fluorescence emission curves of the MPc and reference respectively;  $A$  and  $A_{\text{Std}}$  are the absorbances of the sample and reference, respectively, at the excitation wavelength and  $n$  and  $n_{\text{Std}}$  are the refractive indices of the solvents used for the sample and standard, respectively.

Fluorescence lifetimes are usually performed in either the frequency [229-231] or time domains [232,233], although other techniques involving multi-pulse measurements have also been demonstrated [234]. Time domain measurements are more commonly used. The equipment used for time-domain measurements is based on gating the fluorescence

signal using either time-correlated single-photon counting (TCSPC) techniques [231,235] or gated image intensifiers [232]. Fluorescence lifetime determinations can also be made using the absorbance and emission spectra of MPCs [236,237] in the PhotochemCAD software package [238], which is based on application of the Strickler-Berg equation [239]. The equation is legitimate only for molecules that do not interact with the solvent and that do not, upon excitation, undergo geometric changes. Figure 1.21 shows a typical fluorescence decay curve for QDs, obtained using a TCSPC set-up.

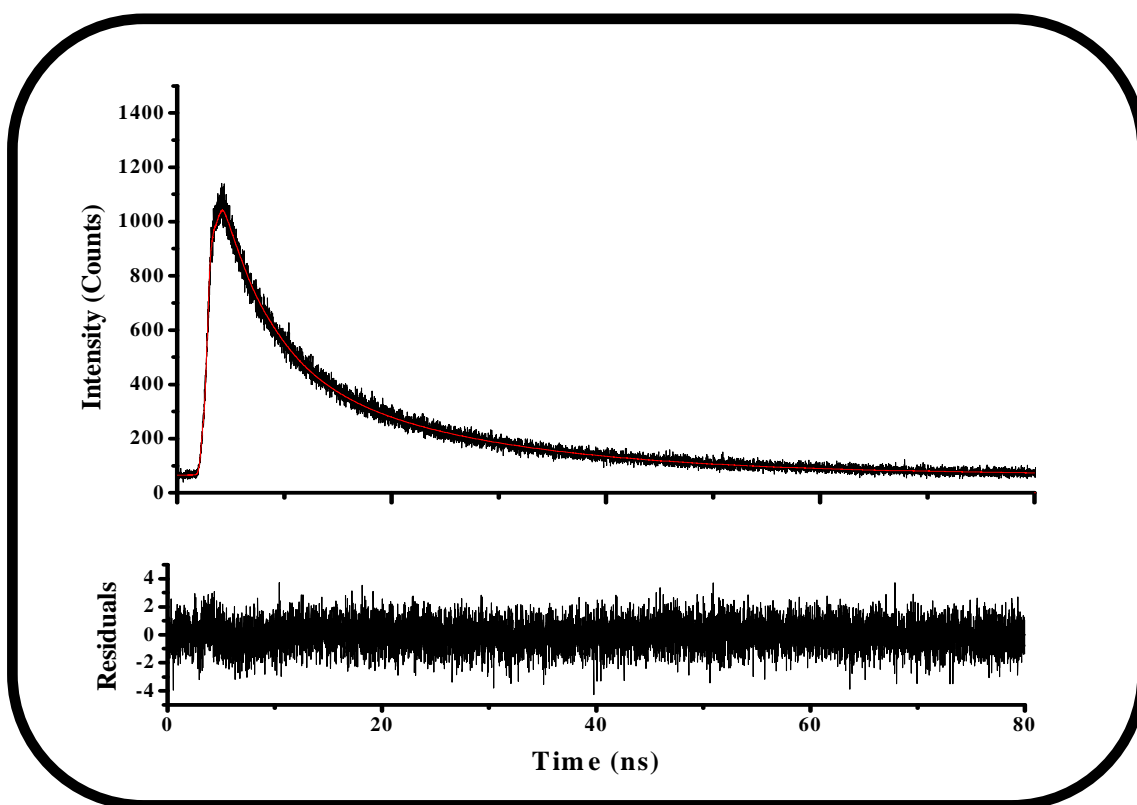


**Figure 1.21:** Typical fluorescence decay curve of QDs.

The fluorescence lifetimes of MPCs are usually of the order of a few nanoseconds ( $10^{-9}$  s). Table 1.3 lists the photophysical properties of some ZnPc and CdPc derivatives [145,240-246]. The results show a strong dependence on the choice of central metal. According to



the SOC theory, the  $\Phi_F$  values of Pcs coordinated to large metals, such as Cd, tend to be lower than those that correspond to small metal ions eg. Zn, as Table 1.3 shows.

There is a lack of photophysical data pertaining to CdPc and HgPcs in general. Therefore the aim of this work is to determine the properties with respect to unsubstituted CdPc (**23**) and HgPc (**24**) derivatives, as well as several new substituted CdPc (**26a-d** and **28a-d**), and HgPc (**27a**) derivatives. Photophysics relating to low-symmetry MPc derivatives is also quite sparse, hence is reported for ZnPc complexes **31** and **32**.

**Table 1.3: Photophysical properties of some MPcs.**

<sup>a</sup> MPc	Solvent	$\Phi_F$	$\Phi_T$	$\tau_T$ ( $\mu$ s)	Ref
ZnPc	DMF	0.30	0.58	330	[145,240,241]
	DMSO	0.18	0.65	350	[145,242]
CdPc	DMF	0.03-0.08	-	27	[243]
	Quinoline	0.03-0.08	-	-	[244]
ZnPc( <i>t</i> -Bu) <sub>4</sub>	Benzene	0.37	0.24	41.1	[245]
ZnPc ( <i>t</i> -Bu) <sub>3</sub> (OH) <sub>2</sub>	Benzene	0.18	0.038	176	[245]
	DMSO	-	0.50	250	[246]

<sup>a</sup>*t*-Bu = *tert*-butyl.

### 1.3.1.3 Förster resonance energy transfer (FRET)

FRET is a photophysical process based on fluorescence. It involves the non-radiative transfer of excitation energy from an excited donor fluorophore to a ground-state acceptor fluorophore, brought into close proximity, which radiatively emits a lower energy photon

(Figure 1.22) [247-249]. As a result, the excited state lifetime of the donor is reduced. The process is driven by dipole-dipole interactions and is largely dependent on the amount of spectral overlap between the donor fluorescence emission spectrum and the acceptor absorption spectrum and minimal center-to-center separation distance ( $r$ ), between the donor and acceptor, to enable efficient through space energy transfer from the donor to the acceptor [250]. The relative orientation of the donor and acceptor transition dipoles also has a significant influence in addition to the fluorescence quantum yield of the donor [248].

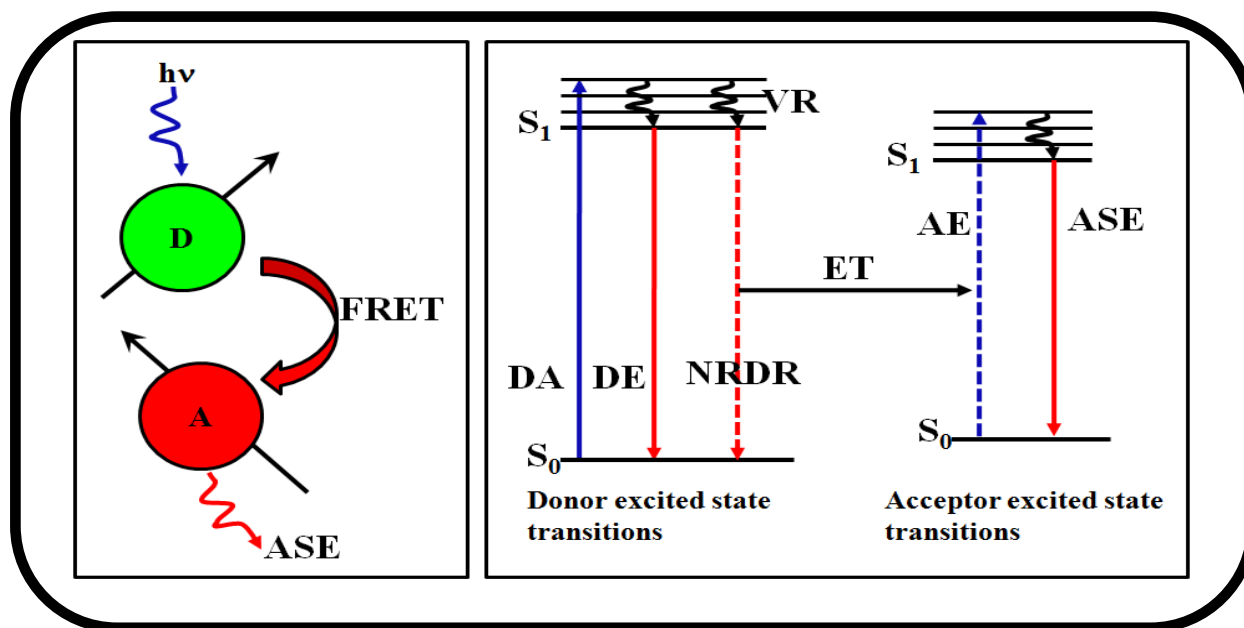


**Figure 1.22: Simplified Jablonski diagram showing the origin of transitions that give rise to Förster resonance energy transfer (FRET). D = donor, A = acceptor, DA = donor absorption, DE = donor emission, VR = vibrational relaxation, NRDR = non-radiative donor relaxation, ET = energy transfer (FRET), AE = acceptor non-radiative excitation, ASE = acceptor sensitized emission.  $S_0$  = singlet ground state and  $S_1$  = singlet excited state [224,249].**

The FRET efficiency accounts for the fraction of excitons transferred from donor to acceptor, by non-radiative means, and can be determined experimentally by monitoring the changes in the donor and/or acceptor fluorescence intensities from the fluorescence quantum yields of the donor in the absence ( $\Phi_{F(D)}$ ) and presence of the acceptor ( $\Phi_{F(DA)}$ ) as shown in Equation 1.5 [248,250-252]:

$$Eff = 1 - \frac{\Phi_{F(DA)}}{\Phi_{F(D)}} \quad (1.5)$$

The FRET efficiency is related to the sixth power, of the donor-to-acceptor center-to-center distance ( $r$ , Å) by Equation 1.6 [247,248]:

$$Eff = \frac{R_0^6}{R_0^6 + r^6} \quad (1.6)$$

where  $R_0$  (the Förster distance, Å) is the critical distance between the donor and the acceptor molecules for which efficiency of energy transfer is 50 %.  $R_0$  is given by Equation 1.7 [247,248];

$$R_0^6 = 8.8 \times 10^{23} \kappa^2 n^{-4} \Phi_{F(D)} J \quad (1.7)$$

Thus it depends on the quantum yield of the donor ( $\Phi_{F(D)}$ ), refractive index of the medium ( $n$ ), the Förster overlap integral ( $J$ ) and  $\kappa^2$ , the dipole orientation factor.  $\kappa^2$  depends on the relative orientation of the donor and acceptor dipoles in space; its value is assumed to be  $2/3$ . This assumption is often made for donor-acceptor pairs in a liquid medium, since their dipole moments are considered to be isotropically oriented during the excited state lifetimes. The use of the isotropic dynamical average ( $\kappa^2 = 2/3$ ) is more appropriate than the static isotropic average ( $\kappa^2 = 0.476$ ) because the donor-acceptor pair is not in a rigid medium.

The Förster overlap integral,  $J$ , is a quantitative measure of the donor-acceptor spectral overlap and is defined by Equation 1.8:

$$J = \int f_D(\lambda)\epsilon_A(\lambda)\lambda^4 d\lambda \quad (1.8)$$

where  $f_D$  is the normalized donor emission spectrum,  $\lambda$  refers to the wavelength of the acceptor (nm) and  $\epsilon_A$  is the molar extinction coefficient ( $M^{-1} \text{ cm}^{-1}$ ) of the acceptor. These FRET parameters are often computed using the program PhotochemCAD [238].

Until recently, QD-Pc interactions *via* a FRET mechanism had received modest attention in literature [46,48,158-166]. In most reports the main interaction avenue is by adsorptive means. There has been limited research on chemically linked conjugates of QDs and photosensitizers, particularly Pcs [46,47,158-163,166]. The chemical linking of QDs to low symmetry phthalocyanines is unknown. Therefore, in this work, the implications of the attachment of a low-symmetry Pc analogue to the terminal carboxyl groups of carboxylic acid thiol capped CdTe QDs have been investigated. Indirect activation of the MPc, *via* FRET is examined and the efficiency of the energy transfer process determined. Although the study is not carried out in aqueous media, which is ideal for biological applications, the study will give an indication of the benefits, if any, of using low-symmetry Pc-QD conjugates.

### 1.3.2 Triplet quantum yields and lifetimes

The triplet state properties of MPcs are often determined by laser flash photolysis, which involves the rapid introduction of an intense pulse of light, using a laser source, into an MPc solution, followed by analysis of the time-evolved electronic absorption signal. In this way, the relative population of ( $\Phi_T$ ) and the time spent ( $\tau_T$ ) in the triplet state ( $T_1$ )

can be determined. The technique essentially monitors the absorption from the  $T_1$  state to a higher  $T_n$  state (Figure 1.19) [225,249]. Apart from triplet absorption detection, flash photolysis also provides information on the excited state lifetime of transient species. A typical triplet state decay curve is shown in (Figure 1.23).

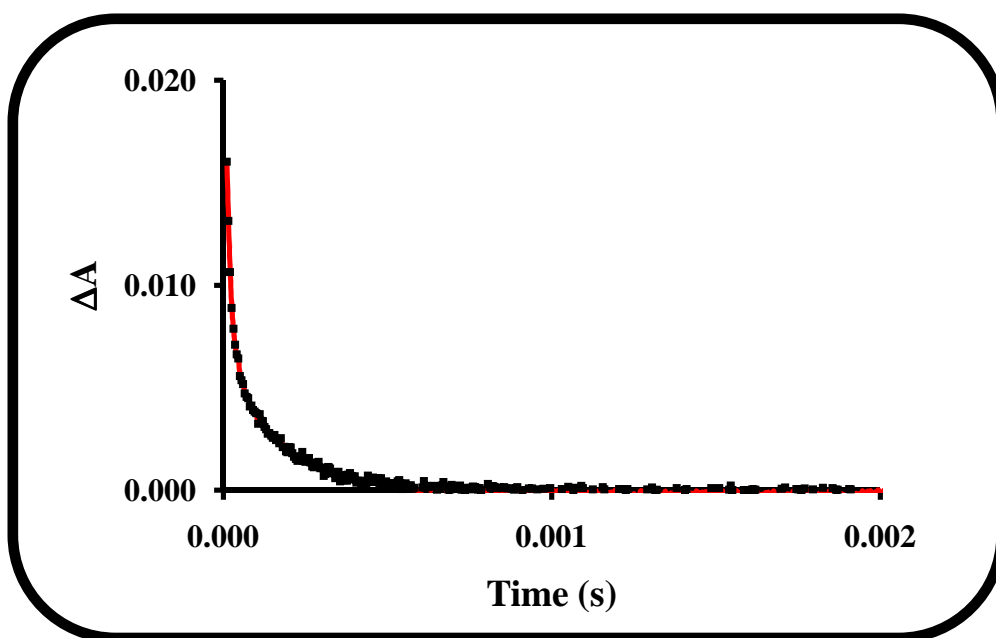


**Figure 1.23:** Typical triplet decay curve of MPcs.

The triplet quantum yield ( $\Phi_T$ ) may be determined by the relative method using Equation 1.9

$$\Phi_T = \Phi_T^{\text{Std}} \cdot \frac{\Delta A_T \cdot \epsilon_T^{\text{Std}}}{\Delta A_T^{\text{Std}} \cdot \epsilon_T} \quad (1.9)$$

where  $\Phi_T^{\text{Std}}$  is the triplet quantum yield of the standard;  $\Delta A_T$  and  $\Delta A_T^{\text{Std}}$  are the changes in the triplet state absorption of the sample and standard respectively;  $\epsilon_T$  and  $\epsilon_T^{\text{Std}}$  refer to the triplet state molar extinction coefficients of the sample and standard respectively and are determined using Equation 1.10 [242]:

$$\varepsilon_T = \varepsilon_S \cdot \frac{\Delta A_T}{\Delta A_S} \quad (1.10)$$

where  $\Delta A_T$  and  $\Delta A_T^{\text{Std}}$  are the changes in the triplet state absorption of the sample and standard respectively and  $\varepsilon_S$  is the singlet state molar extinction coefficient of the sample. The triplet state lifetime ( $\tau_T$ ) is determined by the time resolved absorption measurement described above.

Fitting of the triplet decay curves (as shown in Figure 1.23), using OriginPro 7.5 software has been used in this work for determination of the lifetimes of the MPc transients. MPc  $T_1$  lifetimes are in the range between micro-seconds ( $\mu\text{s}$ ) and milliseconds (ms), Table 1.3. The forbidden  $T_1 \rightarrow S_0$  transition accounts for this longer lifetime.

The triplet state properties intrinsic to phthalocyanines are particularly sensitive to changes that deactivate fluorescence. High triplet state quantum yields ( $\Phi_T$ ) are expected to accompany low fluorescence quantum yields ( $\Phi_F$ ) and *vice-versa*. The  $\Phi_T$  and  $\Phi_F$  values of MPcs in solution are particularly influenced by the nature of the central metal ion; heavy diamagnetic metal ions or paramagnetic metal ions are known to enhance the triplet state yield. Diamagnetic metal ions such as  $\text{Zn}^{2+}$  also promote long lived lifetimes, while a shortened lifetime is experienced in the presence of paramagnetic species, such as  $\text{Cu}^{2+}$ , due to the presence of low-lying d-orbitals which endorse quenching of the  $T_1$  state *via* charge transfer processes. Heavy metals e.g. Cd, show low  $\tau_T$ , Table 1.3. Condensation reactions that result in substitution with heavy atoms, particularly halogens, also result in high  $\Phi_T$ . However, the  $T_1 \rightarrow S_0$  transition may be enhanced as a result of heavy atom induced structural deformation. This results in subsequent reduction in energy transfer efficiency to ground state molecular oxygen (photosensitization). Features

that lead to amplified molecular rigidity lessen the likelihood of non-radiative electronic energy ‘leaking’ which promotes fluorescence [253]. This rigidity feature may also be subjective to solvent properties such as polarity, viscosity, refractive index and temperature. Low  $\Phi_F$  values are often predicted for aggregated MPcs [254,255] and on the departure of molecular symmetry from  $D_{4h}$  in symmetry-lowered Pc analogues [256-258].

Although there have been extensive reports on the photophysical and photochemical parameters associated with MPcs [145,146,157,185,240-246], there is still a need for more in-depth deliberation, particularly with respect to unknown MPc derivatives. The photophysical properties associated with CdPc are shown in Table 1.3. However, there has been no further development with respect to substituted CdPc derivatives. Therefore this work has undertaken an investigation of the photophysics and photochemistry of various aryloxy substituted CdPcs. The properties associated with symmetrically substituted ZnPc derivatives have been reported extensively [145,146,259-261]. The influence of the nature and position of substituents and solvent properties of solvents used is reported in this thesis. The effect of central metal is also investigated with a set of similarly substituted Zn, Cd and HgPcs. Symmetry lowering considerations are also detailed.

The interaction between low-symmetry ZnPc analogues, such as  $\text{ZnPc}(t\text{-Bu})_3(\text{OH})_2$  (Table 1.3), covalently linked to SWCNT has been reported and their photophysical properties studied [33,157]. These conjugates have been explored as photoconducting entities in photovoltaic applications. The adsorptive interaction between a symmetrical ZnPc molecule and carbon nanohorns has been explored for double PDT-PHT cancer

therapy [16]. The aim in this work is to carry out a similar study using novel low-symmetry ZnPc derivatives adsorbed on and chemically linked to SWCNT. Charge transfer, from a charge separated state, to molecular oxygen generates oxygen radicals ( $\text{O}_2^{\bullet -}$ ) and other reactive species such as hydroxyl radicals which subsequently promote the death of nearby cancer cells [262-264]. The aim is to conduct a similar study using low-symmetry ZnPcs adsorbed on and/or linked to SWCNT.

Photophysical properties in relation to QD-Pc interactions are similarly not well established [154,164,165], particularly triplet data pertaining to low-symmetry Pc-QD conjugates. Determination of the triplet state properties of QD-Pc and SWCNT-Pc conjugates in this work are particularly relevant for elucidation of the influence of nanoparticles on the improved efficacy of PDT.

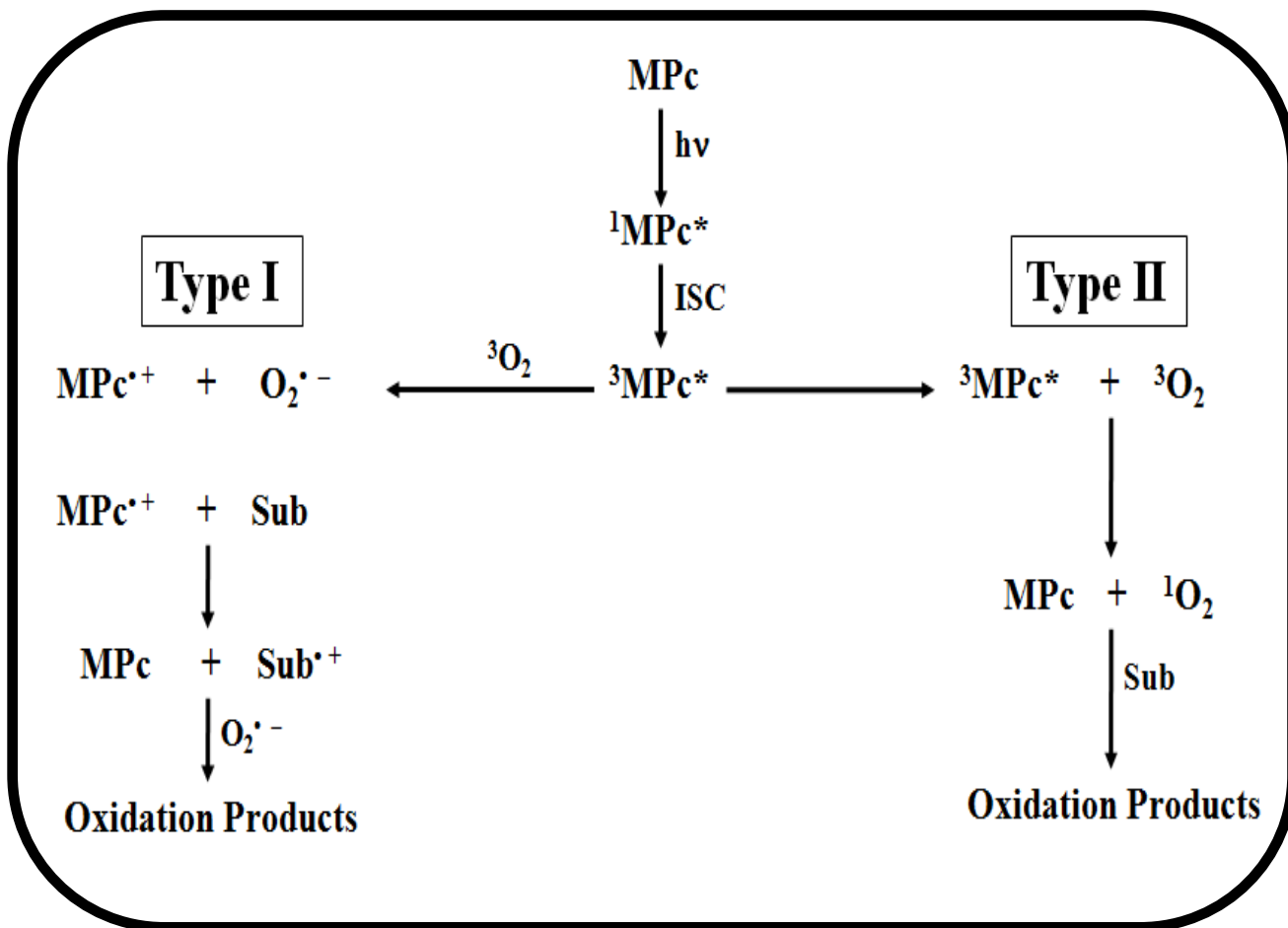
## 1.4 Photochemical Properties

### 1.4.1 Singlet oxygen

Singlet oxygen ( $^1\text{O}_2$ ,  $^1\Delta_g$ ) is believed to be the ‘chief’ cytotoxic species generated by electronic excitation transfer as a result of the interaction between the excited triplet state of an MPc species ( $^3\text{MPc}^*$ ) and ground state molecular oxygen ( $^3\text{O}_2$ ,  $^3\Sigma_g^-$ ) (Scheme 1.4, Type II mechanism).

This process is known as photosensitization and is the predominant method for production of  $^1\text{O}_2$  in the laboratory.  $^1\text{O}_2$  is a highly reactive species responsible for the light-induced oxidative attack in a number of systems, but of particular significance in PDT where it is known to initiate premature death of cancerous tissue and in the photocatalytic conversion of industrially important by-products. The efficiency of the





**Scheme 1.4:** Type I and Type II photochemical mechanisms. Sub = substrate.

photosensitization process is reliant on the transfer of energy from the  $T_1$  state to triplet oxygen. The  $T_1$  state must lie above  $94 \text{ kJ mol}^{-1}$ ; the energy of singlet oxygen above its ground state [101,102]. Triplet states are more significant for photochemical reactions owing to the longer-lived lifetimes i.e.  $T_1 = 10^{-6} \text{ s}$  versus  $S_1 = 10^{-10} \text{ s}$  [265].

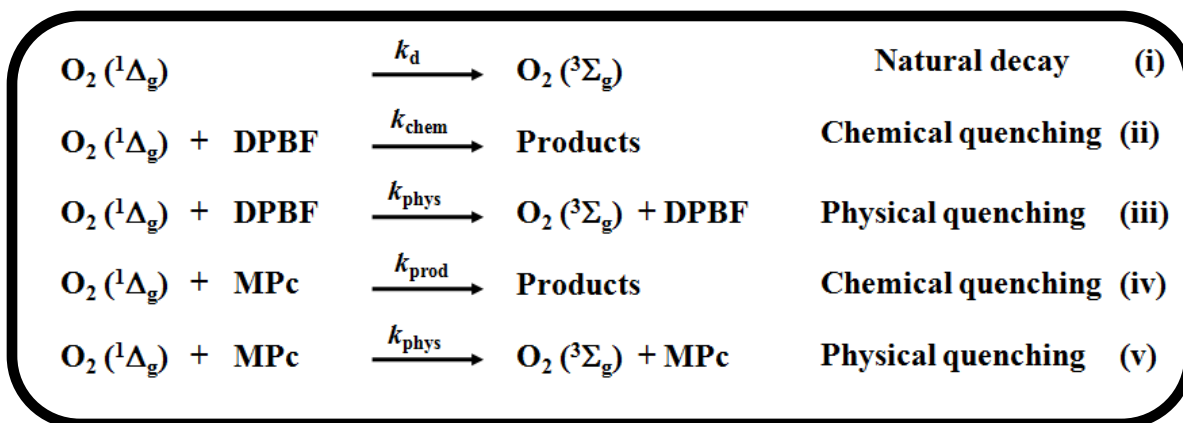
The Type II mechanism, Scheme 1.4, is understood to be the most prominent method of interaction between  ${}^3\text{MPc}^*$  and ground state dioxygen in PDT and most photo-oxidation processes. The Type I mechanism may also lead to photosensitization. The process involves the generation of radical species, by electron transfer or hydrogen atom abstraction, to allow photo-initiated autoxidation (Scheme 1.4) [101].

The quantum yield of singlet oxygen ( $\Phi_{\Delta}$ ) is used as a quantitative measure of the efficiency with which various photosensitizers generate singlet oxygen. The  $\Phi_{\Delta}$  varies as a function of the triplet state properties of the respective MPC molecules i.e. triplet state quantum yield ( $\Phi_T$ ), triplet state lifetime ( $\tau_T$ ), triplet energy ( $E_T$ ), energy transfer efficiency (quantified by  $S_{\Delta}$ ) and substituent quenching abilities. Relative  $\Phi_{\Delta}$  values are often elucidated by a comparative method, using Equation 1.11:

$$\Phi_{\Delta} = \Phi_{\Delta}^{\text{Std}} \cdot \frac{R \cdot I_{\text{abs}}^{\text{Std}}}{R^{\text{Std}} \cdot I_{\text{abs}}} \quad (1.11)$$

where  $\Phi_{\Delta}^{\text{Std}}$  is the singlet oxygen quantum yield of the standard; R and  $R^{\text{Std}}$  are the singlet oxygen quencher (1,3-diphenylisobenzofuran, DPBF) photobleaching rates in the presence of the respective MPC complexes under investigation and the standard respectively;  $I_{\text{abs}}$  and  $I_{\text{abs}}^{\text{Std}}$  are the rates of light absorption by the MPC and standard respectively.

Singlet oxygen quenchers include, DPBF, 1,4-diazabicyclo-octane (DABCO), tetrasodium  $\alpha,\alpha$ -(anthracene-9,10-diyl) dimethylmalonate (ADMA) and sodium azide ( $\text{NaN}_3$ ); the latter two are often used in aqueous conditions, while the former are often employed in organic solvents. The quencher is mixed with the photosensitizer solution, the mixture irradiated and absorption decay of the quencher monitored spectroscopically over a period of time and the values of singlet oxygen generated determined using Equation 1.11. The disappearance of  $^1\text{O}_2$  in the mixture, in the presence of the DPBF can be *via* a series of reactions (Scheme 1.5)



**Scheme 1.5: Photochemical reactions leading to the decay of singlet oxygen in a solution of photosensitizer (MPc) and quencher (DPBF);  $k_d$ ,  $k_{chem}$  and  $k_{phys}$  refer to the rate constants for first order natural decay, chemical and physical quenching by DPBF respectively;  $k_{prod}$  and  $k_p$  are the rate constants for chemical and physical quenching of singlet oxygen by the photosensitizer.**

DPBF acts exclusively as a chemical quencher [266,267] in organic media, therefore reaction (iii) is ignored. In addition, the rate of reaction of singlet oxygen with the photosensitizer is insignificant; therefore (iv) is also ignored. Reaction (v) is also overlooked, as the singlet oxygen quantum yield is not dependent on the photosensitizer (MPc) concentration. Consequently, the rate of decay of singlet oxygen depends entirely on reactions (i) and (ii) resulting in Equations 1.12, for standard (Std) and sample (S) respectively, which becomes Equation 1.11 after manipulation [268].

$$\Phi_{-[DPBF]}^{Std} = \frac{k_{Chem} [DPBF]^{Std} \cdot \Phi_{\Delta}^{Std}}{k_d} \quad (1.12a)$$

$$\Phi_{-[DPBF]}^S = \frac{k_{Chem} [DPBF]^S \cdot \Phi_{\Delta}^S}{k_d} \quad (1.12b)$$

Singlet oxygen can be detected through the use of  $^1\text{O}_2$  quenchers, as shown above, or by the detection of its characteristic luminescence at 1270 nm [269]. With the latter method, the dynamic course of  $^1\text{O}_2$  concentration [ $^1\text{O}_2$ ] can be clearly recorded, following Equation 1.13 as theoretically described in literature [270].

$$I = A \frac{\tau_D}{\tau_T - \tau_D} \left[ \exp\left(-\frac{t}{\tau_T}\right) - \exp\left(-\frac{t}{\tau_D}\right) \right] \quad (1.13)$$

where  $I$  is the luminescence signal intensity of  $^1\text{O}_2$  at time  $t$ ,  $\tau_D$  is the lifetime of  $^1\text{O}_2$ ,  $\tau_T$  is the lifetime of MPC at triplet state, and  $A$  is a coefficient involved in sensitizer concentration and  $^1\text{O}_2$  quantum yield.

$^1\text{O}_2$  quantum yields can then be determined using Equation 1.14:

$$\Phi_{\Delta} = \Phi_{\Delta}^{\text{Std}} \cdot \frac{A \cdot \text{OD}^{\text{Std}}}{A^{\text{Std}} \cdot \text{OD}} \quad (1.14)$$

where  $\Phi_{\Delta}^{\text{Std}}$  is the singlet oxygen quantum yield of the standard;  $A$  and  $A^{\text{Std}}$  refer to the coefficient for the sample and standard respectively and;  $\text{OD}$  and  $\text{OD}^{\text{Std}}$  to the optical density or absorbance of the sample and standard respectively at the excitation wavelength. A typical singlet oxygen decay curve for MPCs is of the form shown in Figure 1.24.

The singlet oxygen producing capabilities of an MPC are affected by the nature of the central metal. The presence of large central metal ions facilitates ISC to the triplet state, through the SOC theory, thus the prospect of  $^1\text{O}_2$  generation is increased. Aluminium and zinc Pc complexes have a closed-shell configuration ( $d^0$  and  $d^{10}$  respectively) and have shown appreciable  $\Phi_{\Delta}$  values in relation to long lived triplet lifetimes. Solvent induced effects also bring about trends [101].

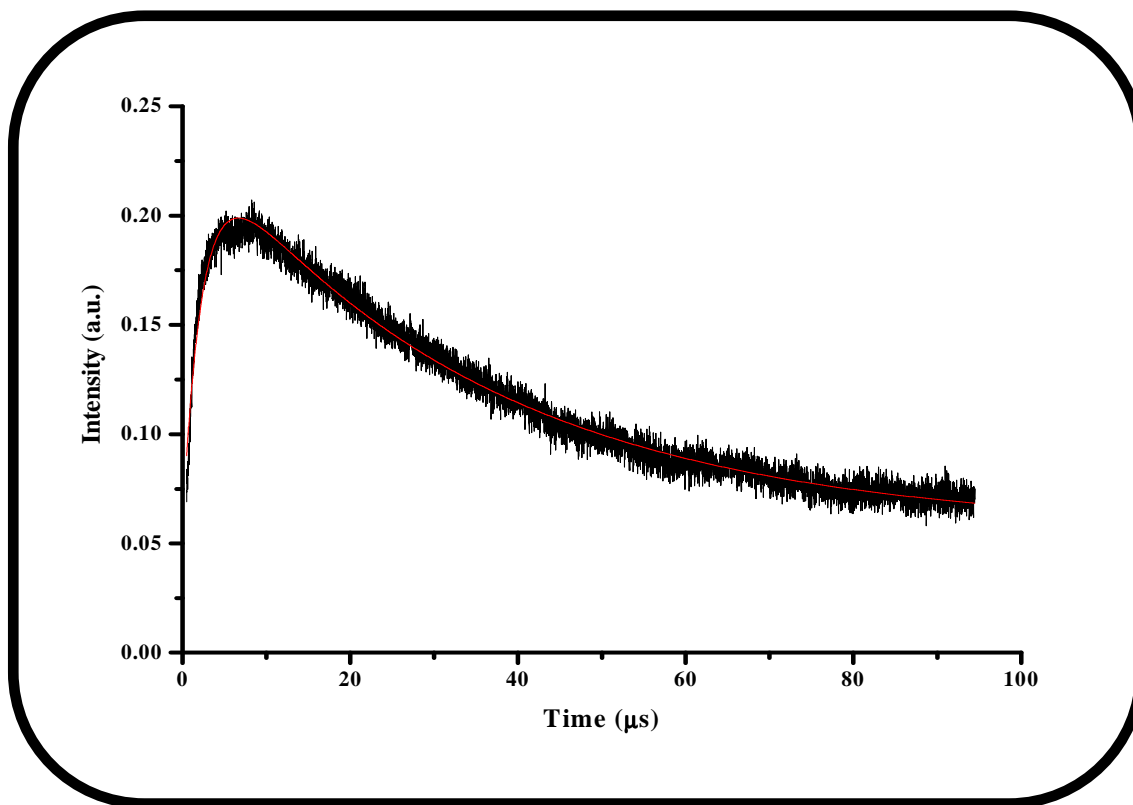


**Figure 1.24:** Typical singlet oxygen decay signal for MPcs.

The photochemistry of a number of aryloxy substituted ZnPc derivatives have been reported (Table 1.4) [145,146,259-261]. However data pertaining to similarly substituted CdPc and HgPc derivatives is yet to be obtained. Heavy metals tend to promote population of the triplet state *via* ISC, through SOC processes, hence improved  $\Phi_{\Delta}$ . Singlet oxygen yields of QD-Pc conjugates give a quantitative measure of the efficiency of PDT; therefore the photochemical properties of these complexes will also be determined in this thesis.

Table 1.4: The photochemical properties associated with some ZnPc derivatives.

MPc	Solvent	$\Phi_{\Delta}$	$\Phi_{Pd} (10^{-5})$	Ref
ZnPc	DMSO	0.67	2.61	[145,146,262]
ZnPc $\alpha$ -(BenzyloxyPhenoxy) <sub>4</sub>	DMSO	0.76	0.50	[261]
ZnPc $\beta$ -(BenzyloxyPhenoxy) <sub>4</sub>	DMSO	0.52	0.33	[261]
ZnPc $\beta$ -( <i>t</i> -Bu) <sub>4</sub>	DMSO	-	0.13	[259]
	EtOH	0.54	-	[260]
ZnPc $\beta$ -( <i>t</i> -Bu-Phenoxy) <sub>4</sub>	DMF	0.42	9.41	[146]
	DMSO	0.60	3.33	[146]

### 1.4.2 Photodegradation

Photodegradation is the photochemical induced oxidative degradation of a molecule into lower molecular weight fragments [271]. It is often a singlet oxygen mediated process, since the ability of macrocyclic metal complexes to react with singlet oxygen has been reported [272-274], and is used to determine the stability of MPc molecules to light. The photodegradation process generally involves oxidative attack of the MPc excited triplet state macrocycle by singlet oxygen *via* a Diels-Alder cycloaddition mechanism, the product of which is the respective substituted phthalimide (Scheme 1.6) [102,272,273]. However, the process may also occur without the involvement of singlet oxygen. Photodegradation varies as a function of the MPc structure i.e. nature of substituents attached to the ring periphery and central metal, solvent, light intensity and the concentration of singlet oxygen since it is a singlet-oxygen mediated process. Electron-



where  $C_0$  and  $C_t$  refer to the respective MPC derivative's concentrations (M) before and after irradiation, respectively;  $V$  is the reaction volume,  $N_A$  the Avogadro's number;  $I_{\text{abs}}$  the overlap integral of the radiation source intensity and the absorption of the MPC in the region of the interference filter transmittance [280],  $S$  is the irradiated cell area ( $2.0 \text{ cm}^2$ ) and  $t$  is the irradiation time, in seconds.

The photochemical properties of ZnPc derivatives are quite widespread [145,146,259-261]. The aim in this thesis is to study the photochemical behaviour of newly synthesized CdPc, HgPc and low-symmetry ZnPc complexes (Figure 1.14). Their ability to generate singlet oxygen and hence their photodegradation yields will determine their efficacy as photosensitizers in the photocatalytic transformation of industrially important molecules.



## 1.5 Summary of Aims of Thesis

The aims of this thesis can be summarized as follows:

1. Synthesis, spectroscopic (ground state electronic absorption and fluorescence), photophysical (fluorescence quantum yields, triplet quantum yields and lifetimes) and photochemical (singlet oxygen quantum yields and photodegradation quantum yields) studies of unsubstituted,  $\alpha$  and  $\beta$ -aryloxy tetra-substituted (zinc, cadmium and mercury complexes) and low-symmetry ZnPc derivatives.
2. Chemical functionalization and characterization (IR, TGA, Raman) of SWCNT.
3. Synthesis and characterization of carboxylic acid thiol capped QDs.
4. Conjugation (*via* adsorption or chemical bonds) of SWCNT and QDs to low symmetry Pcs.
5. Spectroscopic, photophysical and photochemical studies of:-
  - a. Adsorbed and linked low symmetry Pc-SWCNT conjugates
  - b. Mixed and linked low symmetry Pc-QD conjugates.

The MPcs under investigation in this thesis are (Figure 1.14):

Unsubstituted zinc (**ZnPc, 22**), cadmium (**CdPc, 23**) and mercury (**HgPc, 24**) phthalocyanine.

Peripherally tetra pyridyloxy substituted zinc ( **$\beta$ -ZnTPyPc, 25a**) and mercury ( **$\beta$ -HgTPyPc, 27a**) phthalocyanine.

Peripherally and non-peripherally tetra pyridyloxy (**CdTPyPc**), 4-(benzyloxyphenoxy) (**CdTbzPhPc**), phenoxy (**CdTPhPc**), or *tert*-butylphenoxy (**CdTtBuPhPc**) substituted CdPc derivatives (**26a-d** and **28a-d**).

Peripherally tetra *tert*-butyl or 2-mercaptopyridine substituted ZnPc complexes ( $\beta$ -**ZnttbPc, 29** and  $\beta$ -**ZnTMPyPc, 30**).

Low-symmetry tetra substituted ZnPc complexes (**ZnttbIPc, 31**) and (**ZnPc-COOH, 32**).

The nanoparticles used in this study are (Figure 1.11):

Carboxylic acid or ethylamine functionalized SWCNT (**SWCNT-COOH, 1a** and **SWCNT-NH<sub>2</sub>, 1b**).

Mercaptopropionic acid capped CdTe QDs (**CdTe MPA, 2**).

## **2. Experimental**

**Incorporated in this chapter are the experimental procedures used during the course of the study i.e. all synthetic procedures and methods of characterization for all molecules used in this work are reported here.**

## 2.1 Materials

### 2.1.1 Solvents

Benzene, chloroform, dichloromethane (DCM), diethyl ether, *N,N*-dimethylformamide (DMF), dimethylsulfoxide (DMSO), ethanol (EtOH), hexane, methanol (MeOH), tetrahydrofuran (THF), toluene, glacial acetic acid, nitric acid (55 %), sulfuric acid (98 %) and thionyl chloride were purchased from SAARCHEM. Bromine was purchased from Merck. Ammonia (25 %), deuterated chloroform (CDCl<sub>3</sub>), deuterated DMSO (DMSO-d<sub>6</sub>), deuterated pyridine (pyridine-d<sub>5</sub>), nitrobenzene and trifluoroacetic acid (TFA) were purchased from Sigma-Aldrich. All solvents were of reagent grade and purified according to the methods described by Perrin and Armarego [281].

### 2.1.2 Synthesis and photophysicochemical reagents

Biobeads Sx-2 for size exclusion chromatography was purchased from BIO-RAD Laboratories. 1-Ethyl-3-(3-dimethylaminopropyl) carbodiimide (EDC) and *N*-hydroxysuccinimide (NHS) were purchased from Fluka. 1-octanol, silica gel 60 (0.04 – 0.063 mm) and silica gel 60 P F<sub>254</sub> for column and preparative thin layer chromatography (TLC) respectively, were purchased from Merck. Ammonium molybdate, cadmium chloride, ethylenediamine, phenol, potassium carbonate, potassium bromide, sodium borohydride, sodium hydroxide, sodium nitrite were purchased from SAARCHEM. 4-(benzyloxy)phenol, 1,8-diazabicyclo[5.4.0]undec-7-ene (DBU), 4-(3,4-dicyanophenoxy)benzoic acid, 1,3-diphenylisobenzofuran (DPBF), 2-hydroxypyridine, 3-mercaptopropionic acid (MPA), 3-nitrophthalonitrile (**10**), 4-(2-mercaptopyridine), 4-nitrophthalonitrile (**13**), 1-pentanol, 4-*tert*-butylphenol, 4-phenol, 4-*tert*-butylphthalic

anhydride (**48**), cadmium acetate dihydrate, calcium hydride, mercury chloride, phthalonitrile, pyromellitic dianhydride (benzene-1,2,4,5-tetracarboxylic dianhydride, **17**), quinoline, single-walled carbon nanotubes (SWCNT, 0.7 – 1.2 nm in diameter and 2 – 20  $\mu\text{m}$  in length), tellurium powder (200 mesh), thioglycolic acid (TGA), Triton-X 100 (*tert*-octylphenoxypolyethoxyethanol), urea and zinc acetate dihydrate were purchased from Sigma-Aldrich. Reagents were used without any further purification. Ultra pure water of resistivity 18.2  $\Omega$  was obtained from a Milli-Q Water System (Millipore Corp., Bedford, MA, USA) and used for all aqueous solutions and for purification of the SWCNT.

## 2.2 Instrumentation

1. FT-IR spectra (KBr pellets) were recorded on a Perkin-Elmer spectrum 2000 FT-IR spectrometer.
2. Ground state electronic absorption spectra were recorded on a Cary 500 UV/Vis/NIR spectrophotometer.
3.  $^1\text{H}$ -nuclear magnetic resonance ( $^1\text{H}$ -NMR) spectra were obtained in deuterated solvents, using a Bruker EMX 400 MHz NMR spectrometer and a Bruker AVANCE II 600 MHz spectrometer.
4. Elemental analyses were carried out at Rhodes University using a Vario Elementar EL111 Series.
5. MALDI-TOF mass spectra were recorded using an Applied Biosystems Voyager-DE STR at the University of Stellenbosch in Cape Town, South Africa.

6. Magnetic circular dichroism (MCD) spectra were recorded at Tohoku University, Sendai, Japan, with a JASCO J-725 spectrodichrometer equipped with a JASCO electromagnet producing magnetic fields of up to 1.09 T (tesla) with both parallel and anti-parallel fields.
7. Molecular orbital calculations were performed at Tohoku University, Sendai, Japan, with the aid of the G03W software package [221] to analyze the electronic structure of the molecule. The molecular geometries were first optimized at the DFT level using the B3LYP functional with 6-31G(d) basis sets, followed by TD-DFT calculations.
8. Thermal gravimetric analysis (TGA) was carried out using a Perkin-Elmer TGA 7 thermogravimetric analyzer at a heating rate of  $10^{\circ}\text{C min}^{-1}$  in a high-purity nitrogen and air atmosphere. The resultant data was analyzed with Pyris Version 4.01 software.
9. Raman spectra was obtained with a Bruker Vertex 70 – Ram II spectrometer (equipped with a 1064 nm Nd:YAG laser and a liquid nitrogen cooled germanium detector). Solid samples diluted with KBr were used.
10. X-ray powder diffraction patterns were recorded on a Bruker D8, Discover equipped with a proportional counter, using Cu-K $\alpha$  radiation ( $\lambda = 1.5405 \text{ \AA}$ , nickel filter). Data were collected in the range from  $2\theta = 15^{\circ}$  to  $60^{\circ}$ , scanning at  $1^{\circ} \text{ min}^{-1}$  with a filter time-constant of 2.5 s per step and a slit width of 6.0 mm. Samples were placed on a silicon wafer slide. The X-ray diffraction data were treated using the freely-available Eva (evaluation curve fitting) software. Baseline correction was performed on each diffraction pattern by subtracting a spline fitted to the curved background and

the full-width at half-maximum values used in this study were obtained from the fitted curves.

11. Fluorescence emission and excitation spectra were obtained on a Varian Eclipse spectrofluorimeter.
12. Fluorescence lifetimes were measured using a time correlated single photon counting (TCSPC) setup (Figure 2.1) (FluoTime 200, Picoquant GmbH) with a diode laser (LDH-P-670 with PDL 800-B, Picoquant GmbH, 670 nm, 20 MHz repetition rate, 44 ps pulse width) or a light emitting diode (LED) and a linear polariser (PLS-500 with PDL 800-B, Picoquant GmbH, 497 nm, 10 MHz repetition rate). Fluorescence was detected under the magic angle with a peltier cooled photomultiplier tube (PMT) (PMA-C 192-N-M, Picoquant) and integrated electronics (PicoHarp 300E, Picoquant GmbH). A monochromator with a spectral width of about 4 nm or 8 nm was used to select the required emission wavelength band. The response function of the system, which was measured with a scattering Ludox solution (DuPont), had a full width at half-maximum (FWHM) of about 300 ps and 950 ps for the diode laser and LED respectively. The data were analysed with the program FluorFit (Picoquant). The support plane approach [248] was used to estimate the errors of the decay times.

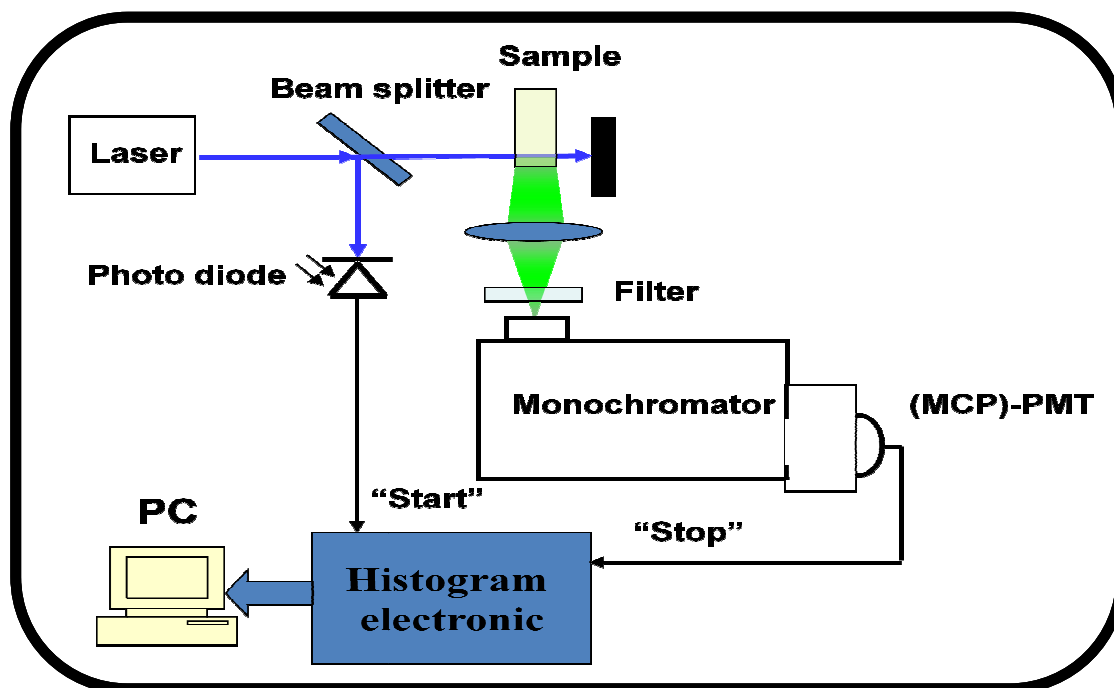


Figure 2.1: Schematic diagram of the TCSPC set-up.

13. A laser flash photolysis system was used for the determination of triplet absorption and decay kinetics (Figure 2.2). The excitation pulses were produced by a Quanta-Ray Nd:YAG laser (1.5 J / 90 ns at 8 Hz), pumping a Lambda Physik FL 3002 dye laser (Pyridin 1 in methanol). The analyzing beam source was from a Thermo Oriel 66902 xenon arc lamp, and a Kratos Lis Projekte MLIS-X3 photomultiplier tube was used as the detector. Signals were recorded with a two-channel, 300 MHz digital real-time oscilloscope (Tektronix TDS 3032C); the kinetic curves were averaged over 256 laser pulses.



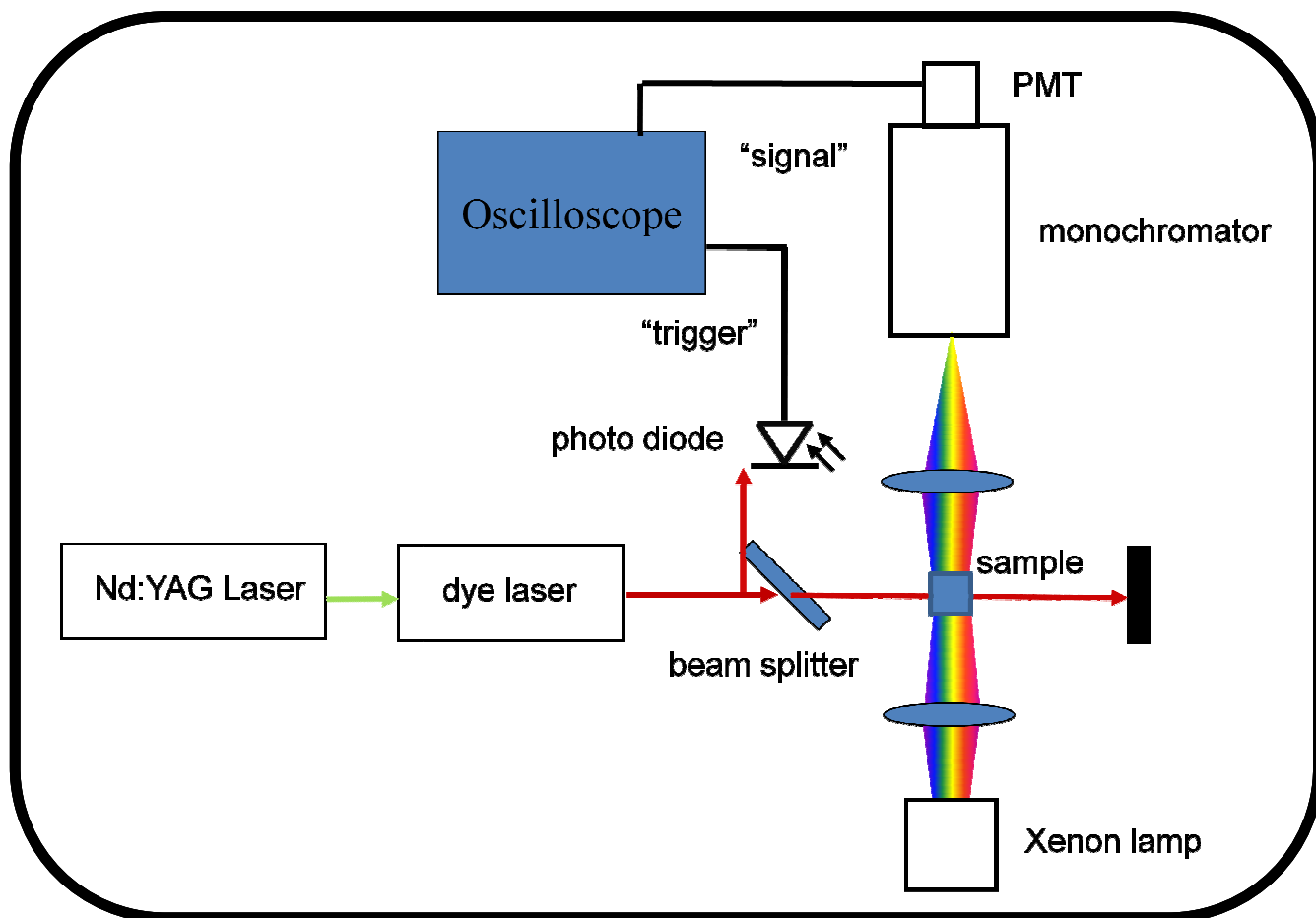
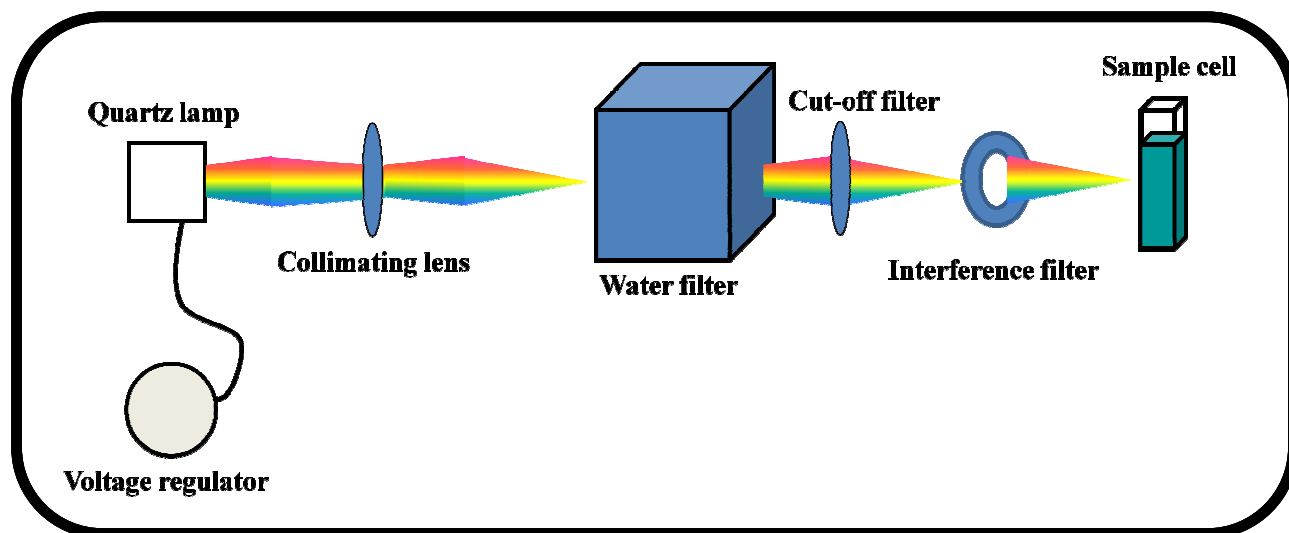


Figure 2.2: Schematic diagram of a laser flash photolysis set-up.

14. Photo-irradiations for singlet oxygen and photodegradation quantum yield determinations were done using the set-up shown in Figure 2.3. This consists of a General Electric Quartz line lamp (300W), a 600 nm glass cut off filter (Schott) and a water filter were used to filter off ultraviolet and infrared radiations respectively and an interference filter (Intor, 670 nm with a band width of 40 nm) which was additionally placed in the light path before the sample.



**Figure 2.3:** Schematic diagram of a photochemical set-up.

15. Light intensities were measured with a POWER MAX 5100 (Molelectron detector incorporated) power meter
16. The singlet oxygen ( $^1\text{O}_2$ ) luminescence at 1270 nm was measured with an ultrasensitive Germanium detector (Edinburgh Instruments, EI-P) combined with a 1000 nm long pass filter (Omega, 3RD 1000 CP) and a 1270 nm band pass filter (Omega, C1275, BP50). Laser pulses were generated by the laser system described above. The near-infrared emission of the sample was focused to the detector by a lens (Edmund, NT 48-157) with a detection direction perpendicular to the excitation laser beam. The detected signals were averaged over 256 laser pulses, with the same oscilloscope described above, to show the dynamic decay of  $^1\text{O}_2$  (Figure 2.4).

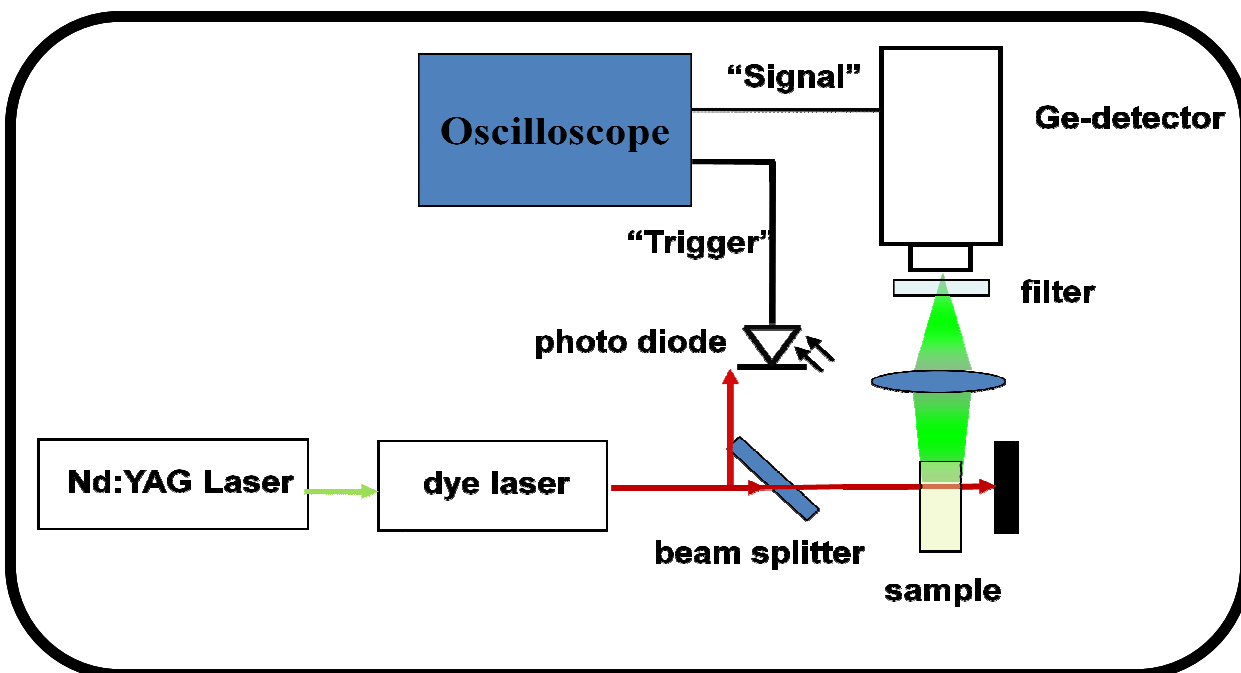


Figure 2.4: Schematic diagram of the singlet oxygen detection set-up.

## 2.3 Methods

### 2.3.1 Absorption studies

The interaction of the nanoparticles used in this study i.e. SWCNT and QDs with MPc complexes was studied spectroscopically. Spectra pertaining to SWCNT alone were compared with spectra obtained upon modification of the nanotubes with functional groups (-COOH, or ethylamine) or MPcs in DMF. The spectra of QDs alone were obtained in aqueous solution, while their interaction with MPc complexes was carried out in a DMF:water (4:1 *v/v*) mixture. This solvent mixture allows for solubilization of the quantum dots and phthalocyanine while maintaining the monomeric nature of the phthalocyanine. Absorption spectra of MPcs alone have been obtained in various solvents. All measurements were performed at room temperature, in a 1 cm quartz cell.

### 2.3.2 Magnetic circular dichroism (MCD) spectra

MCD spectra were obtained at room temperature in a 1cm spectrophotometric quartz cell, using the same MPc solutions used for electronic absorption measurements, with concentrations of  $\sim 10^{-5}$  M. The solutions were placed in the MCD spectrometer and spectra recorded in parallel and anti-parallel magnetic fields.

### 2.3.3 Fluorescence spectra and quantum yields

In order to obtain fluorescence spectra, solutions of MPcs and SWCNT or QDs under investigation, and the required standards, were prepared such that the absorbance of each at the excitation wavelength was  $\sim 0.05$ . For the ZnPc-SWCNT conjugates, absorption corrections (with respect to the carbon nanotubes) were made to ensure an absorbance between 0.04 and 0.05 for ZnPc only. This is to ensure that excitation occurs for ZnPc only. The area under the curves was measured and fluorescence quantum yields ( $\Phi_F$ ) calculated using Equation 1.4 and unsubstituted ZnPc in DMF ( $\Phi_F^{\text{Std}} = 0.30$  [240]) or Rhodamine 6G in ethanol ( $\Phi_F^{\text{Std}} = 0.94$  [248,282]) as standards. The settings on the instrument remained unchanged until the end of the experiment, so that the spectra of the conjugates and the standard were comparable.

### 2.3.4 Fluorescence lifetimes

Fluorescence lifetimes ( $\tau_F$ ) for the MPc-SWCNT and MPc-QD conjugates were determined from TCSPC measurements using the setup shown in Figure 2.1. The ratio of stop to start pulses was kept low (below 0.05) to ensure good statistics. All luminescence decay curves were measured at the maximum of the emission peak and the corresponding

lifetimes obtained by deconvolution of the decay curves using the FluorFit Software program (PicoQuant GmbH, Germany).

### 2.3.5 Triplet quantum yields and lifetimes

Triplet quantum yields ( $\Phi_T$ ) and triplet lifetimes ( $\tau_T$ ) were determined by monitoring and recording triplet absorption and decay kinetic profiles using the laser flash photolysis set-up as shown in Figure 2.2. Solutions of the respective MPc complexes (absorbance  $\sim 1.5$ ) were introduced into a 1 cm pathlength spectrophotometric cell, de-aerated with argon gas for  $\sim 20$  min and irradiated at the Q band with the laser system described above. Triplet quantum yields ( $\Phi_T$ ) of the MPc complexes were determined by the triplet absorption method, Equation 1.9 using ZnPc ( $\Phi_T^{\text{Std}} = 0.58$  in DMF [241], 0.65 in DMSO [283] and 0.65 in toluene [284]) as standard. Triplet lifetimes were determined by exponential fitting of the kinetic curves using OriginPro 7.5 software.

### 2.3.6 Singlet oxygen and photodegradation quantum yields

Singlet oxygen quantum yield ( $\Phi_\Delta$ ) and photodegradation quantum yield ( $\Phi_{\text{Pd}}$ ) experiments were carried out using the experimental set-up shown in Figure 2.3 [278,280]. Singlet oxygen quantum yield ( $\Phi_\Delta$ ) values were determined in air using a 2 mL solution of the respective MPc mixed with DPBF, which acts as a singlet oxygen chemical quencher in organic solvents, in a 1 cm pathlength spectrophotometric quartz cell fitted with a tight-fitting stopper and then photolysed at the Q band using a 300W General electric quartz lamp, as described above. Determinations of photodegradation quantum yields are carried out in a similar manner, but in the absence of a chemical

quencher, where a steady decline in the Q band absorption intensity with time was noted and used for calculation of  $\Phi_{Pd}$  according to Equation 1.15.

Monitoring the degradation of DPBF, at  $\sim 416$  nm, with time allowed the determination of  $\Phi_{\Delta}$  values using Equation 1.11. Chain reactions induced by DPBF in the presence of singlet oxygen often occur [273] therefore the initial concentration of DPBF was lowered to  $\sim 3 \times 10^{-5}$  M for all solutions. The initial quencher concentrations (corresponding to an absorbance of  $\sim 1.0$ ) were kept the same for both the standard and the MPCs. ZnPc in various solvents ( $\Phi_{\Delta}^{Std} = 0.56$  in DMF [273], 0.67 in DMSO [259], 0.53 in THF [285] and 0.58 in toluene [226]) was employed as a standard.

The generation of singlet oxygen from MPC-QD conjugates was determined in air by direct detection of the 1270 nm emission of singlet oxygen using the setup shown in Figure 2.4. Determinations were made in the absence and presence of sodium azide ( $\text{NaN}_3$ ), a physical quencher of singlet oxygen. The dynamic course of  $^1\text{O}_2$  concentration [ $^1\text{O}_2$ ] can be clearly recorded, following Equation 1.13 and  $\Phi_{\Delta}$  thus determined using Equation 1.14, employing ZnPc in DMF ( $\Phi_{\Delta} = 0.56$  [273]) as standard.

## 2.4 Synthesis

### 2.4.1 Functionalization of single-walled carbon nanotubes (Scheme 3.1)

Single-walled carbon nanotubes (SWCNT, 0.7 – 1.2 nm in diameter and 2 – 20  $\mu\text{m}$  in length) were purchased from Sigma-Aldrich and used without any further purification.

**SWCNT:** IR [(KBr)  $\nu_{\text{max}}/\text{cm}^{-1}$ ]: 3438, 2924, 2853, (C-H), 1639 (C=O). [Raman  $\nu_{\text{max}}/\text{cm}^{-1}$ ]: 2540 (G\*), 1595 (G), 1270 (D).

**Functionalization of SWCNT (to form SWCNT-COOH) (1a) (Scheme 3.1(i))**

Following literature methods [6,9,10,22], SWCNT (100 mg, 8.3 mmol of C) were heated at 70°C, for 2 h, in a mixture of sulfuric acid and nitric acid (3:1 by v/v), Scheme 3.1(i).

The acid modified SWCNT were centrifuged with millipore water several times until pH 7 was obtained, giving carboxylic acid functionalized SWCNT, **SWCNT-COOH 1a**.

The tubes were then dried overnight at 70°C to give 65.6 mg of SWCNT-COOH.

**SWCNT-COOH (1a):** IR [(KBr)  $\nu_{\max}/\text{cm}^{-1}$ ]: 3553, 3479, 3414 (O-H), 1639, 1617 (C=O). [Raman  $\nu_{\max}/\text{cm}^{-1}$ ]: 2546 (G\*), 1597 (G), 1276 (D).

**Functionalization of SWCNT with ethylenediamine (to form SWCNT-NH<sub>2</sub>) (1b) (Scheme 3.1(ii))**

Pristine SWCNT (70 mg, 5.8 mmol of C) were mixed with NaNO<sub>2</sub> (93 mg, 1.4 mmol) and ethylenediamine (85 mg, 1.4 mmol). Concentrated H<sub>2</sub>SO<sub>4</sub> (0.061 mL, 1.2 mmol) was added and the mixture heated for 1 h at 60°C. The mixture was then allowed to cool, then DMF added and the mixture centrifuged and washed several times with this solvent and finally with water to remove any un-reacted ethylenediamine from the product.

**SWCNT-NH<sub>2</sub> (1b):** IR [(KBr)  $\nu_{\max}/\text{cm}^{-1}$ ]: 3552, 3478, 3415 (N-H), 2921, 2852 (C-H), 1639, 1617 (N-H). [Raman  $\nu_{\max}/\text{cm}^{-1}$ ]: 2539 (G\*), 1593 (G), 1268 (D).

**2.4.2 Synthesis of quantum dots (2) (Scheme 3.2)**

Thiol capped CdTe quantum dots were prepared by an aqueous hydrothermal method adapted from literature [60,64,65]. A Cd precursor solution was prepared by dissolving CdCl<sub>2</sub>·2H<sub>2</sub>O (2.19 g, 10 mmol) in millipore water (110 mL) in a 3-neck flask, Figure 1.6.

Mercaptocarboxylic acid (2.55 g, 24 mmol) used as a capping agent for the CdTe QDs (**2**), was then added under stirring at room temperature. The solution was then adjusted to pH 12 by dropwise addition of 1 M NaOH and nitrogen gas bubbled through the solution for 1 h. The aqueous solution was then reacted with a NaHTe solution. The typical molar ratio of Cd:Te:Thiol in each experiment was 2:1:4.8. The NaHTe solution was prepared separately by a method described in literature [60,66-68], with little modification. Briefly, 500 mg (13.2 mmol) of NaBH<sub>4</sub> was transferred to a 15 mL 3-neck flask, 10 mL of millipore water was added and nitrogen bubbled through the solution. 640 mg of tellurium powder was added in the flask after which an ice bath was maintained around the reaction flask for cooling. A small outlet was connected to the flask during the reaction to discharge the pressure from the resulting hydrogen. After ~ 8 h, the black tellurium powder disappeared and a white sodium tetraborate precipitate appeared at the bottom of the flask. The resulting clear supernatant contained NaHTe and this was separated and used in the preparation of the required CdTe particles. The freshly prepared oxygen-free NaHTe solution was injected into the Cd precursor solution under vigorous stirring. A rapid change in color occurred at this stage. The solution was then refluxed under air at 100°C for different time periods to control the size of the CdTe QDs. Aliquots of the reaction solution were taken out at regular intervals and the fluorescence emission spectra recorded until the desired wavelength (and hence size) was achieved. Precipitation of the respective QDs from the aqueous solution was achieved using excess EtOH, following which the solutions were centrifuged to obtain solid QD samples (**2**) which were dried in vacuo. The MPA capped CdTe QDs (**2**) synthesized in this work had



an emission peak at 640 nm. The QD sizes were estimated using a polynomial fitting function (Equation 2.1) [286]:

$$D = (9.8127 \times 10^{-7})\lambda^3 - (1.7147 \times 10^{-3})\lambda^2 + (1.0064)\lambda - 194.84 \quad (2.1)$$

where  $\lambda$  refers to the absorption maxima of the QDs. This fitting function is not valid for sizes of quantum dots outside the size range of 1-9 nm [286]. XRD was also employed as discussed in Chapter 3.

**CdTe MPA (2):** IR [(KBr)  $\nu_{\max}/\text{cm}^{-1}$ ]: 3467 (O-H), 2930, 2867 (C-H), 1576 (C=O). UV-Vis (0.1 M NaOH):  $\lambda_{\max}$  nm (log  $\epsilon$ ): 575 (4.54). [Raman  $\nu_{\max}/\text{cm}^{-1}$ ]: 3235, 2827, 1604, 881.

### 2.4.3 Synthesis of unsubstituted MPcs [142-144]

The synthesis of zinc (II) phthalocyanine, ZnPc (**22**) has been well documented in literature [142]. It can also be purchased from suppliers such as Sigma-Aldrich.

**ZnPc (22)** Yield: 71 %. UV-Vis (DMSO):  $\lambda_{\max}$  nm (log  $\epsilon$ ): 342 (4.02), 640 (3.58), 672 (5.38). IR [(KBr)  $\nu_{\max}/\text{cm}^{-1}$ ]: 1605, 1490, 1462, 1441, 1349, 1334, 1279, 1211, 1145, 961, 845, 809, 751, 728.

Unsubstituted cadmium (II) phthalocyanine, CdPc (**23**) and mercury (II) phthalocyanine, HgPc (**24**) were synthesized and purified following a similar reported method [142-144] for ZnPc. Phthalonitrile (1.28 g, 10 mmol) and the corresponding metal salt (2.5 mmol), (CdCl<sub>2</sub> for cadmium (II) phthalocyanine and HgCl<sub>2</sub> for mercury (II) phthalocyanine) were suspended in 1-pentanol (5 mL) and refluxed at 120°C, for 6 h, in the presence of DBU (10 mmol). The dark blue-green precipitate was collected using methanol. The crude

product was then washed with methanol for 48 h, followed by acetone using Soxhlet apparatus.

**CdPc (23)** Yield: 0.30 g (20 %). UV/Vis (DMSO):  $\lambda_{\max}$  nm (log  $\epsilon$ ): 346 (4.67), 612 (4.57), 679 (5.37). IR [(KBr)  $\nu_{\max}/\text{cm}^{-1}$ ]: 3048 (C-H), 1609, 1560 (C-C), 1113, 724 (C-H).  $^1\text{H-NMR}$  (DMSO- $d_6$ ):  $\delta$ , ppm: 9.37 (8-H, m, Pc-H), 8.21 (8-H, m, Pc'-H).

**HgPc (24)** Yield: 0.15 g (8.5 %). UV/Vis (DMSO):  $\lambda_{\max}$  nm (log  $\epsilon$ ): 330 (4.52), 618 (4.27), 681 (5.25). IR [(KBr)  $\nu_{\max}/\text{cm}^{-1}$ ]: 3049, 2541 (C-H), 1845, 1560 (C-C), 1217, 1118, 733, 713 (C-H).  $^1\text{H-NMR}$  (DMSO- $d_6$ ):  $\delta$ , ppm: 9.55 (8-H, bs, Pc-H), 8.20-7.99 (8-H, m, Pc'-H).

#### 2.4.4 Synthesis of mono-substituted phthalonitriles (Schemes 3.3 and 3.4) [117,138,147,183,261,287,288]

**3-(2-Pyridyloxy)phthalonitrile (44a):** In the presence of a steady flow of nitrogen, 2-hydroxypyridine (3.90 g, 41 mmol) and 3-nitrophthalonitrile (**10**) (5.00 g, 29 mmol) were suspended in dry DMSO (30 mL). Anhydrous  $\text{K}_2\text{CO}_3$  (9.70 g, 70 mmol) was added and the mixture stirred at room temperature. Further aliquots of  $\text{K}_2\text{CO}_3$  (2.43 g, 18 mmol) were added portion-wise after 4 h and 24 h of stirring. The reaction mixture was then stirred for a further 24 h. After 48 h total reaction time, the mixture was poured into  $\text{H}_2\text{O}$ , thus resulting in a precipitate that was filtered, washed several times with water and finally recrystallized from MeOH/water (1:1) to give a brownish yellow solid product. Yield: 6.09 g (95 %). IR [(KBr)  $\nu_{\max}/\text{cm}^{-1}$ ]: 2239 ( $\text{C}\equiv\text{N}$ ), 1290 (C-O-C), 1210, 1182, 1162 (C-N).  $^1\text{H-NMR}$  (400 MHz, DMSO- $d_6$ ):  $\delta$ , ppm: 8.28-8.26 (1-H, d, Ar-H), 8.12-

7.93 (2-H, m, Ar-H), 7.78-7.72 (1-H, d, Ar-H), 7.65-7.61 (1-H, t, Ar-H), 6.60-6.58 (1-H, d, Ar-H), 6.46-6.44 (1-H, t, Ar-H).

**3-[(4-Benzyloxy)phenoxy]phthalonitrile (44b):** Synthesis and purification was as described for **44a**, using 3-(4-benzyloxy)phenol (8.40 g, 42 mmol) and **(10)** (6.00 g, 35 mmol) to give a light brown solid product. Yield: 6.84 g (91 %). IR [(KBr)  $\nu_{\max}/\text{cm}^{-1}$ ]: 2228 (C $\equiv$ N), 1244 (C-O-C).  $^1\text{H-NMR}$  (400 MHz, DMSO- $d_6$ ):  $\delta$ , ppm: 7.53 (1-H, s, Ar-H), 7.47-7.32 (6-H, m, Ar-H), 7.05 (5-H, m, Ar-H), 5.10 (2-H, s, CH $_2$ ).

**3-Phenoxyphthalonitrile (44c):** Synthesis and purification was as described for **44a**, using phenol (5.64 g, 60 mmol) and **(10)** (6.00 g, 35 mmol) to give a brownish yellow solid product. Yield: 7.52 g (97 %). IR [(KBr)  $\nu_{\max}/\text{cm}^{-1}$ ]: 2231 (C $\equiv$ N), 1264 (C-O-C).  $^1\text{H-NMR}$  (400 MHz, DMSO- $d_6$ ):  $\delta$ , ppm: 7.08-6.95 (2-H, m, Ar-H), 6.77-6.61 (2-H, m, Ar-H), 6.56-6.35 (4-H, m, Ar-H).

**3-(4-*Tert*-butylphenoxy)phthalonitrile (44d):** Synthesis and purification was as described for **44a**, using 4-*tert*-butylphenol (7.80 g, 51 mmol) and **(10)** (6.00 g, 35 mmol) to give a brownish yellow solid product. Yield: 9.40 g (97 %). IR [(KBr)  $\nu_{\max}/\text{cm}^{-1}$ ]: 2230 (C $\equiv$ N), 1208 (C-O-C).  $^1\text{H-NMR}$  (400 MHz, DMSO- $d_6$ ):  $\delta$ , ppm: 7.84-7.78 (2-H, m, Ar-H), 7.50 (2-H, d, Ar-H), 7.26-7.21 (1-H, m, Ar-H), 7.14 (2-H, d, Ar-H), 1.30 (9-H, s, *t*-Bu).

**4-(2-(Pyridyloxy)phthalonitrile (45a):** Synthesis and purification was as described for **44a**, using 2-hydroxypyridine (7.00 g, 74 mmol) and 4-nitrophthalonitrile (**13**) (8.50 g, 49 mmol) to give a brownish-yellow solid product. Yield: 10.3 g (95 %). IR [(KBr)  $\nu_{\max}/\text{cm}^{-1}$ ]: 2284 (C $\equiv$ N), 1220 (C-O-C).  $^1\text{H-NMR}$  (400 MHz, DMSO- $d_6$ ):  $\delta$ , ppm: 8.34 (1-H, s, Ar-H), 8.27-8.25 (1-H, d, Ar-H), 8.04-8.02 (1-H, d, Ar-H), 7.70 (1-H, d, Ar-H), 7.52 (1-H, t, Ar-H), 6.52-6.49 (1-H, d, Ar-H), 6.37 (1-H, t, Ar-H).

**4-[(4-Benzyloxy)phenoxy]phthalonitrile (45b):** Synthesis and purification was as described for **44a**, using 4-(benzyloxy)phenol (8.40 g, 42 mmol) and (**13**) (6.00 g, 35 mmol) to give a brownish yellow solid product. Yield: 7.18 g (63 %). IR [(KBr)  $\nu_{\max}/\text{cm}^{-1}$ ]: 2229 (C $\equiv$ N), 1236 (C-O-C).  $^1\text{H-NMR}$  (400 MHz, DMSO- $d_6$ ):  $\delta$ , ppm: 7.26 (1-H, d, Ar-H), 6.88 (1-H, s, Ar-H), 6.67-6.48 (6-H, m, Ar-H), 6.36-6.30 (4-H, m, Ar-H), 4.32 (2-H, s, CH $_2$ ).

**4-Phenoxyphthalonitrile (45c):** Synthesis and purification was as described for **44a**, using phenol (5.64 g, 60 mmol) and (**13**) (6.00 g, 35 mmol) to give a brownish yellow solid product. Yield: 7.38 g (96 %). IR [(KBr)  $\nu_{\max}/\text{cm}^{-1}$ ]: 2234 (C $\equiv$ N), 1249 (C-O-C).  $^1\text{H-NMR}$  (400 MHz, CDCl $_3$ ):  $\delta$ , ppm: 7.68 (1-H, d, Ar-H), 7.43 (2-H, t, Ar-H), 7.28 (3-H, m, Ar-H), 7.04 (2-H, d, Ar-H).

**4-(4-*Tert*-butylphenoxy)phthalonitrile (45d):** Synthesis and purification was as described for **44a**, using 4-*tert*-butylphenol (7.80 g, 52 mmol) and (**13**) (6.00 g, 35 mmol) to give a brownish yellow solid product. Yield 9.11 g (94 %). IR [(KBr)  $\nu_{\max}/\text{cm}^{-1}$ ]: 2230

(C≡N), 1240 (C-O-C). <sup>1</sup>H-NMR (400 MHz, CDCl<sub>3</sub>): δ, ppm: 7.70 (1-H, d, Ar-H), 7.47 (2-H, d, Ar-H), 7.25 (2-H, d, Ar-H), 6.99 (2-H, m, Ar-H), 1.34 (9-H, s, *t*-Bu).

**4-(2-Mercaptopyridine)phthalonitrile (46), Scheme 3.4 [147,288]:** Under a steady flow of nitrogen, 2-mercaptopyridine (2.33 g, 21 mmol) and **(13)** (3.63 g, 21 mmol) were dissolved in DMF (30 mL) and the mixture stirred for 15 min at room temperature. Thereafter, anhydrous K<sub>2</sub>CO<sub>3</sub> (7.5 g, 54 mmol) was added portion-wise over a period of 4 h and the reaction mixture left to stir for a further 12 h. The mixture was then added to water and stirred for 30 min. The resulting precipitate was filtered off, washed thoroughly with water, dried and recrystallized from ethanol to give a brownish yellow solid product. Yield: 3.79 g (76 %). IR [(KBr) ν<sub>max</sub>/cm<sup>-1</sup>]: 2231 (C≡N), 1282, 1157, 1129 (C-N), 643 (C-S-C). <sup>1</sup>H-NMR (400 MHz, DMSO-d<sub>6</sub>): δ, ppm: 8.50 (1-H, d, Ar-H), 8.28 (1-H, s, Ar-H), 8.09 (1-H, d, Ar-H), 7.91 (1-H, dd, Ar-H), 7.81-7.68 (1-H, m, Ar-H), 7.46 (1-H, d, Ar-H), 7.35 (1-H, m, Ar-H).

**4-(3,4-Dicyanophenoxy)benzoic acid (47), Scheme 3.4 [138]:** To dry DMSO (30 mL) under nitrogen, was added 3.5 g (25 mmol) of K<sub>2</sub>CO<sub>3</sub>. 4-Hydroxybenzoic acid (2.36 g, 17.1 mmol) and **(13)** (2.0 g, 11.5 mmol) were added to the suspension. After 4 h and 24 h, more K<sub>2</sub>CO<sub>3</sub> (3.5 g, 25 mmol) was added to the mixture. The mixture was stirred at room temperature for 5 days, following which the formed precipitate was dissolved in water (600 ml), and the pH of the solution adjusted to 1 by addition of HCl to give a beige coloured product. Yield: 3.10 g (69 %). IR [(KBr) ν<sub>max</sub>/cm<sup>-1</sup>]: 3088 (C-H), 2231 (C≡N), 1678, 1591 (C=O), 1491, 1254 (C-O-C), 851 (C-H). <sup>1</sup>H-NMR (400 MHz,

DMSO-d<sub>6</sub>):  $\delta$ , ppm: 13.09 (1-H, s, -COOH), 8.13 (1-H, d, 6'-H), 8.03 (2-H, m, 3,5-H), 7.89 (1-H, d, 3'-H), 7.58 (1-H, dd, 5'-H), 7.29 (2-H, m, 2,6-H).

#### 2.4.5 Synthesis of symmetrical aryloxy tetra-substituted MPcs (Scheme 3.3)

##### Tetrakis{2,(3)-pyridyloxyphthalocyaninato}zinc(II) ( $\beta$ -ZnTPyPc, **25a**) [147,288]

Under an inert nitrogen atmosphere, compound **45a** (2.5 g, 14.6 mmol) was dissolved in dry 1-pentanol (~ 15 mL). To this solution, zinc acetate (0.60 g, 2.8 mmol) and DBU (1.49 mL, 10 mmol) were added and the mixture heated under reflux at 160°C for 16 h. The resultant dark-green coloured precipitate was then added to methanol, filtered and purified using methanol and acetone in Soxhlet apparatus to give a dark-green solid which was oven dried at 90°C. Yield: 1.30 g (50 %). UV/Vis (DMSO):  $\lambda_{\max}$  nm (log  $\epsilon$ ): 340 (4.50), 615 (4.32), 680 (5.36). IR [(KBr)  $\nu_{\max}/\text{cm}^{-1}$ ]: 3040 (C-H), 1583 (C-C), 1245 (C-O), 1135, 1096 (C-O-C), 865, 764 (C-H). <sup>1</sup>H-NMR (400 MHz, DMSO-d<sub>6</sub>):  $\delta$ , ppm: 9.36-9.23 (8-H, m, Pc-H), 8.20 (4-H, bs, Pc'-H), 7.71-7.69 (16-H, m, *pyridyloxy*). MALDI-TOF-MS *m/z*: Calc. 950.254 amu; Found: 950.29 amu [M]<sup>+</sup>. Anal. Calc. For C<sub>52</sub>H<sub>28</sub>N<sub>12</sub>O<sub>4</sub>Zn: C (65.72), H (2.97), N (17.69); Found: C (66.60), H (3.01), N (17.92).

##### Tetrakis{2,(3)-pyridyloxyphthalocyaninato}cadmium(II) ( $\beta$ -CdTPyPc, **26a**)

The synthetic and purification procedure for **26a** was similar to that used for complex **25a** using cadmium chloride (CdCl<sub>2</sub>) instead of zinc acetate. Amounts of reagents used were: compound **45a** (2.5 g, 14.6 mmol), 1-pentanol (15 mL) and CdCl<sub>2</sub> (0.60 g, 2.72 mmol). Yield: 1.52 g (56 %). UV/Vis (DMSO):  $\lambda_{\max}$  nm (log  $\epsilon$ ): 355 (4.70), 618 (4.52), 685 (5.30). IR [(KBr)  $\nu_{\max}/\text{cm}^{-1}$ ]: 1614 (C-C), 1205 (C-O), 1133, 1090 (C-O-C), 765 (C-H).

<sup>1</sup>H-NMR (400 MHz, DMSO-d<sub>6</sub>): δ, ppm: 9.47-9.37 (8-H, m, Pc-H), 8.18 (4-H, bs, Pc'-H), 7.71-7.69 (16-H, m, pyridyloxy). MALDI-TOF-MS *m/z*: Calc. 997.264 amu; Found: 998.01 amu [M]<sup>+</sup>. Anal. Calc. For C<sub>52</sub>H<sub>28</sub>N<sub>12</sub>O<sub>4</sub>Cd: C (62.62), H (2.83), N (16.86); Found: C (62.65), H (2.83), N (16.85).

**Tetrakis{2,(3)-(4-benzyloxy)phenoxyphthalocyaninato}cadmium(II) (β-CdTBzPhPc, 26b)**

Synthesis was as outlined for **25a** using the following reagents and quantities: **45b** (0.625 g, 1.82 mmol), cadmium acetate dihydrate (0.120 g, 0.452 mmol), 1-pentanol (~ 2 mL), DBU (0.243 mL, 1.63 mmol). However in terms of purification: the crude product was purified by column chromatography, eluting with CHCl<sub>3</sub>/MeOH (10:1). Soxhlet extraction first with acetone and then with EtOH gave the desired compound **26b**. Yield: 0.15 g (23 %). UV-Vis (DMSO): λ<sub>max</sub> nm (log ε): 341 (4.12), 631 (3.89), 656 (3.90), 688 (4.13). IR [(KBr) ν<sub>max</sub>/cm<sup>-1</sup>]: 2848 (C-H), 1216 (C-O-C). <sup>1</sup>H-NMR (400 MHz, CDCl<sub>3</sub>): δ, ppm: 7.83-7.16 (56-H, m, Ar-H/Pc-H/CH<sub>2</sub>). MALDI-TOF MS *m/z*: Calc. 1417.8 amu; Found: 1418.24 amu [M]<sup>+</sup>. Anal. Calc. For C<sub>84</sub>H<sub>56</sub>N<sub>8</sub>O<sub>8</sub>Cd: C (71.16), H (3.98), N (7.90); Found: C (70.16), H (4.02), N (8.33).

**Tetrakis{2,(3)-phenoxyphthalocyaninato}cadmium(II) (β-CdTPhPc, 26c)**

Following a similar synthetic procedure as in **25a**, **26c** was prepared using **45c** (1.15 g, 5.22 mmol), cadmium acetate (0.50 g, 1.25 mmol excess) and DBU (5 mmol) in 1-octanol (10 mL). Purification according to **26b** was used. Yield: 0.23 g (18 %). UV/Vis (DMSO): λ<sub>max</sub> nm (log ε): 350 (4.83), 613 (4.61), 681 (5.22). IR [(KBr) ν<sub>max</sub>/cm<sup>-1</sup>]: 3167-

3061 (C-H), 1232 (C-O-C).  $^1\text{H-NMR}$  (600 MHz,  $\text{CDCl}_3$ ):  $\delta$ , ppm: 7.70-7.09 (32-H, m, Ar-H/Pc-H). Anal. Calc. For  $\text{C}_{56}\text{H}_{32}\text{N}_8\text{O}_4\text{Cd}$ : C (67.71), H (3.25) N (11.28); Found: C (68.58), H (3.85), N (11.42).

**Tetrakis{2,(3)-*tert*-butylphenoxyphthalocyaninato}cadmium(II) ( $\beta$ -CdTtBuPhPc, 26d)**

Following a similar synthetic and purification procedure as in **25a**, **26d** was prepared using **45d** (1.38 g, 5.00 mmol), cadmium acetate (0.50 g, 1.25 mmol excess) and DBU (5 mmol) in 1-octanol (10 mL). On cooling, the dark green solution was added to MeOH (~50 mL), filtered and chromatographed using silica-gel 60, using THF as the eluting solvent. A dark green solid was obtained once the solvent was removed by evaporation. Yield: 0.25 g (17 %). UV/Vis (DMSO):  $\lambda_{\text{max}}$  nm (log  $\epsilon$ ): 355 (5.08), 613 (4.80), 684 (5.47). IR [(KBr)  $\nu_{\text{max}}/\text{cm}^{-1}$ ]: 2955 (C-H), 1235 (C-O-C).  $^1\text{H-NMR}$  (600 MHz,  $\text{CDCl}_3$ ):  $\delta$ , ppm: 7.82-7.73 (2-H, br s, Pc-H), 7.69 (2-H, dd, Pc-H), 7.57 (3-H, m, Pc-H), 7.51 (5-H, m, Pc-H), 7.42-7.40 (7-H, m, Ar-H), 7.06-7.03 (9-H, m, Ar-H), 1.33 (36-H, s, *t*-Bu). Anal. Calc. For  $\text{C}_{72}\text{H}_{64}\text{N}_8\text{O}_4\text{Cd}$ : C (71.01), H (5.30), N (9.20); Found: C (72.23), H (6.38), N (7.23).

**Tetrakis{2,(3)-pyridyloxyphthalocyaninato}mercury(II) ( $\beta$ -HgTPyPc, 27a)**

The synthetic and purification procedure for **27a** was similar to that used for complex **25a** using mercury chloride ( $\text{HgCl}_2$ ) instead of zinc acetate. Amounts of the reagents were: compound **44a** (2.50 g, 14.6 mmol), 1-pentanol (15 mL) and  $\text{HgCl}_2$  (0.74 g, 2.72 mmol). Yield: 1.20 g (41 %). UV/Vis (DMSO):  $\lambda_{\text{max}}$  nm (log  $\epsilon$ ): 340 (4.55), 623 (4.06), 690



(5.17). IR [(KBr)  $\nu_{\max}/\text{cm}^{-1}$ ]: 3045 (C-H), 1586 (C-C), 1270 (C-O), 1130, 1098 (C-O-C), 748 (C-H).  $^1\text{H}$  NMR (DMSO- $d_6$ ):  $\delta$ , ppm: 9.31-8.94 (8-H, m, Pc-H), 8.19 (4-H, bs, Pc'-H), 7.80-7.68 (16-H, m, *pyridyloxy*). MALDI-TOF-MS  $m/z$ : Calc. 1085.464 amu; Found: 1085.66 amu  $[\text{M}]^+$ . Anal. Calc. For  $\text{C}_{52}\text{H}_{28}\text{N}_{12}\text{O}_4\text{Hg}$ : C (57.53), H (2.60), N (15.49); Found: C (58.30), H (2.64), N (15.68).

#### **Tetrakis{1,(4)-(2-pyridyloxy)phthalocyaninato}cadmium(II) ( $\alpha$ -CdTPyPc, 28a)**

A similar synthetic procedure to that for **25a** was followed employing cadmium acetate instead of zinc acetate. Amounts of reagents were: **44a** (0.396 g, 1.82 mmol), cadmium acetate dihydrate (0.121 g, 0.456 mmol), 1-pentanol (~ 3 mL), DBU (0.243 mL, 1.63 mmol). Purification according to **26b** was used. Yield: 0.09 g (19 %). UV-Vis (DMSO):  $\lambda_{\max}$  nm (log  $\epsilon$ ): 323 (4.40), 389 (4.16), 620 (3.99), 684 (4.80). IR [(KBr)  $\nu_{\max}/\text{cm}^{-1}$ ]: 1620 (C-C), 1110 (C-O-C).  $^1\text{H}$ -NMR (600 MHz, DMSO- $d_6$ ):  $\delta$ , ppm: 8.82-6.15 (28-H, m, Ar-H/Pc-H). MALDI-TOF MS  $m/z$ : Calc. 997.27 amu; Found: 997.84 amu  $[\text{M}+\text{H}]^+$ . Anal. Calc. For  $\text{C}_{52}\text{H}_{28}\text{N}_{12}\text{O}_4\text{Cd}$ : C (62.63), H (2.83), N (16.85); Found: C (62.44), H (2.82), N (16.80).

#### **Tetrakis{1,(4)-(4-benzyloxy)phenoxyphthalocyaninato}cadmium(II)**

##### **( $\alpha$ -CdTBzPhPc, 28b)**

The synthetic procedure for **28b** was similar to that used for complex **26b** using **44b** (0.625 g, 1.82 mmol), dry 1-pentanol (~ 2 mL), cadmium acetate dihydrate (0.121 g, 0.454 mmol) and DBU (0.243 mL, 1.63 mmol). Purification was similar to that reported for **26b**. Yield: 0.17 g (35 %). UV-Vis (DMSO):  $\lambda_{\max}$  nm (log  $\epsilon$ ): 327 (4.81), 397 (4.60),

632 (4.50), 702 (5.32). IR [(KBr)  $\nu_{\max}/\text{cm}^{-1}$ ]: 2954 (C-H), 1199 (C-O-C).  $^1\text{H-NMR}$  (400 MHz, DMSO- $d_6$ ):  $\delta$ , ppm: 9.73-9.03 (4-H, m, Pc-H), 8.66-8.22 (4-H, m, Pc'-H), 8.24-7.68 (28-H, m, Pc'-H, Phenyl-H), 7.70-7.30 (12-H, m, Phenyl-H), 5.64-5.39 (8-H, m, CH<sub>2</sub>). MALDI-TOF MS  $m/z$ : Calc. 1417.8 amu; Found: 1419.12 amu  $[\text{M}+\text{H}]^+$ . Anal. Calc. For C<sub>84</sub>H<sub>56</sub>N<sub>8</sub>O<sub>8</sub>Cd: C (71.16), H (3.98), N (7.90); Found: C (71.15), H (4.66), N (7.73).

#### **Tetrakis{1,(4)-phenoxyphthalocyaninato}cadmium(II) ( $\alpha$ -CdTPhPc, 28c)**

Following a similar synthetic procedure as for **25a**, **28c** was prepared using **44c** (1.10 g, 5.00 mmol), cadmium acetate (~ 0.50 g, 1.25 mmol excess) and DBU (5 mmol) in 1-octanol (10 mL). The crude product was then purified by column chromatography, eluting with THF. Following evaporation of the solvent, the product was purified further by Soxhlet extraction first with acetone and finally with EtOH. Yield: 0.61 g (49 %). UV/Vis (DMSO):  $\lambda_{\max}$  nm (log  $\epsilon$ ): 351 (4.73), 631 (4.56), 698 (5.26). IR [(KBr)  $\nu_{\max}/\text{cm}^{-1}$ ]: 2912 (C-H), 1244 (C-O-C).  $^1\text{H-NMR}$  (600 MHz, CDCl<sub>3</sub>):  $\delta$ , ppm: 7.79 (4-H, d, Pc-H), 7.74 (3-H, br s, Pc-H), 7.43 (8-H, t, Pc-H/Ar-H), 7.30 (5-H, m, Ar-H), 7.28-7.24 (4-H, m, Ar-H), 7.08 (8-H, d, Ar-H). Anal. Calc. For C<sub>56</sub>H<sub>32</sub>N<sub>8</sub>O<sub>4</sub>Cd: C (67.71), H (3.25), N (11.28); Found: C (68.29), H (3.35), N (9.94).

#### **Tetrakis{1,(4)-*tert*-butylphenoxyphthalocyaninato}cadmium(II) ( $\alpha$ -CdTtBuPhPc, 28d)**

A mixture of **44d** (1.38 g, 5.00 mmol), cadmium acetate (0.50 g, 1.25 mmol) and DBU (5 mmol) were heated to 140°C in 1-octanol (10 mL) under a dry, inert nitrogen atmosphere

for 6 h. Purification according to **26d** was used. Yield: 0.35 g (24 %). UV/Vis (DMSO):  $\lambda_{\max}$  nm (log  $\epsilon$ ): 329 (4.96), 629 (4.78), 698 (5.48). IR [(KBr)  $\nu_{\max}/\text{cm}^{-1}$ ]: 2954 (C-H), 1266 (C-O-C).  $^1\text{H-NMR}$  (600 MHz,  $\text{CDCl}_3$ ):  $\delta$ , ppm: 7.79 (2-H, d, Pc-H), 7.74 (3-H, br s, Pc-H), 7.43 (4-H, t, Pc-H/Ar-H), 7.30 (7-H, m, Ar-H), 7.28-7.24 (4-H, m, Ar-H), 7.08 (8-H, d, Ar-H), 1.35 (36-H, s, *t*-Bu). Anal. Calc. For  $\text{C}_{72}\text{H}_{64}\text{N}_8\text{O}_4\text{Cd}$ : C (71.01), H (5.30), N (9.20); Found: C (72.72), H (6.11), N (5.96).

#### 2.4.6 Synthesis of symmetrical *tert*-butyl and alkanethio tetra-substituted MPcs (Scheme 3.5)

##### Tetrakis{2,(3)-*tert*-butylphthalocyaninato}zinc(II) ( $\beta$ -ZnttbPc, **29**, Scheme 3.5) [153,168,289,290]

4-*tert*-butylphthalic anhydride (**48**) (3.86 g, 19 mmol), urea (3.37 g, 56 mmol), zinc acetate (1.04 g, 4.7 mmol) and ammonium molybdate (0.50 g, 0.40 mmol) were suspended in nitrobenzene (5 mL) and heated at 180°C for 8 h. After cooling, the mixture was precipitated with MeOH and washed several times with hot MeOH followed by hot water. The crude product was then purified by silica gel column chromatography eluting first with  $\text{CHCl}_3$ , then  $\text{CHCl}_3/\text{MeOH}$  (9:1) and finally with  $\text{CHCl}_3$ . Yield: 12.8 mg (0.34 %). UV-Vis (DMSO):  $\lambda_{\max}/\text{nm}$  (log  $\epsilon$ ): 351 (4.95), 612 (4.61), 678 (5.44). IR [(KBr)  $\nu_{\max}/\text{cm}^{-1}$ ]: 3424 (C-H), 2923, 2853 (C-H), 1617 (C=O), 1389, 1329 (C-H), 1092 (C-O-C), 598, 522.  $^1\text{H-NMR}$  (400 MHz,  $\text{DMSO-d}_6$ ):  $\delta$ , ppm: 9.40 (5-H, bs, Pc-H), 9.31-9.27 (3-H, m, Pc-H), 8.34 (4-H, bs, Pc-H), 1.79 (36-H, s, *t*-Bu). Anal. Calc. For  $\text{C}_{48}\text{H}_{48}\text{N}_8\text{Zn}$ : C (71.85), H (6.03), N (13.97); Found: C (70.26), H (5.94), N (12.53).

**Tetrakis{2,(3)-mercaptopyridinephthalocyaninato}zinc(II) ( $\beta$ -ZnTMPyPc, 30,  
Scheme 3.5) [154,291]**

A mixture of zinc acetate (0.60 g, 2.8 mmol), **46** (0.50 g, 2.1 mmol), DBU (1.66 mL, 12 mmol) and quinoline (10 mL, doubly distilled over CaH<sub>2</sub>) was stirred at ~ 120°C for 5 h under an inert nitrogen atmosphere. On cooling the solution was precipitated in MeOH and washed several times with the same solvent. The crude product was dissolved in DMF and after concentrating, precipitated with hot EtOH, centrifuged and washed several times with EtOH then acetone. The product was purified by column chromatography using silica gel eluting first with CHCl<sub>3</sub>/MeOH (9:1) and then THF. Yield: 0.16 g (7.5 %). UV-Vis (DMSO):  $\lambda_{\text{max}}$ /nm (log  $\epsilon$ ): 361 (4.45), 619 (4.20), 687 (5.02). IR [(KBr)  $\nu_{\text{max}}$ /cm<sup>-1</sup>]: 3423 (O-H), 2921, 2852 (C-H), 1738, 1637 (C=O), 1452, 1415, 1383 (C-H), 698 (C-S-C). <sup>1</sup>H-NMR (600 MHz, DMSO-d<sub>6</sub>):  $\delta$ , ppm: 9.01-8.74 (8-H, m, Pc-H), 8.60-8.52 (4-H, m, Pc-H), 8.27-8.15 (4-H, m, Ar-H), 7.83-7.74 (4-H, m, Ar-H), 7.49 (4-H, m, Ar-H), 7.26 (4-H, m, Ar-H). Anal. Calc. For C<sub>56</sub>H<sub>46</sub>N<sub>12</sub>S<sub>4</sub>Zn: C (61.56), H (2.78), N (16.57), S (12.64); Found: C (61.45), H (2.72), N (16.52), S (12.53).

**2.4.7 Synthesis of low-symmetry (A<sub>3</sub>B type) tetra-substituted MPcs (Scheme 3.6)  
[137-139]**

**Tris{9 (10), 16 (17), 23 (24)-(tert-butyl)imidophthalocyaninato}zinc(II) (ZnttbIPc, 31)**

A well ground mixture of 4-*tert*-butylphthalic anhydride (**48**), pyromellitic dianhydride (**17**), zinc acetate dihydrate, well dried urea and ammonium molybdate was suspended in a 16:4:1:108:0.0003 molar ratio in nitrobenzene (10 - 15 mL) and heated under reflux to 190°C for *ca.* 8 h. Following removal of the solvent, the dark green solid residue was

washed several times with MeOH, hot water and finally with MeOH. Soxhlet extraction in acetone followed by CHCl<sub>3</sub> afforded a dark green product upon removal of the solvent. The crude product was chromatographed first on silica gel and then on an Sx-2 column using CHCl<sub>3</sub> as the eluent. Recrystallization from a benzene/hexane mixture, provided 277 mg (0.34 mmol) of the desired product in 7.1 % yield. UV/Vis (CHCl<sub>3</sub>):  $\lambda_{\max}$  nm (log  $\epsilon$ ): 356 (4.59), 604 (4.06), 648 (4.56), 668 (4.66), 715 (4.88). IR [(KBr)  $\nu_{\max}/\text{cm}^{-1}$ ]: 3217 (C-H), 1771, 1717, (N-H), 1616, 1356, 1306, 1254, 1115, 1084, 1045, 870, 752, 698, 648, 559, 520. <sup>1</sup>H-NMR (400 MHz, pyridine-d<sub>5</sub>):  $\delta$ , ppm: 13.36 (1-H, s, N-H), 9.94-9.80 (2-H, m, Ar-H), 9.78-9.53 (6-H, m, Ar-H), 8.52-8.50 (3-H, m, Ar-H), 1.84-1.66 (27-H, m, *t*-Bu). Maldi-TOF MS  $m/z$ : Calc. 815.25; Found: 812.72 [M]<sup>3+</sup>. Anal. Calc. For C<sub>46</sub>H<sub>39</sub>N<sub>9</sub>O<sub>2</sub>Zn: C (67.77), H (4.82), N (15.46); Found: C (67.28), H (5.24), N (15.12).

**Tris{9 (10), 16 (17), 23 (24)-(4-(2-mercaptopyridine)-2-(4-carboxyphenoxy)phthalocyaninato}zinc(II) (ZnPc-COOH, 32)**

Complex **47** (1.80 mmol) and 5.40 mmol of **46** were suspended in 25 mL of dry 1-pentanol at 140°C under nitrogen gas. At this temperature, 250 mg (35 mmol) of lithium metal was added and the solution stirred for 15 min. On cooling to room temperature glacial acetic acid (50 mL) was added and the resulting precipitate centrifuged and washed several times with water. The product at this stage is the metal free substituted derivative. To give the metallated derivative the above product was heated at 80°C in DMF (30 mL) for 5 h in the presence of excess zinc (II) acetate dihydrate. The DMF solution was evaporated to dryness and the solid residue washed with water in a centrifuge. The product was dissolved in a minimum amount of DMF and

chromatographed on a silica gel Si60 column with diethyl ether/DMF (9:1) eluent, initially and gradually increasing to 100 % DMF at which point the second desired fraction was collected. Further chromatographic separations with CHCl<sub>3</sub>/MeOH (9:1) were conducted several times with the second fraction containing the desired product **ZnPc-COOH, 32**. Yield: 0.40 g (21 %). UV-Vis (DMSO):  $\lambda_{\text{max}}/\text{nm}$  (log  $\epsilon$ ): 366 (4.85), 619 (5.61), 687 (5.41). IR [(KBr)  $\nu_{\text{max}}/\text{cm}^{-1}$ ]: 3437 (O-H), 1676 (C=O), 1573 (C=C), 1096 (C-O-C), 682, 617 (C-S-C). <sup>1</sup>H-NMR (400 MHz, DMSO-d<sub>6</sub>):  $\delta$ , ppm: 9.00-8.70 (8-H, m, Pc-H), 8.59-8.49 (4-H, d, Pc-H), 8.28-8.12 (4-H, m, Ar-H), 7.82-7.70 (4-H, m, Ar-H), 7.52-7.41 (4-H, m, Ar-H), 7.29-7.17 (4-H, m, Ar-H). Anal. Calc. For C<sub>54</sub>H<sub>29</sub>N<sub>11</sub>O<sub>3</sub>S<sub>3</sub>Zn: C (62.28), H (2.81), N (14.79), S (9.24); Found: C (62.24), H (3.49), N (14.79), S (9.79).

#### 2.4.8 Synthesis of MPc-SWCNT conjugates [18,24,292] (Schemes 5.1 and 5.2)

##### ZnPc(31)-SWCNT-linked (49, Scheme 5.1(i))

The functionalized SWCNT, SWCNT-COOH **1a** (10 mg, 0.83 mmol of C) were suspended in dry DMF (10 mL) and sonicated for several minutes. Following which, EDC (5 mg) and NHS (5 mg) were added and the mixture was stirred at room temperature for 2 h. ZnttbIPc, **31** (10 mg, 0.01 mmol) was then added to activated **1a** and the mixture stirred for 4 days. The solid black product was obtained by centrifuging, washing in DMF and then drying at 70°C. IR [(KBr)  $\nu_{\text{max}}/\text{cm}^{-1}$ ]: 3432 (N-H), 2958, 2922, 2853 (C-H), 1636 (C=O). [Raman  $\nu_{\text{max}}/\text{cm}^{-1}$ ]: 2543 (G\*), 1596 (G), 1290 (D).

**ZnPc(32)-SWCNT-linked (50, Scheme 5.1(ii))**

**ZnPc-COOH, 32** (10.40 mg, 0.01 mmol) was first dissolved in DMF (10 mL), then DCC (32.85 mg, 0.16 mmol) was added to convert the –COOH group into an active carbodiimide ester group. The mixture was left to stir at room temperature under a nitrogen atmosphere for 24 h. Thereafter, amine functionalized SWCNT, **1b** (10 mg, 0.83 mmol of C) was added to the reaction mixture and then left for another 48 h. The solid product was extracted and washed several times with DMF (to remove excess unreacted complex **31** and any DCC intermediate by-products) using a centrifuge. This was followed by oven drying at 70°C to give a dark black-green powder **ZnPc(32)-SWCNT-linked, 50**. IR [(KBr)  $\nu_{\max}/\text{cm}^{-1}$ ]: 3416 (N-H), 2920, 2851 (C-H), 1653 (C=O). [Raman  $\nu_{\max}/\text{cm}^{-1}$ ]: 2548 (G\*), 1597 (G), 1267 (D).

**ZnPc(31):SWCNT-adsorbed (51, Scheme 5.2(i))**

SWCNT-COOH, **1a** (10 mg, 0.83 mmol of C) was sonicated for ~15 mins in dry DMF (40 mL) to give a brown coloured suspension. ZnttbIPc, **31** (10 mg, 0.01 mmol) was then added (resulting in a green coloured suspension) and the mixture stirred for 12 days at which point the green colour had faded to brown (indicating adsorption of the ZnPc on the SWCNT), according to literature [24]. The solid product was separated from the solution by centrifuging and several washings with DMF (to remove excess unreacted **31**) to give the adsorbed species **ZnPc(31):SWCNT-adsorbed, 51**. IR [(KBr)  $\nu_{\max}/\text{cm}^{-1}$ ]: 3551, 3476, 3418 (O-H), 2957, 2923, 2853 (C-H), 1637 (C=O). [Raman  $\nu_{\max}/\text{cm}^{-1}$ ]: 2540 (G\*), 1594 (G), 1275 (D).

**ZnPc(32):SWCNT-adsorbed (52, Scheme 5.2(ii))**

Amine functionalized SWCNT, **1b** (10 mg, 0.83 mmol of C) were sonicated for ~15 mins in dry DMF (40 mL) to give a dark suspension. Complex **32** (5 mg, 0.005 mmol) was then added (resulting in a green coloured suspension) and the mixture stirred for 17 days at which point the green colour had faded (indicating adsorption of the Pc on the SWCNT), according to literature [24]. The solid product was separated from the solution by centrifuging and several washings with DMF (to remove excess unreacted complex **32**) to give the adsorbed species **ZnPc(32):SWCNT-adsorbed, 52**. IR [(KBr)  $\nu_{\max}/\text{cm}^{-1}$ ]: 3433 (O-H), 2922, 2853 (C-H), 1681, 1633 (C=O, N-H). [Raman  $\nu_{\max}/\text{cm}^{-1}$ ]: 2541 (G\*), 1596 (G), 1265 (D).

**2.4.9 Synthesis of MPc-QD conjugates (Scheme 5.3)****ZnPc(31)-QD-linked (53, Scheme 5.3)**

MPA capped CdTe QDs, **2** (7.5 mg) were first dissolved in water (1 mL), then DMF (4 mL) was added, followed by addition of DCC (3.28 mg, 0.016 mmol). The latter is used to convert the -COOH group into an active carbodiimide ester group. The mixture was left to stir at room temperature under an argon atmosphere for 24 h. Thereafter, ZnttbIPc, **31** (0.13 mg,  $1.56 \times 10^{-4}$  mmol) was added to the reaction mixture and then left for another 48 h. The solid product was extracted and washed several times with DMF (to remove excess unreacted complex **31** and any DCC intermediate by-products) and also washed with water to remove unlinked QDs. The washings were continued until the supernatants were clear, giving **ZnPc(31)-QD-linked, 53**. IR [(KBr)  $\nu_{\max}/\text{cm}^{-1}$ ]: 1645 (C=O). [Raman  $\nu_{\max}/\text{cm}^{-1}$ ]: 3184, 3138, 2862, 2147, 1940, 1886, 1086.



**ZnPc(31):QD-mixed (54)**

Experiments were also performed where the QDs (2) were mixed with ZnttbIPc (31) without linking, giving **ZnPc(31):QD-mixed, 54**.

## **Results and Discussion**

- 3. Synthesis and Spectroscopic Characterization**
- 4. Photophysical and Photochemical Properties**
- 5. Interaction of Metallophthalocyanines with  
Nanoparticles**

---

## Publications

The results discussed in the following chapters have been presented in the articles listed below, that have been published or submitted for publication in peer-reviewed journals.

These articles have not been referenced in this thesis:

1. Synthesis and photophysics of new phthalocyanine derivatives of zinc, cadmium and mercury, **Wadzanai Chidawanyika**, Abimbola Ogunsipe, Tebello Nyokong, *New J. Chem.* **31** (2007) 377.
2. Synthesis and solvent effects on the photophysicochemical properties of novel cadmium phenoxy phthalocyanines, **Wadzanai Chidawanyika**, Edith Antunes, Tebello Nyokong, *J. Photochem. Photobiol. A: Chem.* **195** (2008) 183.
3. Spectroscopic and photophysicochemical behaviours of novel cadmium phthalocyanine derivatives tetra-substituted at the alpha and beta positions, **Wadzanai Chidawanyika**, Tebello Nyokong, *J. Photochem. Photobiol. A: Chem.* **202** (2009) 99.
4. Effect of peripheral fused ring substitution on the optical spectroscopy and electronic structure of metal phthalocyanine complexes, **Wadzanai Chidawanyika**, John Mack, Soji Shimizu, Nagao Kobayashi, Tebello Nyokong, *J. Porphyrins Phthalocyanines* **10** (2009) 1053.
5. The synthesis and photophysicochemical properties of low-symmetry zinc phthalocyanine analogues, **Wadzanai Chidawanyika**, Tebello Nyokong, *J. Photochem. Photobiol. A: Chem.* **206** (2009) 169.

6. Characterization of amine-functionalized single-walled carbon nanotube-low symmetry phthalocyanine conjugates, **Wadzanai Chidawanyika**, Tebello Nyokong, *Carbon* (Submitted).
7. Photophysical study of a covalently linked quantum dot-low symmetry phthalocyanine conjugate, **Wadzanai Chidawanyika**, Christian Litwinski, Edith Antunes, Tebello Nyokong, *J. Photochem. Photobiol. A: Chem.* (Submitted).
8. Fluorescence behaviour of a low-symmetry zinc phthalocyanine covalently linked to single-walled carbon nanotubes, **Wadzanai Chidawanyika**, Christian Litwinski, Edith Antunes, Tebello Nyokong, (In preparation).

### **3. Synthesis and Spectroscopic Characterization**

**Reported in this chapter are the syntheses and spectroscopic characterizatn of the nanoparticles i.e. SWCNT and QDs and metallophthalocyanines employed in this work.**

Three sets of nanoparticles have been employed in this work. These have been listed in Table 3.1 below:

**Table 3.1: List of functionalized or synthesized nanoparticles.**

<sup>a</sup> Nanoparticle	Abbreviation	No.
Carboxylic acid functionalized SWCNT	SWCNT-COOH	1a
Ethylamine functionalized SWCNT	SWCNT-NH <sub>2</sub>	1b
MPA capped CdTe QDs	CdTe MPA	2

<sup>a</sup>MPA = mercaptopropionic acid.

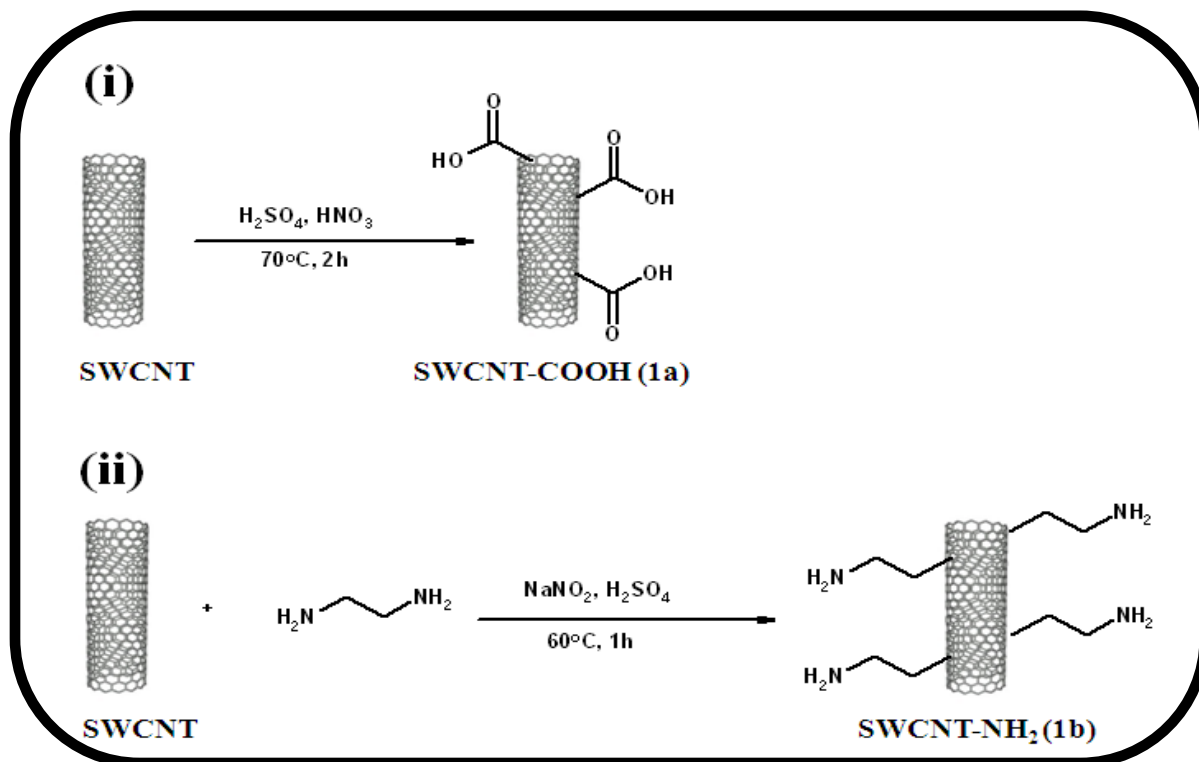
### **3.1 Functionalization, Synthesis and Characterization of Nanoparticles (SWCNT and QDs)**

The single-walled carbon nanotubes (SWCNT) and quantum dots (QDs) used in this thesis were either functionalized or synthesized as previously reported [6,7,9,23,28,60] and their spectroscopic characterization gave features consistent with literature.

#### **3.1.1 Chemical functionalization of SWCNT**

Chemical functionalization of SWCNT can be achieved either by covalent attachment or by non-covalent (adsorption) with planar molecules capable of adsorbing onto the carbon nanotubes surface *via*  $\pi$ - $\pi$  interactions (Figure 1.3 and 1.4) [26,27]. Following functionalization, the carbon nanotubes were characterized using UV-Vis, IR and Raman spectroscopies and by thermal gravimetric analysis (TGA).

The route used to obtain carboxyl-functionalized SWCNT, **1a** has been well documented in literature (Figure 1.4a and Scheme 3.1(i)) [6,9,10,22].



**Scheme 3.1:** Covalent functionalization of SWCNT to form (i) SWCNT-COOH (**1a**) and (ii) SWCNT-NH<sub>2</sub> (**1b**).

Initial reaction of the SWCNT in the presence of  $\text{H}_2\text{SO}_4$  and  $\text{HNO}_3$  facilitates the attachment of the terminal carboxyl groups. The 3:1 concentrated mixture of these two acids is chosen since it is known to intercalate and exfoliate graphite [293]. The functionalization cuts the nanotube bundles and is essential in enhancing their solubility. The synthetic approach adopted for the amine functionalization of the SWCNT is based on a diazonium reaction method developed earlier for the attachment of *para*-substituted benzene rings to SWCNT [7,23,28], however in this case we have made use of a simple alkyl-chain amine, Scheme 3.1(ii).

There are no differences in the nature of the electronic absorption spectra of the pristine SWCNT and those functionalized with carboxylic acid groups (SWCNT-COOH, **1a**) or ethylamine units (SWCNT-NH<sub>2</sub>, **1b**). The spectra are all broad expressing no features in the region of interest.

The FT-IR spectrum corresponding to the carboxylic acid functionalized SWCNT (**1a**, Figure 3.1(i)) and the amine functionalized SWCNT (**1b**, Figure 3.1(ii)) show two strong bands at 1617 and 1639 cm<sup>-1</sup>, which could correspond to the carbonyl (C=O) of the carboxylate that forms as a result of deprotonation of the weak carboxylic acid groups

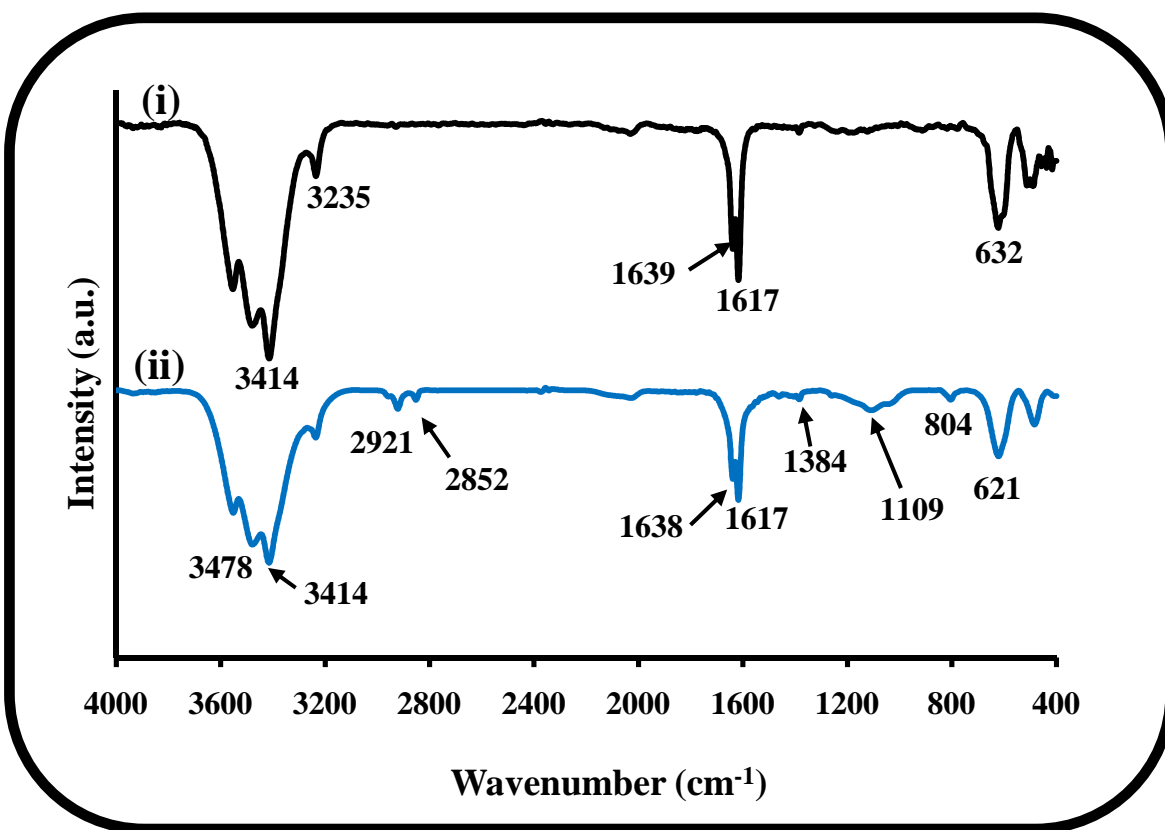


Figure 3.1: FT-IR spectra of (i) carboxylic acid functionalized SWCNT (SWCNT-COOH, **1a**) and (ii) ethylamine functionalized SWCNT (SWCNT-NH<sub>2</sub>, **1b**).



that terminate the nanotubes in **1a** or the NH<sub>2</sub> groups of **1b** [294]. It is difficult to make a distinction between the two (C=O and NH<sub>2</sub>), however the spectrum corresponding to **1b** shows differences below 1600 cm<sup>-1</sup>.

Figure 3.2 shows the room temperature Raman spectra of pristine SWCNT, SWCNT-COOH (**1a**), and SWCNT-NH<sub>2</sub> (**1b**). Raman spectra provide an insight on the extent of functionalization of the SWCNT. The spectra are characteristic of SWCNT with several radial-breathing modes (RBM) between 100 - 400 cm<sup>-1</sup> and a tangential (G band) vibrational mode around 1590 cm<sup>-1</sup>. These two features, RBM and G band, are signatures of SWCNT that have previously been used for nanotube characterization [1,31]. The Raman disorder band (D band) appears, at ~ 1270 cm<sup>-1</sup>, due to disorder on the

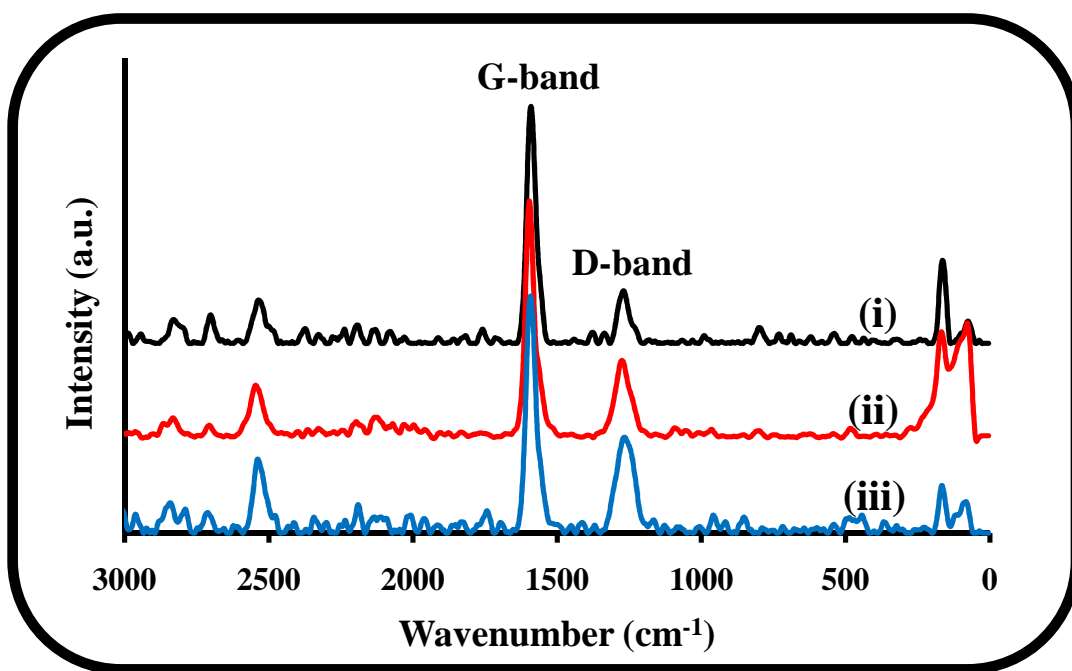


Figure 3.2: Raman spectra of (i) SWCNT, (ii) SWCNT-COOH (**1a**) and (iii) SWCNT-NH<sub>2</sub> (**1b**).

hexagonal lattice on the nanotube sidewalls [31-33,36]. The D band vibration is slightly lower than the reported  $\sim 1355 \text{ cm}^{-1}$  [33]. This could be a result of the preparation or treatment of the carbon nanotubes. Commercially obtained SWCNT often contain numerous impurities which may contribute to the observed shift. A change in the intensity of the D band signifies changes in the structure of the carbon nanotubes i.e. proof of sidewall functionalization [28,33-36], which inadvertently disrupts the  $sp^2$  carbon matrix with  $sp^3$ -hybridized carbon [32]. Shown in Figure 3.2 is an increase in the intensity of the D band upon functionalization, a feature indicative of disruption of the  $sp^2$  carbon hexagonal lattice to  $sp^3$  bonded carbons [31,32,36] due to sidewall functionalization [28,33-35] as a result of the covalent attachment of the COOH or ethylamine groups. The change in the D band intensity is more accurately expressed by a ratio between the integrated intensity of the D band and the integrated intensity of the G band ( $sp^3:sp^2$  carbon ratio) (Equation 3.1) [23,36,37,295].

$$R = \frac{I_D}{I_G} \quad (3.1)$$

Calculations reveal that there is a slight increase in this ratio on functionalization i.e. 0.22 for SWCNT, 0.33 for carboxyl (**1a**) and 0.40 for amine (**1b**) functionalized SWCNT. The slightly higher ratio for **1b** relative to **1a** may be attributed to more efficient sidewall functionalization in the former.

TGA has been used to confirm the structural differences between the pristine carbon nanotubes and functionalized carbon nanotubes. Different thermal decay profiles point to structurally different materials. The thermal decomposition profiles obtained under a steady flow of  $\text{N}_2$ , at a heating rate of  $10^\circ\text{C min}^{-1}$  are shown in (Figure 3.3). The spectra of, SWCNT-COOH, **1a** and SWCNT-NH<sub>2</sub>, **1b** has two decomposition steps, with the first

shallow step, between 50 and 100°C, suggestive of solvent loss. The second main decomposition step from ~ 350 to 700°C is associated with functional group decomposition i.e. of the groups associated with the complexes e.g. –COOH and –NH<sub>2</sub> groups.

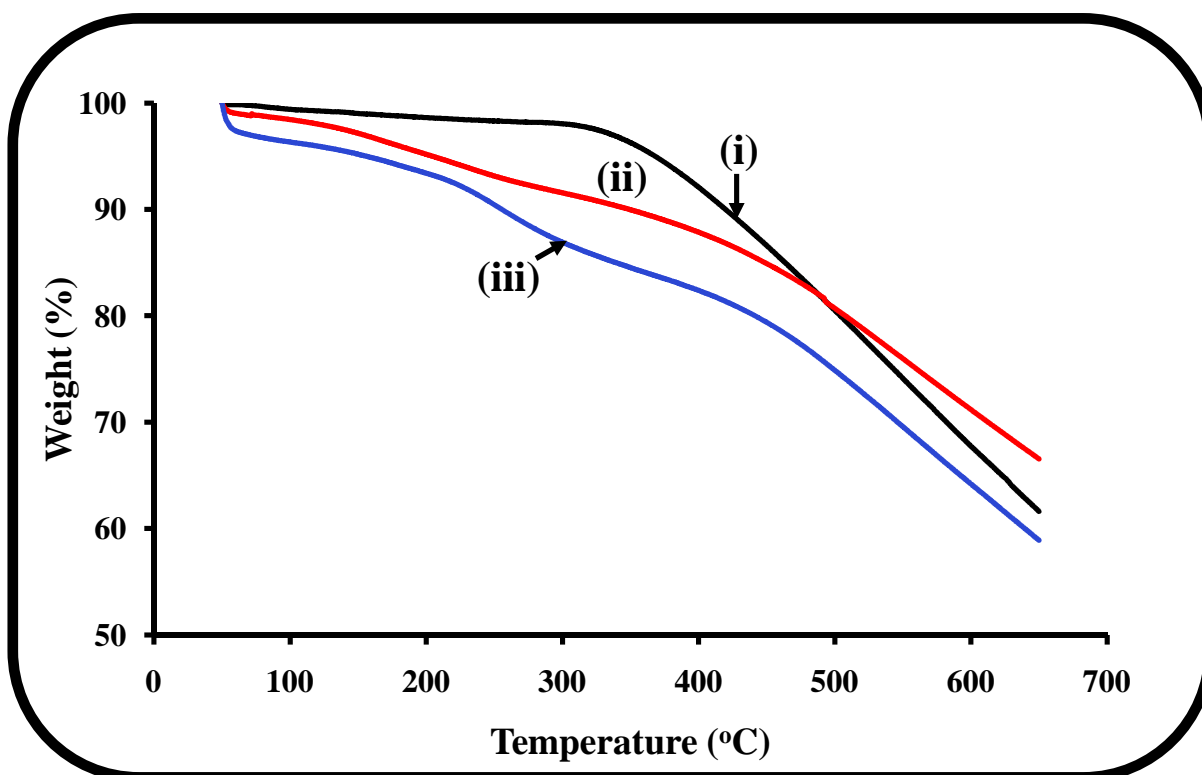
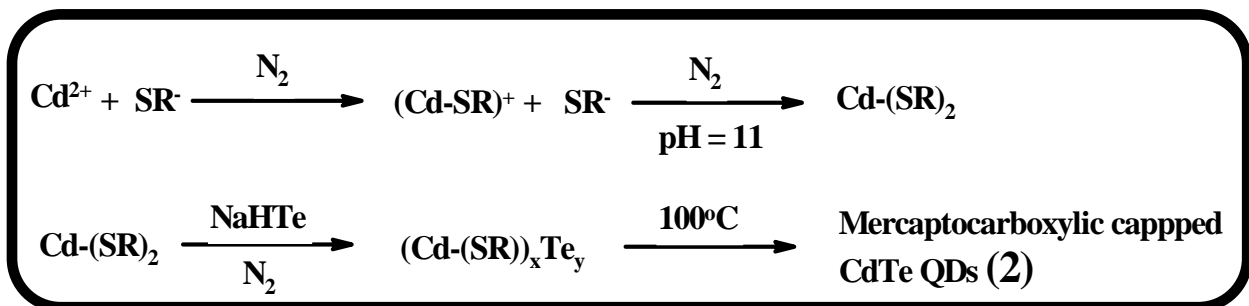


Figure 3.3: TGA profiles of (i) SWCNT, (ii) SWCNT-COOH (1a) and (iii) SWCNT-NH<sub>2</sub> (1b).

### 3.1.2 Mercaptocarboxylic acid capped CdTe QDs

Quantum dot synthesis was carried out following a slightly modified, well established literature method (Scheme 3.2) [60] as explained in the experimental section.



**Scheme 3.2:** Synthesis of mercaptocarboxylic acid capped CdTe QDs.

The CdTe MPA quantum dots synthesized in this work are characterized by broad absorption peaks, with tails extending into the near-infrared region, which are red shifted with an increase in size (Figure 3.4). The emission spectra were narrow as expected, Figure 3.5.

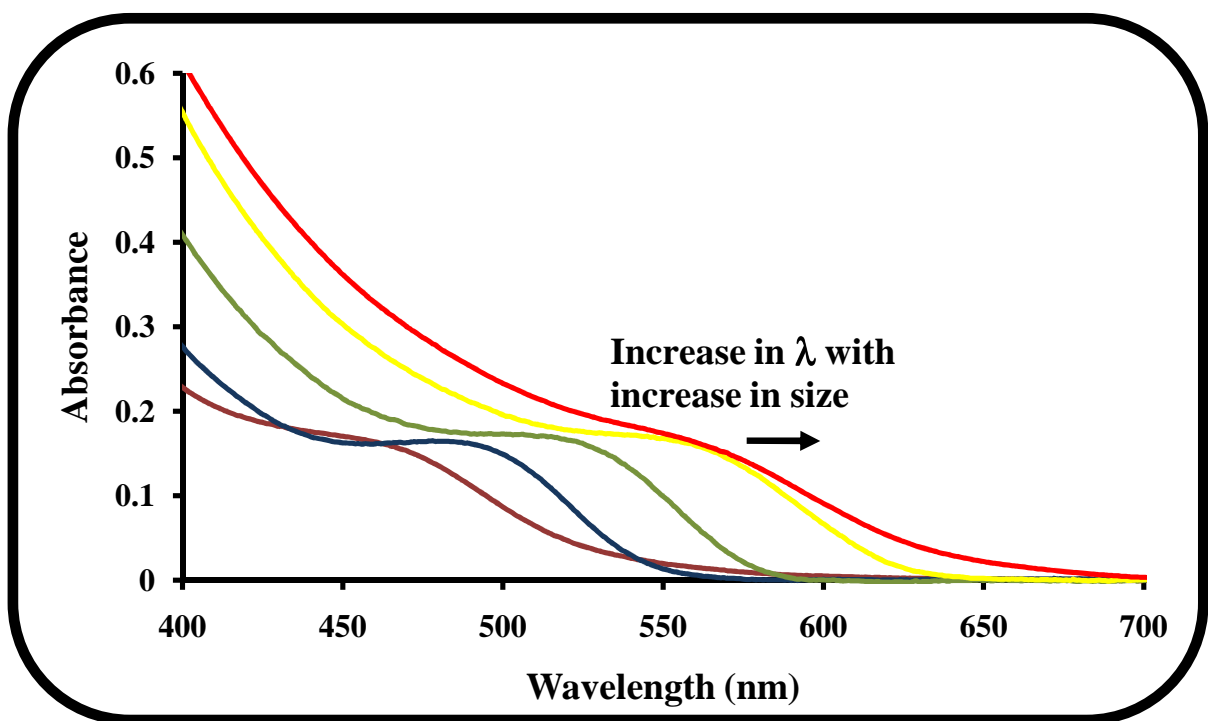


**Figure 3.4:** Ground state electronic absorption spectra of as synthesized MPA capped CdTe QDs (2) in aqueous media.

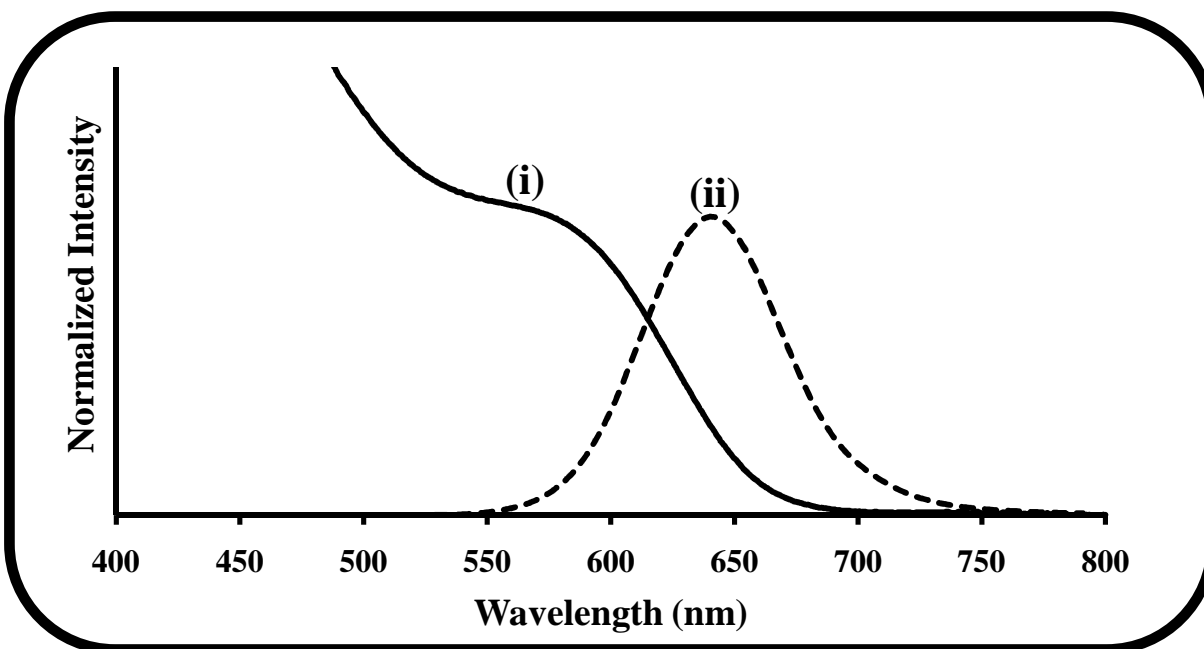


**Figure 3.5: (i) Normalized ground state electronic absorption and (ii) emission spectra of CdTe MPA QDs (2) in 4:1 v/v DMF:water ( $\lambda_{\text{exc}} = 510$  nm).**

The FT-IR spectrum showed an intense characteristic broad O-H band at  $3472\text{ cm}^{-1}$ , C-H vibrations at  $2982$ ,  $2930$  and  $2860\text{ cm}^{-1}$  and asymmetric C=O stretches at  $1656$  and  $1576\text{ cm}^{-1}$ .

XRD was used for particle size determination, Figure 3.6. The diffraction pattern corresponds well with the three characteristic peaks for bulk CdTe structure.

The particle diameter was generated by the computer software using the Scherrer Equation 3.2 (same as Equation 1.1);

$$d(\text{\AA}) = \frac{k\lambda}{\beta \cos\theta} \quad (3.2)$$

XRD generated data related to the main peak at  $\sim 25^\circ$  and gave a particle size of  $3.41\text{ nm}$ .

The QD sizes were also estimated using a polynomial fitting function (Equation 3.3; same as Equation 2.1) [286]:

$$D = (9.8127 \times 10^{-7})\lambda^3 - (1.7147 \times 10^{-3})\lambda^2 + (1.0064)\lambda - 194.84 \quad (3.3)$$

where  $\lambda$  refers to the absorption maxima of the QDs. This fitting function is not valid for sizes of quantum dots outside the size range of 1-9 nm [286].

This size obtained using XRD is slightly smaller but possibly more accurate in comparison to the size determined using the polynomial fitting function i.e. 3.50 nm.

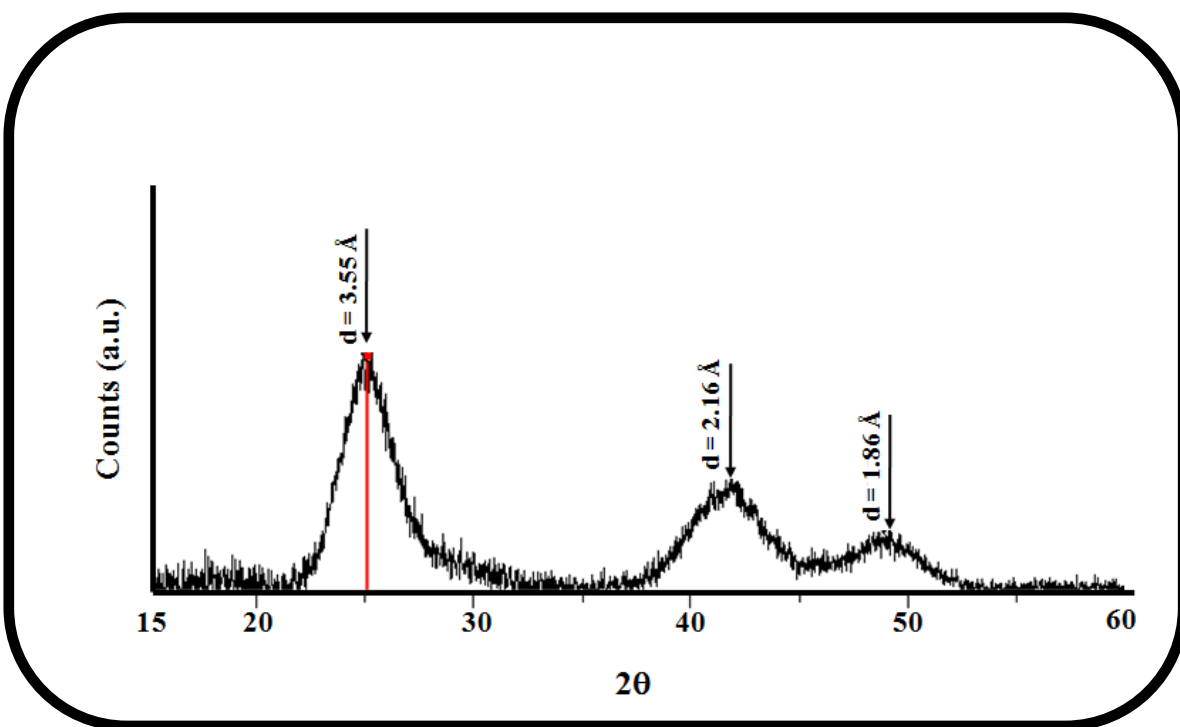


Figure 3.6: X-ray diffractogram of MPA capped CdTe QDs (2).

## 3.2 Metallophthalocyanines

Table 3.2 lists the MPcs reported in this work.

Table 3.2: List of synthesized symmetrically and unsymmetrically tetra-substituted MPcs.

MPc	Abbreviation	No.
Zinc(II)phthalocyanine	ZnPc	22
Cadmium(II)phthalocyanine	CdPc	23
Mercury(II)phthalocyanine	HgPc	24
Tetrakis{2,(3)-pyridyloxyphthalocyaninato}zinc(II)	$\beta$ -ZnTPyPc	25a
Tetrakis{2,(3)-pyridyloxyphthalocyaninato}cadmium(II)	$\beta$ -CdTPyPc	26a
Tetrakis{2,(3)-(4-benzyloxy)phenoxyphthalocyaninato}cadmium(II)	$\beta$ -CdTBzPhPc	26b
Tetrakis{2,(3)-phenoxyphthalocyaninato}cadmium(II)	$\beta$ -CdTPhPc	26c
Tetrakis{2,(3)- <i>tert</i> -butylphenoxyphthalocyaninato}cadmium(II)	$\beta$ -CdTtBuPhPc	26d
Tetrakis{2,(3)-pyridyloxyphthalocyaninato}mercury(II)	$\beta$ -HgTPyPc	27a
Tetrakis{1,(4)-pyridyloxyphthalocyaninato}cadmium(II)	$\alpha$ -CdTPyPc	28a
Tetrakis{1,(4)-(4-benzyloxy)phenoxyphthalocyaninato}cadmium(II)	$\alpha$ -CdTBzPhPc	28b
Tetrakis{1,(4)-phenoxyphthalocyaninato}cadmium(II)	$\alpha$ -CdTPhPc	28c
Tetrakis{1,(4)- <i>tert</i> -butylphenoxyphthalocyaninato}cadmium(II)	$\alpha$ -CdTtBuPhPc	28d
Tetrakis{2,(3)- <i>tert</i> -butylphthalocyaninato}zinc(II)	$\beta$ -ZnttbPc	29
Tetrakis{2,(3)-mercaptopyridinephthalocyaninato}zinc(II)	$\beta$ -ZnTMPyPc	30
Tris{9 (10), 16 (17), 23 (24)-( <i>tert</i> -butyl)imidophthalocyaninato}zinc(II)	ZnttbIPc	31
Tris{9 (10), 16 (17), 23 (24)-(4-(2-mercaptopyridine)-2-(4-carboxyphenoxy)phthalocyaninato}zinc(II)	ZnPc-COOH	32

### 3.2.1 Unsubstituted MPcs

The synthesis of the unsubstituted derivatives zinc(II)phthalocyanine (**ZnPc**, **22**), cadmium(II)phthalocyanine (**CdPc**, **23**) and mercury(II)phthalocyanine (**HgPc**, **24**) was carried out according to a well established procedure [142-144]. ZnPc is also available commercially.

The IR spectra indicated the loss of the characteristic nitrile stretch at  $\sim 2300\text{ cm}^{-1}$ , (indicative of phthalonitriles) on formation of the various metal substituted Pc's. The  $^1\text{H}$ -NMR spectra for the unsubstituted derivatives was similar and indicated the 8 non-peripheral protons as a singlet between 9.55 and 9.37 ppm while the peripheral protons resonated upfield as a broad singlet, integrating for 8 protons, between 8.28 and 7.99 ppm.

The absorption spectra of complexes **22**, **23** and **24**, show typical monomeric behaviour in DMSO and DMF (Figure 3.7). These complexes remain monomeric up to  $\sim 2 \times 10^{-5}\text{ M}$ . CdPc and HgPc are insoluble in  $\text{CHCl}_3$ , DCM and THF, while ZnPc is soluble in all, though sparingly so in  $\text{CHCl}_3$  and DCM. The shift to longer wavelengths with the increase in size of the central metal is due to an increase in electron density.



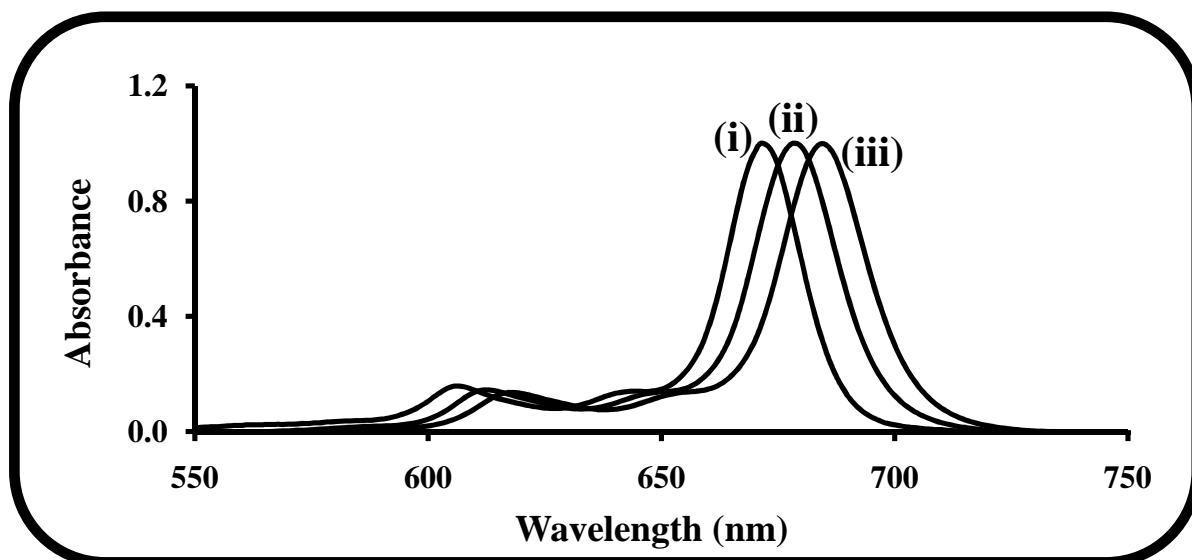


**Figure 3.7:** Ground state electronic absorption spectra of (i) ZnPc (**22**), (ii) CdPc (**23**) and (iii) HgPc (**24**) in DMSO. Concentrations: ZnPc =  $1.5 \times 10^{-5}$  M, HgPc and CdPc =  $1.0 \times 10^{-5}$  M.

Table 3.3 lists the spectral properties of unsubstituted Pc complexes of zinc (**22**), cadmium (**23**) and mercury (**24**), in various organic solvents. In the table, it can be observed that the molar extinction coefficients of the MPcs vary with the size of the central metal ion, with the value being highest for **22** and least for **24**.

**Table 3.3:** Spectral properties of unsubstituted MPc complexes 22, 23 and 24 in various organic solvents.

MPc	Solvent	<sup>a</sup> Q band, $\lambda_{\max}$ /nm	Log $\epsilon$
ZnPc (22)	Toluene	672	5.25
	THF	668	5.48
	DMF	670	5.37
	DMSO	672	5.38
CdPc (23)	DMF	674	5.38
	DMSO	679	5.36
HgPc (24)	DMF	681	5.11
	DMSO	684	5.25

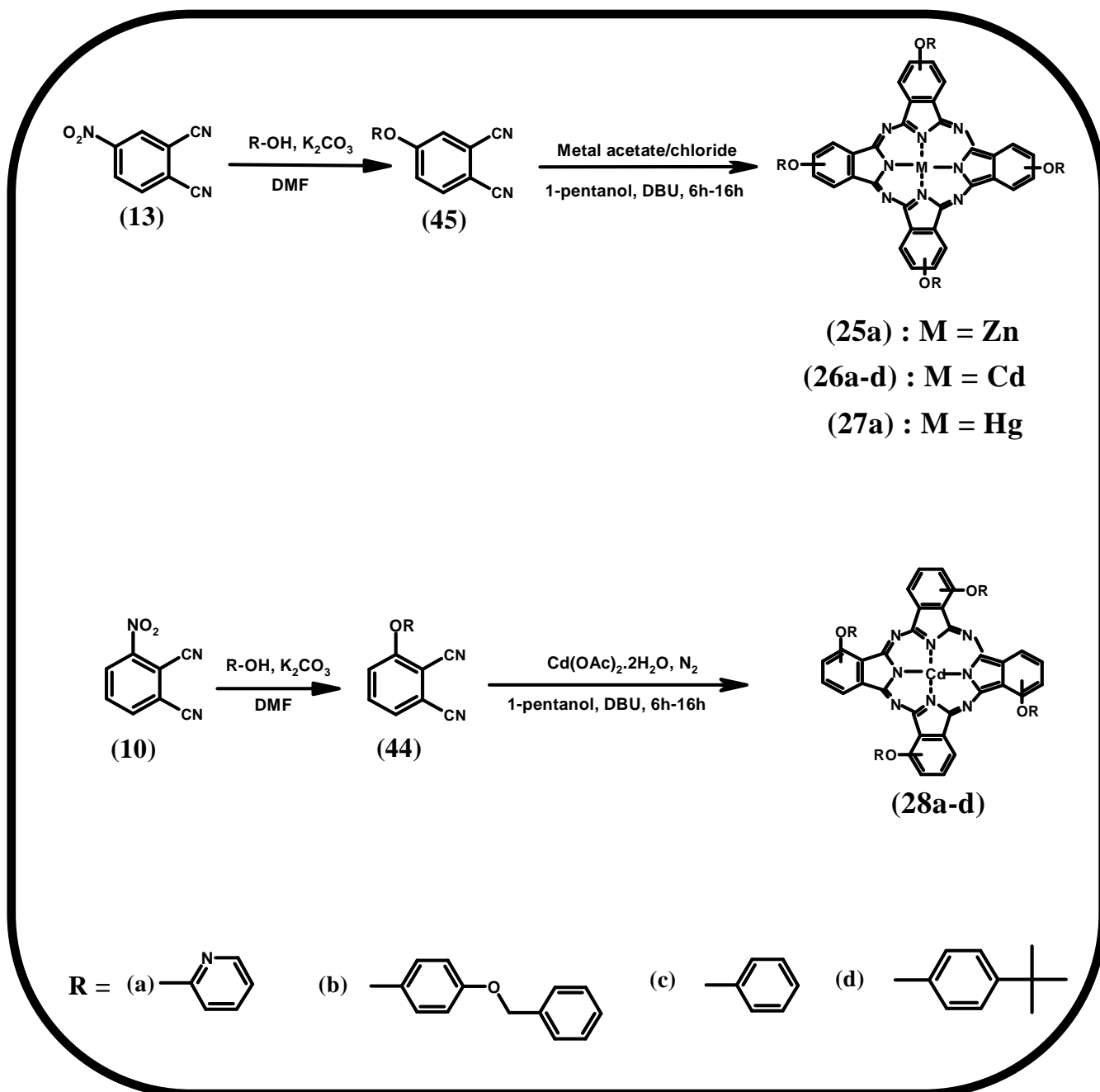
<sup>a</sup> $\lambda_{\max}$  = wavelength maximum.

### 3.2.2 Symmetrically tetra-substituted metallophthalocyanine derivatives

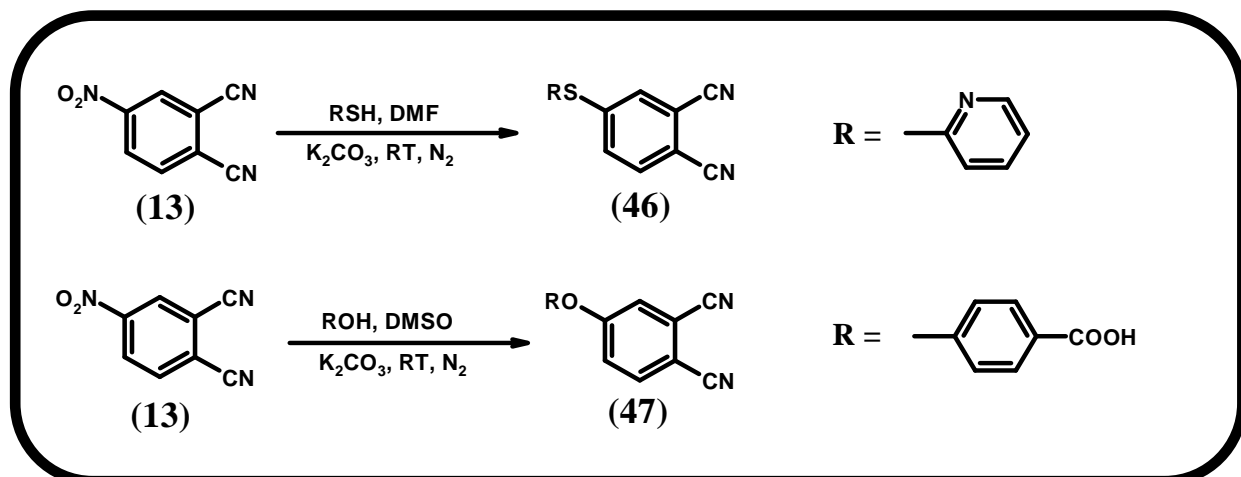
#### 3.2.2.1 Mono-substituted phthalonitriles

The substitution reaction of a nitro derivative with a phenol derivative to give mono-substituted 2-pyridyloxy, 4-(benzyloxyphenoxy), phenoxy, 4-*tert*-butylphenoxy phthalonitrile derivatives (**44a-d**, **45a-d**, Scheme 3.3) has been well documented and has been shown to proceed *via* a base catalyzed nucleophilic displacement reaction mechanism [296]. The syntheses of 2-mercaptopyridine (**46**) and 4-(phenoxy)benzoic acid (**47**) substituted phthalonitriles were carried out under slightly different conditions (Scheme 3.4) [138,147,288]. However, in all cases, the substitution reactions were

performed at room temperature under an inert atmosphere (using either nitrogen or argon) as stated in literature [117,296-301].



**Scheme 3.3:** Synthetic routes to Zn(II), Cd(II) and Hg(II) tetra-aryloxy  $\beta$ -substituted (25a, 26a-d and 27a) and  $\alpha$ - (28a-d) Pc complexes.



**Scheme 3.4:** Syntheses of mono-substituted phthalonitriles, **46** and **47**.

Following the necessary purification procedures, the characteristic nitrile ( $\text{C}\equiv\text{N}$ ) stretch, at  $\sim 2300\text{ cm}^{-1}$ , was found in the FT-IR spectra of all substituted phthalonitriles prepared in this work.  $^1\text{H-NMR}$  was used for further structural characterization and the results are in agreement with the predicted structures, as indicated in the experimental section.

### 3.2.2.2 Symmetrical aryloxy tetra-substituted MPc derivatives

Zinc, cadmium and mercury aryloxy substituted Pc complexes were synthesized by treatment of the corresponding substituted phthalonitriles with the necessary metal salts i.e.  $\text{Zn}(\text{OAc})_2$ ,  $\text{CdCl}_2$  (or  $\text{Cd}(\text{OAc})_2$ ) or  $\text{HgCl}_2$  in the presence of a high boiling solvent such as 1-pentanol or 1-octanol and DBU (Scheme 3.3). DBU acts as a nucleophilic base which permits the reaction to proceed under more mild conditions while also preventing the formation of side products typical of reactions that make use of strong bases [297]. The cyclotetramerization reaction affords the peripherally or non-peripherally substituted complexes **25a**, **26a-d**, **27a**, **28a-d**. All complexes formed are tetra-substituted; however, the use of different precursors i.e. 3-nitrophthalonitrile (**10**) or 4-nitrophthalonitrile (**13**)

results in substitution patterns at different points of the MPc macrocycle i.e.  $\alpha$ - or  $\beta$ -substituted MPcs, each with their own unique solution and solid-state properties [296]. The complexes were purified by column chromatography, Soxhlet extraction of the impurities or a combination of the two, to give yields ranging from 17 % to 60 %. All complexes exhibit excellent solubility in highly polar organic solvents, such as DMF and DMSO.  $\text{CHCl}_3$ , DCM, THF and toluene have also been used as solvents; however MPc complexes such as **25a**, **26a** and **27a** exhibited limited solubility in these weakly polar solvents, which may be in response to the polar nature of the pyridyloxy substituents attached to the MPc ring. The new complexes were characterized by various spectroscopic methods; IR,  $^1\text{H-NMR}$ , UV-Vis and elemental analyses and were in agreement with the predicted structures as indicated in the experimental section (Chapter 2). The IR spectra show the loss of the characteristic nitrile stretch at  $\sim 2300\text{ cm}^{-1}$  (indicative of phthalonitriles) on formation of the various metal substituted Pcs. The complexes showed characteristic aromatic C-H stretching between  $3167\text{ cm}^{-1}$  and  $3045\text{ cm}^{-1}$ , aliphatic C-H stretching at  $\sim 2955\text{-}2848\text{ cm}^{-1}$  and vibrations due to ether linkages (C-O-C) at  $1266\text{-}1216\text{ cm}^{-1}$  as shown by the spectrum of **28d** ( $\alpha$ -CdTtBuPhPc) in Figure 3.8.

Owing to the presence of isomers in tetra-substituted complexes and Pc aggregation as a result of the high concentrations used for NMR measurements [153], the  $^1\text{H-NMR}$  spectra of the complexes show complex splitting patterns and poorly resolved signals. However, on close investigation, the data gave the correct number of protons in accordance with the predicted structures. The differences in the chemical shifts of the spectra of **28a-d** and **26a-d** is a function of the different substitution patterns, i.e.  $\alpha$ -

substituted (non-peripheral) phenoxy complexes versus the  $\beta$ -substituted (peripheral) phenoxy complexes. The type of substituents introduced at these positions is also significant.

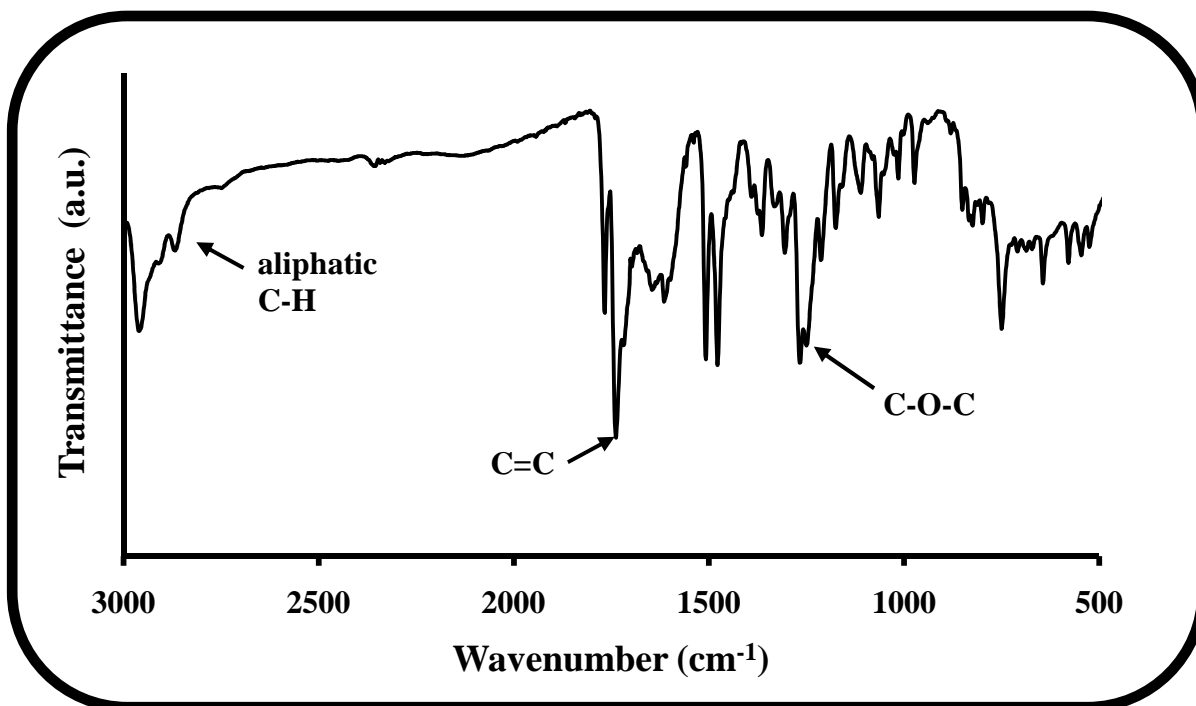


Figure 3.8: FT-IR spectrum of  $\alpha$ -CdTtBuPhPc (28d).

The ground state electronic absorption spectra of the aryloxy substituted MPc complexes in various solvents showed, for the most part, sharp, intense single Q band maxima depicting monomeric behaviour up to  $1 \times 10^{-5}$  M (Figure 3.9 and Figure 3.10).

The  $\alpha$ -substituted derivatives (**28b-d**) occur with red-shifted spectra, relative to that of the  $\beta$ -derivatives (**26b-d**), Figure 3.10, Table 3.4. Substitution at the  $\alpha$ -positions gives a larger destabilization of the highest occupied molecular orbital (HOMO), resulting in a smaller HOMO-LUMO band separation [302], the extent of which is further enhanced on the introduction of electron-donating groups such as the phenoxy, *tert*-butylphenoxy and benzyloxyphenoxy groups employed in this work. However, the pyridyloxy  $\alpha$ -derivative

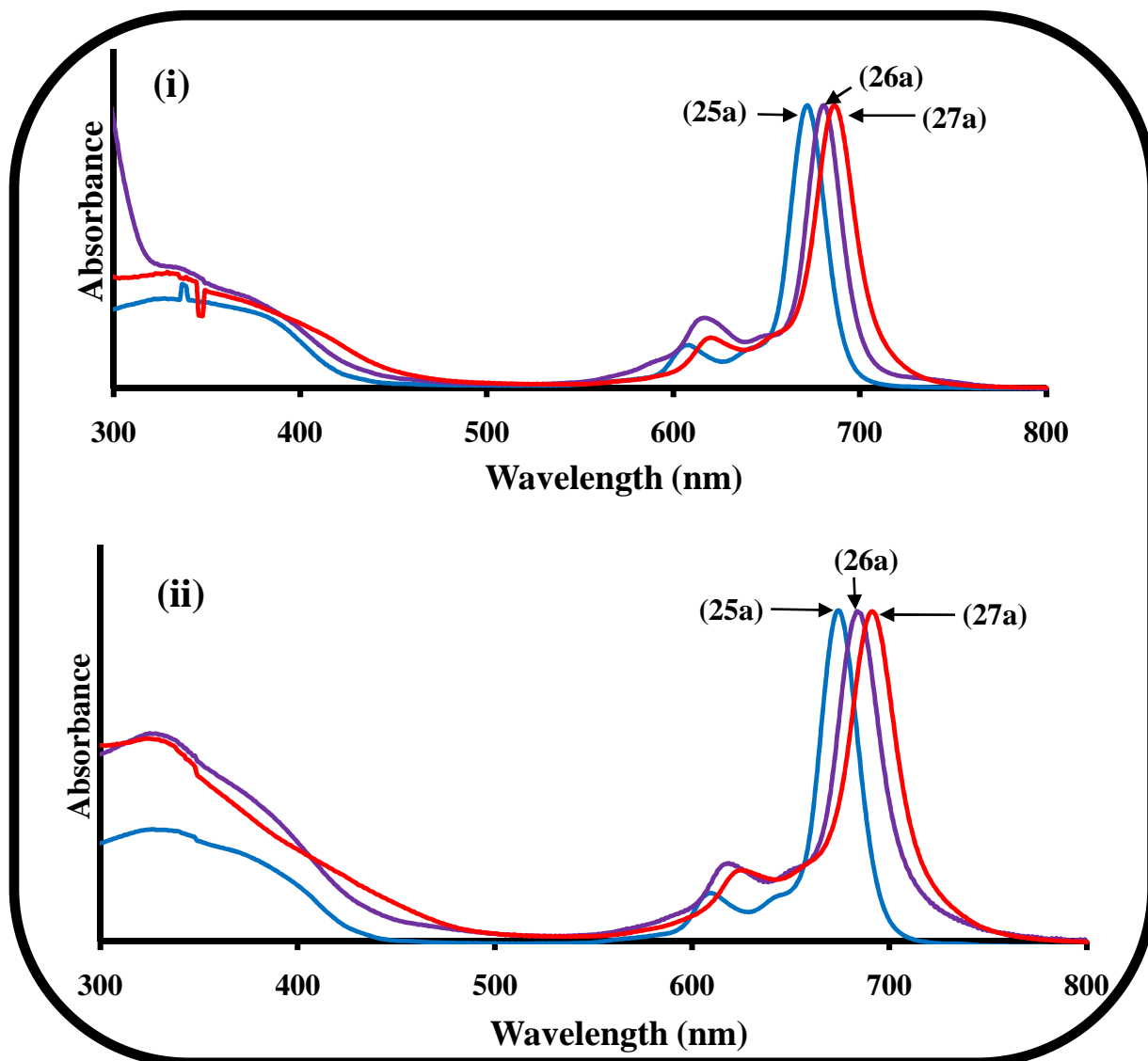


Figure 3.9: Ground state electronic absorption spectra of Zn(II), Cd(II) and Hg(II) tetra-pyridyloxy substituted complexes 25a, 26a and 27a in (i) DMF and (ii) DMSO. (Concentration =  $\sim 5.0 \times 10^{-6}$  M).

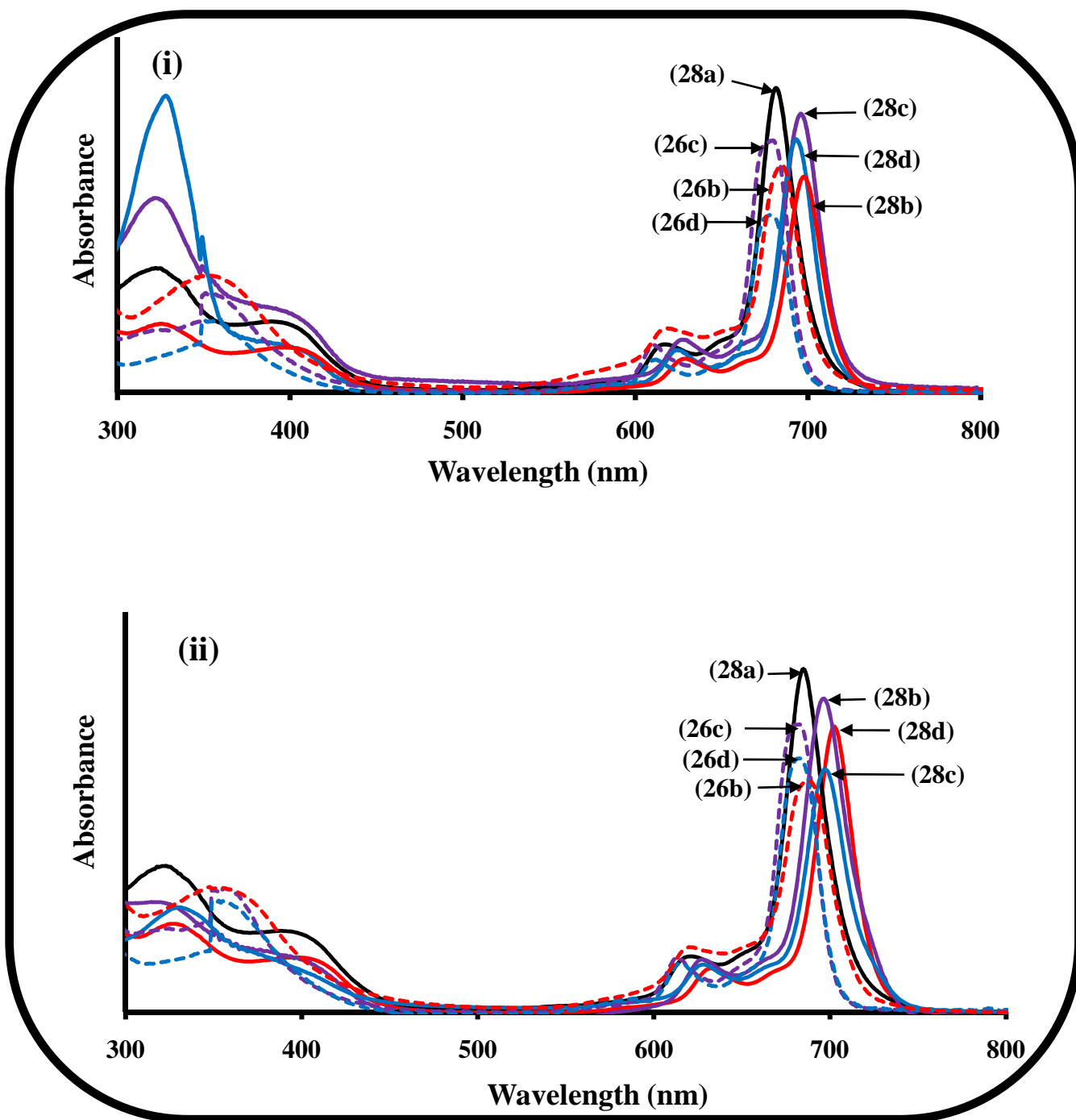


Figure 3.10: Ground state electronic absorption spectra of Cd(II) tetra (a) pyridyloxy, (b) phenoxy, (c) *tert*-butylphenoxy and (d) benzyloxyphenoxy  $\alpha$ -substituted (28a-d) and  $\beta$ -substituted (26b-d) Pc complexes in (i) DMF and (ii) DMSO (Concentrations =  $\sim 5.0 \times 10^{-6}$  M).



**Table 3.4:** Spectral properties of Zn(II), Cd(II) and Hg(II) tetra-aryloxy substituted MPc complexes in different solvents.

MPc	Solvent	Q band, $\lambda_{\max}$ /nm	Log $\epsilon$
$\beta$ -ZnTPyPc (25a)	DMF	673	5.18
	DMSO	680	5.36
$\beta$ -CdTPyPc (26a)	DMF	682	5.11
	DMSO	685	5.30
$\beta$ -CdTBzPhPc (26b)	Toluene	704, 668	5.08
	CHCl <sub>3</sub>	703, 667, 636	4.12, 4.30, 4.35
	THF	700, 664, 634	4.15, 4.34, 4.38
	DCM	701, 666, 634	4.03, 4.24, 4.32
	DMF	684	5.29
	DMSO	688	5.32
	$\beta$ -CdTPhPc (26c)	Toluene	681
$\beta$ -CdTPhPc (26c)	CHCl <sub>3</sub>	681	5.18
	THF	677	5.13
	DMF	677	5.22
	DMSO	681	5.23
$\beta$ -CdTtBuPhPc (26d)	Toluene	681	5.38
	CHCl <sub>3</sub>	681	5.43
	THF	678	5.34

Table 3.4 contd.

MPc	Solvent	Q band, $\lambda_{\max}/\text{nm}$	Log $\epsilon$
$\beta$ -CdTtBuPhPc (26d) contd.	DMF	678	5.46
	DMSO	684	5.47
$\beta$ -HgTPyPc (27a)	DMF	685	5.08
	DMSO	690	5.18
$\alpha$ -CdTPyPc (28a)	CHCl <sub>3</sub>	684	4.89
	THF	682	4.86
	DCM	683	4.75
	DMF	682	5.11
	DMSO	684	5.30
$\alpha$ -CdTBzPhPc (28b)	Toluene	701	5.08
	CHCl <sub>3</sub>	707	5.56
	THF	699	5.33
	DCM	703	5.27
	DMF	698	5.29
$\alpha$ -CdTPhPc (28c)	DMSO	702	5.32
	Toluene	694	5.21
	CHCl <sub>3</sub>	700	5.23
	THF	693	5.14
	DMF	694	5.25

Table 3.4 contd.

MPc	Solvent	Q band, $\lambda_{\max}/\text{nm}$	Log $\epsilon$
$\alpha$ -CdTPhPc (28c) contd.	DMSO	698	5.26
$\alpha$ -CdTtBuPhPc (28d)	Toluene	694	5.39
	CHCl <sub>3</sub>	700	5.44
	THF	693	5.36
	DMF	694	5.46
	DMSO	698	5.48

(28a) and  $\beta$ -derivative 26a showed no significant differences. The Q band maxima of the  $\alpha$ -substituted complexes were also found to shift to longer wavelengths as follows pyridyloxy (a) < phenoxy (c)  $\equiv$  *tert*-butylphenoxy (d) < benzyloxyphenoxy (b) for substituted CdPc complexes in DMF and DMSO (Table 3.4). This may be in response to the increase in electron donating ability of these substituents from pyridyloxy to benzyloxyphenoxy. In general, for all complexes (25a, 26a-d, 27a and 28a-d), a change in the solvent is accompanied by a change in the position of the Q band. It has been suggested previously that the solvent's refractive index affects its Q band maxima [180,226]. Solvents with strong coordinating properties such as DMF and DMSO (with donor numbers of 26.6 and 29.8 kcal mol<sup>-1</sup> respectively [296,303,304]) interact with the Pc molecule (through either the sulfur or oxygen atoms [305,306]) which gives rise to a more stable lowest unoccupied molecular orbital (LUMO) and thus results in a smaller HOMO-LUMO band separation resulting in red-shifted Q bands in these solvents. A

change in the central metal ion is also significant, as observed by the data corresponding to **25a**, **26a** and **27a** (Figure 3.9) where the order of the Q band positions is **27a** > **26a** > **25a**; this is the order of extent of destabilization of the HOMO in the complexes. Mercury having more electrons in its atomic structure (more reducing), destabilizes the HOMO more than cadmium and zinc do, hence bringing about a shorter HOMO-LUMO separation and consequently the most red-shifted spectra.

The spectra of some of the MPc complexes showed deviations from monomeric behaviour. Complexes **25a** and **26a** were aggregated in CHCl<sub>3</sub> (Figure 3.11) and DCM. The aggregating tendencies of MPc complexes in non-coordinating solvents are well documented [180,183], and are attributed to the formation of  $\pi$ - $\pi$  interactions between adjacent MPc rings. Coordinating solvents are axially ligated to the central metals in the MPc complexes, thereby preventing columnar aggregation. Addition of a surfactant, Triton X-100 ( $1 \times 10^{-4}$  M) to a CHCl<sub>3</sub> (or DCM) solution of **25a** or **26a** results in partial disaggregation into monomers, as seen in Figure 3.11. Complex **27a** is also monomeric in DMF and DMSO (Figure 3.9) but is demetallated in CHCl<sub>3</sub> (Figure 3.12) and DCM, as evidenced by a split in the Q band, typical of demetallation in MPc complexes [176]. Studies have shown that in chlorinated solvents, MPcs undergo oxidation, with the formation of HCl as a by-product [182], which in certain cases reacts with the MPc to cause demetallation. The diagonal N-N distance of the Pc core is 3.96 Å [176]. The Hg<sup>2+</sup> ion, with a radius of 110 pm [307], is expected to be out of the plane of the Pc ring since a smaller metal ion such as Mg<sup>2+</sup>, with a radius of 71 pm [307] is out of the plane of the Pc ring [176]. Thus, the mercury atom in **27a** protrudes out of the planar phthalocyanine ring, making the molecule highly susceptible to demetallation.

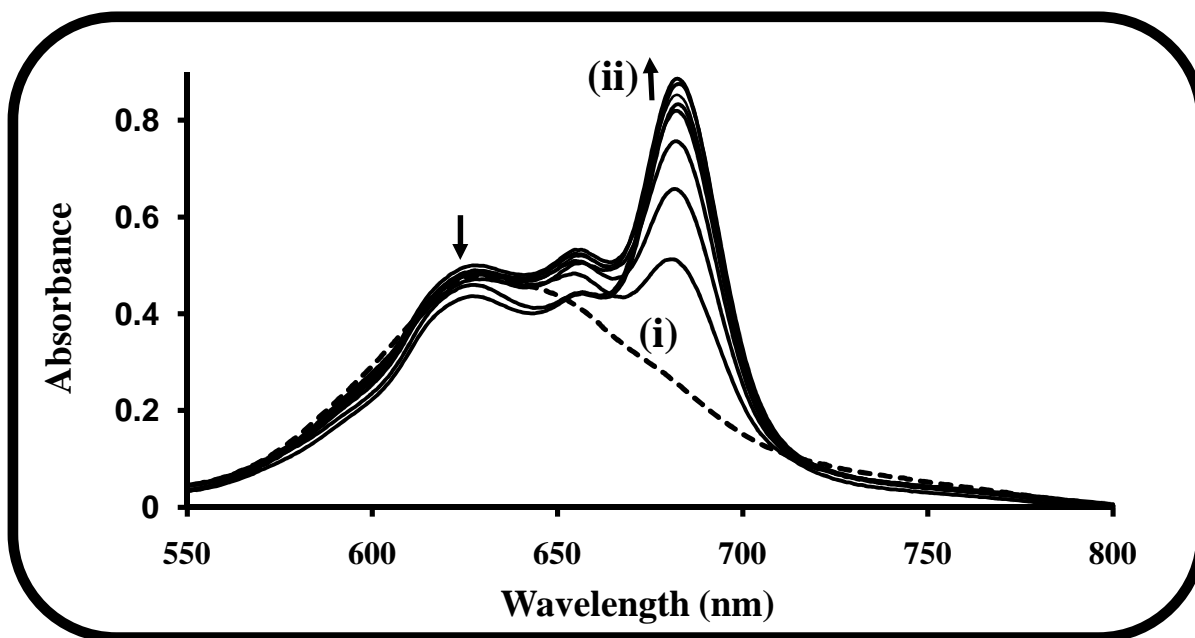


Figure 3.11: Disaggregation absorption spectra of  $\beta$ -CdTPyPc (26a) using different concentrations of Triton X-100 and a constant concentration of 26a =  $2.4 \times 10^{-6}$  M in  $\text{CHCl}_3$ . Triton X-100 concentrations: (i) 0,  $0.2 \times 10^{-4}$ ,  $0.3 \times 10^{-4}$ ,  $0.4 \times 10^{-4}$ ,  $0.5 \times 10^{-4}$ ,  $0.6 \times 10^{-4}$ ,  $0.8 \times 10^{-4}$ ,  $0.9 \times 10^{-4}$  and (ii)  $1 \times 10^{-4}$  M.

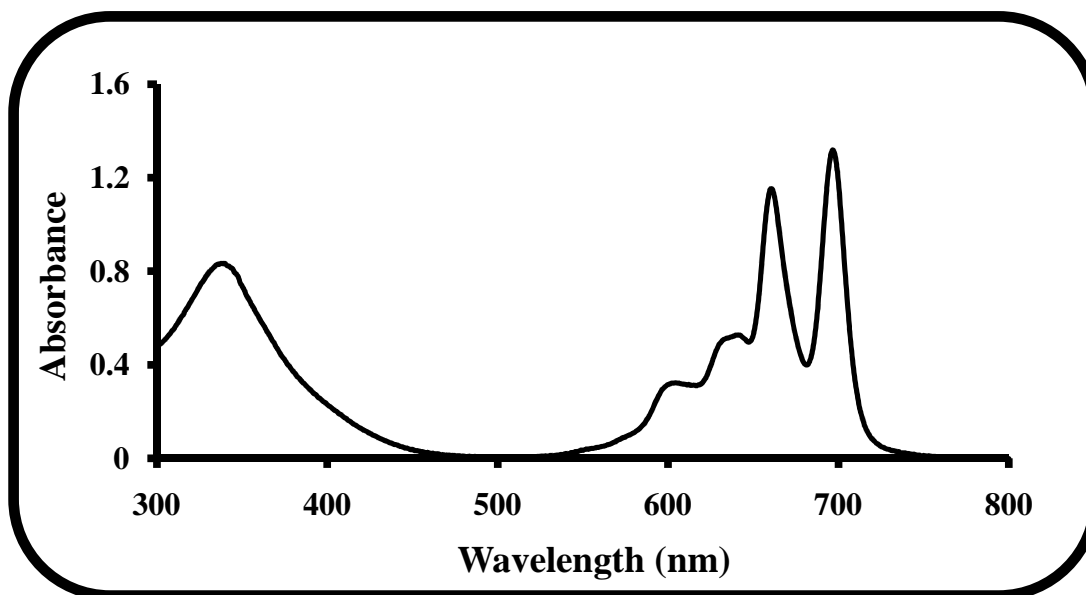
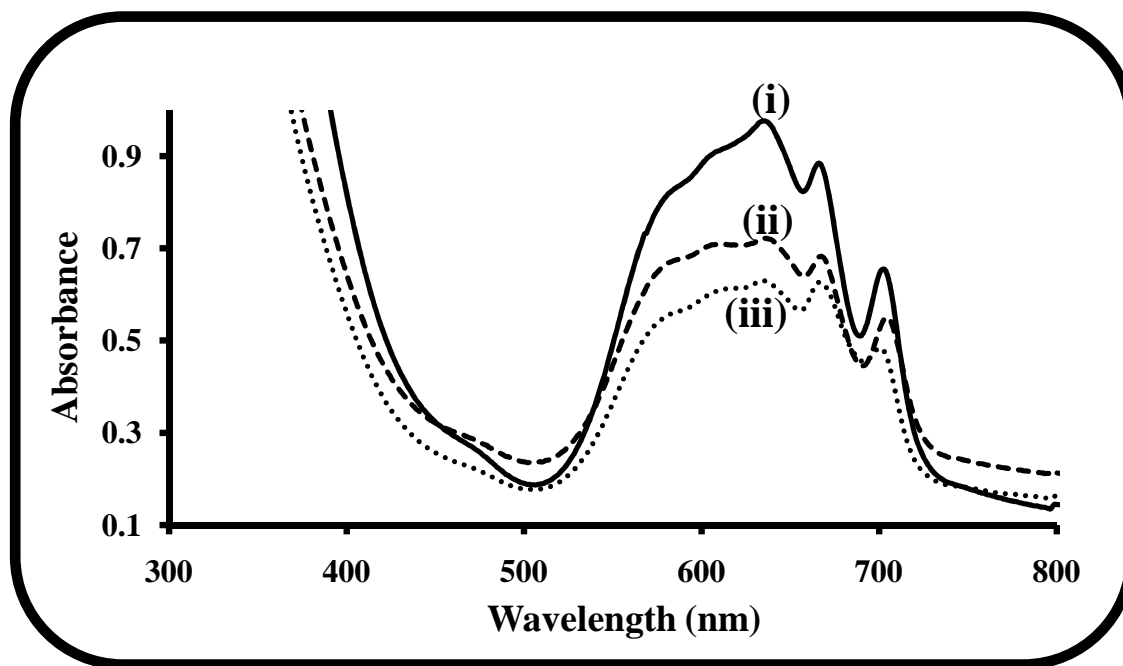


Figure 3.12: Ground state electronic absorption spectrum of  $\beta$ -HgTPyPc (27a) in  $\text{CHCl}_3$ . Concentration of 27a =  $8.7 \times 10^{-6}$  M.

Complex **26b** also showed interesting spectral behaviour in chlorinated solvents. In this case, spectra are characterized by a very broad band extending from ~ 550 nm to 700 nm, Figure 3.13. Studies with **26a**, as discussed above, showed broadened spectra in

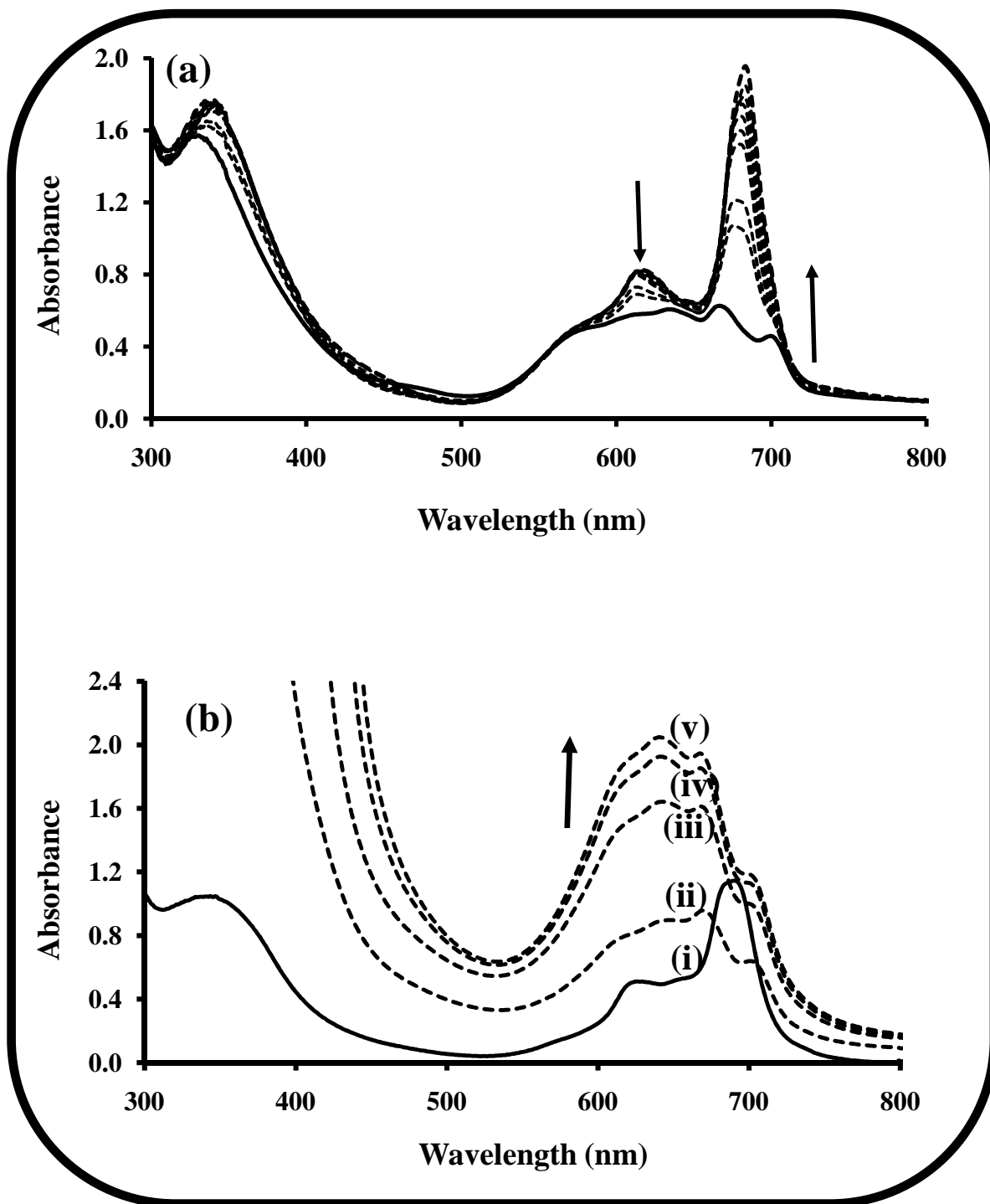


**Figure 3.13:** Ground state electronic absorption spectra of  $\beta$ -CdTBzPhPc (**26b**) in (i) DCM (concentration =  $4.63 \times 10^{-5}$  M), (ii)  $\text{CHCl}_3$  (concentration =  $2.55 \times 10^{-5}$  M) and (iii) THF (concentration =  $2.42 \times 10^{-5}$  M).

chlorinated solvents; where the addition of Triton X-100 led to partial disaggregation into monomers. However in the case of **26b**, no change occurred on addition of the surfactant to solutions of **26b**, which is an indication that this complex is in a monomeric state. The observed spectra may be attributed to differences in solvent properties i.e. coordinating nature, where coordinating solvents such as pyridine, DMF and DMSO (Figure 3.10) are capable of axial ligation to the central metal in MPc complexes. The oxidizing nature of the solvents may also play a role; chlorinated solvents are known to oxidize some MPc complexes [182]. The presence of two sharp peaks in the 700 nm area for **26b** in  $\text{CHCl}_3$

and DCM, Figure 3.13, suggests partial demetallation. A recent report by Chambrier *et al.* has shown that successive additions of iodine (an oxidizing agent) give rise to phthalocyanines with similar absorption spectra to that shown in Figure 3.11 with absorptions between 550 – 650 nm [148]. It was shown that such spectra is typical of triple-decker and higher oligomeric complexes often formed more readily with phthalocyanine ligands substituted with alkenyl substituents at the ring periphery [308]. However there was no evidence of such oligomers for **26b**. The addition of a reducing agent ( $\text{NaBH}_4$ ) to solutions that gave rise to the spectra in Figure 3.13, gave some form of reversal of the observed spectrum i.e. a change to more monomeric species (Figure 3.14a); suggesting the presence of an initially oxidized form. These changes were only observed in solvents of low co-ordination number i.e. THF,  $\text{CHCl}_3$  and DCM, which are prone to promoting oxidation [182].  $\text{CHCl}_3$  in particular is slightly acidic and is known to result in the oxidation of the phthalocyanine molecule [145,182,278]. Demetallation of **26b** occurred in toluene. Oxidation, using  $\text{Br}_2$ , of **26b** in a coordinating solvent i.e. DMSO resulted in spectra similar to that obtained in  $\text{CHCl}_3$ , DCM and THF (Figure 3.14b), suggesting that the spectra in Figure 3.13 is partly due to oxidation. However, what is unusual is the increase in absorption intensity on increments of  $\text{Br}_2$ . Typical phthalocyanine oxidation is often expected to give a decrease in absorption intensity in the Q band region. Addition of bromine to solutions of **26b** in  $\text{CHCl}_3$  resulted in spectral changes shown in Figure 3.14c. The two sharp peaks near 700 nm increased in intensity, suggesting that oxidation with bromine results in demetallation. Addition of zinc acetate to a solution of **26b** in DCM resulted in the collapse of the two sharp bands confirming

that the peaks were due to demetallation. Thus in DCM,  $\text{CHCl}_3$ , THF and toluene, complex **26b** showed some oxidation and partial demetallation.





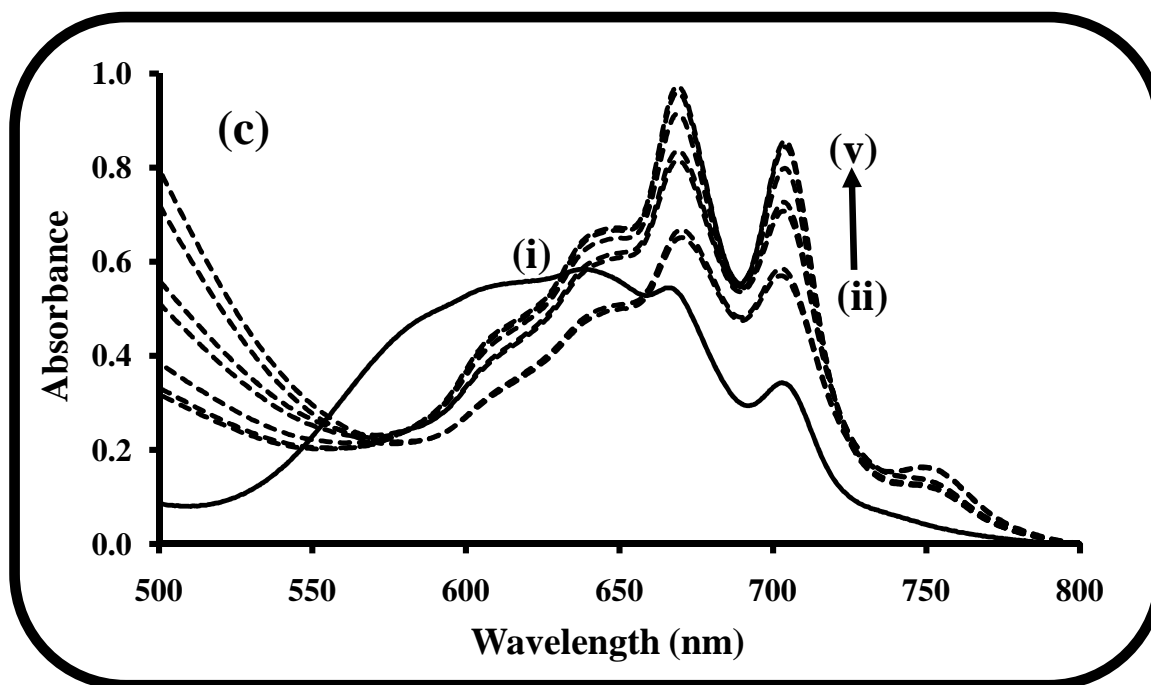


**Figure 3.14:** Ground state electronic absorption spectra of (a)  $\beta$ -CdTBzPhPc (**26b**) (initial concentration =  $\sim 2.84 \times 10^{-5}$  M) in THF on successive addition of NaBH<sub>4</sub>, (b) **26b** (concentration =  $\sim 7.29 \times 10^{-5}$  M) in DMSO (i), on addition of Br<sub>2</sub> fumes (ii-v) and (c) **26b** (concentration =  $2.73 \times 10^{-5}$  M) in CHCl<sub>3</sub> (i) on successive addition of Br<sub>2</sub> fumes (ii-v).

Cadmium complexes **26c**, **26d**, **28c** and **28d** showed a small band between 740 and 750 nm in toluene, CHCl<sub>3</sub> and THF (Figure 3.15(i)). In literature this has been referred to as the 'X' band, a feature which has been attributed to the flexible  $\sigma$  attachment of phenoxy (C-O-C) groups at the Pc-periphery [309-311]. This flexibility allows the groups to 'twist' about the bond and induce a slight loss in symmetry, hence splitting the Q band [312]. The band near 750 nm was observed for complexes **26c** and **26d** only in CHCl<sub>3</sub>, while it was observed for complexes **28c** and **28d** in CHCl<sub>3</sub>, THF and toluene. However, this band was not observed in DMF and DMSO. Thus this band is solvent dependent

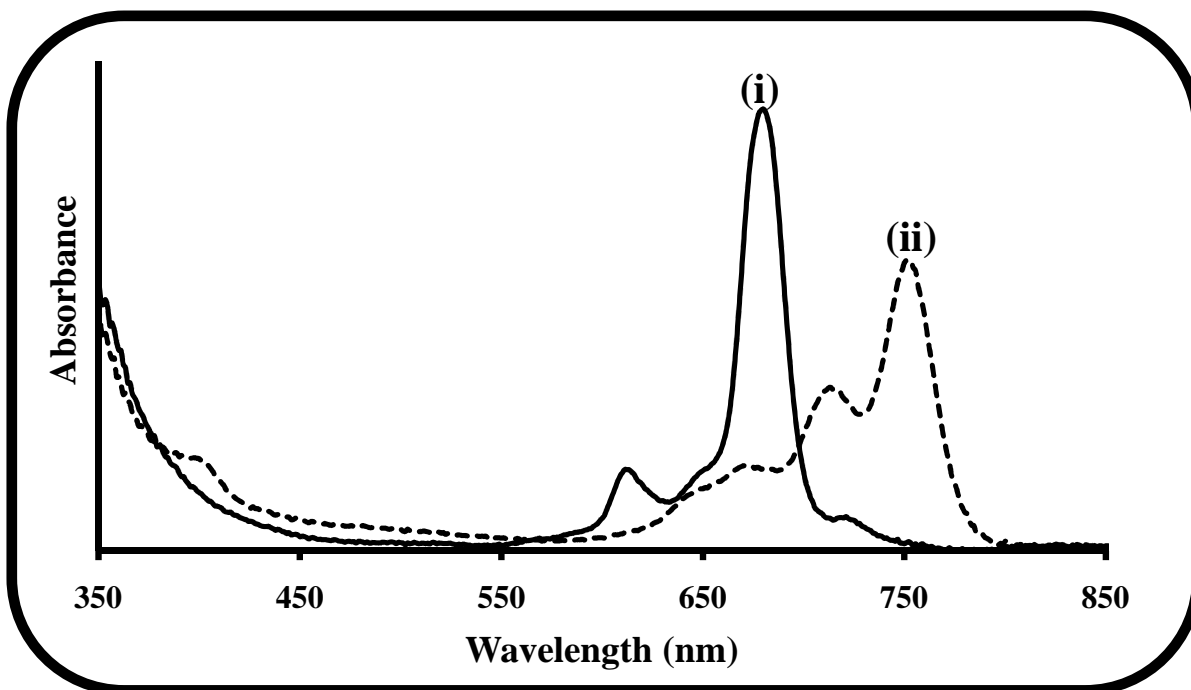


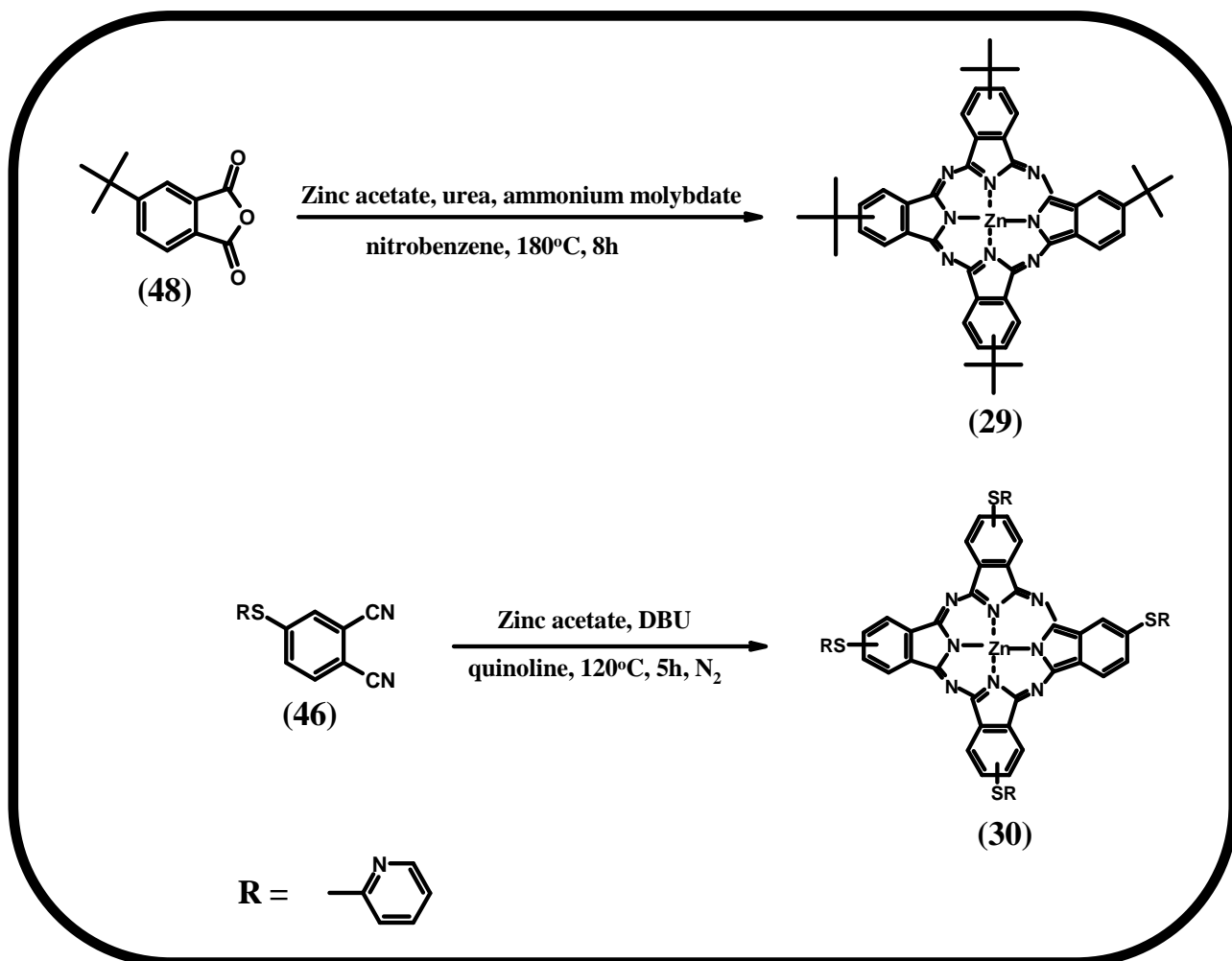
**Figure 3.15:** Protonation of  $\beta$ -CdTPhPc (**26c**) (concentration =  $\sim 4.0 \times 10^{-6}$  M) in  $\text{CHCl}_3$  using TFA. Spectra in the absence (i) and presence (ii) of  $2.0 \times 10^{-3}$  M TFA.

hence may not be due to the phenoxy group twisting discussed above. Toluene and THF also have small amounts of acid (hence the 'X' band is observed in these solvents). In DMSO and DMF the band is not observed since these solvents do not contain acid.

Figure 3.15 shows the expected spectral changes due to protonation of **26c** using trifluoroacetic acid (TFA), a protonating agent. The figure shows the enhancement of the band at 750 nm on protonation, thus confirming that this band may be due to protonation.

### 3.2.2.3 Symmetrical *tert*-butyl and alkanethio tetra-substituted MPcs

The symmetrical zinc analogues,  $\beta$ -ZnttbPc (**29**) and  $\beta$ -ZnTMPyPc (**30**) were synthesized according to literature reported methods [290,291] as shown in Scheme 3.5. Complex **29** was obtained by the anhydride method [153,168,289,290], making use of a *tert*-butyl



**Scheme 3.5:** Synthetic route to zinc tetra *tert*-butyl ( $\beta$ -ZnttbPc, 29) and 2-mercaptopyridine ( $\beta$ -ZnTMPyPc, 30) substituted phthalocyanine complexes.

substituted phthalic anhydride (48) as starting material which is converted to the zinc phthalocyanine (29) in the presence of urea, zinc acetate and with ammonium molybdate as a catalyst. This method relies on the use of high-boiling solvents, therefore quinoline was used for the procedure. Cyclotetramerization of the thiol-substituted phthalonitrile (46) with zinc acetate in the presence of DBU gave complex 30. The complexes were obtained in relatively low yields 0.34 % and 7.5 % respectively. Such low yields may be a consequence of the extensive purification steps employed.

Both complexes show good solubility in most organic solvents, and in particular those selected for this study, namely CHCl<sub>3</sub>, DCM, DMF, DMSO and THF. Complex **29** also shows solubility in toluene. Characterization techniques used include IR, UV-Vis, <sup>1</sup>H-NMR, and elemental analyses, giving data that is in accordance with the predicted structure of the molecule, as shown in the experimental section. IR spectra showed the characteristic C-H vibrations for **29** at 2923 and 2853 cm<sup>-1</sup> while C-S-C vibrations, for **30**, appeared at 698 cm<sup>-1</sup>. The <sup>1</sup>H-NMR spectra of **29** showed ring protons at 9.40 ppm, 9.31-9.27 ppm and at 8.34 ppm, and peaks corresponding to the *tert*-butyl groups at 1.79 ppm. <sup>1</sup>H-NMR spectra of **30** showed well resolved  $\alpha$ -ring protons between 9.01 and 8.74 ppm and between 8.60 and 8.52 ppm for the  $\beta$ -ring protons. A series of protons, attributed to the thiol-substituents, were observed between 8.27 and 7.26 ppm. Integration of all the peaks gave data in good agreement with the predicted number of protons for each complex.

The ground state electronic absorption spectra of **29** and **30** showed monomeric behaviour in CHCl<sub>3</sub>, as evidenced by a single Q band typical of metallated Pc complexes (Figure 3.16). Similar spectra were obtained for both derivatives in DCM, DMF, DMSO and THF. The spectral properties of **29** and **30** are listed in Table 3.5; which indicates a red-shift of 8-10 nm and 13-22 nm in the position of the Q band for **30** relative to **29** and ZnPc (**22**) (Table 3.3) respectively. This can be attributed to the use of electron-donating sulfur substituents, as sulfur donates electron density to the phthalocyanine ring, resulting in an extension of the ring  $\pi$ -conjugation.

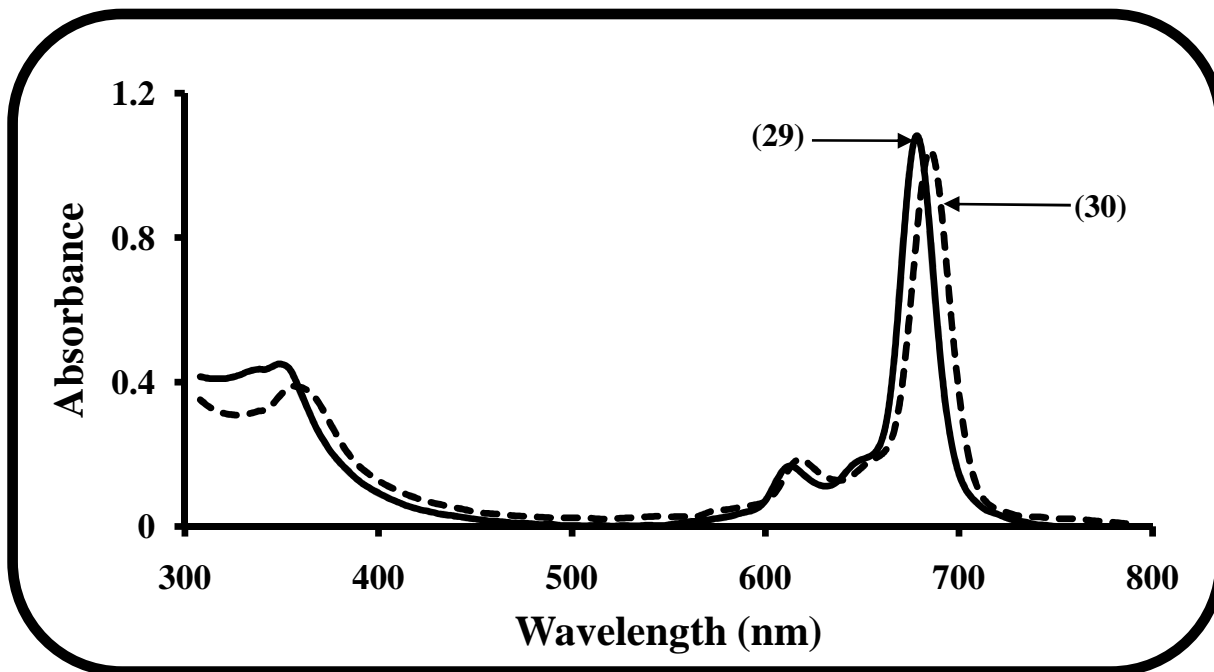


Figure 3.16: Ground state electronic absorption spectra of  $\beta$ -ZnttbPc (29) and  $\beta$ -ZnTMPyPc (30) in  $\text{CHCl}_3$  (concentration =  $\sim 4.0 \times 10^{-6}$  M).

**Table 3.5:** Spectral data of zinc(II) phthalocyanine complexes, 29, 30, 31 and 32 in various organic solvents.

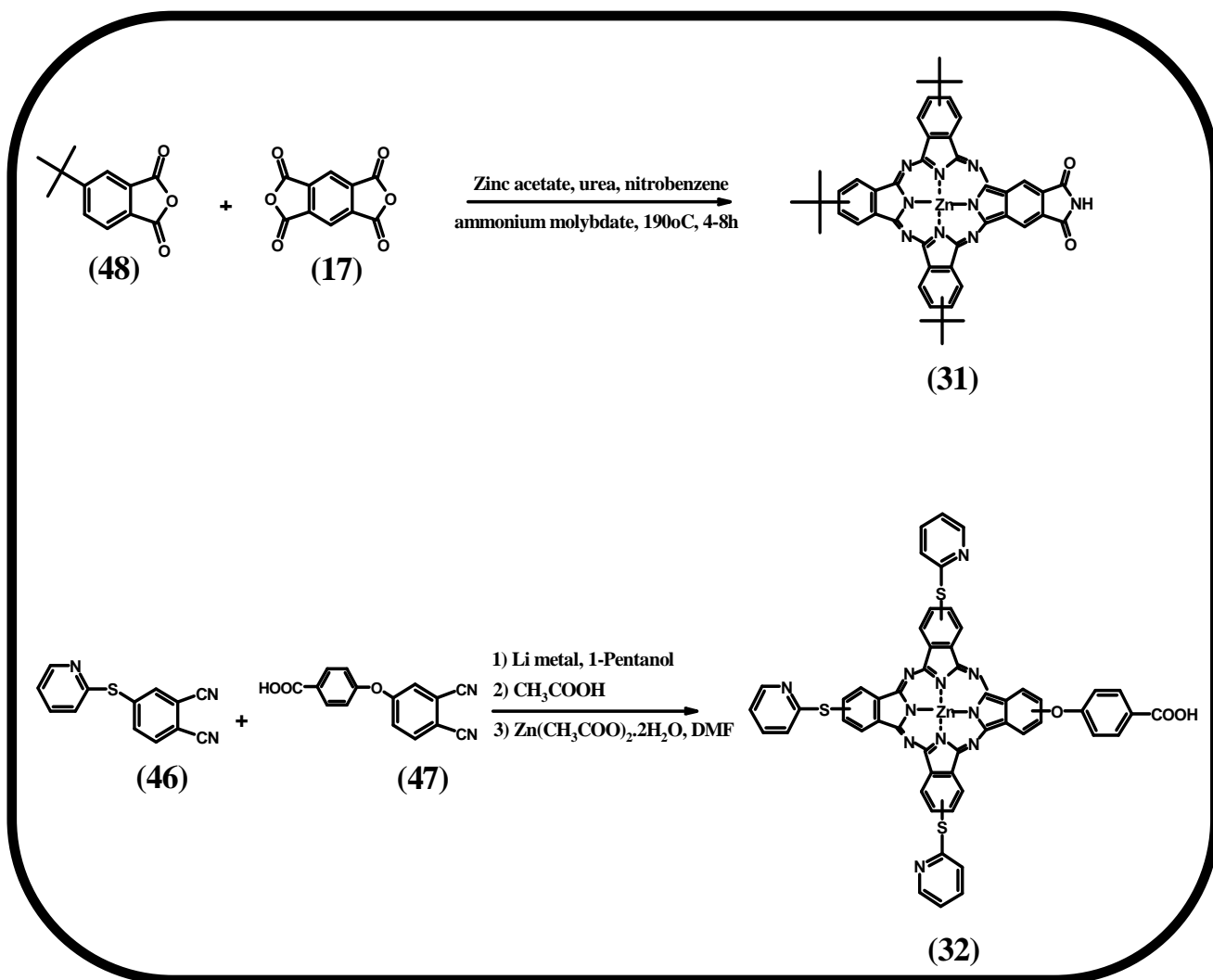
MPc	Solvent	Q band, $\lambda_{\max}/\text{nm}$	Log $\epsilon$
$\beta$ -ZnttbPc (29)	Toluene	677	4.95
	CHCl <sub>3</sub>	678	4.99
	THF	671	5.44
	DCM	677	5.03
	DMF	674	5.42
	DMSO	678	5.44
	$\beta$ -ZnTMPyPc (30)	CHCl <sub>3</sub>	686
THF		680	5.10
DCM		686	4.84
DMF		684	5.06
DMSO		687	5.02
ZnttbIPc (31)	Toluene	708, 668	4.92, 4.79
	CHCl <sub>3</sub>	715, 668	4.90, 4.67
	THF	701, 661	4.96, 4.82
	DCM	712, 667	4.85, 4.70
	DMF	707, 665	4.90, 4.80
	DMSO	708, 668	4.90, 4.81
ZnPc-COOH (32)	CHCl <sub>3</sub>	686	5.43

Table 3.5 contd.

MPc	Solvent	Q band, $\lambda_{\max}/\text{nm}$	Log $\epsilon$
ZnPc-COOH (32) contd.	THF	681	5.06
	DCM	685	5.10
	DMF	683	5.45
	DMSO	687	5.41

### 3.2.3 Low-symmetry ( $A_3B$ type) tetra-substituted MPcs

Low symmetry 3:1 type phthalocyanine derivatives can be synthesized using several different approaches i.e. statistical condensation employing two different phthalonitriles [133,137,313], ring opening of a subphthalocyanine [132,314-316] or reaction of a polymer-bonded phthalonitrile with differently substituted dicarbonitriles in solution followed by cleavage of the formed phthalocyanine [130,317]. Statistical condensation was employed in this work to synthesize ZnttbIPc (**31**) and ZnPc-COOH (**32**) (Scheme 3.6). Pyromellitic dianhydride (**17**), and 4-*tert*-butyl phthalic anhydride (**48**) were employed as starting materials, for the synthesis of **31**. A 3:1 ratio of reactants is known to give the highest yields of the desired 3:1 compound when using precursors of similar reactivity [140,318-320]. An increase in the reaction ratio is often required when the reactivity of the precursors differs markedly, however. A 4:1 molar ratio of anhydride (**48**) to dianhydride (**17**) was, therefore, used in this work. The presence of bulky *tert*-butyl groups facilitates solubility in organic solvents, suppresses aggregation and facilitates chromatographic separation [122].



**Scheme 3.6: Syntheses of low-symmetry zinc(II) phthalocyanine derivatives ZnttbIPc (31) and ZnPc-COOH (32).**

The standard 3:1 molar ratio was employed for 4-(3,4-dicyanophenoxy)benzoic acid (47) and 4-(2-mercaptopyridine) phthalonitrile 46 in the presence of 1-pentanol and lithium metal, to give the metal free substituted phthalocyanine. Reacting this product in DMF with excess zinc acetate affords the desired low-symmetry derivative ZnPc-COOH (32, Scheme 3.6). Mixed condensation reactions have a significant drawback given the fact that product mixtures of radially symmetric Pcs and mono-, di- and tri-substituted Pcs are



inevitably formed, but this approach remains the standard strategy used in the preparation of these derivatives [321].

Complexes **31** and **32** are structurally related to the symmetrical analogues  $\beta$ -ZnttbPc **29** and  $\beta$ -ZnTMPyPc **30** respectively; differing only by one substituent group. Therefore, for the most part, **31** and **32** possess similar spectroscopic characteristics as **29** and **30** respectively. Thus **31** and **32** exhibit excellent solubility in  $\text{CHCl}_3$ , DCM, DMF, DMSO and THF. IR, UV-Vis,  $^1\text{H-NMR}$ , mass spectra and elemental analyses were used for characterization, as reported in the experimental section. The characteristic nitrile ( $\text{C}\equiv\text{N}$ ) stretch of phthalonitriles **46** and **47** is absent from the IR spectra of complex **32**. N-H stretches due to the imide group attached to the periphery of **31** occur at 1771 and 1717  $\text{cm}^{-1}$ . The IR spectra of **32** shows the C=O vibrations at 1676  $\text{cm}^{-1}$ , C-S-C vibrations at 617  $\text{cm}^{-1}$  and the C-O-C vibrations were also observed at 1096  $\text{cm}^{-1}$ . The  $^1\text{H-NMR}$  spectra is fully consistent with the target structures. For complex **31**, the imide N-H signal lies furthest downfield since the proton is highly deshielded, as a result of the ring current effect associated with the Pc macrocycle. There is a downfield shift of the signals of the two adjacent  $\alpha$ -protons, 9.94 – 9.80 ppm, for similar reasons. The peaks for the six remaining  $\alpha$ -protons appear as a multiplet between 9.78 – 9.53 ppm. The  $\beta$ -position proton peak lies between 8.52 – 8.50 ppm. The upfield signal at 1.84 – 1.66 ppm can be assigned to the highly shielded *tert*-butyl protons. The  $^1\text{H-NMR}$  spectrum of **32** shows the 8 non-peripheral protons as a poorly resolved multiplet between 9.00 and 8.70 ppm. The peripheral ring protons are found between 8.59 and 8.49 ppm and are followed by a series of aromatic protons pertaining to the 2-mercaptopyridine and carboxyphenoxy groups. The terminal proton of the carboxyl group is often difficult to observe, as in this

case which accounts for its absence in the  $^1\text{H-NMR}$  spectrum. The resolution of the  $^1\text{H-NMR}$  signals is low due to the presence of structural isomers associated with the fact that the substituent groups (*tert*-butyl for **31** and 2-mercaptopyridine and carboxyphenoxy for **32**) can be located on either  $\beta$ -carbon. MALDI-TOF MS and elemental analysis provide data that further support the predicted structures.

The ground state electronic absorption spectrum corresponding to **32** in  $\text{CHCl}_3$  is shown in Figure 3.17 and indicates a slightly broadened but typical monomeric phthalocyanine spectrum with no splitting of the Q band [138,322,323]. The complex has the same Q

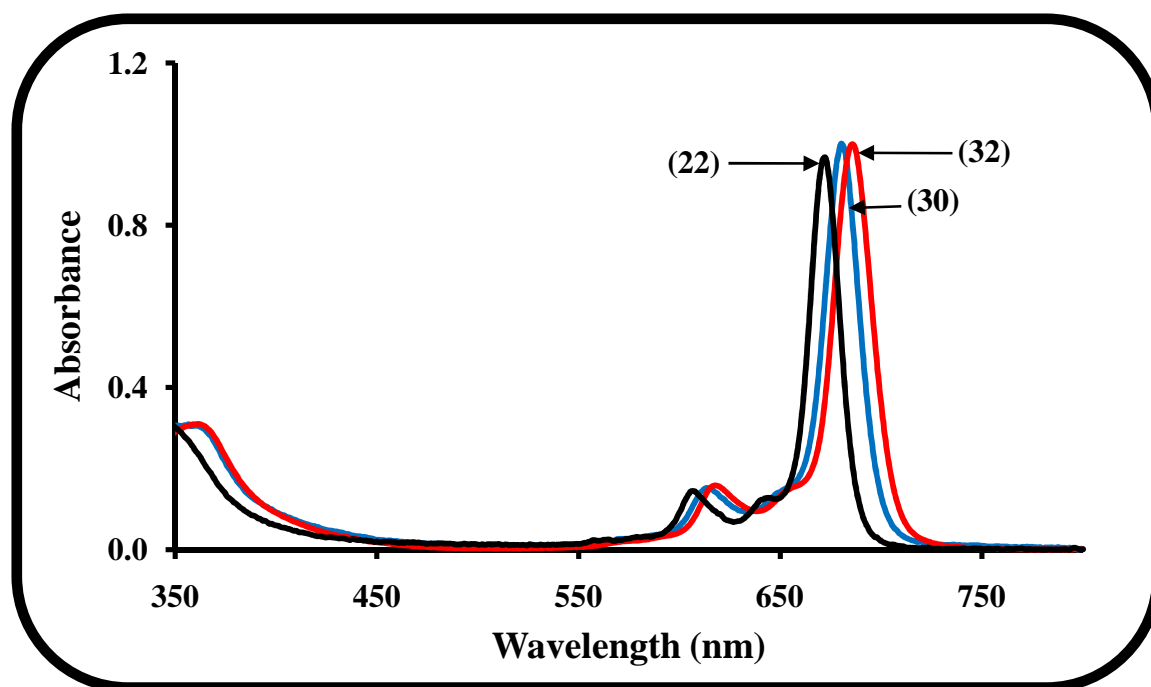


**Figure 3.17:** Ground state electronic absorption spectra of ZnPc (**22**) in  $\text{CHCl}_3$ ,  $\beta$ -ZnTMPycPc (**30**) in THF (concentration =  $\sim 1.31 \times 10^{-5}$  M) and ZnPc-COOH (**32**) in  $\text{CHCl}_3$  (concentration =  $\sim 4.74 \times 10^{-6}$  M).

band maximum as complex **30** (Table 3.5) (considering the same solvent), the presence of one extra sulfur does not result in red-shifting in **30** (Table 3.5). In DCM, **32** shows

broadening which may be associated with rare J-type aggregation, Figure 3.18. The red-shifted broadening also suggests there may be protonation. However, the addition of a surfactant, Triton X-100, to the DCM solution of **32** results in disaggregation to give a slightly blue shifted monomeric peak.

Of note, with regard to compound **32**, is its unsplit Q band in all solvents used for this study (similar to that of the symmetrical analogue **30**). The spectrum of low symmetry derivatives is often characterized by a split in the main phthalocyanine Q band peak due to transitions to non-degenerate orbitals. However, only slight broadening is observed for **32**, suggesting only a slight lowering of the symmetry.

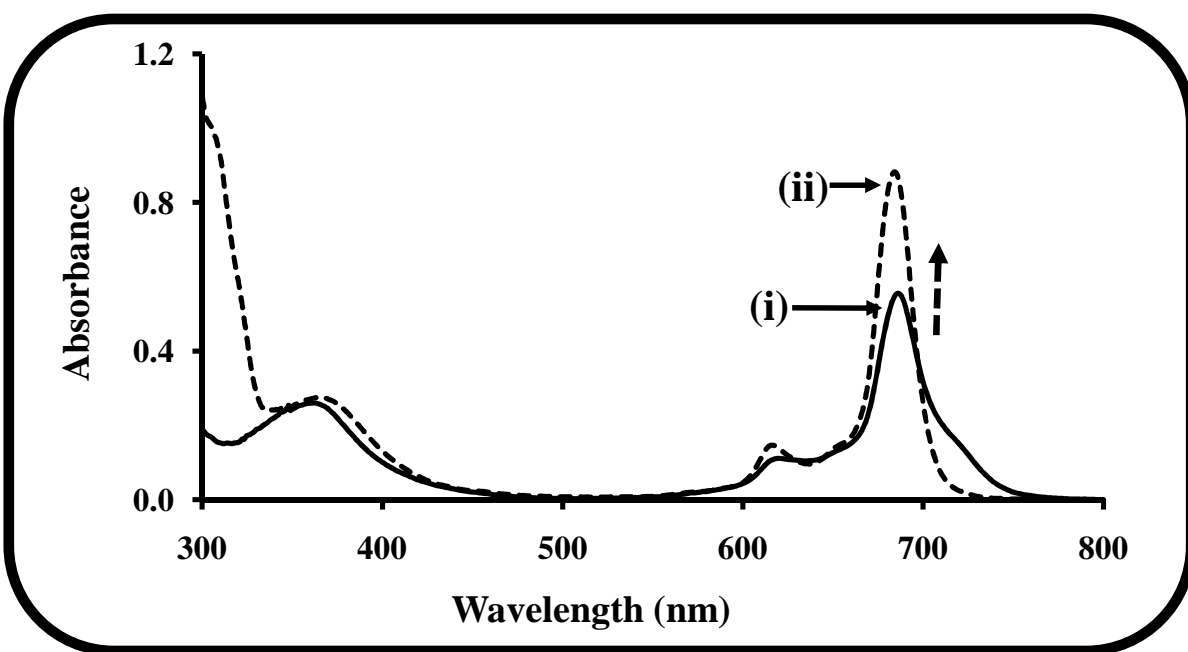


**Figure 3.18:** Electronic absorption spectra of ZnPc-COOH (**32**) in DCM (i) in the absence of Triton X-100 (concentration =  $4.41 \times 10^{-6}$  M) and (ii) in the presence of Triton X-100.

Complex **31**, however shows a spectrum more typical of a low-symmetry derivative i.e. a lowering in the symmetry of the phthalocyanine molecule (from  $\beta$ -ZnttbPc (**29**)- $D_{4h}$  to

ZnttbIPc (**31**)- $C_{2v}$ ), accompanied by a split in the phthalocyanine Q band giving rise to a  $Q_x$  and  $Q_y$  band at 715 and 668 nm respectively (in  $CHCl_3$ ) (Figure 3.19) as a result of

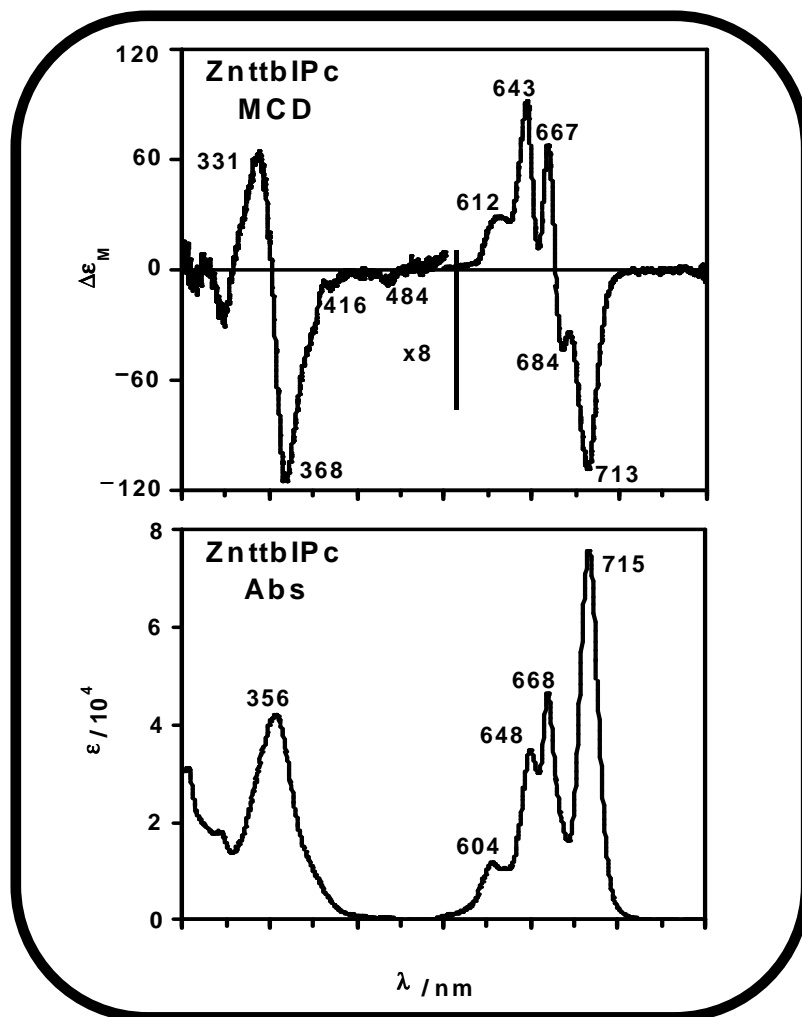


**Figure 3.19:** Electronic absorption and MCD spectra of ZnttbIPc (**31**) in  $CHCl_3$  (concentration =  $\sim 7.0 \times 10^{-6}$  M).

two separate transitions from the highest occupied molecular orbital (HOMO;  $a_{1u}$ ) to the lowest unoccupied molecular orbitals (LUMO;  $e_{gx}^*$  and  $e_{gy}^*$ ). The terminal fused imido-ring may have resulted in the red-shift of the main Q band at 715 nm compared to the Q band position of symmetrical tetra *tert*-butyl substituted  $\beta$ -ZnttbPc (**29**). In chlorinated solvents such as  $CHCl_3$  and DCM the Q band exists at slightly longer wavelengths for **31**

(Table 3.5). Often such a bathochromic shift is a function of an increase in solvent polarity; however this then brings to question the behaviour in DMF and DMSO, which are solvents of even higher polarity and are expected to have longer wavelength absorption bands. The low absorption coefficients of **31** (versus those of **29**) as listed in Table 3.5 may be of concern; however it has been found in earlier literature that the absorption coefficients of Q bands tend to decrease with a decrease in molecular symmetry [132].

Also shown in Figure 3.19 is the MCD spectrum of **31** in  $\text{CHCl}_3$ . The  $B_1/B_2$  band region is very similar to that of ZnPc with the MCD spectrum being dominated by a broad intense positive pseudo- $\mathcal{A}_1$  term. The peaks for the component Faraday  $\mathcal{B}_0$  terms lie at 331 and 368 nm. Marked differences (compared to symmetric MPcs) can be observed in the Q band region between 600 – 800 nm where spectral band widths are typically much narrower leading to greater resolution of the main electronic and vibrational bands. Two negative  $\mathcal{B}_0$  terms at 684 and 713 nm are followed at higher energy by positive  $\mathcal{B}_0$  terms at 643 and 667 nm and a broader  $\mathcal{B}_0$  term at 612 nm, which is followed at higher energy by a weak tail of absorbance. A weak derivative-shaped feature at 416 nm can be assigned tentatively as the 2nd  $\pi \rightarrow \pi^*$  band. A weak negative  $\mathcal{B}_0$  term at 484 nm is not observed in the spectrum of ZnPc (**22**) (Figure not shown) [171,324].

DFT geometry optimizations using the B3LYP functional with 6-31G(d) basis sets, were also carried out, for a ZnttbIPc (**31**) model structure without the peripheral *tert*-butyl groups (ZnIPc). Calculated electronic absorption spectra were derived from TD-DFT calculations on this basis, Figure 3.20 and Table 3.6. The calculation accurately predicts

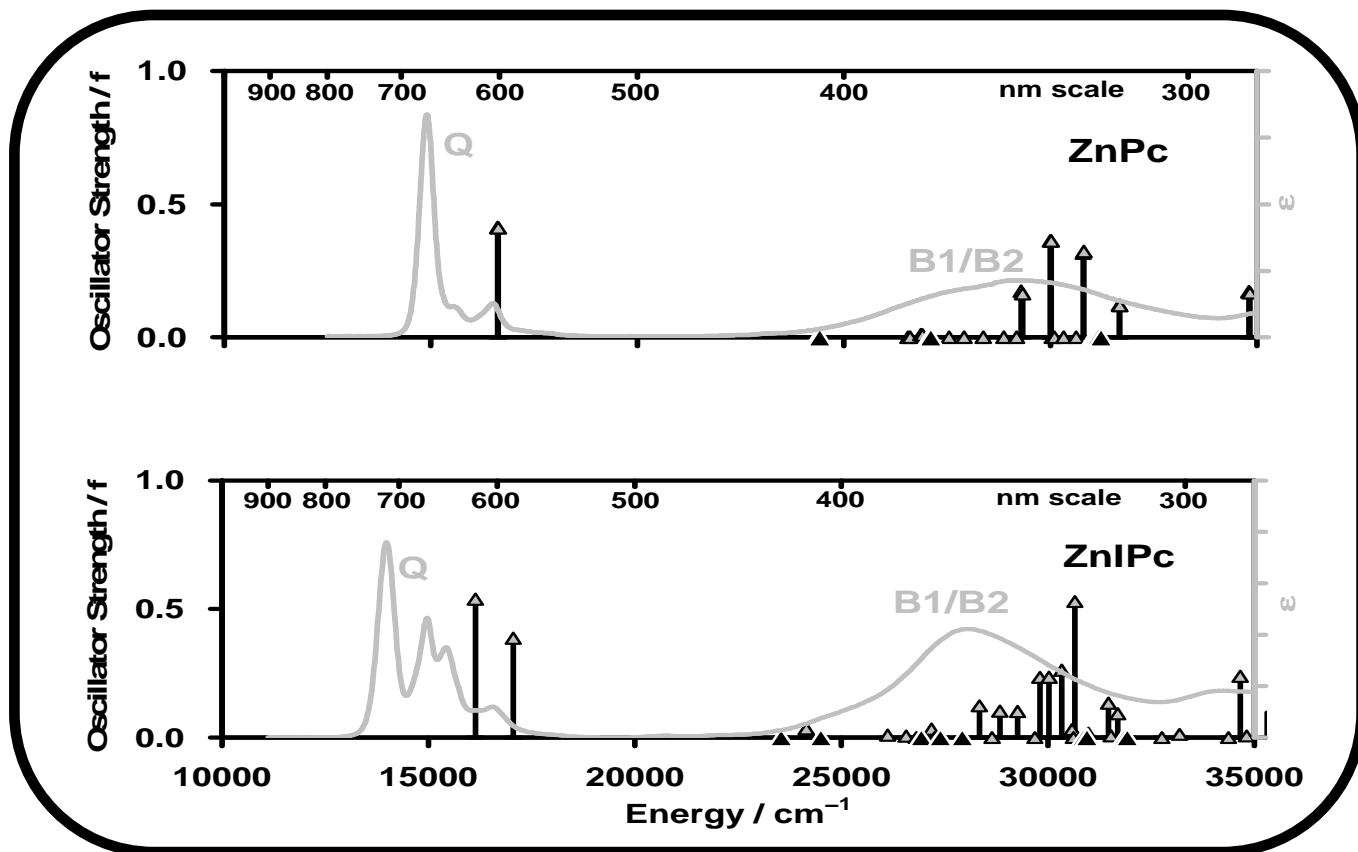


**Figure 3.20:** The experimental (gray line plotted against right hand axes) and TD-DFT (triangles denoting band energies and oscillator strengths) electronic absorption spectra of ZnPc (22) and ZnIPc. Light gray triangles are used for  $\pi \rightarrow \pi^*$  transitions, while larger black triangles denote  $n \rightarrow \pi^*$  transitions associated with lone pair orbitals of the nitrogens. No vibrational bands are calculated in the TD-DFT spectrum so the number of bands does not match what is observed in the experimental data. Details of the calculated spectra are provided in Table 3.6.

the magnitude of the splitting of the Q band but the band energies are overestimated as is typically observed for porphyrinoid TD-DFT calculations [219]. The splitting of the Q band into  $x$ - and  $z$ - polarized components due to the presence of the fused peripheral imido group along the  $z$ -axis results in significantly sharper peaks than are usually

observed in the Q band region for MPc complexes (Figure 3.19, Figure 3.20). A similar splitting was recently reported by Kobayashi and Nakai [210] in the optical spectra of NiPc complexes partially substituted with strongly electron withdrawing trifluorosulfonyl substituents at the  $\alpha$ -positions in which the splitting of the Q band is comparable to what is observed for H<sub>2</sub>Pc. In the UV-region, a complex set of coupled oppositely-signed  $\mathcal{B}_0$  terms are predicted, while only a single pair is observed in the MCD spectrum. Greater predicted complexity than what is observed experimentally in the UV region has been reported previously both for TD-DFT calculations of radially symmetric and low symmetry porphyrinoids [219,220]. The energies of the frontier MOs of **22**, and ZnIPc, which are associated with Gouterman's 4-orbital model are broadly similar, Figure 3.21. There are marked differences between the Q<sub>vib</sub> bands of **22** and **31**, Figure 3.20. The two repeating sequences of Faraday  $\mathcal{B}_0$  terms with +/-/+ sign patterns in ascending energy terms to the red of 604 nm in the MCD spectrum of (CN<sup>-</sup>)ZnPc as found by Mack *et al.* [324] are replaced by what appears to be a single coupled pair of intense oppositely signed Faraday  $\mathcal{B}_0$  terms at 643 and 687 nm, which overlap the symmetry-split Q<sub>00</sub> bands.

Table 3.6: TD-DFT calculated spectra of ZnPc (22) and ZnIPc.

ZnPc (22, $D_{4h}$ )							
# <sup>a</sup>	Sym <sup>b</sup>	$\nu^c$	Ex <sup>d</sup>	f <sup>e</sup>	$\lambda^f$	Wavefunction <sup>g</sup> =	Band <sup>h</sup>
1	<sup>1</sup> A <sub>1g</sub>	----	----	----	---	groundstate	---
2 [3]	<sup>1</sup> E <sub>u</sub>	16.6	14.9	0.41	602	72% 1a <sub>1u</sub> → 1e <sub>gx</sub> *; 10% 1a <sub>2u</sub> → 1e <sub>g</sub> *; ...	Q (x/y)
4 [5]	<sup>1</sup> E <sub>g</sub>	24.4	----	0.00	410	98% 1b <sub>1g</sub> <sup>N</sup> → 1e <sub>gx</sub> *; ...	n → π* (-)
8 [9]	<sup>1</sup> E <sub>u</sub>	26.9	23.5	0.01	372	89% 1b <sub>2u</sub> → 1e <sub>gx</sub> *; ...	2 <sup>nd</sup> π → π* (x/y)
10 [11]	<sup>1</sup> E <sub>g</sub>	27.1	----	0.00	369	97% 1b <sub>2g</sub> <sup>N</sup> → 1e <sub>gx</sub> *; ...	n → π* (-)
17 [18]	<sup>1</sup> E <sub>u</sub>	29.3	27.2	0.17	341	46% 2a <sub>2u</sub> → 1e <sub>gy</sub> *; 40% 1a <sub>2u</sub> → 1e <sub>gy</sub> *; ...	B1 (x/y)
19 [20]	<sup>1</sup> E <sub>u</sub>	30.0	----	0.36	333	78% 1b <sub>1u</sub> → 1e <sub>gy</sub> *; ...	π → π* (x/y)
25 [26]	<sup>1</sup> E <sub>u</sub>	30.7	29.8	0.32	325	37% 2a <sub>2u</sub> → 1e <sub>gy</sub> *; 28% 1a <sub>2u</sub> → 1e <sub>gy</sub> *; 12% 2a <sub>1u</sub> → 1e <sub>gx</sub> *; ...	B2 (x/y)
31 [32]	<sup>1</sup> E <sub>u</sub>	31.7	----	0.12	316	89% 1a <sub>1u</sub> → 2e <sub>gy</sub> *; ...	π → π* (x/y)
33 [34]	<sup>1</sup> E <sub>u</sub>	34.8	35.5	0.17	287	89% 2a <sub>1u</sub> → 2e <sub>gx</sub> *; ...	N (x/y)
ZnIPc (C <sub>2v</sub> )							
# <sup>a</sup>	Sym <sup>b</sup>	$\nu^c$	Ex <sup>d</sup>	f <sup>e</sup>	$\lambda^f$	Wavefunction <sup>g</sup> =	Band <sup>h</sup>
1	<sup>1</sup> A <sub>1</sub>	----	----	----	---	groundstate	---
2	<sup>1</sup> A <sub>1</sub>	16.1	14.3	0.54	620	73% 1a <sub>2</sub> (1a <sub>1u</sub> ) → 1a <sub>2</sub> *(1e <sub>gy</sub> *); ...	Q (z)
3	<sup>1</sup> B <sub>1</sub>	17.1	14.7	0.39	586	73% 1a <sub>2</sub> (1a <sub>1u</sub> ) → 1b <sub>2</sub> *(1e <sub>gx</sub> *); ...	Q (x)
4	<sup>1</sup> A <sub>2</sub>	23.5	----	0.00	425	98% 1a <sub>1</sub> <sup>N</sup> (1b <sub>1g</sub> <sup>N</sup> ) → 1a <sub>2</sub> *(1e <sub>gy</sub> *); ...	n → π* (-)
6	<sup>1</sup> B <sub>2</sub>	24.5	----	0.00	408	98% 1a <sub>1</sub> <sup>N</sup> (1b <sub>1g</sub> <sup>N</sup> ) → 1b <sub>2</sub> *(1e <sub>gx</sub> *); ...	n → π* (y)
7	<sup>1</sup> B <sub>1</sub>	26.1	23.8	0.01	383	54% 1b <sub>2</sub> (1b <sub>2u</sub> ) → 1a <sub>2</sub> *(1e <sub>gy</sub> *); 35% 2b <sub>2</sub> → 1a <sub>2</sub> *(1e <sub>gy</sub> *); ...	2 <sup>nd</sup> π → π* (x)
11	<sup>1</sup> B <sub>2</sub>	26.9	----	0.00	365	85% 2b <sub>1</sub> <sup>N</sup> (1b <sub>2g</sub> <sup>N</sup> ) → 1a <sub>2</sub> *(1e <sub>gy</sub> *); 11% 1b <sub>1</sub> <sup>N</sup> (imido <sup>N</sup> ) → 1a <sub>2</sub> *(1e <sub>gy</sub> *); ...	n → π* (y)
13	<sup>1</sup> A <sub>1</sub>	27.3	24.3	0.00	367	70% 1b <sub>2</sub> (1b <sub>2u</sub> ) → 1b <sub>2</sub> *(1e <sub>gx</sub> *); 17% 2a <sub>2</sub> (1e <sub>gy</sub> ) → 1a <sub>2</sub> *(1e <sub>gy</sub> *); ...	2 <sup>nd</sup> π → π* (z)
15	<sup>1</sup> A <sub>2</sub>	27.9	----	0.00	358	94% 2b <sub>1</sub> <sup>N</sup> (1b <sub>2g</sub> <sup>N</sup> ) → 1b <sub>2</sub> *(1e <sub>gx</sub> *); ...	n → π* (-)
16	<sup>1</sup> B <sub>1</sub>	28.3	----	0.12	353	46% 4b <sub>2</sub> (2e <sub>gx</sub> ) → 1a <sub>2</sub> *(1e <sub>gy</sub> *); 31% 3b <sub>2</sub> (1e <sub>gx</sub> ) → 1a <sub>2</sub> *(1e <sub>gy</sub> *); ...	π → π* (x)
18	<sup>1</sup> B <sub>1</sub>	28.8	27.6	0.10	347	43% 5b <sub>2</sub> (2a <sub>2u</sub> ) → 1a <sub>2</sub> *(1e <sub>gy</sub> *); 27% 4b <sub>2</sub> (2e <sub>gx</sub> ) → 1a <sub>2</sub> *(1e <sub>gy</sub> *); 10% 2b <sub>2</sub> (1a <sub>2u</sub> ) → 1a <sub>2</sub> *(1e <sub>gy</sub> *); ...	B1 (x)
19	<sup>1</sup> A <sub>1</sub>	29.3	----	0.10	342	34% 3a <sub>2</sub> (1b <sub>1u</sub> ) → 1a <sub>2</sub> *(1e <sub>gy</sub> *); 24% 2b <sub>2</sub> (1a <sub>2u</sub> ) → 1b <sub>2</sub> *(1e <sub>gx</sub> *); 18% 4a <sub>2</sub> (2e <sub>gy</sub> ) → 1a <sub>2</sub> *(1e <sub>gy</sub> *); 10% 4b <sub>2</sub> (2e <sub>gx</sub> ) → 1b <sub>2</sub> *(1e <sub>gx</sub> *); ...	π → π* (z)
21	<sup>1</sup> B <sub>1</sub>	29.8	----	0.23	335	43% 3a <sub>2</sub> (1b <sub>1u</sub> ) → 1b <sub>2</sub> *(1e <sub>gx</sub> *); 12% 1a <sub>2</sub> (1a <sub>1u</sub> ) → 3b <sub>2</sub> *(1b <sub>2u</sub> *); ...	π → π* (x)
22	<sup>1</sup> A <sub>1</sub>	30.0	31.0	0.23	333	32% 4a <sub>2</sub> (2e <sub>gy</sub> ) → 1a <sub>2</sub> *(1e <sub>gy</sub> *); 23% 2b <sub>2</sub> (1a <sub>2u</sub> ) → 1b <sub>2</sub> *(1e <sub>gx</sub> *); 12% 5b <sub>2</sub> (2a <sub>2u</sub> ) → 1b <sub>2</sub> *(1e <sub>gx</sub> *); 12% 4b <sub>2</sub> (2e <sub>gx</sub> ) → 1b <sub>2</sub> *(1e <sub>gx</sub> *); ...	B1 (z)
23	<sup>1</sup> B <sub>1</sub>	30.3	----	0.26	329	29% 5b <sub>2</sub> (2a <sub>2u</sub> ) → 1a <sub>2</sub> *(1e <sub>gy</sub> *); 18% 4a <sub>2</sub> (2e <sub>gy</sub> ) → 1b <sub>2</sub> *(1e <sub>gx</sub> *); 15% 3a <sub>2</sub> (1b <sub>1u</sub> ) → 1b <sub>2</sub> *(1e <sub>gx</sub> *); 12% 3b <sub>2</sub> (1e <sub>gx</sub> ) → 1a <sub>2</sub> *(1e <sub>gy</sub> *); ...	π → π* (x)
26	<sup>1</sup> A <sub>1</sub>	30.7	----	0.53	326	34% 4a <sub>2</sub> (2e <sub>gy</sub> ) → 1a <sub>2</sub> *(1e <sub>gy</sub> *); 29% 3b <sub>2</sub> (1e <sub>gx</sub> ) → 1b <sub>2</sub> *(1e <sub>gx</sub> *); 11% 1a <sub>2</sub> (1a <sub>1u</sub> ) → 3a <sub>2</sub> *(1b <sub>1u</sub> *); 10% 4b <sub>2</sub> (2e <sub>gx</sub> ) → 1b <sub>2</sub> *(1e <sub>gx</sub> *); ...	π → π* (z)
30	<sup>1</sup> A <sub>1</sub>	31.5	----	0.13	318	37% 5b <sub>2</sub> (2a <sub>2u</sub> ) → 1b <sub>2</sub> *(1e <sub>gx</sub> *); 19% 5a <sub>2</sub> (2a <sub>1u</sub> ) → 1a <sub>2</sub> *(1e <sub>gy</sub> *); 18% 1a <sub>2</sub> (1a <sub>1u</sub> ) → 3a <sub>2</sub> *(1b <sub>1u</sub> *); ...	π → π* (z)
38	<sup>1</sup> A <sub>1</sub>	34.7	----	0.24	288	54% 5a <sub>2</sub> (2a <sub>1u</sub> ) → 1a <sub>2</sub> *(1e <sub>gy</sub> *); 10% 1a <sub>2</sub> (1a <sub>1u</sub> ) → 172(2e <sub>gy</sub> *); ...	N (z)
40	<sup>1</sup> B <sub>1</sub>	35.3	----	0.10	283	84% 5a <sub>2</sub> (2a <sub>1u</sub> ) → 1b <sub>2</sub> *(1e <sub>gx</sub> *); ...	N (x)



<sup>a</sup>The number of the state assigned in terms of ascending energy within the INDO/s calculation. Only states located below 50 000 cm<sup>-1</sup> resulting from allowed electronic transitions with an oscillator strength of greater than 0.01 are included. <sup>b</sup>Symmetry of the state. <sup>c,d</sup>The calculated and observed band energies (10<sup>3</sup> cm<sup>-1</sup>). <sup>e</sup>Calculated oscillator strength. <sup>f</sup>Calculated band wavelength in nm. <sup>g</sup>The calculated wave functions based on the eigenvectors predicted by INDO/s. In the case of ZnIPc the corresponding MOs based on *D*<sub>4h</sub> symmetry are provided in parentheses to enable comparison with the calculated spectrum of ZnPc. One-electron transitions associated with Gouterman's 4-orbital model are shown in bold. N as a superscript refers to lone pair MOs associated with pyrrole- and aza-nitrogens. Only eigenvectors greater than 5 % are included. <sup>h</sup>Band assignment described in the text with band polarizations in parentheses.

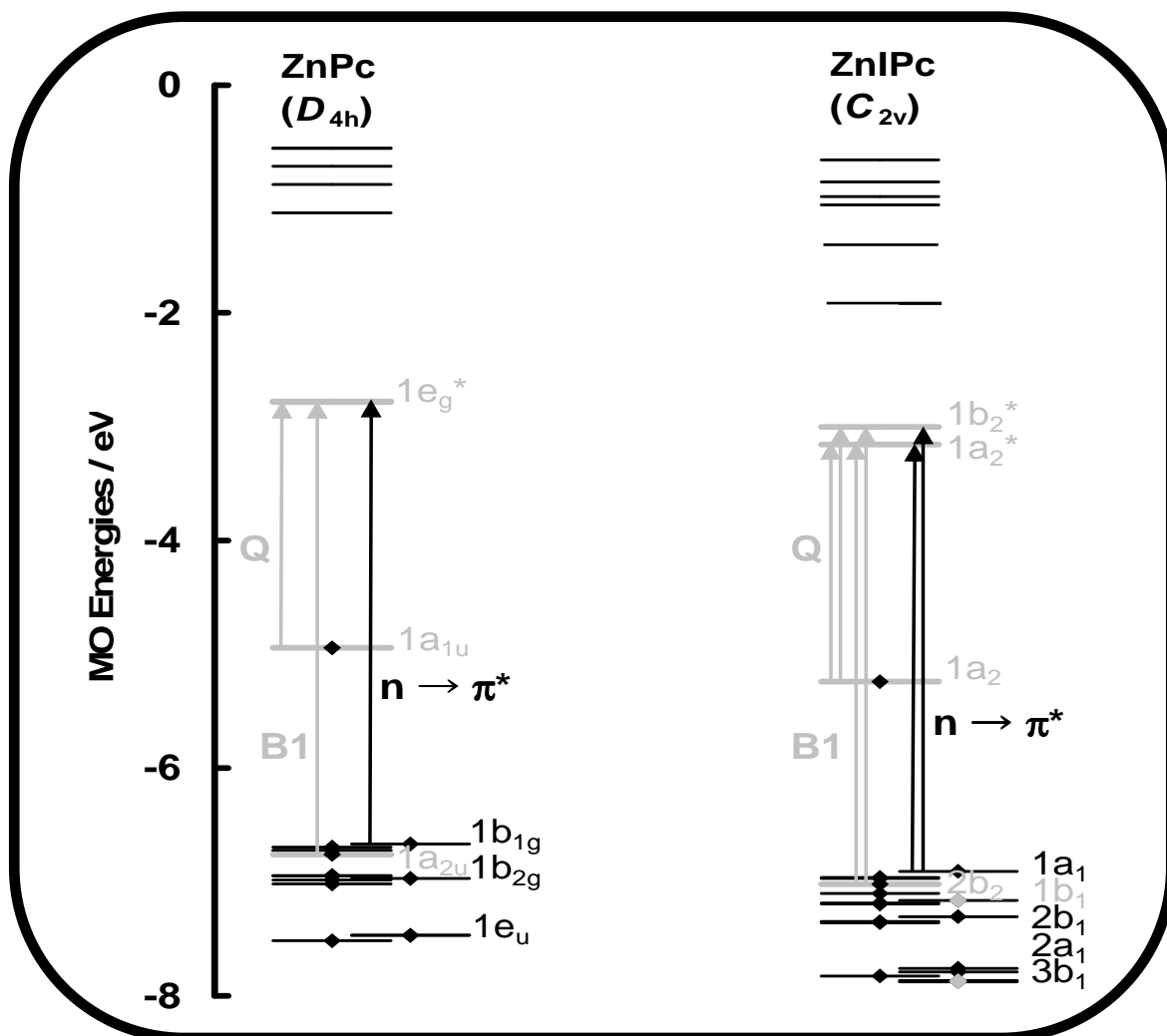


Figure 3.21: MO energy diagrams for ZnPc (22) and ZnIPc between 0 and  $-8$  eV. Diamonds are used to denote occupied MOs. The four frontier  $\pi$ -MOs from Gouterman's 4-orbital model [170] are shown in gray. Transitions between these MOs are predicted to provide significant contributions to the main Q and B<sub>1</sub> bands in the spectra of ZnIPc. MOs associated primarily with the lone pair MOs associated with the aza- and pyrrole-nitrogens and the peripheral imido groups are offset to the right. Gray diamonds are used to distinguish occupied MOs primarily associated with the imido group of ZnIPc.

### 3.3 Conclusions

Symmetrical zinc, cadmium and mercury phthalocyanine derivatives have been successfully synthesized and characterized by various spectroscopic means. All the complexes are soluble in highly polar solvents such as DMF and DMSO. Some of the complexes are soluble in highly polar solvents such as DMF and DMSO. Some of the complexes tend to exhibit limited solubility in toluene,  $\text{CHCl}_3$ , THF and DCM. MPcs containing heavy metal ions, such as Cd or Hg, exhibit interesting spectral behaviour, with some complexes showing extensive aggregation and others indicating spectra typical of oxidation. The synthesis and spectroscopic characterization of novel low-symmetry zinc complexes has also been reported, where the influence of a lowering in symmetry has been investigated with respect to the properties of various solvents and can be used to give deeper insight into the electronic structure of phthalocyanines. All complexes synthesized gave spectroscopic data indicating high purity and in accordance with the predicted structures.

## **4. Photophysical and Photochemical Properties**

**The photophysicochemical properties of the QDs and MPcs synthesized are discussed. For the MPcs, comparisons are made with respect to the presence of different metal ions, substituents, substitution positions and solvent properties.**

## 4.1 Fluorescence Spectra

### 4.1.1 Nanoparticles (SWCNT and QDs)

The functionalized SWCNT used in this work do not show any fluorescence in the UV-Vis region. Therefore there are no spectra pertaining to these compounds.

The normalized fluorescence emission spectra of the MPA capped CdTe QDs (2) synthesized in this work are shown in Figure 4.1. With increasing size, the emission spectra are characterized by narrow peaks (full width at half maximum (FWHM) of  $\sim 72$  nm at a wavelength of 640 nm) with good symmetry. Figure 4.1 gives an indication of how the QDs show size dependent luminescence properties, with emission wavelengths ranging from  $\sim 540$  to 640 nm, at which point the growth process was terminated.

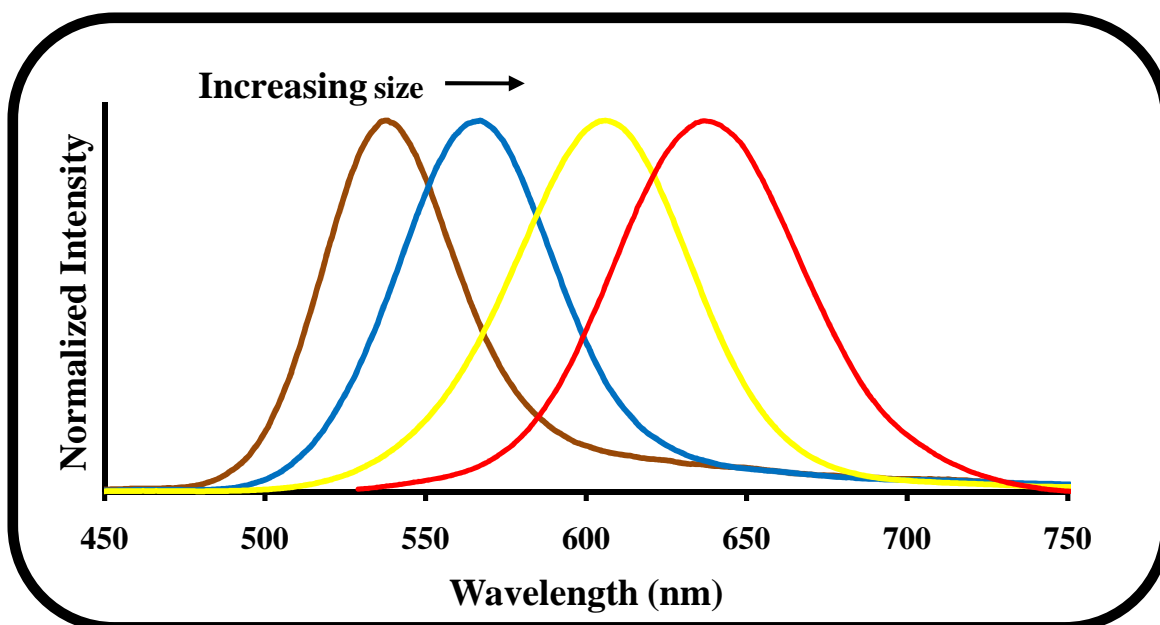


**Figure 4.1:** Normalized fluorescence emission spectra of as-synthesized mercaptopropionic acid capped CdTe QDs (2) in aqueous media.

CdTe QDs capped with thiols are known to aggregate in acidic conditions due to detachment of surface ligands [325]. Aggregation of QDs results in red shifting in the

emission spectra accompanied by broadening and decrease in the fluorescence lifetime [326]. Solvents also have an effect on the aggregation nature of CdTe QDs [326]. However, in this case, there was no change in the emission spectrum of the QDs recorded from direct synthesis conditions in NaOH or when recorded using DMF:water (4:1 v/v) mixture, (Figure 4.2, Table 4.1), showing that DMF has no effect on QDs.

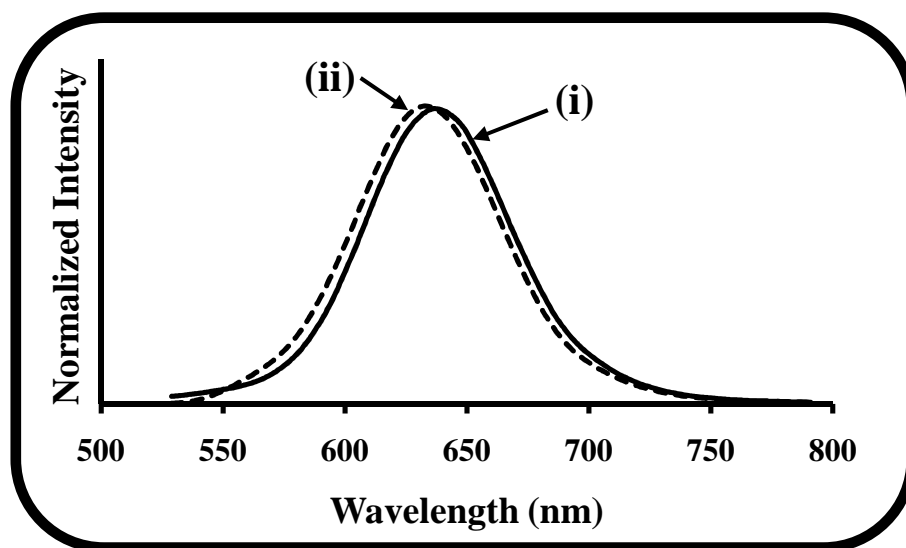


Figure 4.2: Comparison of fluorescence emission spectra of CdTe MPA QDs (2) in (i) 0.1 M NaOH and (ii) DMF:water (4:1) solvent mixture.

Table 4.1: Spectral properties, fluorescence quantum yields and lifetimes of MPA capped CdTe QDs (2) in various solvents.

CdTe MPA QDs (2)	Solvent	Refractive Index ( $n_D$ )	<sup>a</sup> Emission $\lambda_{max}$ (nm)	$\Phi_{F(QD)}$ ( $\pm 0.01$ )	$\tau_{F-1}$ (ns) ( $\pm 0.5$ )	$\tau_{F-2}$ (ns) ( $\pm 0.2$ )
	0.1 M NaOH	1.333	640	0.41	26.3	4.3
DMF:water	1.419	638	0.09	26.4	3.4	

<sup>a</sup> $\lambda_{exc} = 510$  nm.

## 4.1.2 Metallophthalocyanines

### 4.1.2.1 Symmetrically substituted metallophthalocyanines

The fluorescence excitation and emission spectra of **22-24**, **28b**, **29**, **30** reported here are typical of phthalocyanine complexes in all solvents; i.e. emission occurs at longer wavelengths than absorption, with Stokes shifts ranging from 3 nm to 19 nm (Table 4.2).

The fluorescence excitation spectra are mirror images of the emission spectra and are similar to the absorption spectra as shown in Figure 4.3 for  $\beta$ -ZnTMPyPc (**30**).

The closeness of the Q band maxima for absorption and excitation spectra shows that there are no changes in the configuration of the complexes following excitation.

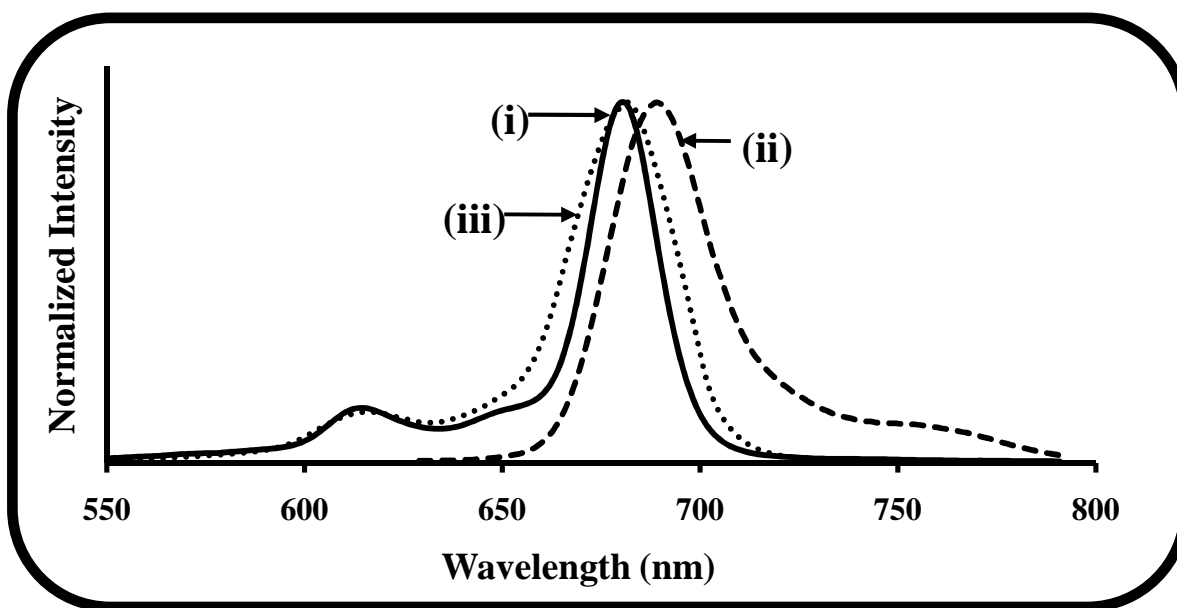


Figure 4.3: Normalized (i) absorption, (ii) fluorescence emission and (iii) excitation spectra of  $\beta$ -ZnTMPyPc (**30**) in THF ( $\lambda_{\text{exc}} = 610$  nm).

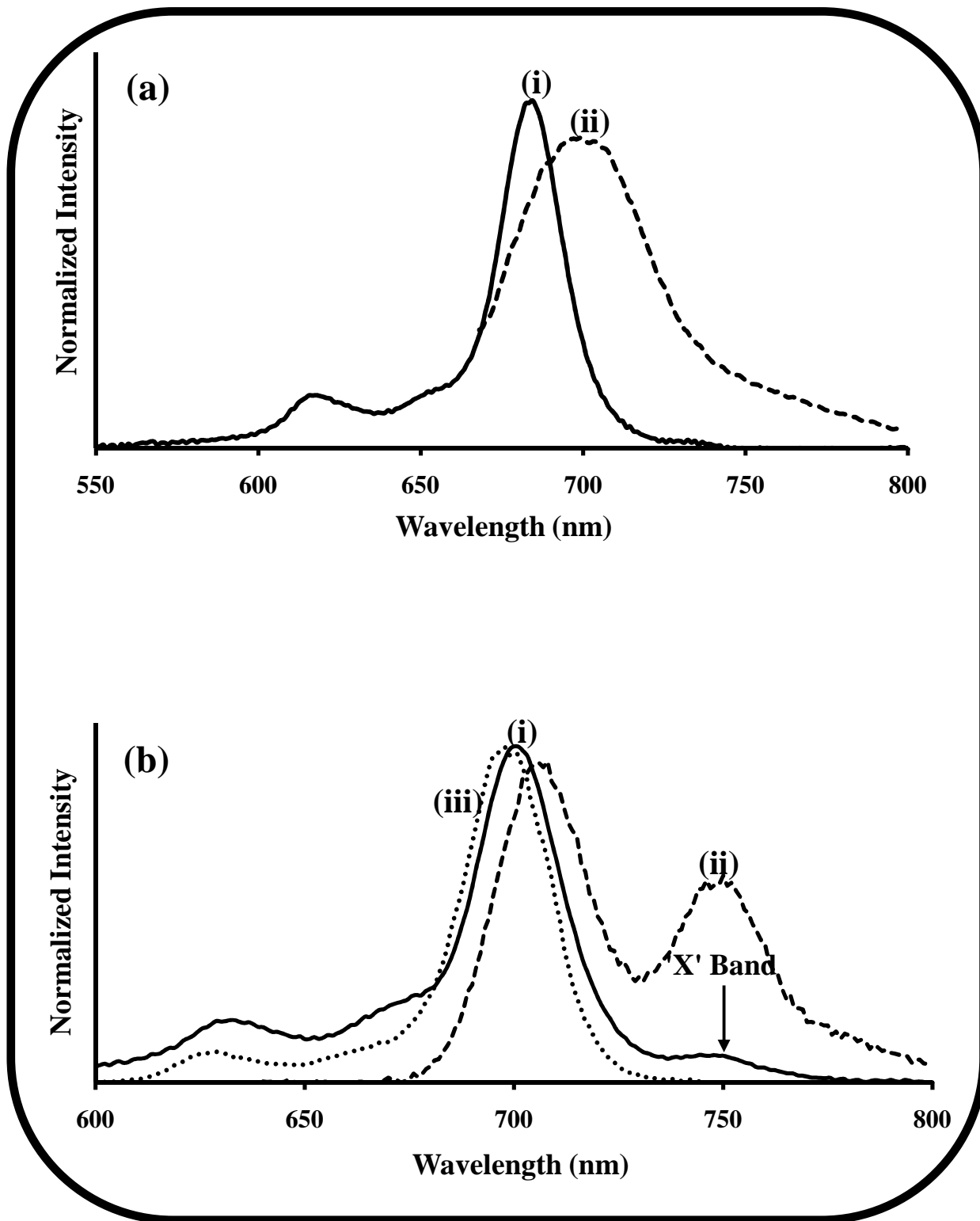
As discussed earlier,  $\beta$ -ZnTPyPc (**25a**),  $\beta$ -CdTPyPc (**26a**),  $\beta$ -CdTTPhPc (**26c**),  $\beta$ -CdTtBuPhPc (**26d**),  $\beta$ -HgTPyPc (**27a**),  $\alpha$ -CdTPyPc (**28a**),  $\alpha$ -CdTPhPc (**28c**),  $\alpha$ -CdTtBuPhPc (**28d**), and  $\beta$ -CdTBzPhPc (**26b**) showed spectra which were solvent dependent. Hence, there is a lack of mirror symmetry in the absorption and fluorescence emission spectra, in some solvents (especially chlorinated ones). In DMF and DMSO the emission spectra were mirror images of the absorption spectra for these complexes.

The mercury complex (**27a**) showed an emission spectrum that differs from the absorption in that the emission is broad, (Figure 4.4a), suggesting loss of symmetry in the fluorescing molecule, in chlorinated solvents.

A large splitting of the Q band was observed in the emission spectra for complexes **28c** and **28d** in toluene, CHCl<sub>3</sub> and THF, (Figure 4.4b for **28d**), showing that upon excitation, the loss of symmetry, discussed earlier with respect to the absorption spectra, becomes more enhanced as shown by the presence of the much higher intensity of the 'X' band (Figure 4.4b). This is further proof that  $\alpha$ - (non-peripheral) substitution is affected by protonation to a larger extent, which also affects emission spectra.

The excitation spectrum of **26b** consistently shows a split peak, in the Q band region, in toluene, CHCl<sub>3</sub>, THF and DCM (Figure 4.4c), suggesting a change in the nature of the molecule following absorption of light and excitation, probably due to a change in symmetry. The excitation spectrum of **26b** was similar to the absorption spectrum of an unmetallated derivative, suggesting that loss of symmetry is due to demetallation.





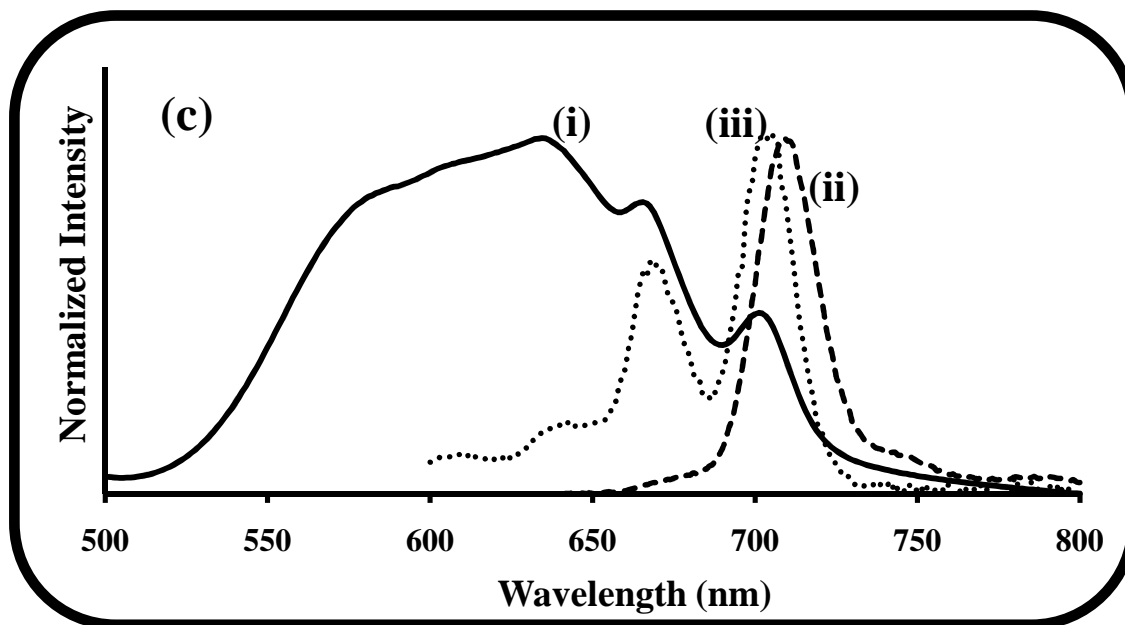


Figure 4.4: Normalized (i) absorption, (ii) fluorescence emission and (iii) excitation spectra of (a)  $\beta$ -HgTPyPc (27a) in DMSO (concentration =  $\sim 2.3 \times 10^{-6}$  M), (b)  $\alpha$ -CdTtBuPhPc (28d) in  $\text{CHCl}_3$  (concentration =  $\sim 7.5 \times 10^{-7}$ ) and (c)  $\beta$ -CdTBzPhPc (26b) in DCM (concentration =  $\sim 5.25 \times 10^{-5}$  M). ( $\lambda_{\text{exc}}$  = 640 nm for (a), 610 nm for (b) and 620 nm for (c)).

#### 4.1.2.2 Low-symmetry metallophthalocyanines

For the low symmetry complex **31** there is also a lack of mirror symmetry in the absorption and fluorescence emission spectra in all solvents; although the excitation spectra are similar to the absorption. A single red-shifted monomeric peak as shown in Figure 4.5 characterizes the emission spectrum of **31**. This is because fluorescence occurs from the lowest energy vibrational band ( $\nu_0$ ) of  $S_1$  (i.e. a transition from one energy level rather than two as is the case for the absorption spectrum of **31**). The emission is thus of

lower energy than the absorption band, i.e. the short-lived excited singlet state ( $S_1$ ) relaxes to a lower energy conformation before it emits [101].

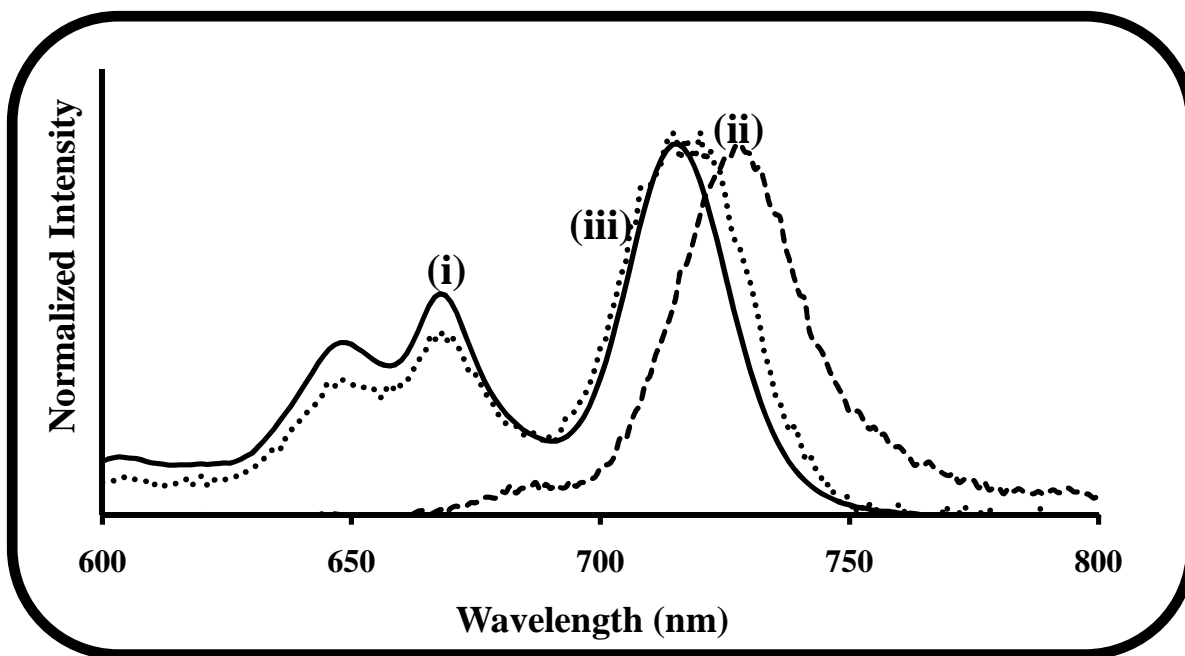


Figure 4.5: Normalized (i) absorption, (ii) fluorescence emission and (iii) excitation spectra of ZnttbIPc (**31**) in  $\text{CHCl}_3$  (concentration =  $\sim 5.19 \times 10^{-6}$  M). ( $\lambda_{\text{exc}} = 610$  nm).

The emission and excitation spectra of the low-symmetry derivative, ZnPc-COOH **32**, is typical of symmetrically substituted metallophthalocyanine complexes, where the excitation spectra are identical to absorption and fluorescence emission spectra are mirror images of the absorption spectra (Figure 4.6). This is surprising since the structure of **32** suggests that the excitation should show a split peak indicative of a lowering in symmetry. As stated earlier this suggests there is only a slight lowering in molecular symmetry for **32**.

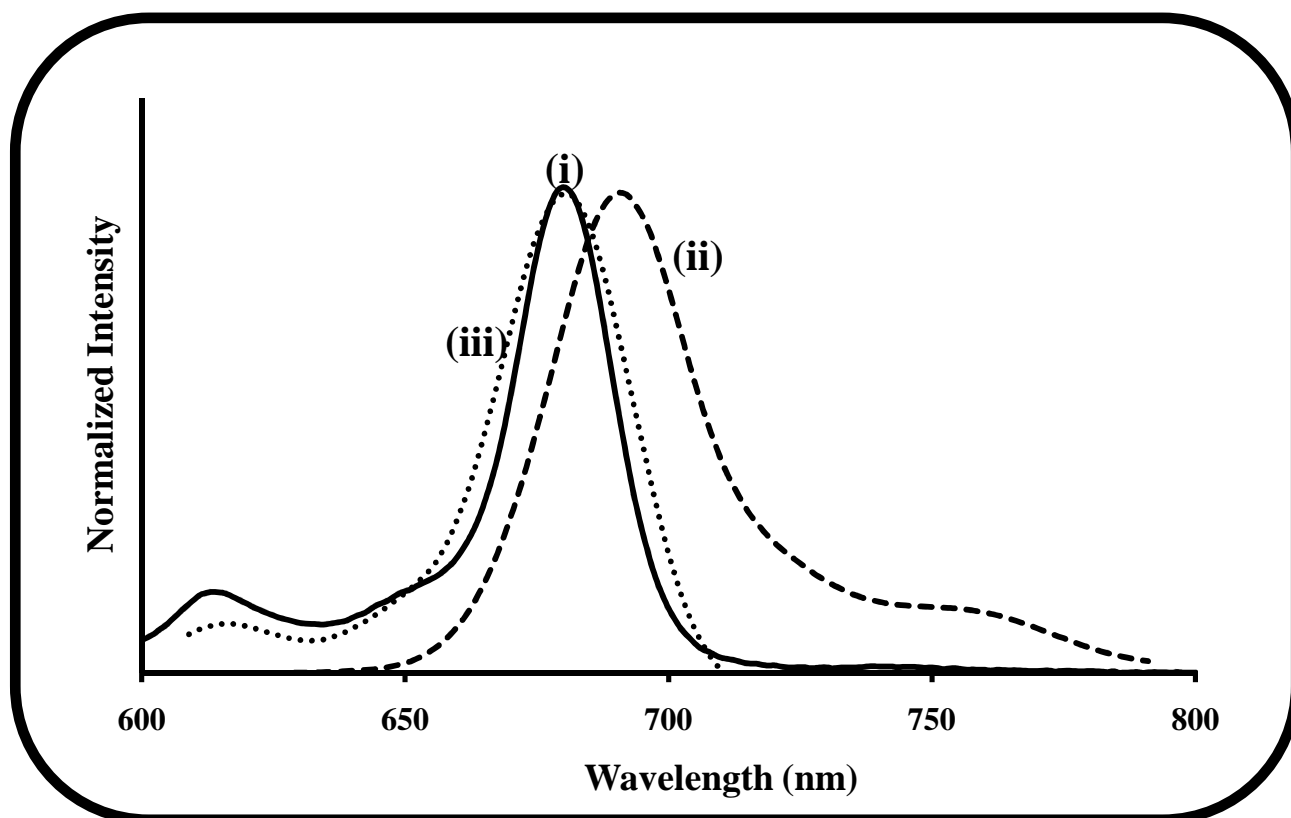


Figure 4.6: Normalized (i) absorption, (ii) fluorescence emission and (iii) excitation spectra of ZnPc-COOH (32) in THF (concentration =  $\sim 4.0 \times 10^{-6}$  M). ( $\lambda_{\text{exc}}$  = 610 nm).

Table 4.2: Fluorescence data of all complexes studied in various organic solvents.

MPc	Solvent	Q band	<sup>a</sup> Emission	<sup>b</sup> Excitation	$\Phi_F$ ( $\pm 0.01$ )
		$\lambda_{max}$ (nm)	$\lambda_{Em}$ (nm)	$\lambda_{Exc}$ (nm)	
ZnPc (22)	Toluene	672	675	672	0.13
	THF	668	672	668	0.23
	DMF	670	676	670	0.30
	DMSO	672	682	672	0.17
CdPc (23)	DMF	674	683	674	0.02
	DMSO	679	691	679	0.02
HgPc (24)	DMF	681	700	675	0.02
	DMSO	684	698	670	0.01
$\beta$ -ZnTPyPc (25a)	DMF	673	684	673	0.17
	DMSO	680	686	680	0.08
$\beta$ -CdTPyPc (26a)	DMF	682	695	682	0.02
	DMSO	685	698	685	0.01
$\beta$ -CdTBzPhPc (26b)	Toluene	704, 668	709	705, 668	0.14
	CHCl <sub>3</sub>	703, 667, 636	711	706, 669	0.25
	THF	700, 664, 634	707	705, 668	0.21
	DCM	701, 666, 634	709	705, 668	0.27
	DMF	684	697	685	0.13
	DMSO	688	699	689	0.10

Table 4.2 contd.

MPc	Solvent	Q band $\lambda_{\max}$ (nm)	Emission $\lambda_{\text{Em}}$ (nm)	Excitation $\lambda_{\text{Exc}}$ (nm)	$\Phi_{\text{F}}$ ( $\pm 0.01$ )
$\beta$ -CdTPhPc (26c)	Toluene	681	687	680	0.13
	CHCl <sub>3</sub>	681	688	681	0.27
	THF	677	683	675	0.29
	DMF	677	687	678	0.29
	DMSO	681	691	681	0.20
$\beta$ -CdTtBuPhPc (26d)	Toluene	681	687	681	0.14
	CHCl <sub>3</sub>	681	689	681	0.27
	THF	678	686	678	0.27
	DMF	678	685	678	0.32
	DMSO	684	692	685	0.21
$\beta$ -HgTPyPc (27a)	DMF	685	702	677	0.01
	DMSO	690	704	676	<0.01
$\alpha$ -CdTPyPc (28a)	CHCl <sub>3</sub>	684	701	697, 684	0.17
	THF	682	699	683	0.18
	DCM	683	696	685	0.18
	DMF	682	695	684	0.16
	DMSO	684	705	689	0.16
$\alpha$ -CdTBzPhPc (28b)	Toluene	701	714	704	0.14

Table 4.2 contd.

MPc	Solvent	Q band $\lambda_{\max}$ (nm)	Emission $\lambda_{\text{Em}}$ (nm)	Excitation $\lambda_{\text{Exc}}$ (nm)	$\Phi_{\text{F}}$ ( $\pm 0.01$ )
$\alpha$ -CdTBzPhPc (28b) contd.	CHCl <sub>3</sub>	707	722	713	0.15
	THF	699	710	697	0.18
	DCM	703	719	707	0.15
	DMF	698	713	699	0.19
	DMSO	702	718	706	0.05
$\alpha$ -CdTPhPc (28c)	Toluene	694	770, 700	695	0.05
	CHCl <sub>3</sub>	700	746, 703	698	0.39
	THF	693	772, 698	692	0.47
	DMF	694	699	696	0.31
	DMSO	698	706	702	0.06
$\alpha$ -CdTtBuPhPc (28d)	Toluene	694	770, 702	696	0.27
	CHCl <sub>3</sub>	700	750, 708	698	0.49
	THF	693	714, 698	693	0.50
	DMF	694	700	698	0.53
	DMSO	698	706	700	0.06
$\beta$ -ZnttbPc (29)	Toluene	677	683	678	0.08
	DMF	674	684	674	0.23
	DMSO	678	687	678	0.14

Table 4.2 contd.

MPc	Solvent	Q band $\lambda_{\max}$ (nm)	Emission $\lambda_{\text{Em}}$ (nm)	Excitation $\lambda_{\text{Exc}}$ (nm)	$\Phi_{\text{F}}$ ( $\pm 0.01$ )
$\beta$ -ZnTMPyPc (30)	DMF	684	694	684	0.19
	DMSO	687	698	686	0.10
ZnttbIPc (31)	Toluene	708, 668	719	709, 667	0.05
	DMF	707, 665	721	712, 666	0.08
	DMSO	708, 668	721	713, 667	0.10
ZnPc-COOH (32)	DMF	683	695	685	0.25
	DMSO	687	700	687	0.16

<sup>a</sup> $\lambda_{\text{Em}}$  = fluorescence emission wavelength, <sup>b</sup> $\lambda_{\text{Exc}}$  = fluorescence excitation wavelength.

## 4.2 Fluorescence Quantum Yields and Lifetimes

### 4.2.1 Nanoparticles (QDs)

The quantum yield of fluorescence for the CdTe MPA QDs (2) was calculated using Equation 1.4, shown as Equation 4.1:

$$\Phi_{\text{F}} = \Phi_{\text{F}}^{\text{Std}} \frac{F \cdot A_{\text{Std}} \cdot n^2}{F_{\text{Std}} \cdot A \cdot n_{\text{Std}}^2} \quad (4.1)$$

A quantum yield of 0.41 was obtained for the QDs in 0.1M NaOH. Studies in a mixture of DMF and water gave a yield of 0.09 (Table 4.1). The decrease in the mixture may be attributed to a change in the solvent properties, particularly the refractive index (for water



= 1.333 and DMF:water = 1.419). The  $\Phi_F$  values also often increase with increasing viscosity according to the Förster-Hoffmann equation, Equation 4.2 [327]:

$$\text{Log } \Phi_F = C + \log \eta \quad (4.2)$$

The fluorescence lifetime ( $\tau_F$ ) of **2** was determined using a time correlated single photon counting setup (TCSPC). The data in NaOH or DMF:water mixture remained unchanged (Figure. 4.7), further confirming lack of aggregation and indicates there is not much influence of a change in solvent, with respect to the lifetimes of the QDs in NaOH ( $\tau_{F-1} = 26.3$  ns and  $\tau_{F-2} = 4.3$  ns) and DMF:water ( $\tau_{F-1} = 26.4$  ns and  $\tau_{F-2} = 3.4$  ns) (Table 4.1). The presence of biexponential decay kinetics is a common occurrence for QDs. Literature suggests that the short lifetime component may be attributed to the intrinsic recombination of initially populated core states [328-330]. The origin of the longer lifetime component may be due to the involvement of surface states in the carrier recombination process [331]. The increase in radiative lifetime as a result of trapping of carrier states, by surface states, is a well established feature [329]. Therefore, it seems plausible that this may account for the data we have obtained. However, other researchers contradict this theory and suggest the faster decay component may rather be attributed to the surface states [332,333]. The difference in the short lifetime component that we obtained, under the influence of different solvents, may also support this theory, since a change in the solvent may exert more influence on the surface state properties of the QDs as opposed to the core. Therefore at this stage assignments cannot be made with respect to the origin of the short and long lifetime components.

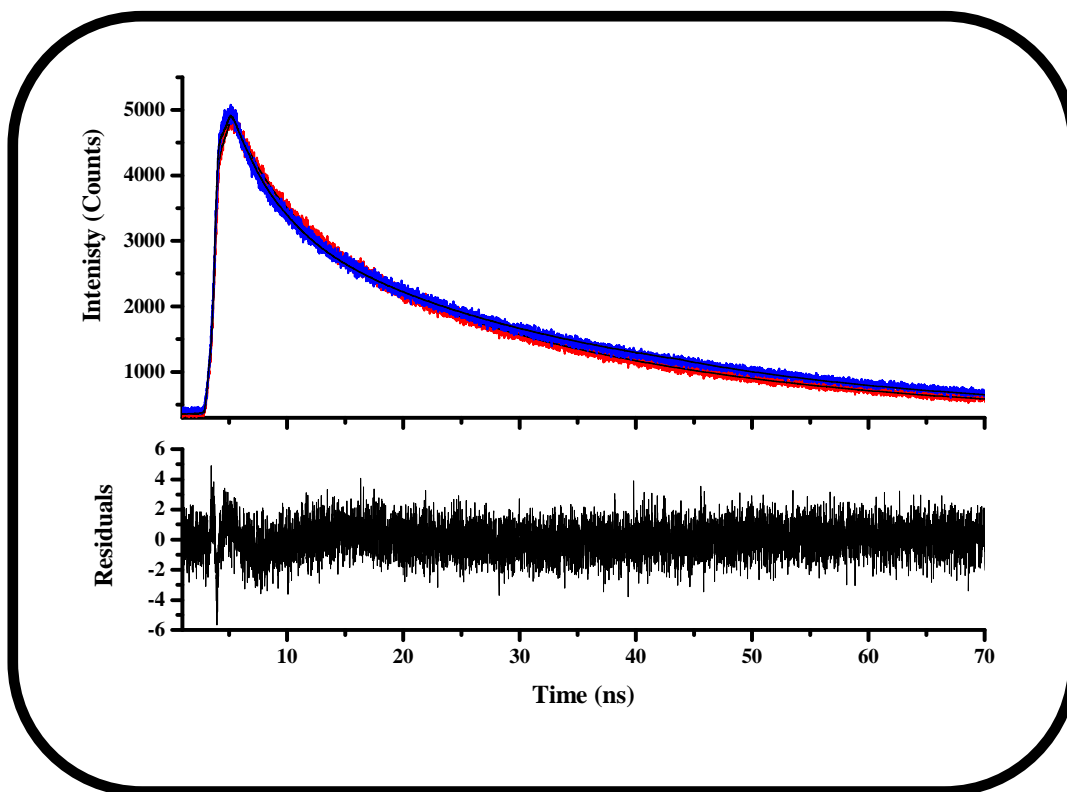


**Figure 4.7:** Photoluminescence decay curves of CdTe MPA QDs (2) in 0.1 M NaOH (red) and DMF:water (4:1) solvent mixture (blue).

#### 4.2.2 Metallophthalocyanines

Fluorescence quantum yields ( $\Phi_F$ ) were calculated in various solvents using Equation 4.1 and are shown in Table 4.2. The influence of the central metal ion is immediately evident on comparison of corresponding zinc, cadmium and mercury Pc derivatives and considering the same solvent. The order of fluorescence quantum yield values is ZnPc (22) > CdPc (23)  $\cong$  HgPc (24) and ZnTPyPc (25a) > CdTPyPc (26a) > HgTPyPc (27a). This order is expected on grounds of spin-orbit coupling induced by the respective central metal ions. Hg(II), being the heaviest of the three metal ions, brings about the strongest SOC, thereby increasing the likelihood of the spin-forbidden intersystem crossing and an

attendant decrease in the spin-allowed fluorescence and internal conversion. Under this circumstance, the Hg(II) derivatives are also expected to give the highest triplet quantum yield values, and the Zn(II) derivatives, the lowest.

In general, the effect of introducing substituents to peripheral ( $\beta$ ) and non-peripheral ( $\alpha$ ) positions on the MPc ring is a reduction in  $\Phi_F$  values (comparing the same solvent), compared to those of the unsubstituted analogues (Table 4.2). The substituents perhaps encourage the deactivation of the excited singlet state *via* non-radiative means (intersystem crossing and internal conversion) rather than *via* fluorescence.

In general, higher  $\Phi_F$  values were observed for the  $\alpha$ -CdPc derivatives compared to corresponding  $\beta$ -derivatives in DMF. However, the situation is reversed in DMSO, where the  $\beta$ -complexes show much higher quantum yields; this excludes the  $\alpha$ - (**28a**) and  $\beta$ -CdTPyPc (**26a**) complexes in this solvent. Comparison of  $\Phi_F$  values obtained in different solvents, found that values in DMSO are generally the lowest, which could be explained by the premise that DMSO itself contains heavy sulfur atoms, which tend to promote intersystem crossing to the triplet state, *via* spin-orbit coupling, and deactivate molecules against non-radiative transitions to the ground state. There were however exceptions for ZnPc (**22**),  $\beta$ -CdTPhPc (**26c**),  $\beta$ -CdTtBuPhPc (**26d**),  $\beta$ -ZnttbPc (**29**) and ZnttbIPc (**31**) in toluene. The low solvent viscosity of toluene can be used to account for the low  $\Phi_F$  values in this solvent relative to data obtained in higher viscosity solvents such as DMF and DMSO. There is increased possibility of deactivation of the excited state by radiationless transitions such as internal conversion (IC) in low viscosity solvents [226], see also Equation 4.2.

An increase in  $\Phi_F$  values has been reported with the use of electron-donating nature of the substituents [275]. Table 4.2 generally shows lower  $\Phi_F$  values for pyridyloxy and phenoxy substituted Cd complexes ( $\beta$ -CdTPyPc **26a**,  $\beta$ -CdTPhPc **26c**,  $\alpha$ -CdTPyPc **28a**, and  $\alpha$ -CdTPhPc **28c**) compared to the *tert*-butyl-phenoxy substituted complexes ( $\beta$ -CdTtBuPhPc **26d** and  $\alpha$ -CdTtBuPhPc **28d**). An exception in this instance, is the benzyloxyphenoxy substituted derivatives ( $\beta$ -CdTBzPhPc **26b** and  $\alpha$ -CdTBzPhPc **28b**), which show unexpected low values, despite the high electron donating ability of the substituent. Thus the  $\Phi_F$  values were found to decrease in the order *tert*-butylphenoxy > phenoxy > benzyloxyphenoxy > pyridyloxy.

The  $\Phi_F$  values of low symmetry complex **32** are higher than for the symmetrical derivative **30** in both DMF and DMSO (Table 4.2). This is reversed for **29** and **31**, where the low symmetry derivative (**31**) is less fluorescent than the symmetrical (**29**) compound in toluene, DMF and DMSO. With respect to the low symmetry derivatives, compound **32** is more fluorescent than **31** in DMF and DMSO (Table 4.2). The data for **31** does not vary significantly, with a change in solvent, although the yields are considerably low. The low fluorescence quantum yields for **31** could be a result of intramolecular quenching of the excited singlet state by the amino group [334,335].

### 4.3 Triplet State Quantum Yields and Lifetimes of MPc Complexes

The lowest excited triplet states of light-absorbing molecules are populated as a result of intersystem crossing from the lowest excited singlet states. The fact that this spin-forbidden process takes place at all is as a result of spin-orbit coupling. Therefore  $\Phi_T$  values provide a measure of the fraction of absorbing molecules that undergo intersystem

**Table 4.3:** Triplet state quantum yields and lifetimes of the MPcs studied in different organic solvents.

MPc	Solvent	$\Phi_F$ ( $\pm 0.01$ )	$\Phi_T$	$\Phi_{IC}$	$\tau_T$ ( $\mu s$ )
<b>ZnPc (22)</b>	Toluene	0.13	0.65 <sup>a</sup>	0.22	340 <sup>b</sup>
	DMF	0.30	0.58 <sup>c</sup>	0.12	330 <sup>d</sup>
	DMSO	0.17	0.65 <sup>e</sup>	0.18	350
<b>CdPc (23)</b>	DMF	0.02	0.77	0.21	5
	DMSO	0.02	0.70	0.28	30
<b>HgPc (24)</b>	DMF	0.02	0.86	0.12	4
	DMSO	0.01	0.87	0.12	40
<b><math>\beta</math>-ZnTPyPc (25a)</b>	DMF	0.17	0.68	0.15	7
	DMSO	0.08	0.80	0.12	350
<b><math>\beta</math>-CdTPyPc (26a)</b>	DMF	0.02	0.85	0.13	5
	DMSO	0.01	0.83	0.16	30
<b><math>\beta</math>-CdTBzPhPc (26b)</b>	Toluene	0.14	0.82	0.04	30
	DMF	0.13	0.77	0.10	5
	DMSO	0.10	0.36	0.54	30
<b><math>\beta</math>-CdTPhPc (26c)</b>	Toluene	0.13	0.87	0.00	4
	DMF	0.29	0.40	0.31	90
	DMSO	0.20	0.61	0.19	190

Table 4.3 contd.

MPc	Solvent	$\Phi_F$ ( $\pm 0.01$ )	$\Phi_T$	$\Phi_{IC}$	$\tau_T$ ( $\mu s$ )
$\beta$ -CdTtBuPhPc (26d)	Toluene	0.14	0.76	0.10	5
	DMF	0.32	0.41	0.27	100
	DMSO	0.21	0.54	0.25	260
$\beta$ -HgTPyPc (27a)	DMF	0.01	0.90	0.09	4
	DMSO	<0.01	0.89	0.11	20
$\alpha$ -CdTPyPc (28a)	DMF	0.16	0.70	0.14	10
	DMSO	0.16	0.61	0.23	40
$\alpha$ -CdTBzPhPc (28b)	Toluene	0.14	0.51	0.35	30
	DMF	0.19	0.53	0.28	7
	DMSO	0.05	0.38	0.57	9
$\alpha$ -CdTPhPc (28c)	Toluene	0.05	0.73	0.22	6
	DMF	0.31	0.49	0.20	20
	DMSO	0.06	0.66	0.28	130
$\alpha$ -CdTtBuPhPc (28d)	Toluene	0.27	0.49	0.24	5
	DMF	0.53	0.56	0.09	10
	DMSO	0.06	0.61	0.34	150
$\beta$ -ZnttbPc (29)	Toluene	0.08	0.40	0.52	4
	DMF	0.23	0.71	0.06	20

Table 4.3 contd.

MPc	Solvent	$\Phi_F$ ( $\pm 0.01$ )	$\Phi_T$	$\Phi_{IC}$	$\tau_T$ ( $\mu s$ )
$\beta$ -ZnttbPc (29) contd.	DMSO	0.14	0.73	0.13	200
$\beta$ -ZnTMPyPc (30)	DMF	0.19	0.74	0.07	4
	DMSO	0.10	0.73	0.17	160
ZnttbIPc (31)	Toluene	0.05	0.41	0.54	6
	DMF	0.08	0.77	0.15	70
	DMSO	0.10	0.82	0.08	180
ZnPc-COOH (32)	DMF	0.25	0.68	0.07	8
	DMSO	0.16	0.82	0.02	230

<sup>a</sup>[286], <sup>b</sup>[268], <sup>c</sup>[241], <sup>d</sup>[145], <sup>e</sup>[283].

crossing (ISC) to the triplet state. Triplet lifetimes ( $\tau_T$ ) also give a measure of the efficiency of a photosensitizer such as the phthalocyanines discussed in this work. The  $\Phi_T$  and  $\tau_T$  values for the MPc complexes studied, in different solvents, are listed in Table 4.3. The  $\Phi_T$  values were calculated using Equation 4.3 (same as Equation 1.9)

$$\Phi_T = \Phi_T^{\text{Std}} \cdot \frac{\Delta A_T \cdot \epsilon_T^{\text{Std}}}{\Delta A_T^{\text{Std}} \cdot \epsilon_T} \quad (4.3)$$

Transient absorption curves can be obtained for the various complexes by using argon degassed solutions and exciting the Q band maximum wavelength. The point of maximum triplet absorption is determined using a plot similar to that of **31** in toluene

(Figure 4.8a(i)), which shows a Q band shape, at the triplet state, that is similar to the ground state electronic absorption spectrum (although the split is not as well defined)

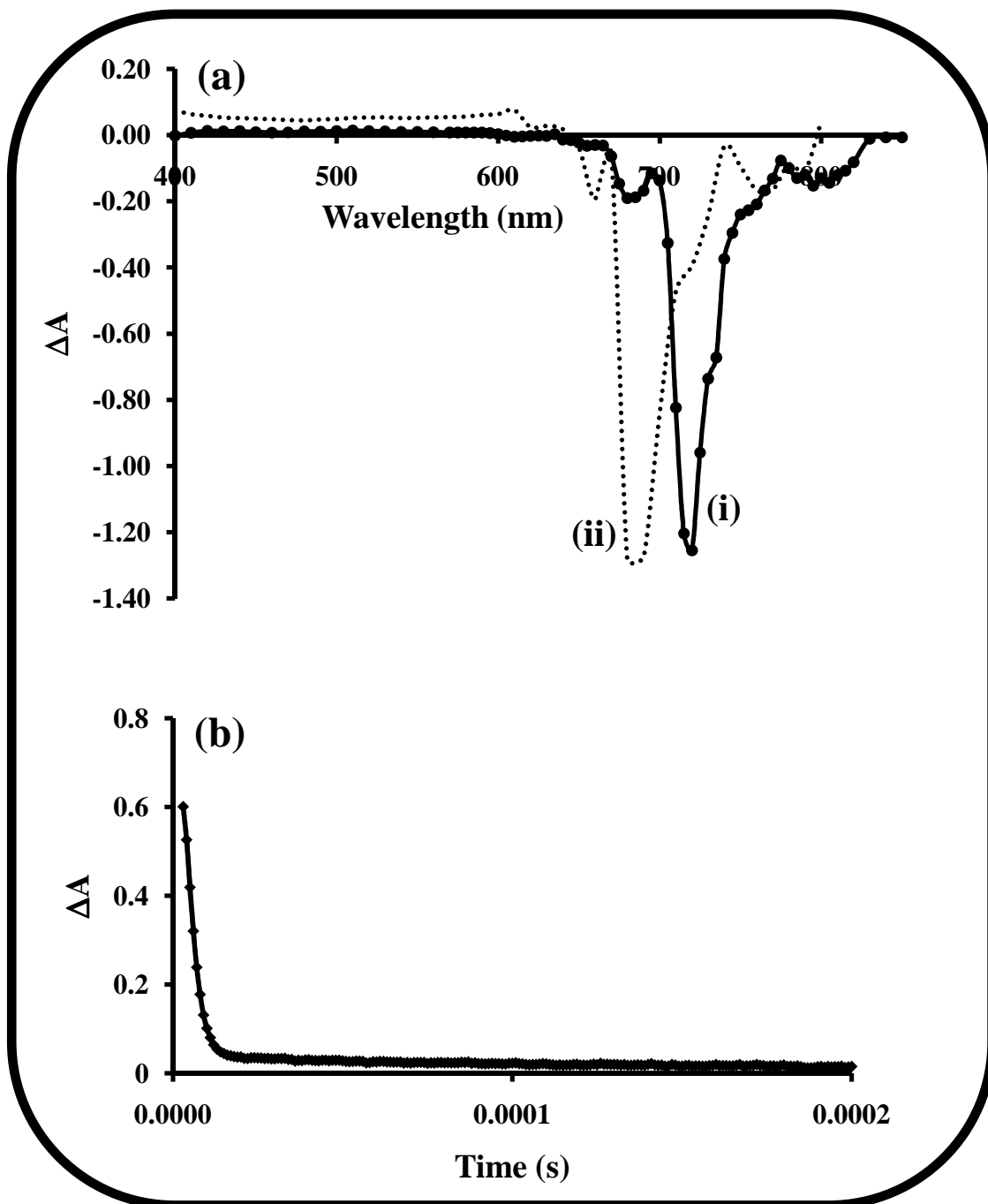


Figure 4.8: (a) Transient absorption spectra of (i) ZnttbIPc (31) and (ii)  $\beta$ -CdTtBuPhPc (26d) in toluene (concentration =  $\sim 2.0 \times 10^{-5}$  M).  $\lambda_{\text{Exc}} = 708$  nm. (b) Triplet decay curve for 26d.



indicating there is no change in the structure of the molecule following excitation. The transient absorption spectra of the aryloxy complexes tend to show peak broadening above 700 nm as shown in Figure 4.8a(ii) for  $\beta$ -CdTtBuPhPc (**26d**). It is believed that the changes in the spectra are a result of symmetry loss, following photoexcitation, as a result of the attachment of flexible  $\sigma$ -bonded substituents (C-O-C bond between phenoxy substituents and the Pc-ring). Twisting of these groups about the  $\sigma$ -bonds distorts the molecules and so a slight loss of symmetry occurs [336]. A similar effect was observed for octaphenoxy zinc phthalocyanine, in which case the twisting of the ring substituents resulted in ground state absorption spectral changes [226]. Phthalocyanines typically show a transient absorption between 450 and 550 nm. The maxima of the complexes studied ranged between 490 and 545 nm. Shown in Figure 4.8b is the triplet decay curve of **31**, which is typical of MPc complexes which obey second order decay kinetics. This is typical of MPc complexes at the high concentrations used ( $> 1 \times 10^{-5}$  M), due to triplet-triplet recombination [337]. The concentrations employed in this work were in this range; hence triplet-triplet recombination is expected. Triplet data was obtained in toluene, DMF and DMSO. The lack of reference standards in  $\text{CHCl}_3$ , THF and DCM prevented the determination of data in these solvents.

MPc complexes in which the strongest spin-orbit coupling is induced should have the highest triplet quantum yield ( $\Phi_T$ ) values. In Table 4.3, the order of variance of  $\Phi_T$  values is consistent with the strengths of the induced spin-orbit coupling in the complexes (when considering the central metal ion), i.e. Hg(II) complexes (**24** and **27a**) show the highest values while Zn(II) complexes (**22** and **25a**) show the least values.

The presence of ring substituents generally brought about increases in  $\Phi_T$  values, implying that the substituents, used in this work, induce spin-orbit coupling.

Since fluorescence and triplet yields are complementary processes, low  $\Phi_F$  values should be accompanied by a subsequent increase in values determined for  $\Phi_T$ , and this trend is generally followed as indicated by the data shown in Table 4.3, with the exception of the benzyloxyphenoxy derivatives **26b**, **28b** and complex **29** which show considerably low  $\Phi_T$  in DMSO, which do not correspond to their low  $\Phi_F$  values (Table 4.3).

In DMF and DMSO, higher  $\Phi_T$  were found for the  $\alpha$ -substituted CdPc derivatives (**28c** and **28d**) than for the corresponding  $\beta$ -substituted derivatives (**26c** and **26d**). However, the value of  $\Phi_T$  for peripherally substituted **26b** is larger than for non-peripherally substituted **28b** in toluene and DMF and are almost equal in DMSO. Larger triplet yields (in DMF and DMSO) were also observed for peripherally substituted **26a** than for the non-peripheral derivative **28a**, suggesting that peripheral substitution, particularly for these complexes, enhances intersystem crossing to the triplet state. In toluene, the  $\Phi_T$  values are also often lower for  $\alpha$ -substituted derivatives (**28b-d**) compared to  $\beta$ -substituted (**26b-d**) ones. In DMF, the substituents follow the same trend as the fluorescence data; in which case the pyridyloxy complexes (**26a** and **28a**) give the largest  $\Phi_T$  values. The overall order of decreasing  $\Phi_T$  values is pyridyloxy > benzyloxyphenoxy > phenoxy  $\cong$  *tert*-butylphenoxy.

There were no huge differences in  $\Phi_T$  values that were obtained for **31** and **32** relative to their corresponding symmetrical counterparts (**29** and **30**) in DMF suggesting little influence of lowering in molecular symmetry. However, both complexes **31** and **32** gave the highest yields in DMSO in comparison to **29** and **30**.

There is a large variation in the values determined in different solvents, from as low as 4  $\mu\text{s}$  to 350  $\mu\text{s}$  (Table 4.3). Phthalocyanines containing heavy central metal ions are expected to exhibit short lived lifetimes.

As expected,  $\tau_T$  values for the Cd(II) (**23** and **26a**) and Hg(II) (**24** and **27a**) complexes are generally lower than those for similar Zn(II) derivatives (**22** and **25a**); this is attributed to the heavy atom effect, which induces intersystem crossing from the excited triplet state to the ground state. Table 4.3 shows that the order of triplet lifetimes with respect to the central metal ions is Zn(II) > Cd(II) > Hg(II), with HgPc (**24**) in DMSO presenting an exception.

In general, ring substituents reduce the lifetime of the molecules in the triplet state, since there is a reduction in the lifetime in going from an unsubstituted molecule e.g. ZnPc (**22**) to the peripherally ring substituted derivatives listed in Table 4.3 in different solvents. This is as a result of the presence of heavy atoms (heavy atom effect) within the modified phthalocyanine structure.

Lifetimes were in general relatively long-lived in DMSO relative to data obtained in DMF and toluene, which may be attributed to the highly viscous nature of DMSO. High viscosity solvents, such as DMSO, cause more efficient deactivation of non-radiative transitions of excited state molecules, which normally occur in response to numerous diffusion-like molecular movements. These diffusion-like movements (which enhance non-radiative deactivation of excited states) are less frequent in DMSO than in DMF and toluene; as a result, triplet lifetimes are longer in DMSO.

Considering the different substituent groups, the *tert*-butylphenoxy substituted CdPcs (**28d** and **26d**) gave the longest lifetimes in DMSO (150  $\mu\text{s}$  and 260  $\mu\text{s}$  respectively) in

comparison to the pyridyloxy [**28a** (40  $\mu$ s) and **26a** (30  $\mu$ s)], benzyloxyphenoxy [**28b** (9  $\mu$ s) and **26b** (30  $\mu$ s)] and phenoxy [**28c** (130  $\mu$ s) and **26c** (190  $\mu$ s)] Cd derivatives.

Following laser irradiation, some of the complexes discussed in this work were partly degraded as depicted by a decrease in absorption intensity in the absorption spectra. In the case of the pyridyloxy-substituted derivatives (**26a** and **28a**), slight broadening and shifting of the spectra, to the red, was observed (Figure 4.9). These changes may be

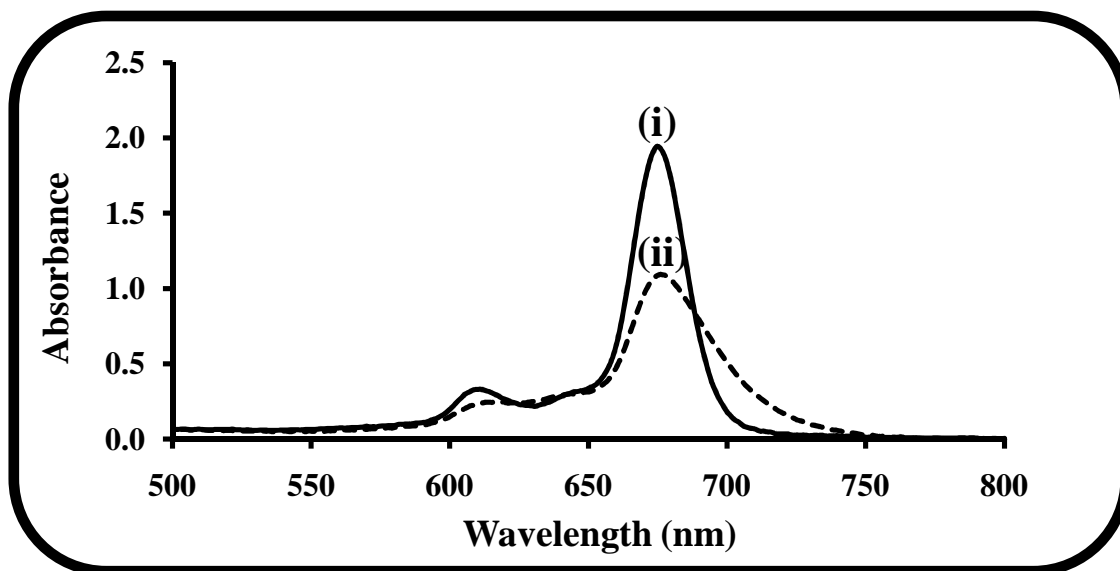


**Figure 4.9:** Absorption spectra of  $\beta$ -CdTPyPc (**26a**), in DMSO, (i) before and (ii) after laser photolysis.

ascribed to photoinduced twisting pyridine groups about the flexible  $\sigma$ -bonds that attach them to the local MPc ring. The extent of this twisting varies with intensity of light applied where more intense light (laser light) results in a more significant drop in intensity and shift in wavelength. The possibility of oxidation or reduction of the complexes was ruled out by the addition of reducing or oxidizing agents after laser

irradiation. The original spectra could not be regenerated by exposure of the final solution to air, the addition of reducing or oxidizing agents or by a change in temperature.

The quantum yields of internal conversion ( $\Phi_{IC}$ ), which deactivates the excited singlet states, have also been calculated (Table 4.3) using Equation 4.4

$$\Phi_{IC} = 1 - (\Phi_F + \Phi_T) \quad (4.4)$$

which assumes that only three intrinsic processes (fluorescence, intersystem crossing and internal conversion) jointly deactivate the excited singlet state of an MPc molecule. However, the data shown in Table 4.3 offers no well defined trend among the complexes.

## 4.4 Singlet Oxygen and Photodegradation Quantum Yields of MPc Complexes

### 4.4.1 Singlet oxygen quantum yields ( $\Phi_{\Delta}$ )

The cytotoxic species, singlet dioxygen ( $^1O_2$ ;  $^1\Delta_g$ ) is believed to be the product of an energy transfer process from the triplet excited state of a metallated phthalocyanine molecule ( $^3MPc^*$ ) to triplet ground state dioxygen ( $^3O_2$ ;  $^3\Sigma_g^-$ ). Using UV-Vis spectroscopy, the absorption decay of a singlet oxygen quencher, 1,3-diphenylisobenzofuran (DPBF), was monitored at  $\sim 416$  nm over a period of time (Figure 4.10) and the values of singlet oxygen generated determined using Equation 4.5 (same as Equation 1.11).

$$\Phi_{\Delta} = \Phi_{\Delta}^{Std} \cdot \frac{R \cdot I_{abs}^{Std}}{R^{Std} \cdot I_{abs}} \quad (4.5)$$

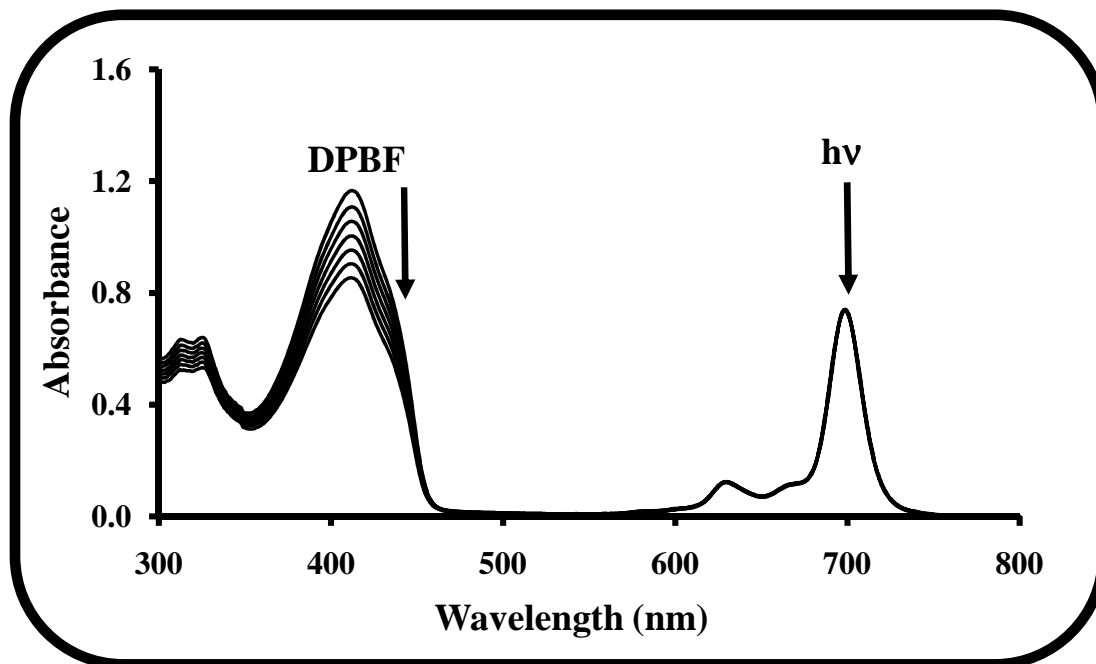


**Figure 4.10:** Typical electronic absorption spectra for the determination of singlet oxygen quantum yield for  $\alpha$ -CdTBzPhPc (28b) in THF (concentration =  $3.4 \times 10^{-6}$  M). DPBF initial concentration =  $\sim 5.0 \times 10^{-5}$  M. Irradiation wavelength =  $670 \pm 20$  nm.

The singlet oxygen quantum yields calculated, in different organic solvents, for the MPc complexes discussed in this work are presented in Table 4.4. No photobleaching effects were observed during the determinations for all compounds in the Q band region.

**Table 4.4:** Singlet oxygen and photodegradation quantum yields of MPcs studied in different organic solvents.

MPc	Solvent	${}^a\Phi_T$	${}^{a,b}\Phi_\Delta$	${}^aS_\Delta$	${}^{b,c,d}\Phi_{Pd} (x 10^{-5})$
ZnPc (22)	Toluene	0.65 <sup>c</sup>	0.58 <sup>f</sup>	0.89	0.19
	CHCl <sub>3</sub>	-	0.57	-	-
	THF	-	0.53 <sup>g</sup>	-	3.05
	DMF	0.58 <sup>h</sup>	0.56 <sup>i</sup>	0.96	2.23
	DMSO	0.65 <sup>j</sup>	0.67 <sup>k</sup>	1.03	2.61
CdPc (23)	DMF	0.77	0.58	0.75	0.19
	DMSO	0.70	0.78	1.11	0.05
HgPc (24)	DMF	0.86	0.57	0.66	0.15
	DMSO	0.87	0.82	0.94	0.09
$\beta$ -ZnTPyPc (25a)	DMF	0.68	0.40	0.59	<sup>c</sup>
	DMSO	0.80	0.46	0.57	<sup>c</sup>
$\beta$ -CdTPyPc (26a)	DMF	0.85	0.64	0.75	<sup>c</sup>
	DMSO	0.83	0.74	0.89	<sup>c</sup>
$\beta$ -CdTBzPhPc (26b)	Toluene	0.82	0.04	0.06	<sup>d</sup>
	CHCl <sub>3</sub>	-	0.02	-	<sup>d</sup>
	THF	-	0.03	-	<sup>d</sup>
	DMF	0.77	0.39	0.51	35.8
	DMSO	0.36	0.23	0.64	<sup>d</sup>

Table 4.4 contd.

MPc	Solvent	<sup>a</sup> $\Phi_T$	<sup>a,b</sup> $\Phi_\Delta$	<sup>a</sup> $S_\Delta$	<sup>b,c,d</sup> $\Phi_{Pd}$ (x 10 <sup>-5</sup> )
$\beta$ -CdTPhPc (26c)	Toluene	0.87	0.32	0.37	0.98
	CHCl <sub>3</sub>	-	0.19	-	4.40
	THF	-	0.31	-	2.72
	DMF	0.40	0.39	0.97	3.55
	DMSO	0.61	0.41	0.67	0.42
$\beta$ -CdTtBuPhPc (26d)	Toluene	0.76	0.33	0.43	0.92
	CHCl <sub>3</sub>	-	0.19	-	3.84
	THF	-	0.27	-	0.07
	DMF	0.41	0.26	0.63	2.47
	DMSO	0.54	0.35	0.65	0.41
$\beta$ -HgTPyPc (27a)	DMF	0.90	0.56	0.62	<sup>c</sup>
	DMSO	0.89	0.78	0.88	<sup>c</sup>
$\alpha$ -CdTPyPc (28a)	CHCl <sub>3</sub>	-	0.50	-	<sup>c</sup>
	THF	-	0.52	-	55.7
	DMF	0.70	0.60	0.86	<sup>c</sup>
	DMSO	0.61	0.44	0.72	61.1
$\alpha$ -CdTBzPhPc (28b)	Toluene	0.51	0.33	0.65	56.3
	CHCl <sub>3</sub>	-	0.26	-	61.5
	THF	-	0.42	-	10.9



Table 4.4 contd.

MPc	Solvent	<sup>a</sup> $\Phi_T$	<sup>a,b</sup> $\Phi_\Delta$	<sup>a</sup> $S_\Delta$	<sup>b,c,d</sup> $\Phi_{Pd}$ (x 10 <sup>-5</sup> )
$\alpha$ -CdTBzPhPc (28b) contd.	DCM	-	-	-	118
	DMF	0.53	0.41	0.77	16.3
	DMSO	0.38	0.31	0.81	9.2
$\alpha$ -CdTPhPc (28c)	Toluene	0.73	0.58	0.79	2.53
	CHCl <sub>3</sub>	-	0.31	-	2.20
	THF	-	0.43	-	4.01
	DMF	0.49	0.42	0.86	3.89
	DMSO	0.66	0.80	1.21	2.86
$\alpha$ -CdTtBuPhPc (28d)	Toluene	0.49	0.40	0.82	1.80
	CHCl <sub>3</sub>	-	0.49	-	3.30
	THF	-	0.44	-	1.67
	DMF	0.56	0.56	1.00	2.13
	DMSO	0.61	0.59	0.97	0.19
$\beta$ -ZnttbPc (29)	Toluene	0.40	0.54	1.35	21.4
	CHCl <sub>3</sub>	-	0.51	-	1350
	THF	-	0.53	-	0.17
	DCM	-	-	-	89.96
	DMF	0.71	0.46	0.65	4.68
	DMSO	0.73	0.55	0.75	0.40

Table 4.4 contd.

MPc	Solvent	<sup>a</sup> $\Phi_T$	<sup>a,b</sup> $\Phi_\Delta$	<sup>a</sup> $S_\Delta$	<sup>b,c,d</sup> $\Phi_{Pd}$ (x 10 <sup>-5</sup> )
$\beta$ -ZnTMPyPc (30)	CHCl <sub>3</sub>	-	0.40	-	3.99
	THF	-	0.47	-	0.04
	DCM	-	-	-	1.67
	DMF	0.74	0.40	0.54	6.26
	DMSO	0.73	0.48	0.66	0.31
ZnttbIPc (31)	Toluene	0.41	0.51	1.24	0.19
	CHCl <sub>3</sub>	-	0.57	-	2.49
	THF	-	0.51	-	0.05
	DCM	-	-	-	0.64
	DMF	0.77	0.45	0.58	1.65
	DMSO	0.82	0.59	0.72	0.07
ZnPc-COOH (32)	CHCl <sub>3</sub>	-	0.49	-	8.37
	THF	-	0.62	-	0.27
	DCM	-	-	-	0.17
	DMF	0.68	0.63	0.93	6.93
	DMSO	0.82	0.64	0.78	0.11

<sup>a</sup>Values undetermined due to lack of reference standards in different solvents for

$\Phi_T$ ,  $\Phi_\Delta$  and  $S_\Delta$ , <sup>b</sup>Values undetermined due to limited solubility,

<sup>c</sup>Phototransformation, <sup>d</sup>No change in absorption intensity with time, <sup>e</sup>[284], <sup>f</sup>[226],

<sup>g</sup>[285], <sup>h</sup>[241], <sup>i</sup>[273], <sup>j</sup>[283], <sup>k</sup>[259].

It is clear from Table 4.4 that CdPc and HgPc derivatives (**23**, **24**, **26a** and **27a**) show higher  $\Phi_{\Delta}$  values than their ZnPc counterparts (though there is not much difference for the unsubstituted derivatives in DMF), which could be ascribed, in principle, to the higher triplet state population in Cd and Hg-containing derivatives (**23**, **24**, **26a** and **27a**). Values for the HgPc derivatives, HgPc (**24**) and  $\beta$ -HgTPyPc (**27a**) are in some cases lower than those of the corresponding CdPc derivatives, considering the same solvent.

Table 4.4 shows that the  $\alpha$ -substituted phenoxy and *tert*-butylphenoxy CdPc derivatives  $\alpha$ -CdTPhPc (**28c**) and  $\alpha$ -CdTtBuPhPc (**28d**) show higher  $\Phi_{\Delta}$  values than their corresponding  $\beta$ -substituted derivatives **26c** and **26d**. The values of  $\Phi_{\Delta}$  were, however higher for the  $\beta$ -substituted complex  $\beta$ -CdTPyPc (**26a**) compared to the corresponding  $\alpha$ -derivative **28a** in DMF and DMSO. The reverse is true for CdTBzPhPc **28b** and **26b**, which follow a similar trend to **28c** and **28d**, where yields are lowest for the peripherally substituted derivative **26b** in all solvents where values could be obtained. The very low  $\Phi_{\Delta}$  values of **26b** compared to **28b** in THF,  $\text{CHCl}_3$  and toluene are due to the partial oxidation and demetallation discussed earlier, with regard to the absorption spectra (Chapter 3). The behaviour of the pyridyloxy and benzyloxyphenoxy derivatives also differs when considering complexes with the same substituent but different point of substitution i.e. **28a** versus **26a** and **28b** versus **26b**. There is a trend towards lower yields for phthalocyanines substituted with benzyloxyphenoxy groups, suggesting that these groups quench the ability of molecules to produce singlet oxygen efficiently.

The singlet oxygen yields of  $\beta$ -ZnttbPc (**29**) and  $\beta$ -ZnTMPyPc (**30**) have been calculated and comparisons made with their corresponding low symmetry derivatives ZnttbIPc (**31**) and ZnPc-COOH (**32**). In the case of **29** and **31**, the highest yields occur in DMSO, with

the lowest values occurring in DMF for both compounds. The singlet oxygen yields for **32** in DMSO, DMF and THF are similar (0.64, 0.63 and 0.62 respectively). Although lower singlet oxygen quantum yields prevail for **30**, compared to **32**, similarly there is not much variation in the same solvents (0.48, 0.40 and 0.47, for DMSO, DMF/CHCl<sub>3</sub> and THF, respectively) (Table 4.4).

Solvent effects on photochemical properties depend on the solvents' polarities and coordinating power. In Table 4.4, there appears to be no distinct trend regarding solvent effects; however  $\Phi_{\Delta}$  values for **28d** increased with an increase in the solvent polarity. Some of the lowest values tend to occur in CHCl<sub>3</sub>, a feature attributed to the protic nature of the solvent. Solvent-singlet oxygen interactions in protic solvents have been found to cause deactivation of the singlet oxygen species formed, hence accounting for the low singlet quantum yields in such solvents [101].  $S_{\Delta}$  (Equation 4.6) gives a measure of the

$$S_{\Delta} = \frac{\Phi_{\Delta}}{\Phi_T} \quad (4.6)$$

efficiency of excitation energy transfer from the triplet state photosensitiser to ground state molecular oxygen. A value close to unity suggests high transfer efficiency. Values could only be determined in toluene, DMF and DMSO, due to the lack of suitable reference standards in CHCl<sub>3</sub>, THF and DCM. Overall there is efficient generation of singlet oxygen as reflected by the  $S_{\Delta}$  values in Table 4.4. The  $S_{\Delta}$  values for some complexes are slightly larger than 1, but within experimental error these values are close to unity.

The data in Table 4.4 reflects generally higher transfer efficiencies for CdPcs substituted at the  $\alpha$ -positions as opposed to those substituted at the CdPc  $\beta$ -positions. Substitution at the peripheral positions possibly results in quenching of the triplet state.

$S_{\Delta}$  values are generally the highest in DMSO which could be related to the lifetimes of the triplet states in this solvent. In DMSO, triplet lifetimes are longer; hence there is more time for diffusional collisions with  $O_2$  ( $^3\Sigma_g^-$ ) than in other solvents, resulting in more efficient energy transfer. The low  $S_{\Delta}$  for **26b** in this solvent may also be due to partial oxidation and demetallation as discussed earlier.

#### 4.4.2 Photodegradation quantum yields

Monitoring the photo-induced decomposition of MPc complexes can be used to determine the stability of these derivatives under intense light. It is especially important when considering phthalocyanines that may be applied as photocatalysts for the degradation of pollutants and transformation of alkenes and alkanes [102,338-340]. The degradation of phthalocyanine molecules often occurs *via* attack by singlet oxygen in an oxidative process [272,274]. It is characterized by the decrease in absorption intensity, in the Q and B band regions, without the appearance of new bands in the visible region or a shift in the maxima on exposure of the MPc to intense light. Figure 4.11 (for ZnPc-COOH **32**) shows typical spectral changes that are observed during the photodegradation of MPcs. Theory suggests that the efficiency of the process should depend on the  $\Phi_{\Delta}$  values. Variations in solvent properties and molecular structure (substituents and central metal) may also be used to account for the photodegradation data ( $\Phi_{Pd}$ ) which is calculated using Equation 4.7 (Equation 1.15).

$$\Phi_{Pd} = \frac{(C_o - C_t)VN_A}{I_{abs}St} \quad (4.7)$$

Data shown in Table 4.4 indicates that photodegradation is generally more pronounced in

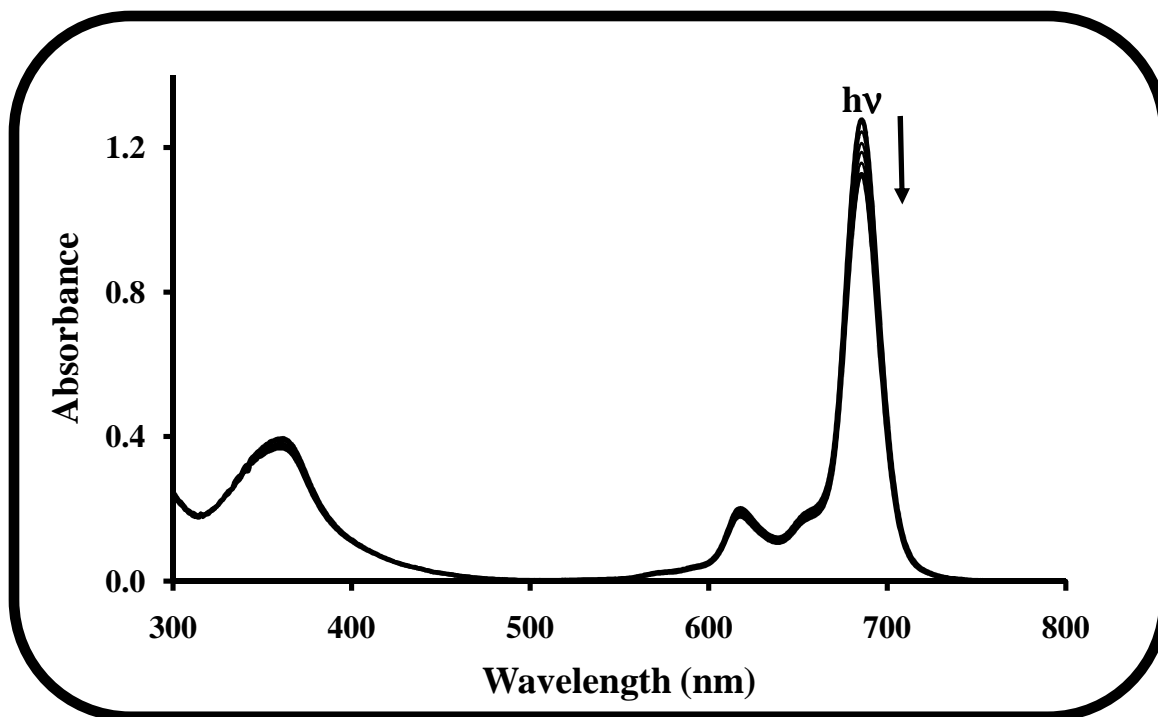


**Figure 4.11: Photodegradation spectral changes of ZnPc-COOH (32) in CHCl<sub>3</sub> (initial concentration =  $\sim 5.0 \times 10^{-6}$  M). Irradiation wavelength =  $670 \pm 20$ .**

chlorinated solvents i.e. CHCl<sub>3</sub> and DCM. The photodegradation quantum yield is particularly pronounced for  $\beta$ -ZnttbPc (**29**) in CHCl<sub>3</sub> ( $\Phi_{\text{Pd}} = 1350 \times 10^{-5}$ ), due to the extremely low basicity of this solvent, which leaves the MPc molecule open to oxidative attack [145,182,278]. Chlorinated solvents also tend to encourage Type I radical photooxidation (Scheme 1.4) which may also account for the significant photodegradation quantum yields in such solvents. DMSO, being a strongly coordinating and highly solvating solvent, is capable of axial coordination to the central metal atom thus partially shielding the Pc from oxidative attack [279]. Thus, the  $\Phi_{\text{Pd}}$  values in DMSO are in general lower in comparison to those in non-coordinating and poorly coordinating solvents such as toluene, CHCl<sub>3</sub>, THF and DCM thus implying higher

photostability of these complexes in strongly coordinating solvents. DMSO is also more basic hence stabilizes the Pc ring against oxidative attack.

Substituents may also confer some stability to the Pc ring. Electron-donating ring substituents enhance the probability of Pc ring photooxidation, while electron-withdrawing groups reduce it [275]. This can be used to account for the values obtained for ZnttbIPc (**31**) and ZnPc-COOH (**32**). The data for these complexes fall within the range expected of stable phthalocyanines, due to the fused imido ring (for **31**) and the terminal carboxyl group of **32** which tend to stabilize the Pc ring against oxidative attack, thus making the Pc entity more resistant to oxidative degradation. The highly electron-donating nature of pyridyloxy and benzyloxyphenoxy groups accounts for the high  $\Phi_{\text{Pd}}$  values for the complexes substituted with these groups i.e.  $\alpha$ -CdTPyPc **28a**,  $\alpha$ -CdTBzPhPc **28b** and  $\beta$ -CdTBzPhPc **26b**. Substituents at non-peripheral positions of the macrocycle are known to result in a stabilizing effect an order of magnitude greater than substitution at the peripheral positions [275]. However, as shown in Table 4.4, the non-peripherally substituted derivatives  $\alpha$ -CdTPhPc (**28c**) and  $\alpha$ -CdTtBuPhPc (**28d**) showed less stability than the corresponding peripherally substituted derivatives  $\beta$ -CdTPhPc (**26c**) and  $\beta$ -CdTtBuPhPc (**26d**) in toluene and THF, but the latter complexes are less stable in  $\text{CHCl}_3$  and conform to no particular trend in DMF and DMSO.

Photodegradation quantum yields could not be expressed as such for the pyridyloxy-substituted derivatives  $\beta$ -ZnTPyPc (**25a**),  $\beta$ -CdTPyPc (**26a**),  $\beta$ -HgTPyPc (**27a**) and  $\alpha$ -CdTPyPc (**28a**), as they underwent a phototransformation process, as indicated by a shift in the Q band maxima (Figure 4.12). These changes depict some distortion of the pyridyloxy-substituted phthalocyanine macrocycle on exposure to intense light. A similar

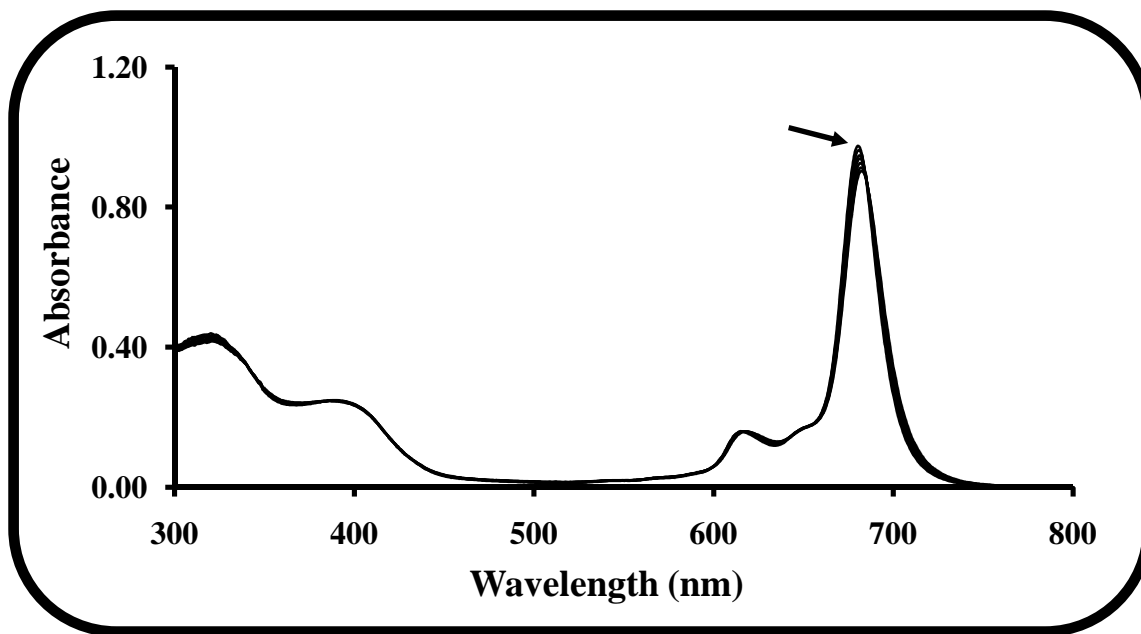


**Figure 4.12: Changes in absorption spectra of  $\alpha$ -CdTPyPc (28a) (initial concentration =  $\sim 1.50 \times 10^{-5}$  M) in DMF on photolysis.**

effect has been observed on exposure to laser light as previously discussed.

Attempts to degrade **26b** in most solvents (toluene,  $\text{CHCl}_3$ , THF, DCM and DMSO) were unsuccessful, with no decrease in absorption intensity. Except for DMSO, these are the same solvents in which **26b** is shown to have unusual or broadened absorption spectra. This suggests that these complexes are very stable, and may be a consequence of the initial partial oxidation mentioned earlier and low  $\Phi_{\Delta}$  values.

## 4.5 Conclusions

The photophysical and photochemical properties associated with the molecules synthesized in this work were determined and found to vary as a function of the central metal ion, substitution position ( $\alpha$  vs  $\beta$ ) and solvent properties. The HgPc complexes show enhanced triplet quantum yields relative to their ZnPc and CdPc counterparts. Non-



coordinating solvents promote the loss of symmetry, which becomes more pronounced upon excitation, while the pyridyloxy substituents were found to experience a similar change in molecular structure owing to their structural flexibility. The oxidizing ability of chlorinated and poorly coordinating solvents was used to account for the unusual spectrum of the benzyloxyphenoxy peripherally substituted CdPc derivative. The same solvent properties have been used to account for the extreme photodegradation quantum yields obtained in these solvents. The photophysical and photochemical parameters of the complexes studied show that they have potential in both industrial applications, as photocatalysts, or in medical applications such as PDT (zinc complexes only, due to the toxicity of the others).

## **5. Interaction of Metallophthalocyanines with Nanoparticles**

**This chapter discusses the interaction between the low symmetry metallophthalocyanines reported in this work and single-walled carbon nanotubes (SWCNT) or quantum dots (QDs) with respect to spectroscopic behaviour and photophysicochemical properties.**

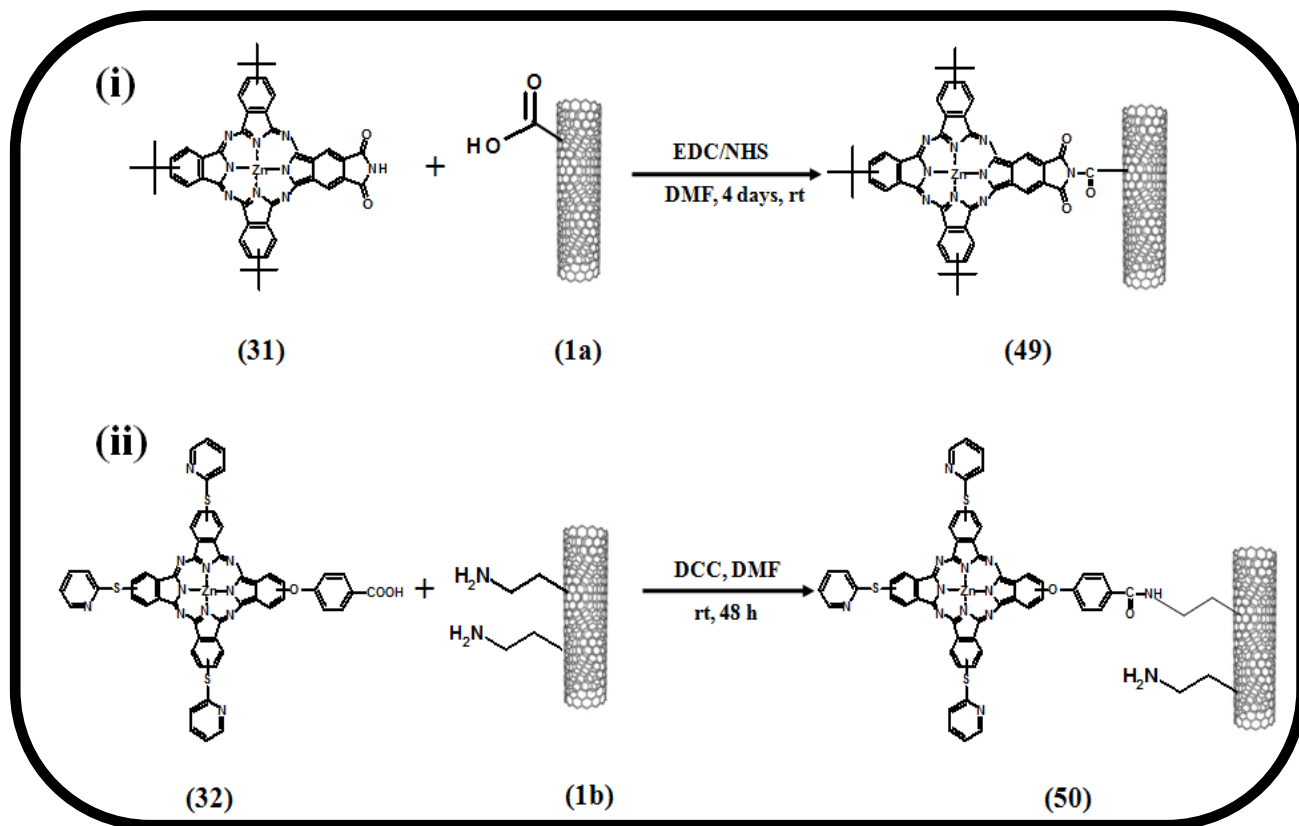
## 5.1 Interaction of Metallophthalocyanines with Single-Walled Carbon Nanotubes

Reports on the use of unsymmetrically substituted phthalocyanines for coordination of carbon nanotubes are rare [33,157,341,342], due to the difficulty in obtaining these complexes. Monosubstitution of phthalocyanines ensures only one linking point of Pc to SWCNT, allowing for a more defined structure of the conjugate. Non-covalent immobilization is often preferred since it is known to preserve the  $\pi$ -network of carbon nanotubes and thus their electronic and catalytic properties [24,26,343]. This work thus aims to explore the synthesis and photophysical properties of two low-symmetry phthalocyanine molecules i.e. ZnttbIPc (**31**) and ZnPc-COOH (**32**), covalently linked to (Scheme 5.1) or adsorbed on (Scheme 5.2) the chemically functionalized SWCNT discussed earlier; SWCNT-COOH (**1a**) and SWCNT-NH<sub>2</sub> (**1b**) respectively. It is possible for more than one Pc molecule to link to the SWCNT, but in each case (**31** and **32**) there is only one functional site on the ZnPc derivative.

### 5.1.1 Synthesis and spectroscopic characterization of MPc-SWCNT conjugates

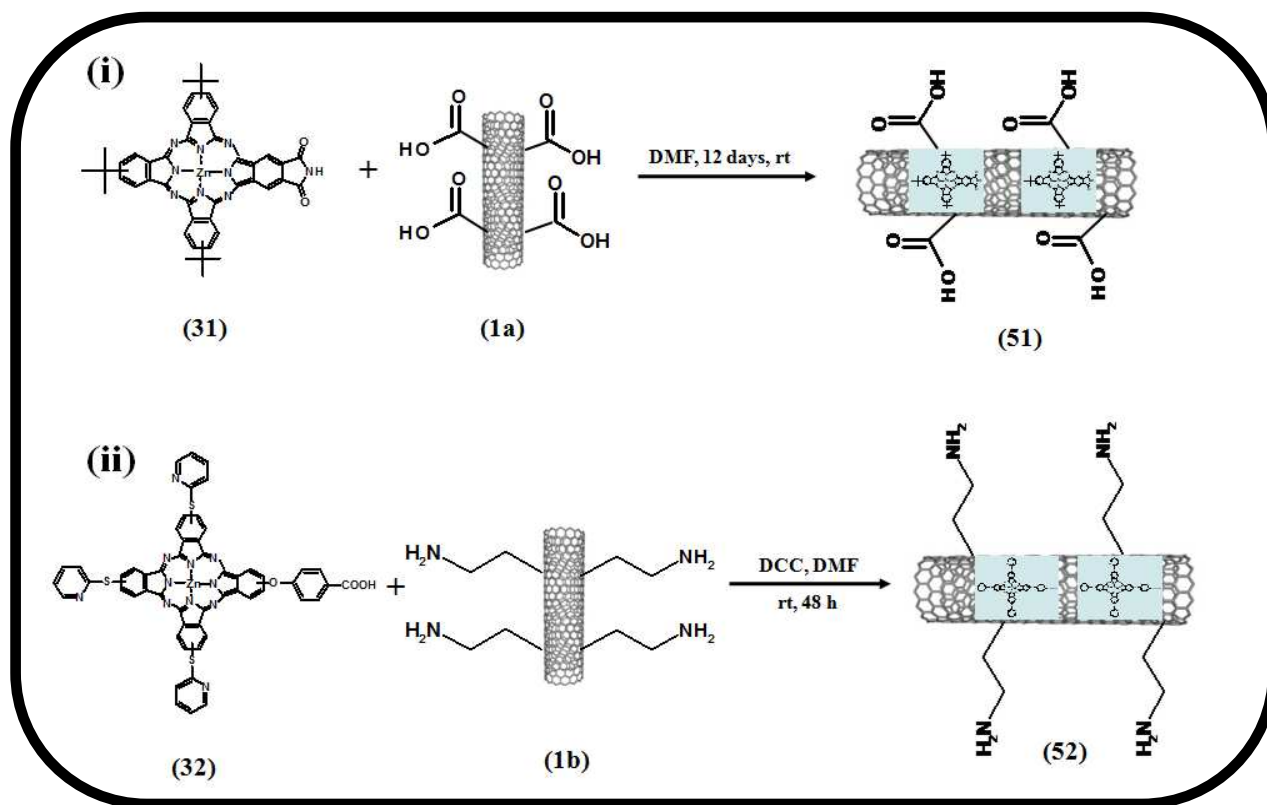
Formation of the linked conjugates ZnPc(**31**)-SWCNT-linked (**49**) and ZnPc(**32**)-SWCNT-linked (**50**) was achieved by making use of either 1-ethyl-3-(3-dimethylaminopropyl) carbodiimide (EDC) or dicyclohexylcarbodiimide (DCC) as coupling agents and facilitate formation of an amide bond between the imide-ring fused Pc, **31** and the carboxylic acid functionalized carbon nanotubes (**1a**) (Scheme 5.1(i)) or between the amine functionalized carbon nanotubes (**1b**) and the mono-phenoxy carboxy group attached to the periphery of complex **32** (Scheme 5.1(ii)) [18]. The adsorbed

complexes ZnPc(**31**):SWCNT-adsorbed (**51**) and ZnPc(**32**):SWCNT-adsorbed (**52**) were obtained *via*  $\pi$ - $\pi$  stacking interactions [24,292], (Scheme 5.2).



**Scheme 5.1:** Synthesis routes to (i) ZnPc(**31**)-SWCNT-linked (**49**) and (ii) ZnPc(**32**)-SWCNT-linked (**50**). Some structural features omitted for clarity. (Structures are not drawn to scale).

FT-IR, UV-Vis and Raman spectroscopy and thermal gravimetric analysis (TGA) were used for characterization of the formed conjugates. The FT-IR spectra of SWCNT-COOH (**1a**) prior to and following linking with **31** are shown in Figure 5.1. The SWCNT, **1a** show two strong bands at 1617 and 1639  $\text{cm}^{-1}$ , Figure 5.1(i). As discussed earlier (Chapter 3), similar bands are observed for the amine functionalized SWCNT, **1b**. Therefore, these bands may correspond either to the carbonyl (C=O) of the carboxylate



**Scheme 5.2:** Synthesis routes to (i) ZnPc(31):SWCNT-adsorbed (51) and (ii) ZnPc(32):SWCNT-adsorbed (52). (Structures are not drawn to scale).

that forms as a result of deprotonation of the weak carboxylic acid groups that terminate the nanotubes (**1a**) or the  $\text{NH}_2$  groups associated with **1b**. Upon reaction of the carboxyl-terminated SWCNT with ZnttbIPc a single broad peak, due to the carbonyl of the resultant amide bond, appears at  $1636\text{ cm}^{-1}$ , Figure 5.1(ii). The shift, relative to the functionalized carbon nanotubes, may be attributed to extended conjugation. The  $-\text{NH}$  stretch that appears at  $3432\text{ cm}^{-1}$  for **49** can be attributed to interaction of the lone pair of electrons associated with the nitrogen atom (involved in the amide bond) and any water molecules that may be present. Residual peaks that appear at lower wavenumbers i.e.  $1260$  and  $797\text{ cm}^{-1}$  are due to **31** alone, Figure 5.1(iii). Shown in Figure 5.2(i), are the IR spectra of **1b** (i), ZnPc-COOH **32** (ii) and ZnPc(**32**)-SWCNT-linked (**50**). As expected,

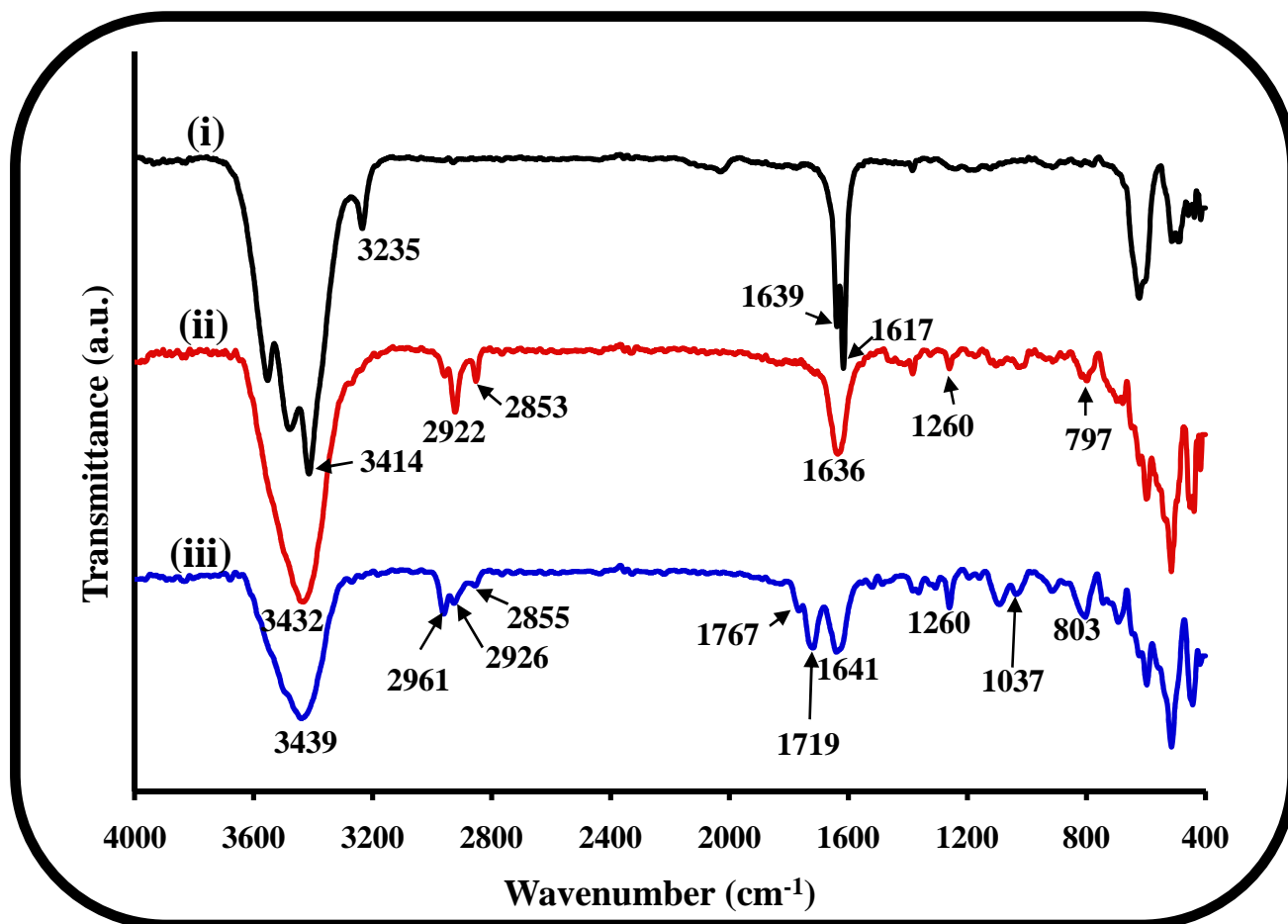


**Figure 5.1:** FT-IR spectra of (i) SWCNT-COOH (**1a**) (ii) ZnPc(**31**)-SWCNT-linked (**49**) and (iii) ZnttbIPc (**31**).

C-H stretches between 2850 and 2922 cm<sup>-1</sup> are present in all species (Figure 5.2) under investigation. Structural variation in going from **1b** to the linked conjugate **50** is confirmed by the differences in the spectral patterns of the two, particularly between 1630-1653 cm<sup>-1</sup> where peaks are found to correspond either to the -NH stretch of the amide bond or the C=O stretch associated with complex **32** or an overlap of the two. The peak at 1653 cm<sup>-1</sup> in ZnPc(**32**)-SWCNT-linked **50** is the higher frequency, C=O stretching, amide I band, typical of primary amides. The second amide II band, is chiefly

N-H bending, and occurs at lower frequencies ( $\sim 1637\text{ cm}^{-1}$ ). The spectrum corresponding to complex **32** shows a broad signal at  $3435\text{ cm}^{-1}$  due to the -OH group of the phenoxy carboxy unit. There are numerous other peaks, characteristic of phthalocyanine macrocycles i.e.  $1385$ ,  $1016$  and  $803\text{ cm}^{-1}$ , which are also evident in the linked conjugate Figure 5.2(iii).

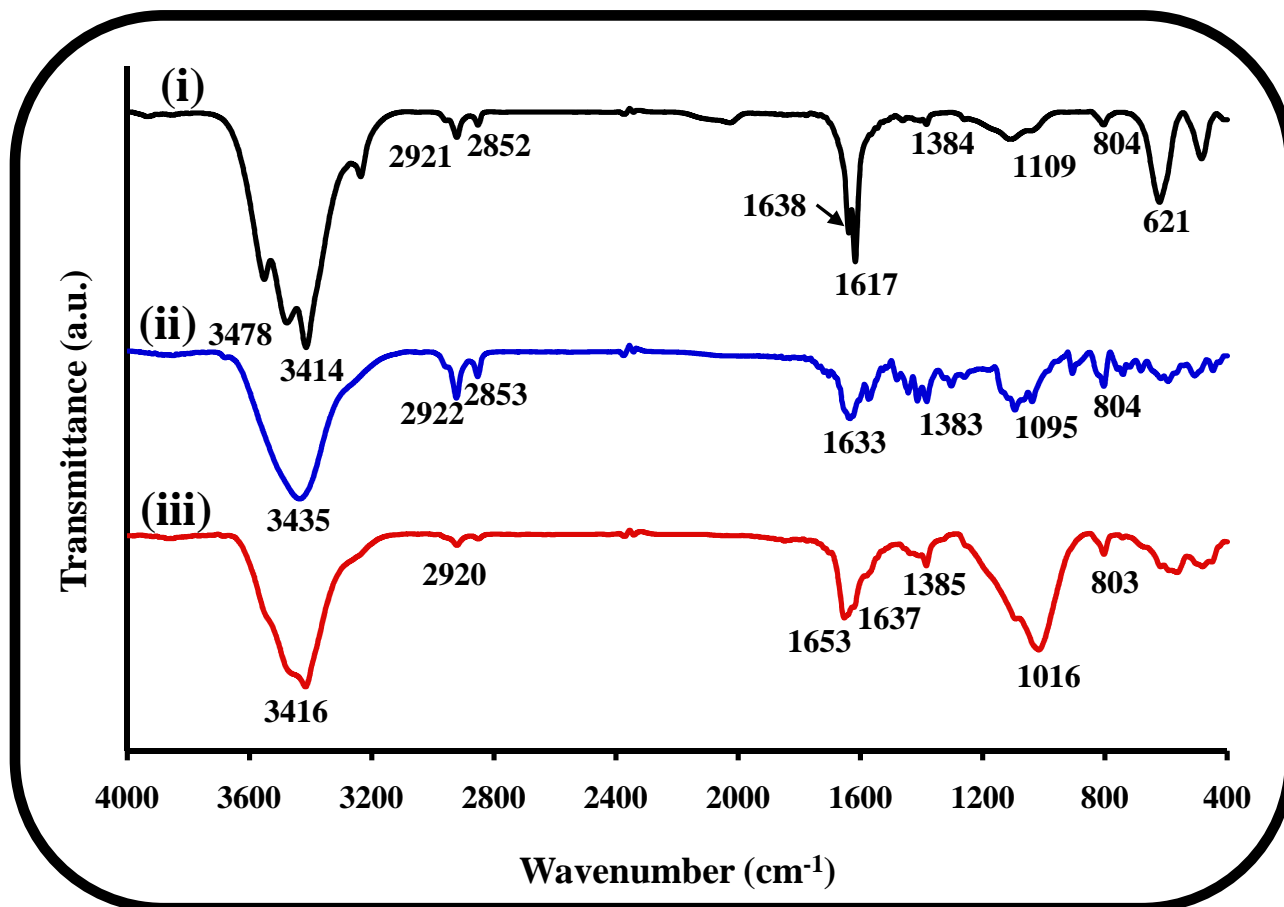
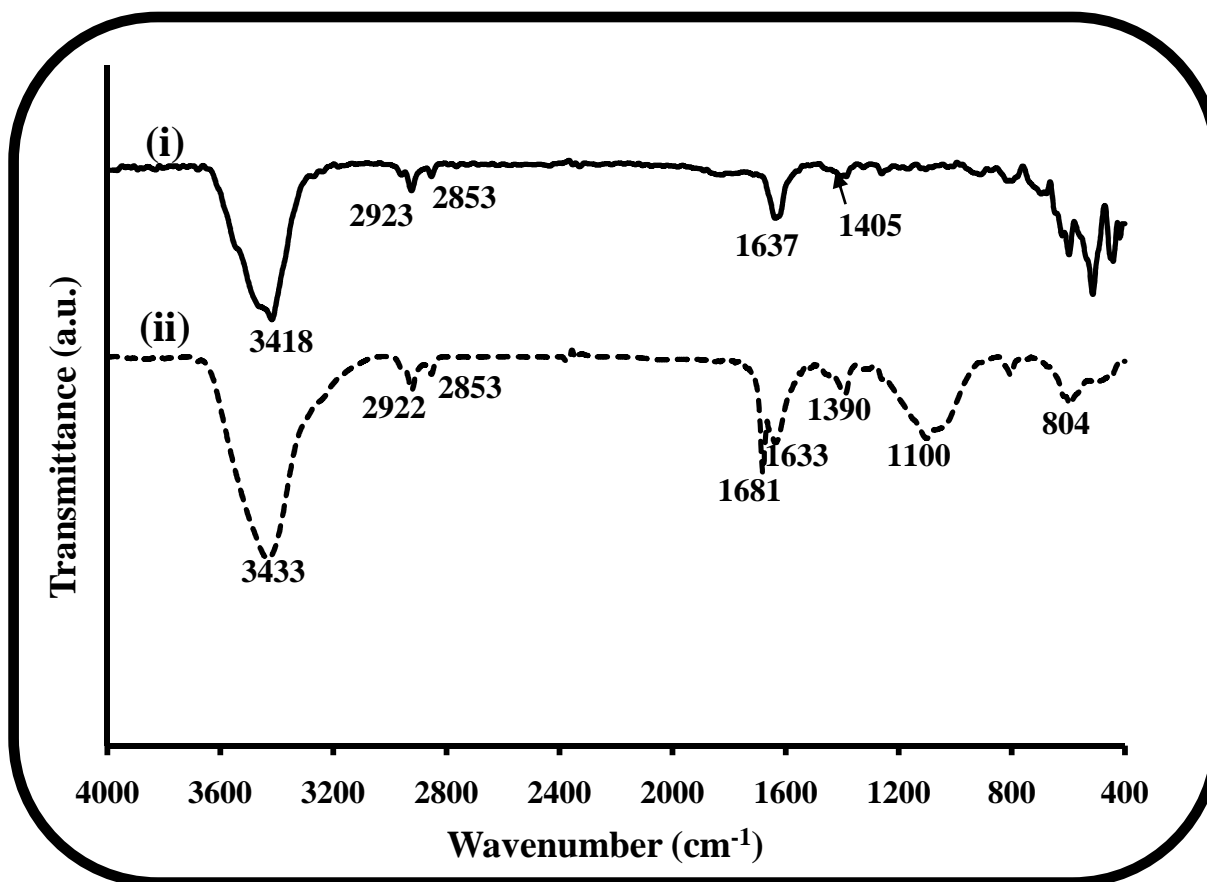


Figure 5.2: FT-IR spectra of (i) SWCNT-NH<sub>2</sub> (**1b**), (ii) ZnPc-COOH (**32**) and (iii) ZnPc(**32**)-SWCNT-linked (**50**).

The IR spectra of the adsorbed complexes **51** and **52** are shown in Figure 5.3. The spectrum of **51** is characterized by peaks at  $3418$  and  $1637\text{ cm}^{-1}$ ; which correspond to the

-COOH functional groups on the nanotube surface. The sharp peaks at 2923 and 2853  $\text{cm}^{-1}$  are representative of the C-H stretches of the *tert*-butyl groups. These peaks are also



**Figure 5.3:** FT-IR spectra of (i) ZnPc(31):SWCNT-adsorbed (51) and (ii) ZnPc(32):SWCNT-adsorbed (52).

clearly evident in the phthalocyanine spectrum (Figure 5.1(iii)), but slightly shifted. The shift of the  $3432\text{ cm}^{-1}$  peak in **49** to  $3418\text{ cm}^{-1}$  in **51** may be a result of electron delocalization due to  $\pi$ - $\pi$  interactions in the latter, i.e. non-covalent functionalization of **31** on **1a** was achieved *via*  $\pi$ - $\pi$  stacking [24,192]. Not much variation exists in the spectral patterns of the linked conjugate **50** and adsorbed **52** conjugates (Figure 5.2 and Figure 5.3); however there are slight peak shifts. For example, the peak due to C-C-C



bending at  $1109\text{ cm}^{-1}$ , in the amine functionalized carbon nanotubes (**1b**), shifts to  $1100$  and  $1016\text{ cm}^{-1}$ , due to extended conjugation on interaction with complex **32**, for the linked (**50**) and adsorbed (**52**) conjugates respectively. The shift from  $1100$  to  $1016\text{ cm}^{-1}$  can further be explained by the different modes of interaction i.e. adsorption versus covalent attachment. The broadening of the peaks in this ( $1000 - 1100\text{ cm}^{-1}$ ) region may be attributed to the interaction between the phthalocyanine macrocycle and carbon nanotube backbone. These observations, though not definite, suggest that **31** and **32** were successfully attached to SWCNT.

The ground state electronic absorption spectra corresponding to pristine **31** (i), pristine carbon nanotubes (SWCNT) (ii), oxidized nanotubes **1a** (iii), **49** (iv), **51** (v) and **31** mixed (without allowing time for adsorption) with **1a** (1:9 w/w) (vi) in DMF is shown in Figure 5.4. A split (due to unsymmetrical nature) Q band with peaks at  $707$  and  $666\text{ nm}$  and a B band at  $357\text{ nm}$  characterizes **31**, Figure 5.4(i), Table 5.1. Not much difference exists in the nature of the spectra of the pristine SWCNT and those functionalized with carboxylic acid groups **1a** Figure 5.4(ii) and (iii). Literature has shown that the absorption spectrum of **1a** consists of broad featureless curves that extend into the near-infrared region [22].

Conjugate **49**, shown in Figure 5.4(iv) has a broadened spectrum in the Q band region, indicating a substantial change in the structure i.e. further evidence for the covalent attachment. The broadening may be a consequence of the chemical bond formation between **1a** and **31**. The linked conjugate, **49** has peaks which correspond to the main absorption bands (Q bands) of the phthalocyanine unit at  $704\text{ nm}$ ,  $665\text{ nm}$  and  $648\text{ nm}$  i.e. evidence for the presence of the phthalocyanine unit, Figure 5.4(iv), Table 5.1. A slight shift in the position of the bands indicates some perturbation of the  $\pi$ -system i.e. some

electronic communication between the electron donating phthalocyanine and the electron-accepting SWCNT [33,344]. A red shift and extensive broadening of the Q band

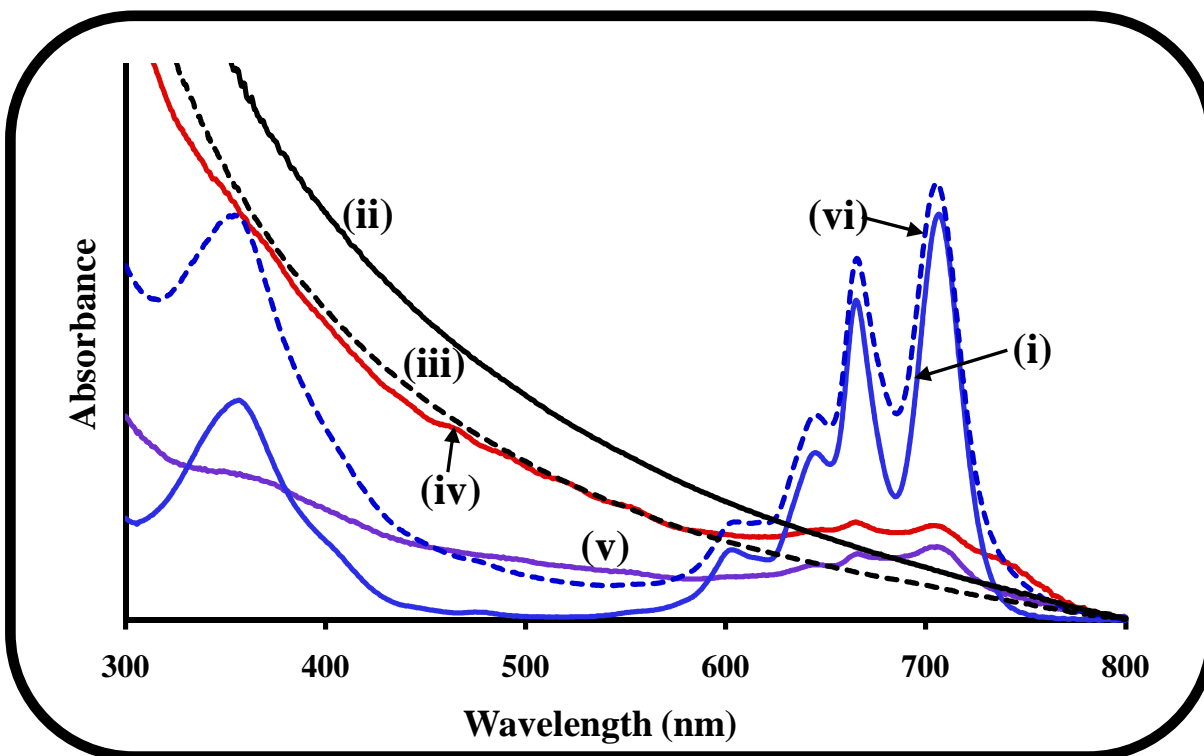


**Figure 5.4:** Ground state electronic absorption spectra of (i) ZnPtIPc (31), (ii) SWCNT, (iii) SWCNT-COOH (1a), (iv) ZnPc(31)-SWCNT-linked (49), (v) ZnPc(31):SWCNT-adsorbed (51) and (vi) ZnPtIPc+SWCNT mixed composite (1:9 w/w) in DMF ( $0.2 \text{ mg ml}^{-1}$ ).

has been reported [345] on coordination of a bisphthalocyanine to SWCNT. The red shift was attributed to strong intramolecular interactions [345,346]. In this work the broadening of the Q band is observed, but the slight shifting is to the blue rather than the red either due to the electron withdrawing nature of the C=O groups attached to the SWCNT or due to aggregation of the phthalocyanine species on interaction with the nanotubes. The spectrum corresponding to the adsorbed species **51**, Figure 5.4(v) is

**Table 5.1:** Absorption and fluorescence properties of linked and adsorbed MPc-SWCNT conjugates.

Compound	Q band $\lambda_{\max}/\text{nm}$	Emission <sup>a</sup> $\lambda_{\text{Em}}/\text{nm}$	Excitation $\lambda_{\text{Exc}}/\text{nm}$	Stokes Shift/nm	$\Phi_{\text{F}}$ ( $\pm 0.01$ )	$\tau_{\text{F}}$ ( $\pm 0.04$ )
ZnttbIPc (31)	707, 666	721	712, 666	14	0.08	1.75
ZnPc-COOH (32)	683	695	685	12	0.25	2.42
ZnPc(31)-SWCNT-linked (49)	704, 665	715	714, 666	11	<0.01 (13.3) <sup>b</sup>	1.75
ZnPc(32)-SWCNT-linked (50)	683	693	687	10	0.04 (6.3) <sup>b</sup>	2.52
ZnPc(31):SWCNT-adsorbed (51)	706, 666	715	713, 667	9	0.01 (7.6) <sup>b</sup>	1.96
ZnPc(32):SWCNT-adsorbed (52)	684	694	687	10	0.06 (4.2) <sup>b</sup>	2.42

<sup>a</sup> $\lambda_{\text{exc}}$  at 610 nm. <sup>b</sup>Values in brackets represent quenching factors  $\left( \frac{\Phi_{\text{F(ZnPc)}}}{\Phi_{\text{F(ZnPc-Linked/Adsorbed)}}} \right)$

similar to that of **49**, Figure 5.4(iv) with peaks at 706 nm, 666 nm and 643 nm. However the adsorbed and linked species also show broadening in the Soret band region due to the presence of SWCNT. A physically mixed (not allowing for time to adsorb) composite of **31** and **1a** shows no marked difference from that of pristine **31**, Figure 5.4(vi).

Figure 5.5 shows the absorption spectra, in DMF, corresponding to complex **32** (i), **1b** (ii), **50** (iii) and **52** (iv). Complex **32** is characterized by a distinct monomeric Q band at

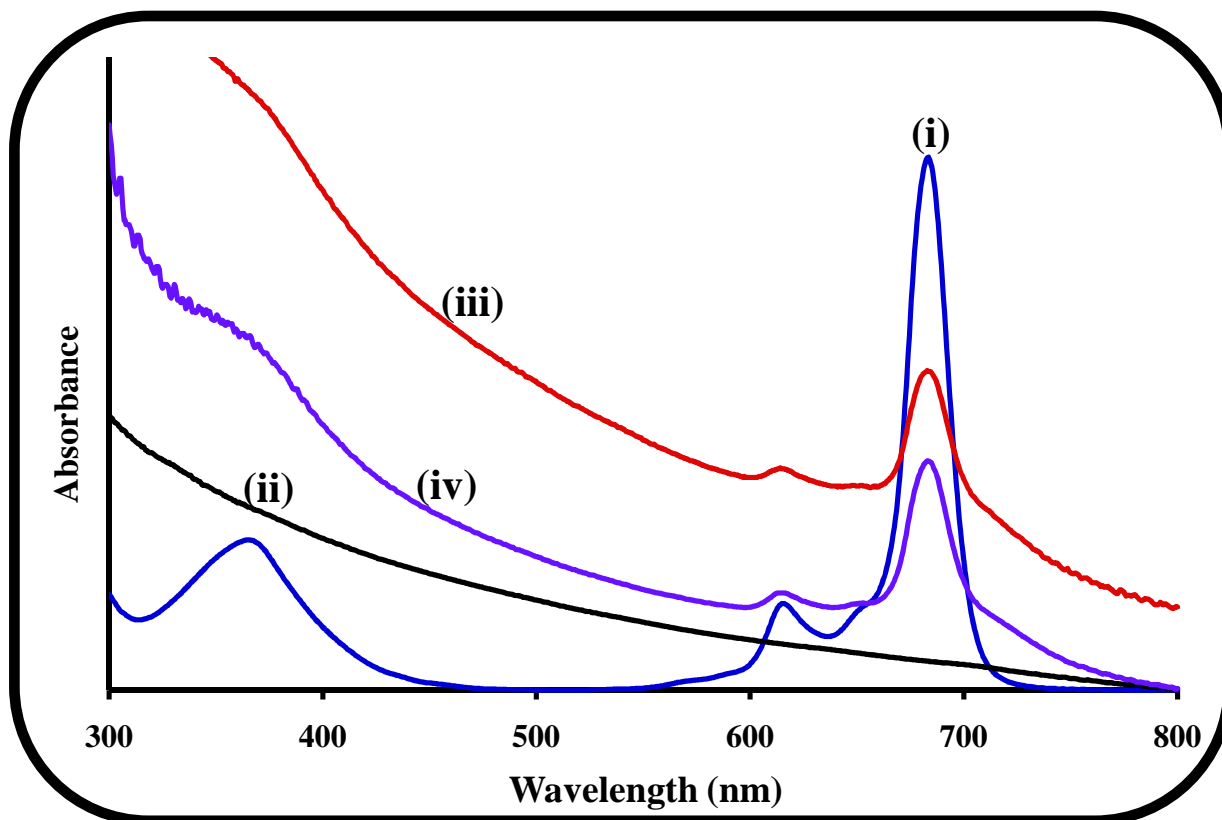


**Figure 5.5:** Ground state electronic absorption spectra of (i) complex **32**, (ii) SWCNT-NH<sub>2</sub> (**1b**), (iii) ZnPc(**32**)-SWCNT-linked (**50**) and (iv) ZnPc(**32**):SWCNT-adsorbed (**52**) in DMF (0.2 mg ml<sup>-1</sup>).

683 nm (Figure 5.5(i), Table 5.1). The presence of this peak in both conjugates (linked and adsorbed) is proof of the presence of the phthalocyanine unit. It appears that the attachment of the amine grouping (attached to the SWCNT), although electron donating, does not exert any significant influence on the absorption spectra of both the adsorbed and linked species i.e. no shifting of the Q band is observed. It is suspected that the amine group alone is insufficient to give such an effect, however the use of a phenylamine functional group may prove slightly more effective [295]. The spectrum corresponding to **1b** is similar to **1a** (Figure 5.4(iii)), expressing no features in the region of interest.

The Raman spectra for the conjugates are shown in Figure 5.6 and Figure 5.7. The Raman spectra obtained for SWCNT **1a**, **49** and **51** (Fig. 5.6), show slight variations in the position of the main features (G band, D band), although small these are significant and point to structurally different materials. The intensity of the D band (relative to the G band) decreases on modification of the SWCNT backbone i.e. from SWCNT to **1a** to **49** and **51**. The opposite effect is observed for **1b**, **50** and **52** (Figure 5.7). However, both events suggest that addition of the phthalocyanine moiety modifies the CNT surface,

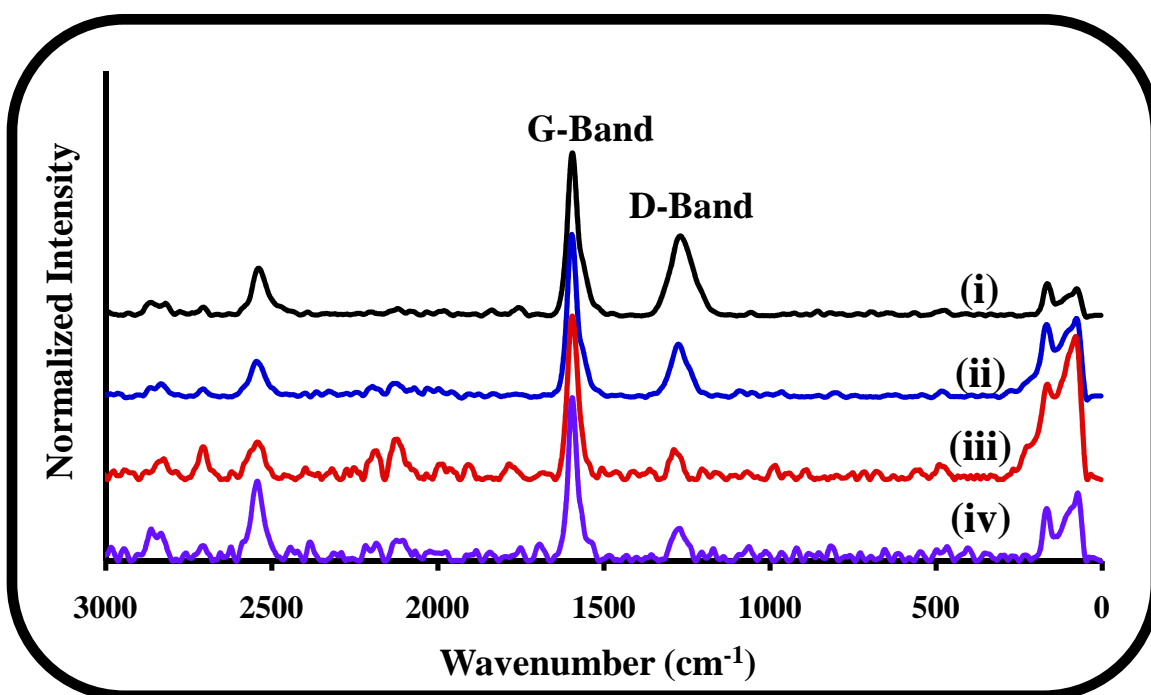


**Figure 5.6:** Raman spectra of (i) SWCNT, (ii) SWCNT-COOH (**1a**) (iii), ZnPc(31)-SWCNT-linked (**49**) and (iv) ZnPc(31):SWCNT-adsorbed (**51**). The intensities have been normalized with respect to the G band.

which may be further evidence for the formation of the adsorbed and linked conjugates. The D:G band ratio gives a measure of the degree of side-wall functionalization. Calculations for the D:G band ratio shows an increase in the ratio on additional

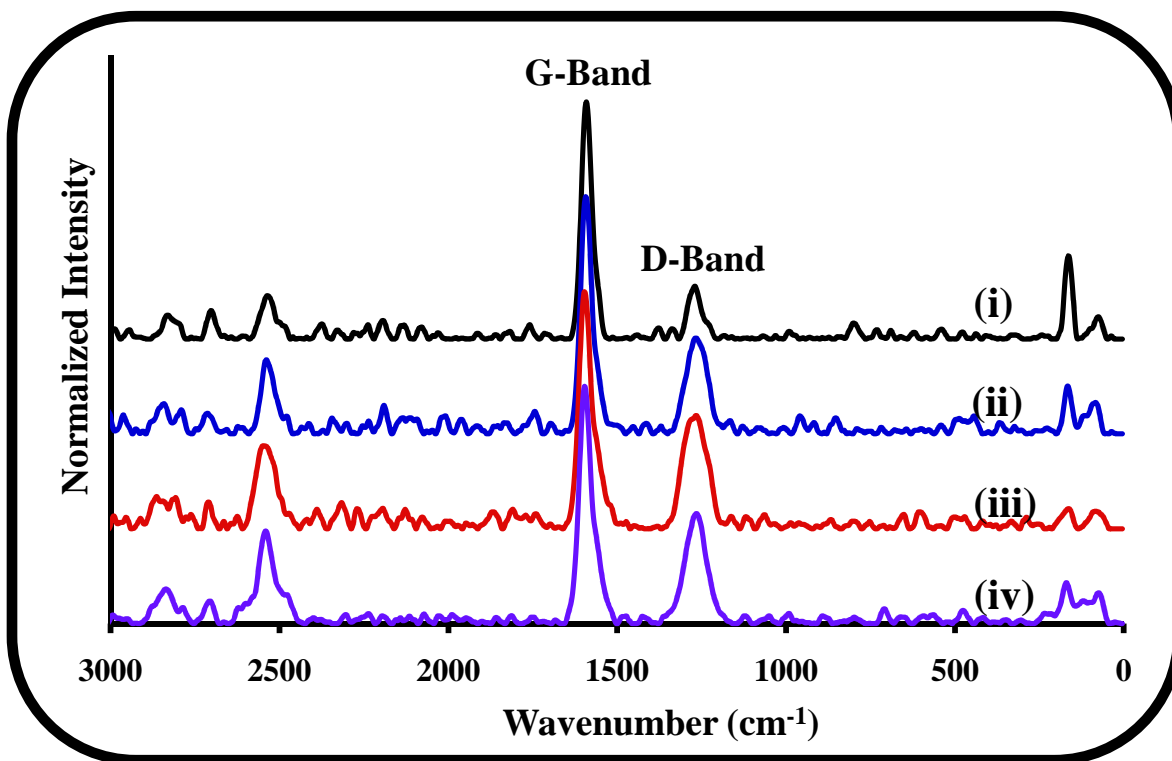


**Figure 5.7:** Raman spectra of (i) SWCNT (ii) SWCNT-NH<sub>2</sub> (**1b**) (iii) ZnPc(**32**)-SWCNT-linked (**50**) and (iv) ZnPc(**32**):SWCNT-adsorbed (**52**). The intensities have been normalized with respect to the G band.

modification with the phthalocyanine moiety, **32** to form the linked and adsorbed units i.e. 0.48 for **50** (Figure 5.7(iii)) and 0.46 for **52** (Figure 5.7(iv)). However, a decrease in the ratio is observed for **49** (0.18, Figure 5.6(iii)) and **51** (0.20, Figure 5.6(iv)). The diazonium approach adopted for amine functionalization, in this work, is specific for side-wall functionalization [7,23,295], whereas the introduction of carboxyl groups occurs primarily at the open ends of the carbon nanotubes [6,9,10]. Therefore, the decrease in the ratio, for **49** and **51** relative to **1a**, may be due to less efficient side-wall functionalization. The ratios of the adsorbed and linked conjugates are however only marginally different.

Structural differences between the functionalized carbon nanotubes (**1a** and **1b**) and the linked (**49** and **50**) or adsorbed (**51** and **52**) conjugates were further confirmed using thermal gravimetric analysis (TGA). It is immediately apparent that the profiles for **31** and the linked (**49**) or adsorbed (**51**) complexes are quite different (Figure 5.8). Weight

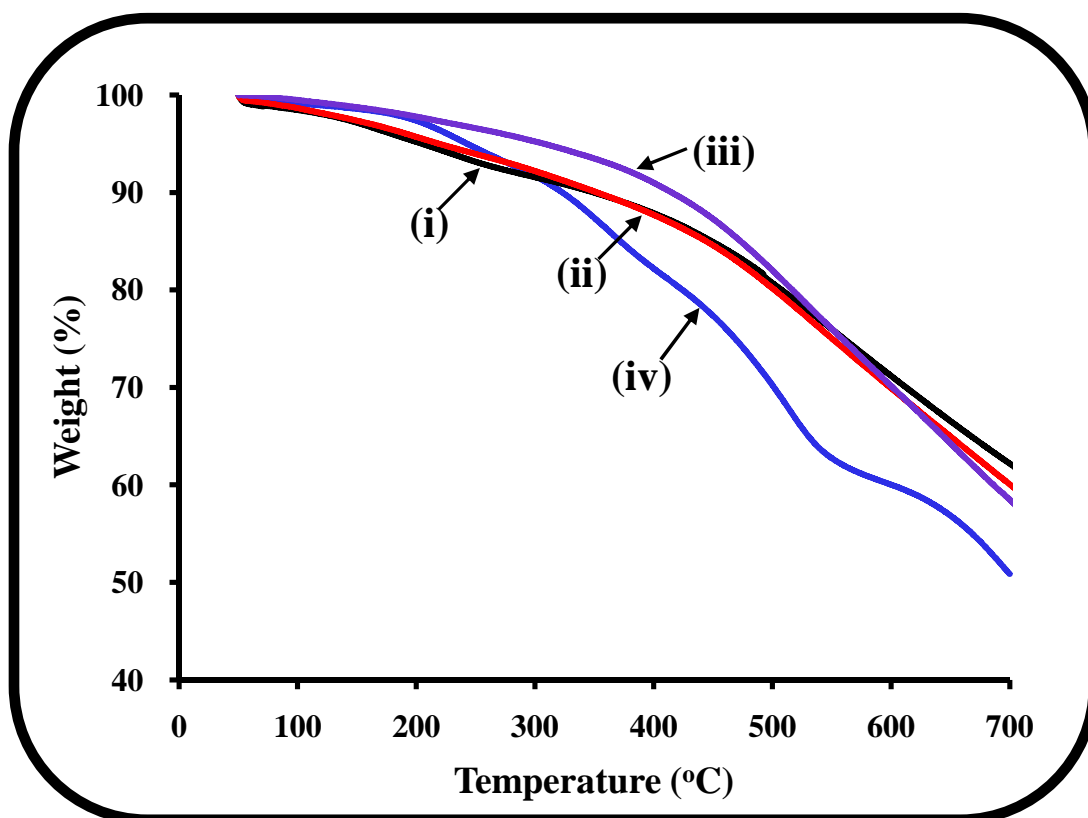


**Figure 5.8:** TGA profiles of (i) SWCNT-COOH (**1a**), (ii) ZnPc(**31**)-SWCNT-linked (**49**), (iii) ZnPc(**31**):SWCNT-adsorbed (**51**) and (iv) ZnttbIPc (**31**) ( $10^{\circ}\text{C min}^{-1}$  under  $\text{N}_2$ ).

loss may be attributed to solvent loss or decomposition of functional groups associated with the molecules involved e.g. carboxyl groups of the oxidized carbon nanotubes or the amino group involved in formation of the amide bond [24,33,157,342]. The thermal decay profile, corresponding to **31** (Figure 5.8(iv)), shows four shallow decomposition

stages. The first step between  $\sim 140$  and  $250^{\circ}\text{C}$  suggests solvent loss. The second and third stages are the main decomposition steps but could also be phase changes. The fourth step is further decomposition but not complete decomposition as it does not reach 0 % at  $700^{\circ}\text{C}$ . The thermal profile of the linked system (**49**, Figure 5.8(ii)) is remarkably similar to that of the functionalized SWCNT (Figure 5.8(i)), with two decomposition steps. The first step ( $\sim 150 - 290^{\circ}\text{C}$ ) could once again be attributed to solvent loss. The second step from  $320^{\circ}\text{C}$  is associated with decomposition. The thermal profile obtained for **51**, Figure 5.8(iii), is markedly different from that for the linked complex (Figure 5.8(ii)) and this difference could be attributed to the presence of a chemical bond in the latter. The SWCNT (not shown in Figure 5.8) decompose to 56 % of their original mass, **1a** to 46 %, **49** to 50 %, **51** to 54 % and **31** decomposes to 49 % at  $700^{\circ}\text{C}$ . Using these percentages the weight loss due to the functional groups may be estimated to be 10 % for **1a**, 6 % for **49** and 2 % for **51**. Using the formula reported in literature [157], the number of functional groups in **1a** was then estimated as 1 per 34 carbon atoms, 1:1120 in **49** and 1:3510 in **51**. The values present a rough estimation since pristine **31** decomposes to 49 %. The low ratio of functional groups to carbon atoms of 1:3510 in **51**, compared to 1:1120 in **49**, is unusual and may be a consequence of the reaction conditions i.e. the process does not facilitate the adsorption of numerous phthalocyanine (**31**) units on the SWCNT surface. This may be in relation to the extent of side-wall functionalization discussed earlier. However, such a low degree of functionalization may be favourable as it preserves the intrinsic electronic properties of carbon nanotubes [33].

The thermal decay profiles corresponding to conjugates formed with **32** and **1b** are shown in Figure 5.9. Similar to the conjugates discussed above, the initial mass loss



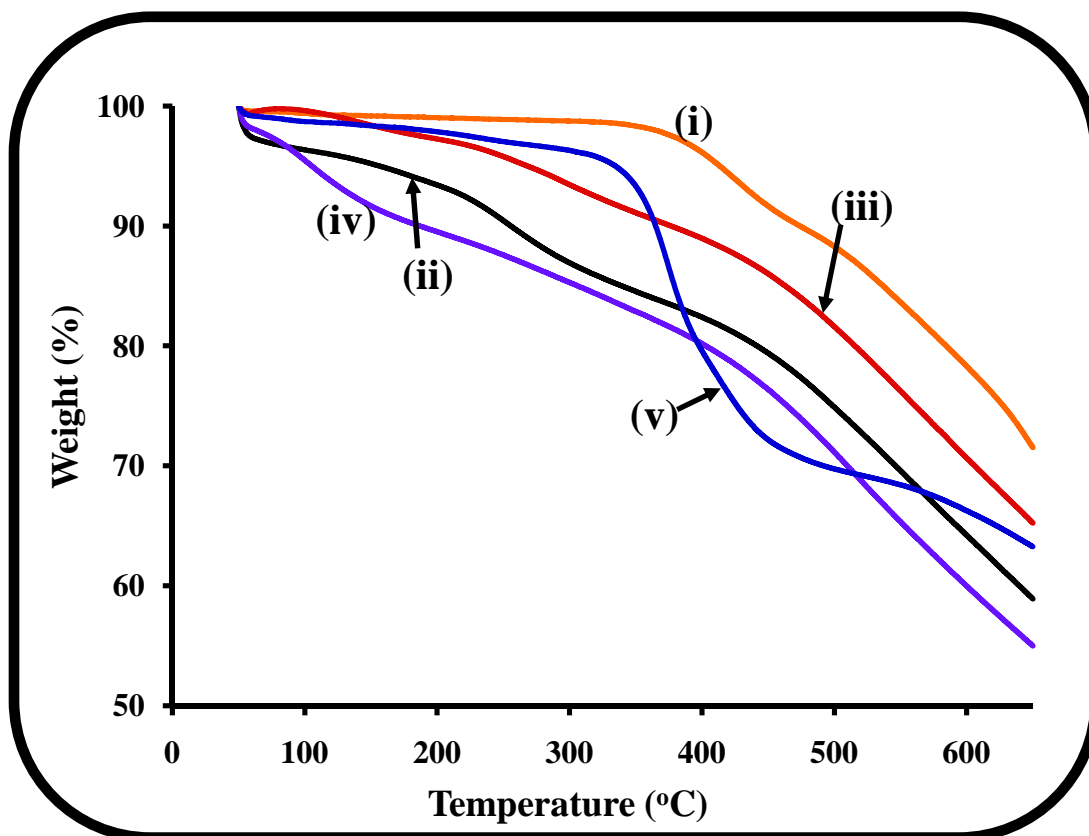


**Figure 5.9:** TGA profiles of (i) SWCNT, (ii) SWCNT-NH<sub>2</sub> (**1b**), (iii) ZnPc(32)-SWCNT-linked (**50**), (iv) ZnPc(32):SWCNT-adsorbed (**52**) and (v) ZnPc-COOH (**32**) (10°C min<sup>-1</sup> under N<sub>2</sub>).

experienced for each sample between 50 and 100°C may be attributed to solvent losses. Any accompanying weight loss, above 200°C may be ascribed to functional group decomposition i.e. of the -NH<sub>2</sub> groups associated with the complexes. The pristine SWCNT decompose to 71 % of their original mass, amine functionalized SWCNT **1b** to 59 %, **50** to 65 %, **52** to 55 % and pristine complex **32** decomposes to 63 % at 650°C. Using these percentages the weight loss due to the functional groups may be estimated to be 12 % for **1b**, 16 % for **52** and 6 % for **50**. Using the same calculation as above [157], TGA results allow an estimate of 1 amine functional group per 37 carbon atoms in

functionalized SWCNT (**1b**), 1:482 in **52** and 1:1430 in **50**. Since **32** alone decomposes only to 63 %, the values above are a very rough estimate. The low ratio of functional group to carbon atoms of 1:1430 for **50** compared to 1:482 for **52** and 1:37 for **1b** suggests that chemical functionalization makes the conjugate stable and results in the presence of fewer ZnPc (**32**) molecules linked to the carbon nanotube surface. The greater decomposition of the adsorbed species relative to the linked, suggests the presence of a larger number of functional groups prone to thermal decomposition. It seems more likely, however, that the presence of a covalent bond in the linked form limits the extent of decomposition attainable, for the same functional groups.

### 5.1.2 Fluorescence spectra, quantum yields and lifetimes

The emission behaviour of complexes **31** and **32** was discussed in Chapter 4. The fluorescence spectra of **31** or **32** linked or adsorbed on SWCNT were obtained by exciting at the same wavelength and at constant absorption (following subtraction of absorption due to SWCNT). This is to avoid inner filter effects which lead to a decrease in the emission intensity as a result of reabsorption of the emitted radiation due to high optical densities, sample turbidity or strong overlap of the absorption and emission spectra [227,248]. The fluorescence emission spectra of all the conjugates, ZnPc(**31**)-SWCNT-linked, **49** (Figure 5.10(ii)), ZnPc(**32**)-SWCNT-linked, **51** (Figure 5.11(ii)), ZnPc(**31**):SWCNT-adsorbed, **50** (Figure 5.10(iii)) and ZnPc(**32**):SWCNT-adsorbed, **52** (Figure 5.11(iii)) show a distinct phthalocyanine Q band emission peak, however the intensity is substantially reduced in the presence of the carbon nanotubes relative to the pristine complexes **31** (Figure 5.10(i)) and **32** (Figure 5.11(i)), a feature which may be

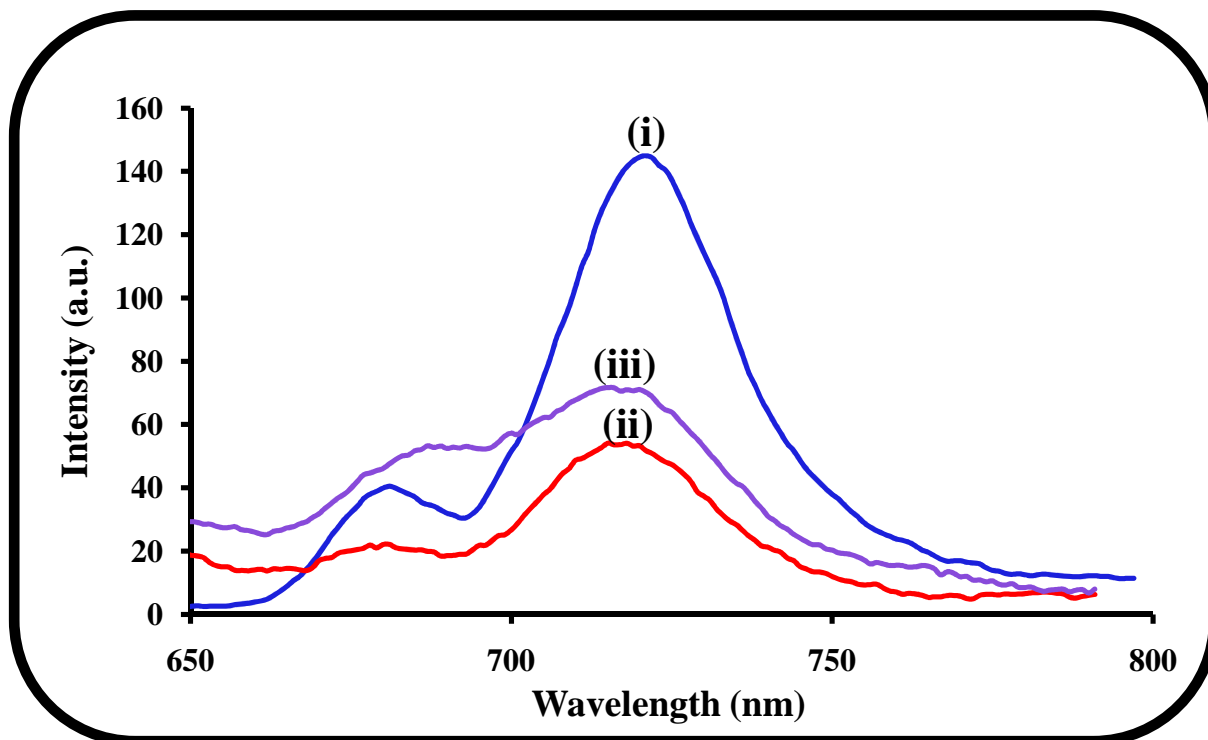


**Figure 5.10:** Fluorescence emission spectra of (i) ZnttbIPc (**31**), (ii) ZnPc(**31**)-SWCNT-linked (**49**) and (iii) ZnPc(**31**):SWCNT-adsorbed (**51**) in DMF. (Curves for **49** and **51** have been corrected for carbon nanotubes absorbance and multiplied by a factor of 10). ( $\lambda_{\text{exc}} = 610 \text{ nm}$ ).

attributed to rapid intersystem crossing (ISC) to populate the triplet state as a result of the heavy atom effect. It is more feasible that this effect is due to an electron transfer mediated process (Figure 5.12) from the electron-donating phthalocyanine moiety to the electron accepting SWCNT resulting in rapid deactivation of the photoexcited phthalocyanine [342] (this was confirmed by the lack of triplet absorption or singlet depletion curves using laser flash photolysis). As already stated, fluorescence in phthalocyanine complexes such as **31** often occurs from the lowest energy vibrational band ( $\nu_0$ ) of  $S_1$  (i.e. a transition from one energy level), resulting in one fluorescence

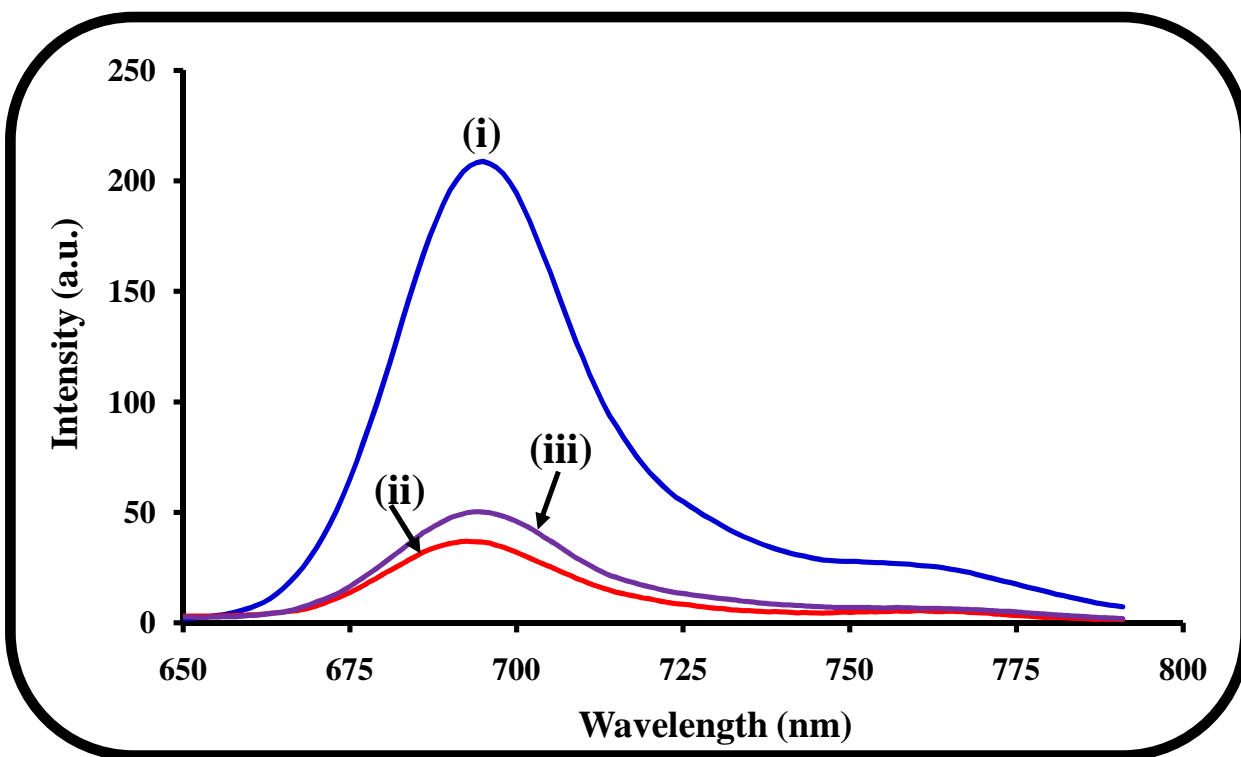


**Figure 5.11:** Fluorescence emission spectra of (i) ZnPc-COOH (**32**), (ii) ZnPc(**32**)-SWCNT-linked (**50**) and (iii) ZnPc(**32**):SWCNT-adsorbed (**52**) in DMF. (Curves for **50** and **52** have been corrected for carbon nanotube absorption). ( $\lambda_{\text{exc}} = 610 \text{ nm}$ ).

peak [101,347]. However transitions from the lowest energy vibrational band ( $\nu_0$ ) to other vibrational levels in the  $S_0$  state can also occur, which accounts for the presence of two peaks in the fluorescence spectra, as in this case; where the fluorescence spectra of **31** (alone, linked or adsorbed) in DMF show two peaks, with the low energy peak being less intense (Figure 5.10), as was also observed in Figure 4.5 (Chapter 4).

The likelihood of an electron transfer mediated process, as shown in Figure 5.12 for conjugates of **31** or **32**, is further expressed by the low fluorescence quantum yields ( $\Phi_F$ ) obtained in the presence of the carbon nanotubes. The absorption contribution of the SWCNT has been accounted for in these calculations in order to ensure that the data

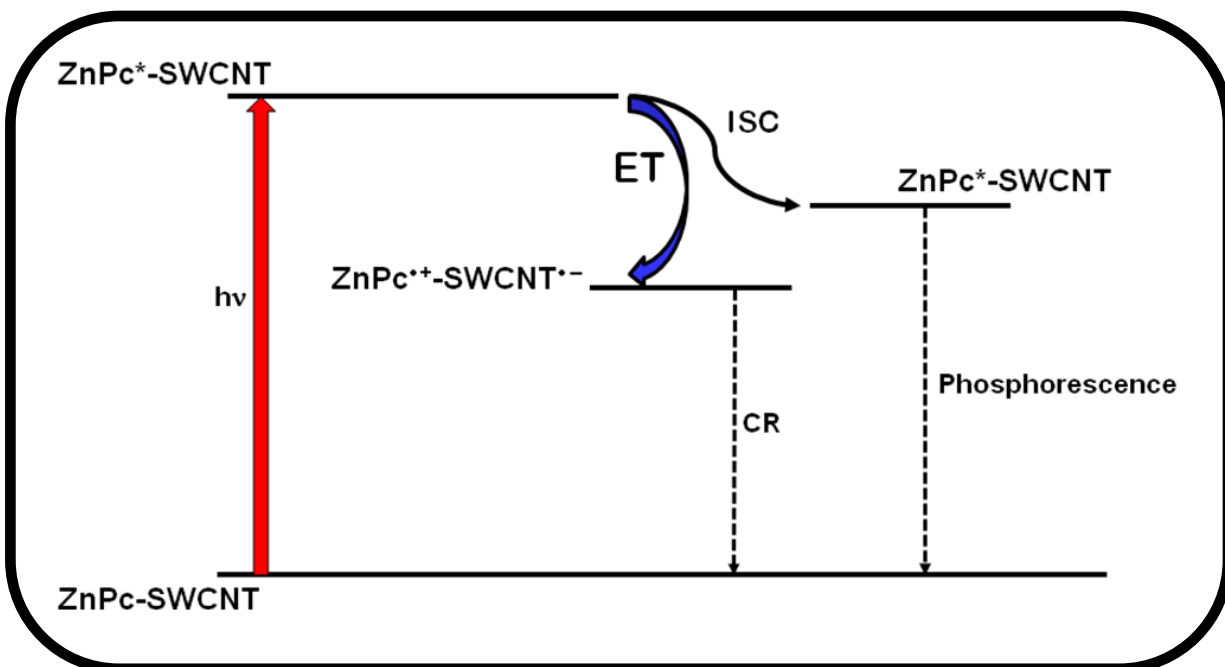


**Figure 5.12: Possible deactivation pathways of ZnttbIPc (31) or ZnPc-COOH (32) upon photoexcitation. (ET = electron transfer, ISC = intersystem crossing, CR = charge recombination).**

expressed refers to the phthalocyanine unit. Comparison of the fluorescence quantum yields ( $\Phi_F$ ) gives quenching factors ( $\Phi_{F(\text{ZnPc})}/\Phi_{F(\text{ZnPc-SWCNT})}$ ) of 13.3 and 7.6 (Table 5.1) for **49** and **51** respectively and 6.3 and 4.2 for **50** and **52**. These values suggest that the interaction that occurs due to the existence of a formal bond between the phthalocyanine unit and the SWCNT is more effective in lowering the quantum yield (as a result of faster electron transfer) as opposed to the  $\pi$ - $\pi$  interaction.

Time-resolved fluorescence measurements indicate a mono-exponential decay for the pristine Pcs **31** and **32**, with fluorescence lifetimes ( $\tau_F$ ) of 1.75 and 2.42 ns respectively (Figure 5.13, Table 5.1). This falls within the range typical for most monomeric metallated phthalocyanines. The lifetime of the Pcs **31** and **32** in the adsorbed and linked

conjugates unexpectedly also showed typical mono-exponential decay curves, with lifetimes that correspond essentially to the presence of free monomeric Pc (Table 5.1). Surprisingly, there was no decrease in lifetimes, for the Pcs in the conjugates.

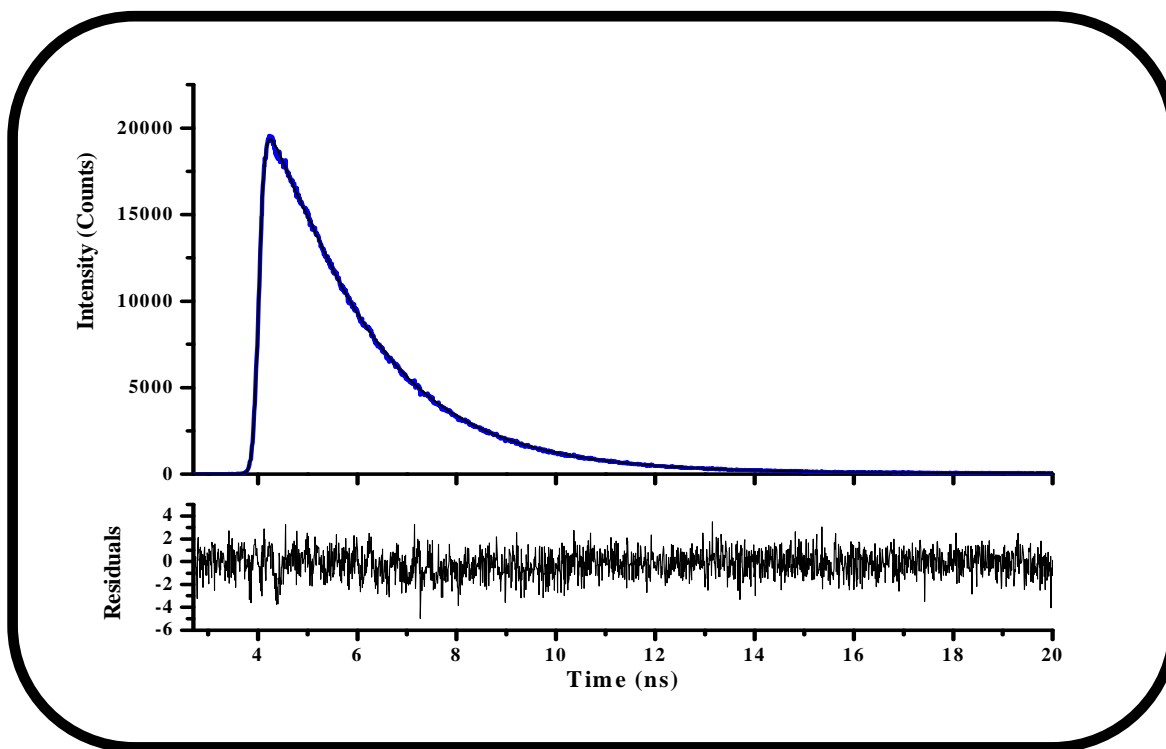


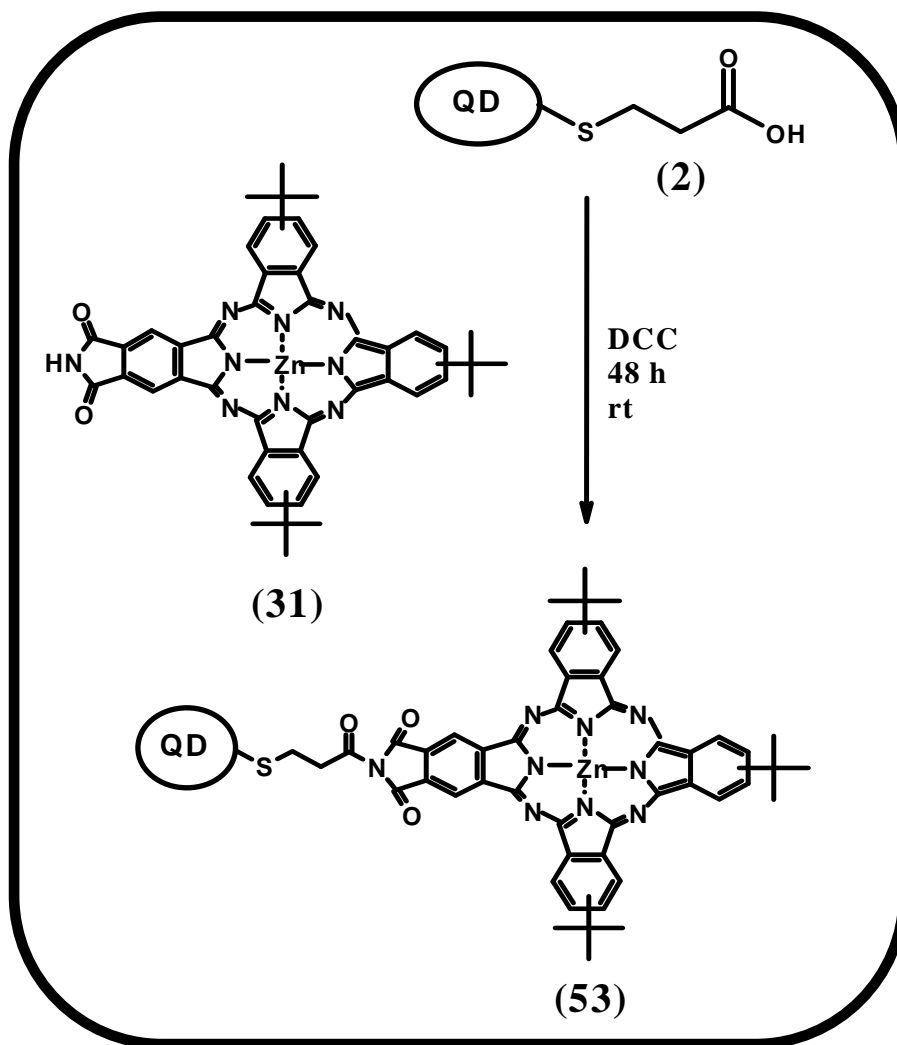
**Figure 5.13:** Fluorescence decay profile for ZnPc(31)-SWCNT-linked (49) in DMF.

## 5.2 Interaction of Metallophthalocyanines with Quantum Dots

The low symmetry complex, ZnttbIPc (**31**) was used in this study. Studies were conducted with a covalently linked conjugate of **31** and the mercaptopropionic acid capped CdTe quantum dots (**2**), formed as shown in Scheme 5.3, and with a mixed conjugate; subsequent studies were used to determine the influence of a covalent bond on the photophysicochemical properties. Studies for these conjugates were performed in a 4:1 (v/v) DMF:water solution to enable solubilization of the quantum dots and phthalocyanine while maintaining the monomeric nature of the phthalocyanine.

### 5.2.1 Synthesis and spectroscopic characterization of MPc-QD conjugates

Studies with the developed CdTe MPA QDs (**2**) were carried out upon coupling of the QDs with ZnttbIPc (**31**) using DCC (a coupling agent often used in organic solvents) to activate the carboxylic acid end of the thiol groups and thus give a linked conjugate,



Scheme 5.3: Synthetic route to ZnPc(31)-QD-linked conjugate (53).

ZnPc(31)-QD-linked (53). In this case the carboxylic acid groups that terminate the (MPA) thiol groups used to passivate the QD surface were linked to the imide group of

**31** via an amide bond (Scheme 5.3). Studies with a mixture of **31** and **2** i.e. ZnPc(**31**):QD-mixed (**54**) were also conducted.

FT-IR spectroscopy gave evidence of the formation of the amide bond for **53**. A broad band at  $1645\text{ cm}^{-1}$  that can be attributed to the carbonyl (C=O) stretch of the resultant amide bond is shown in Figure 5.14(iv). Such a band was not observed for **2** alone, **31** alone or for **54** (Figure 5.14).

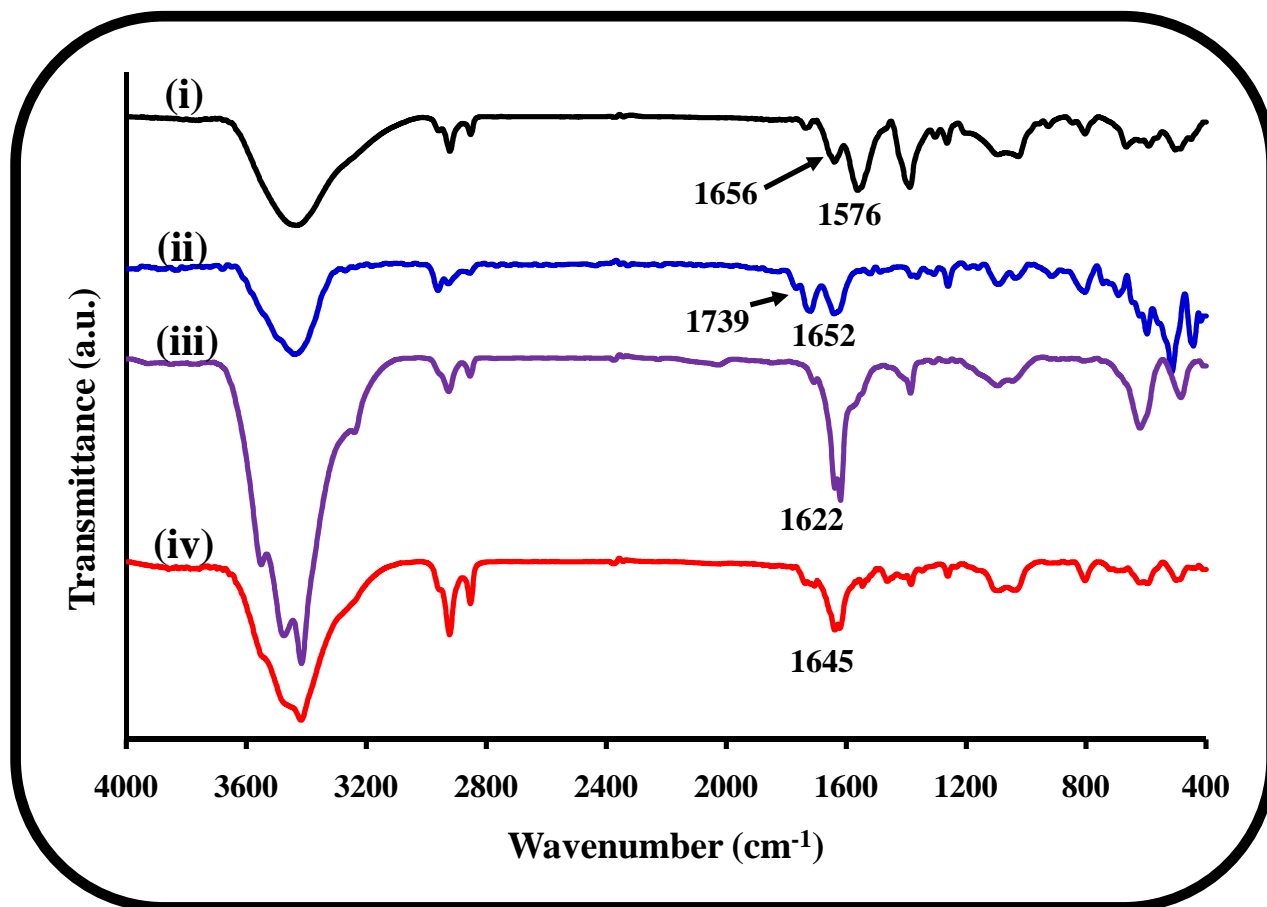


**Figure 5.14:** FT-IR spectra of (i) CdTe MPA QDs (**2**), (ii) ZnttbIPc (**31**), (iii) ZnPc(**31**):QD-mixed (**54**) and (iv) ZnPc(**31**)-QD-linked (**53**).

Raman spectra were additionally employed to characterize the new conjugate, Figure 5.15. The main difference between the linked (**53**, Figure 5.15(iv)) and mixed (**54**, Figure



5.15(iii) conjugates was the position of the main peaks attributed to the phthalocyanine structure at 2851 and 2870  $\text{cm}^{-1}$  respectively. The position of this peak (2870  $\text{cm}^{-1}$ ) in **31** alone (Figure 5.15(ii)) is similar to that in **54**, suggesting minimal structural readjustment; its change in shape for **53** suggests the presence of a change in the molecular structure as a result of bond formation between the QDs and Pc (**31**). Also apparent is the substantial decrease in intensity of the peak due to the QDs at  $\sim 3235 \text{ cm}^{-1}$  (Figure 5.15(i)) in both the mixed and linked conjugates. The peaks at  $\sim 1600 \text{ cm}^{-1}$  in both **31** and **2** also appear reduced in both conjugates.

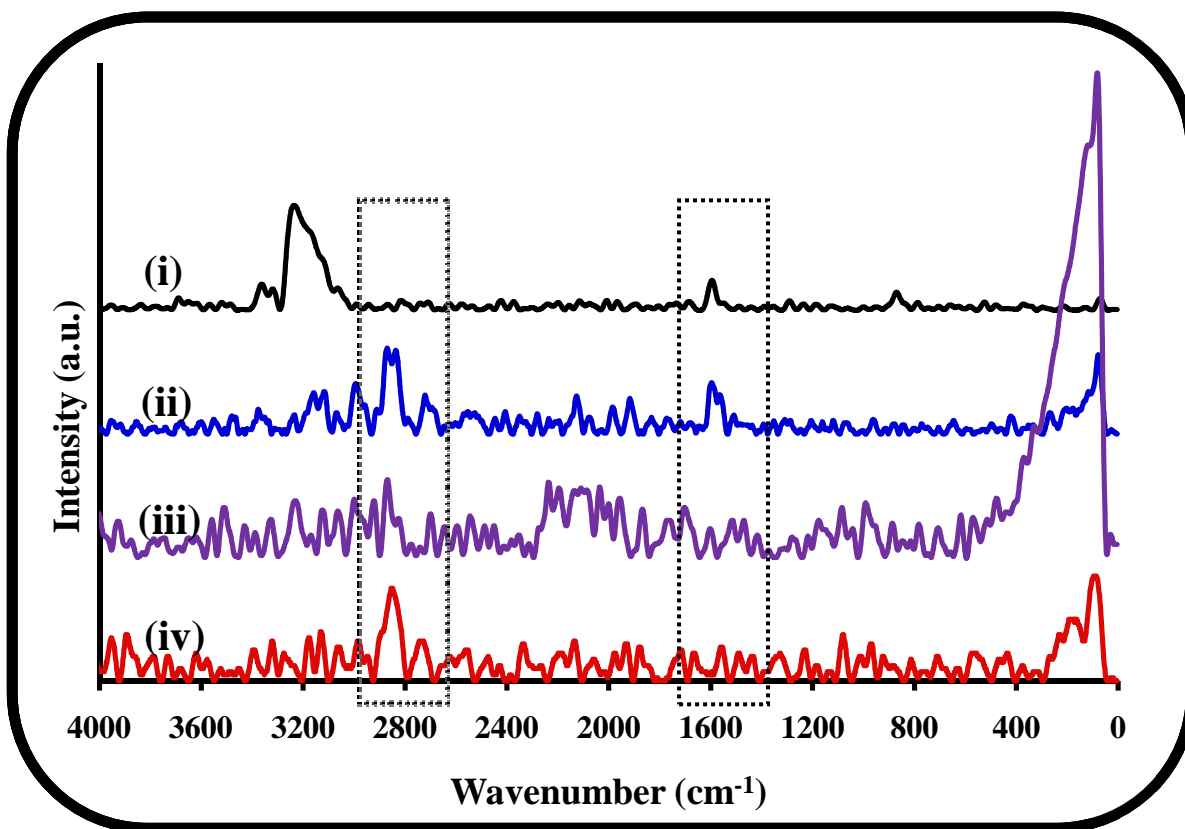
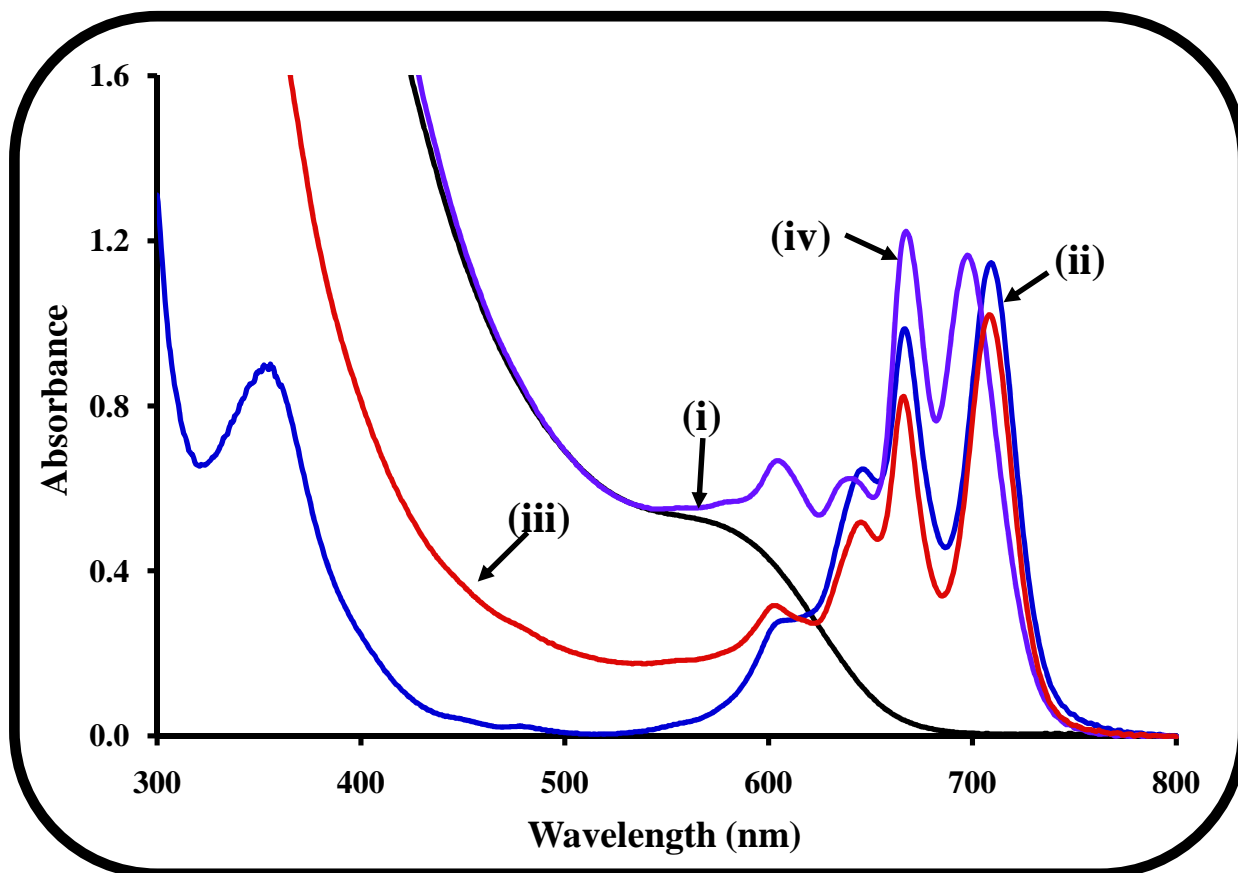


Figure 5.15: Raman spectra of (i) CdTe MPA QDs (**2**), (ii) ZnttbIPc (**31**), (iii) ZnPc(**31**):QD-mixed (**54**) and (iv) ZnPc-QD-linked (**53**).

UV-Vis absorption spectra were used for further characterization of the mixed and linked species in the DMF:water solvent mixture (Figure 5.16). This solvent mixture allows for



**Figure 5.16:** Ground state electronic absorption spectra of (i) CdTe MPA QDs (2), (ii) ZnttbIPc (31), (iii) ZnPc(31)-QD-linked (53) and (iv) ZnPc(31):QD-mixed (54) in 4:1 ( $v/v$ ) DMF:water solution.

solubilization of the quantum dots while maintaining the phthalocyanine in its monomeric form. A split (due to unsymmetrical nature) Q band with peaks at 707 and 666 nm characterizes **31** (Table 5.1). Interestingly there was a shift in the high energy component of the Q band of **54** towards higher energies (707 to 695 nm). This is indicative of non-specific binding of the MPcs onto the surface of QDs. No significant shift in the Q band of **31** was observed on introduction of the QDs for the linked form.

This difference in spectra between the linked and mixed is an indirect way of confirming the linkage. There was an increase in the absorption in the 500 nm region for **53** and **54** due to the presence of QDs. The linked conjugate, **53** shows lower absorption in the 500 nm region than **54**, due to different amounts of QDs in the two. For the mixture (**54**), the interaction is probably in the form of adsorption.

### 5.2.2 Fluorescence quantum yields and lifetimes

Fluorescence quantum yields ( $\Phi_{F(QDs)}$ ) of CdTe MPA QDs (**2**) were calculated using Equation 1.4, also shown as Equation 4.1 and are listed in Table 5.2. The quantum yields of QDs in the linked (**53**) and mixed (**54**) forms are reduced relative to  $\Phi_F$  values of the QDs alone, suggesting that the interaction with **31** results in a quenching of the QD fluorescence. This is a regular occurrence for QDs in the presence of phthalocyanine units [46,154,158,164,165] and the quenching has been attributed to the transfer of energy from donor QDs to phthalocyanine acceptor molecules. This results in a lowering of QD fluorescence intensity, in either a Pc-QD-linked or Pc:QD-mixed species, and therefore a reduction in fluorescence quantum yields of the QDs. Non-radiative (NR) decay processes may also be used to account for the decline in  $\Phi_F$  values. The  $\Phi_F$  of **31** ( $\Phi_{F(ZnPc)}$ ) was calculated to be 0.08 which is the same as the value determined in DMF alone (Table 4.2), hence showing no influence from the presence of water. The  $\Phi_{F(ZnPc)}$  were not determined in the presence of QDs (linked or mixed), since excitation of **31** without exciting the QDs was not possible due to the broad absorption of the QDs. Fluorescence lifetimes ( $\tau_F$ ) have been determined for the QDs alone in NaOH and the 4:1 v/v DMF:water mixture (Table 4.1) as well as for conjugates **53** and **54** (Table 5.3). The

**Table 5.2:** Fluorescence quantum yields and photophysical parameters of ZnttbIPc (31) in the presence of QDs in DMF:water (4:1 v/v). Values in brackets refer to data for 31 alone.

Compound	${}^a\Phi_{\text{F(QDs)}}$	${}^b\Phi_{\text{F(QD)}}^{\text{Linked/Mix}}$	${}^c\Phi_{\text{T(ZnPc)}}^{\text{Linked/Mix}}$	${}^d\Phi_{\Delta(\text{ZnPc})}^{\text{Linked/Mix}}$	$\Phi_{\text{IC(ZnPc)}}^{\text{Linked/Mix}}$	${}^e\tau_{\text{T(ZnPc)}}^{\text{Linked/Mix}}$ ( $\mu\text{s}$ )
ZnPc(31)-QD-linked (53)	0.09	0.02	0.73 (0.77)	<sup>f</sup> (0.45)	0.26 (0.15)	48 (70)
ZnPc(31):QD-mixed (54)	0.09	0.04	0.81 (0.77)	0.53 (0.45)	0.15 (0.15)	15 (70)

${}^a\Phi_{\text{F(QDs)}}$  = fluorescence quantum yield of QDs alone ( $\lambda_{\text{exc}} = 510 \text{ nm}$ );  ${}^b\Phi_{\text{F(QD)}}^{\text{Linked/Mix}} =$

fluorescence quantum yields of QDs (2) in the linked conjugate ZnPc(31)-QD-linked (53) ( $\lambda_{\text{exc}} = 510 \text{ nm}$ ) or in the mixture ZnPc(31):QD-mixed (54) ( $\lambda_{\text{exc}} = 510 \text{ nm}$ );  ${}^c$

$\Phi_{\text{T(ZnPc)}}^{\text{Linked/Mix}} =$  triplet quantum yields of ZnttbIPc (31) in 53 or 54 ( $\lambda_{\text{exc}} = 666 \text{ nm}$ );  ${}^d$

$\Phi_{\Delta(\text{ZnPc})}^{\text{Linked/Mix}} =$  singlet oxygen quantum yields of 31 in 53 or 54 ( $\lambda_{\text{exc}} = 666 \text{ nm}$ );  ${}^e$

$\Phi_{\text{IC(ZnPc)}}^{\text{Linked/Mix}} =$  quantum yields of internal conversion of 31 in 53 or 54;  ${}^f$ Value

undetermined due to weak signal.

data obtained is shown in Table 5.3, which indicates there is not much change for the mixed conjugate, 54 ( $\tau_{\text{F-1}} = 28.6 \text{ ns}$  and  $\tau_{\text{F-2}} = 3.2 \text{ ns}$ ), compared to 26.4 and 3.4 ns for QD alone, for which we expect slightly faster relaxation times due to energy transfer. In this case, there may be numerous QD-Pc interactions, due to random distribution of donor-acceptor (QD-Pc) separations, owing to the lack of a formal bond. Hence, the

presence of numerous acceptors (Pcs) at more than one distance results in complex decays. As a result, the signal is dominated by the free QDs due to the poor interaction. However, the linked conjugate, **53** shows faster decay components which can be explained by the presence of a distinct bond between the QDs and Pc, which enable better interaction between the two and results in extensively quenched lifetimes (Table 5.3), which is a clear indication of energy transfer.

**Table 5.3: Time resolved fluorescence data for CdTe MPA QDs (2) alone and in conjugates 53 and 54 in DMF:water (4:1 v/v).**

Compound	<sup>a</sup> Relative A <sub>1</sub>	$\tau_{F-1}$ (ns) ( $\pm 0.5$ )	<sup>a</sup> Relative A <sub>2</sub>	$\tau_{F-2}$ (ns) ( $\pm 0.3$ )
CdTe MPA QD (2)	0.57	26.4	0.43	3.4
ZnPc(31)-QD-linked (53)	0.21	9.6	0.79	1.7
ZnPc(31):QD-mixed (54)	0.57	28.6	0.43	3.2

<sup>a</sup>A = amplitude of fluorescence decay signal.

### 5.2.3 Förster resonance energy transfer (FRET)

The spectral overlap between the fluorescence emission of the CdTe MPA QDs (**2**) with the absorption spectrum of **31** is shown in Figure 5.17. The QDs in the linked, **53** and the mixed, **54**, form were excited at 510 nm, where **31** does not absorb, and this resulted in a large decline of the QD emission accompanied by stimulated emission of **31** at ~ 720 nm (Figure 5.18(ii)), for **53** and 718 nm (Figure 5.19(ii)), for **54** respectively. This increase in fluorescence emission for **31** in the presence of the MPA-capped QDs infers transfer of

energy, *via* FRET, from **2** to **31**. Although there is stimulated emission for **31** in the linked conjugate (**53**), the extent of this emission is reduced in comparison to the mixed species. This may be attributed to the relative concentrations of **31** and **2** present in solution. This makes any comparisons with the mixed species difficult. No significant

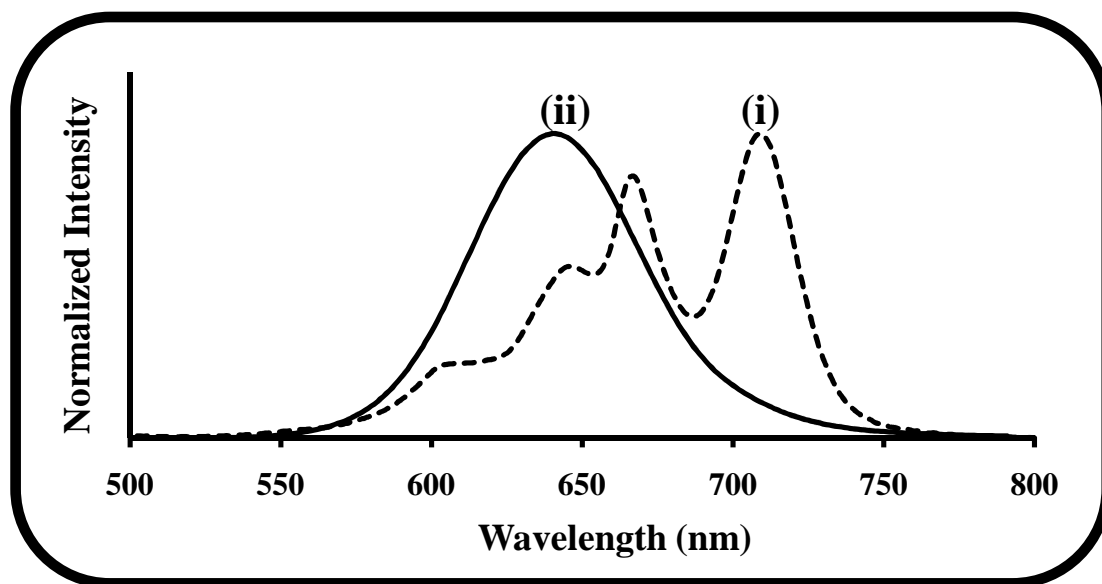


**Figure 5.17:** Normalized ground state electronic absorption spectrum of (i) ZnttbIPc (**31**) and (ii) normalized fluorescence emission spectrum of CdTe MPA QD (**2**) in 4:1 v/v DMF:water solution ( $\lambda_{\text{exc}} = 510$  nm).

emission was observed for **31** alone on excitation at 510 nm (Figure 5.18(iii) and 5.19(iii)). The presence of a second broad band at  $\sim 680$  nm in the emission spectra of QDs, for both the mixed and linked conjugates may be attributed to exposure of surface defects at the QD surface which results in radiative recombination as a result of conjugation [192,348,349]. This may also contribute to the reduction in QD fluorescence intensity [350].

The efficiency with which FRET occurs is known to be dependent on several parameters, namely the spectral overlap ( $J$ ) (Equation 5.1, same as Equation 1.7), the values of which

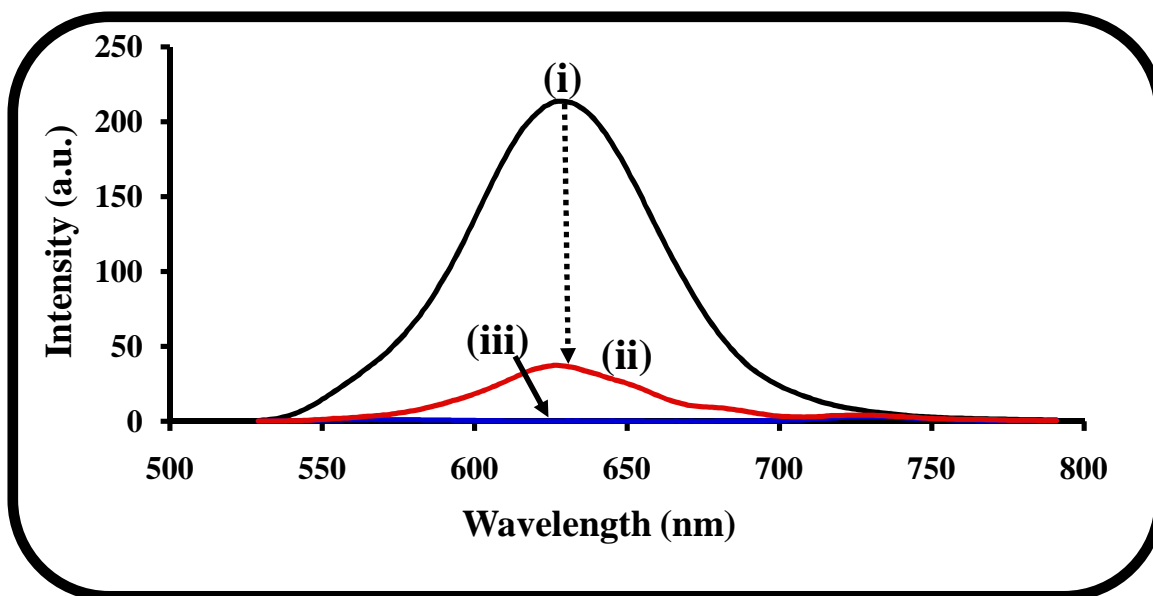


Figure 5.18: Fluorescence emission spectra of (i) CdTe MPA QDs (2) alone, (ii) ZnPc(31)-QD-linked (53) and (iii) ZnttbIPc (31) alone in 4:1  $v/v$  DMF:water solution ( $\lambda_{\text{exc}} = 510$  nm).

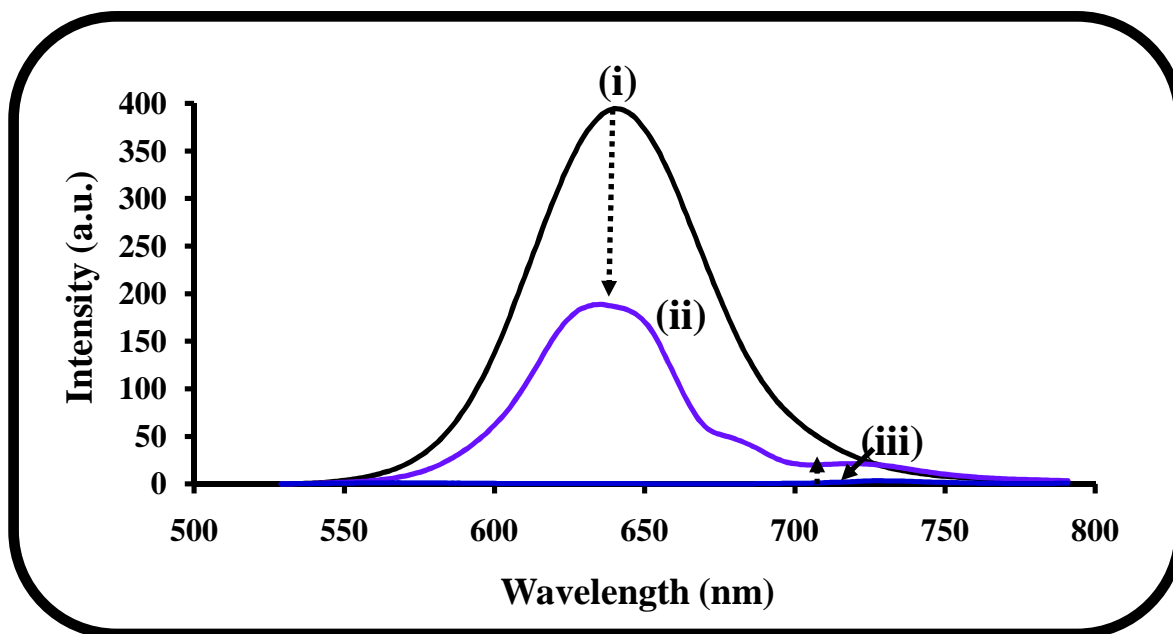


Figure 5.19: Fluorescence emission spectra of (i) CdTe MPA QDs (2) alone, (ii) ZnPc(31)-QD:mixed (54) and (iii) ZnttbIPc (31) alone in 4:1  $v/v$  DMF:water solution ( $\lambda_{\text{exc}} = 510$  nm).

are shown in Table 5.4 are estimated by the overlap of the QD emission and ZnttbIPc absorption (Figure 5.17).

$$J = \int f_{QD}(\lambda)\epsilon_{ZnPc}(\lambda)\lambda^4 d\lambda \quad (5.1)$$

**Table 5.4: Energy transfer parameters for ZnPc(31)-QD-linked (53) and ZnPc(31):QD-mixed (54) interactions in DMF:water (4:1 v/v).**

Compound	$J$ ( $\times 10^{-13} \text{ cm}^6$ )	$R_0$ ( $\times 10^{-10} \text{ m}$ )	$r$ ( $\times 10^{-10} \text{ m}$ )	$Eff_{ss}$
ZnPc(31)-QD-linked (53)	6.40	44.68	34.70	0.82
ZnPc(31):QD-mixed (54)	6.40	44.68	44.08	0.52

The value obtained for the mixed (54) and linked (53) conjugate, is quite large but lies within the expected range found for interactions with other phthalocyanine molecules [154,164,165]. A large  $J$  value is an indication of good spectral overlap and thus enhanced FRET efficiency. The Förster distance,  $R_0$  (Å) is the critical distance between the donor and acceptor molecules for which energy transfer is 50 % [247] is also shown in Table 5.4. The center-to-center separation distance,  $r$  (Å), between donor and acceptor were 44.08 Å and 34.70 Å, for the mixed and linked respectively. These values were calculated using Equation 5.2 (Equation 1.6) and shown

$$Eff_{ss} = \frac{R_0^6}{R_0^6 + r^6} \quad (5.2)$$



in Table 5.4. These values are  $< 80 \text{ \AA}$  which suggests that there is a high probability of energy transfer (FRET) [350] from the synthesized CdTe MPA QDs (**2**) to **31**, and in particular for **55**. The steady state FRET efficiencies ( $Eff_{ss}$ ) shown in Table 5.4, were calculated using Equations 5.3 and reflect relatively high transfer efficiencies i.e. 0.52

$$Eff_{ss} = 1 - \frac{\Phi_{F(QD)}^{Linked}}{\Phi_{F(QD)}} \quad (5.3a)$$

$$Eff_{ss} = 1 - \frac{\Phi_{F(QD)}^{Mix}}{\Phi_{F(QD)}} \quad (5.3b)$$

and 0.82 for the mixed and linked respectively. It appears that the large  $J$  values in combination with the small values of  $r$  result in ease of energy transfer and thus the high transfer efficiencies reflected in Table 5.4. The efficiency determined for **54** is lower than for **53**. In the mixed conjugate, interactions between the QD and Pc occur only through Van der Waals interactions. Therefore energy transfer occurs only through space resulting in lower transfer efficiencies. Similar behavior has been observed for the interaction between SiPcs bearing methyl and *tert*-butyl axial ligands and CdSe QDs [159]. The higher efficiency determined for **53** suggests the amide linkage brings the donor MPA capped QDs (**2**) and the acceptor ZnttbIPc (**31**) into closer proximity (smaller  $r$  than for **54**), resulting in better spectral overlap between the QD emission and Pc absorption and increased interaction, which thus facilitates better FRET. However it is also feasible that the FRET efficiency observed for the linked species is also inclusive of non-radiative processes, due to the strong involvement of surface states that may deactivate the QD fluorophores. Thus the data obtained may not be a true reflection of FRET alone. FRET efficiencies can also be computed based on fluorescence lifetime

measurements of the donor (QDs), in the absence ( $\tau_D$ ) and presence ( $\tau_{DA}$ ) of the acceptor (**31**) by using Equation 5.4;

$$Eff_{tr} = 1 - \frac{\tau_{DA}}{\tau_D} \quad (5.4)$$

However, this equation makes the assumption that the decay of the donor is a single exponential in the absence ( $\tau_D$ ) and presence ( $\tau_{DA}$ ) of acceptor and thus holds rigorously only for a homogeneous system (i.e. identical donor-acceptor complexes) in which the donor and donor-acceptor complex have single-exponential decays [248]. Such single-exponential decays are rare in biomolecules. Thus for donor-acceptor systems decaying with multiexponential lifetimes the energy transfer efficiency must be calculated from the amplitude weighted lifetimes, Equation 5.5;

$$\tau_i = \sum_i \alpha_i \tau_i \quad (5.5)$$

where  $\alpha_i$  is the relative amplitude contribution to the lifetime  $\tau$ . Therefore, in this case the amplitude weighted time constants for  $\tau_D$  and  $\tau_{DA}$ , have been used, to determine the transfer efficiency, for the linked species (**53**), using Equation 5.4. Efficiencies determined, for **53**, by steady state fluorescence and TCSPC were similar at 0.82 (by steady state fluorescence, Table 5.4) and 0.80 (by TSCPC), hence showing the compatibility of the two techniques.

#### **5.2.4 Triplet quantum yields and lifetimes**

The triplet quantum yields of ZnttbIPc (**31**) in the presence of QDs (mixed or linked) are shown in Table 5.2. An increase in ( $\Phi_T$ ) was observed on introduction of the QDs i.e. increase from 0.77 to 0.81 for ZnPc(**31**):QD-mixed (**54**). The increase may be attributed

to the presence of heavy Cd and Te atoms, which encourage ISC i.e. the heavy atom effect. The increase in triplet yield in the presence of QDs has been observed before [154,164,165], Table 5.2. ZnPc(31)-QD-linked (53) gave a slightly lower yield of 0.73. This may be in relation to a lower concentration of phthalocyanine units attached to the QDs as opposed to what may be present in the mixed species.

Figure 5.20 shows the transient absorption spectra of ZnttbIPc (31) in the absence and presence of MPA capped CdTe QDs (2) and indicates not much difference upon excitation with laser light.

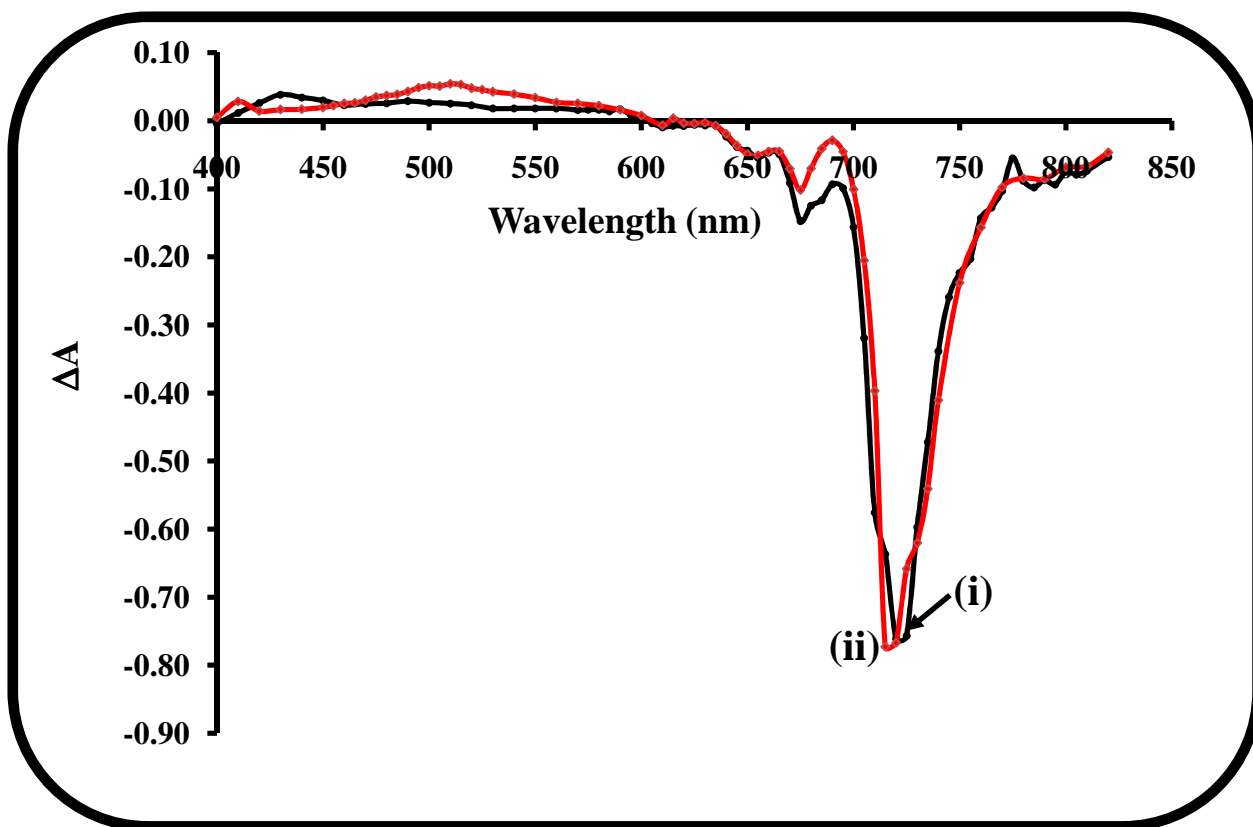


**Figure 5.20:** Normalized transient absorption spectra of (i) ZnttbIPc (31) and (ii) ZnPc(31):QD-mixed (54) in DMF (concentration of 31 =  $\sim 1.90 \times 10^{-5}$  M). ( $\lambda_{\text{exc}} = 666$  nm).

A reduction in the triplet state lifetimes ( $\tau_T$ ) of **31** in **53** and **54** may be related to the increase in size as a result of conjugation and the presence of heavy atoms such as Cd and Te.

There is an increase in  $\Phi_{IC}$  value for **53** ( $\Phi_{IC} = 0.26$ ) compared to that for **31** alone ( $\Phi_{IC} = 0.15$ ), while for the mixed complex **54** there is no change in  $\Phi_{IC}$  value ( $= 0.15$ ); this suggests that ZnttbIPc molecules become more deactivated through internal conversion as a result of linking to the CdTe MPA QDs.

### 5.2.5 Singlet oxygen quantum yields

Singlet oxygen quantum yields were determined using Equation 5.6 (Equation 1.13), with

$$\Phi_{\Delta} = \Phi_{\Delta}^{Std} \cdot \frac{A \cdot I^{Std}}{A^{Std} \cdot I} \quad (5.6)$$

a decay curve as shown in Figure 5.21. Excitation was at 666 nm where ZnttbIPc (**31**) absorbs. In the presence of CdTe MPA QDs i.e. ZnPc(**31**):QD-mixed (**54**), the singlet oxygen quantum yields were found to increase slightly, suggesting that the QDs enhance the transfer of energy from the triplet excited state of **31** to ground state molecular  $O_2$ . In general, QDs alone do not produce significant amounts of  $^1O_2$  (1 %) [351]. However they exert some influence on the singlet oxygen generating capabilities of complex **31**. The efficiency of singlet oxygen generation is dependent on the amount of molecules that populate the triplet state i.e. triplet quantum yield ( $\Phi_T$ ) and their lifetime in this state (triplet lifetime,  $\tau_T$ ). High triplet yields and long lifetimes encourage increased molecular interactions between the triplet state of the photosensitizer (**31**) and ground state oxygen resulting in higher singlet oxygen yields. Therefore the higher  $\Phi_{\Delta}$  for **54** relative to **31** alone may be in response to higher population of the triplet state, as discussed above,

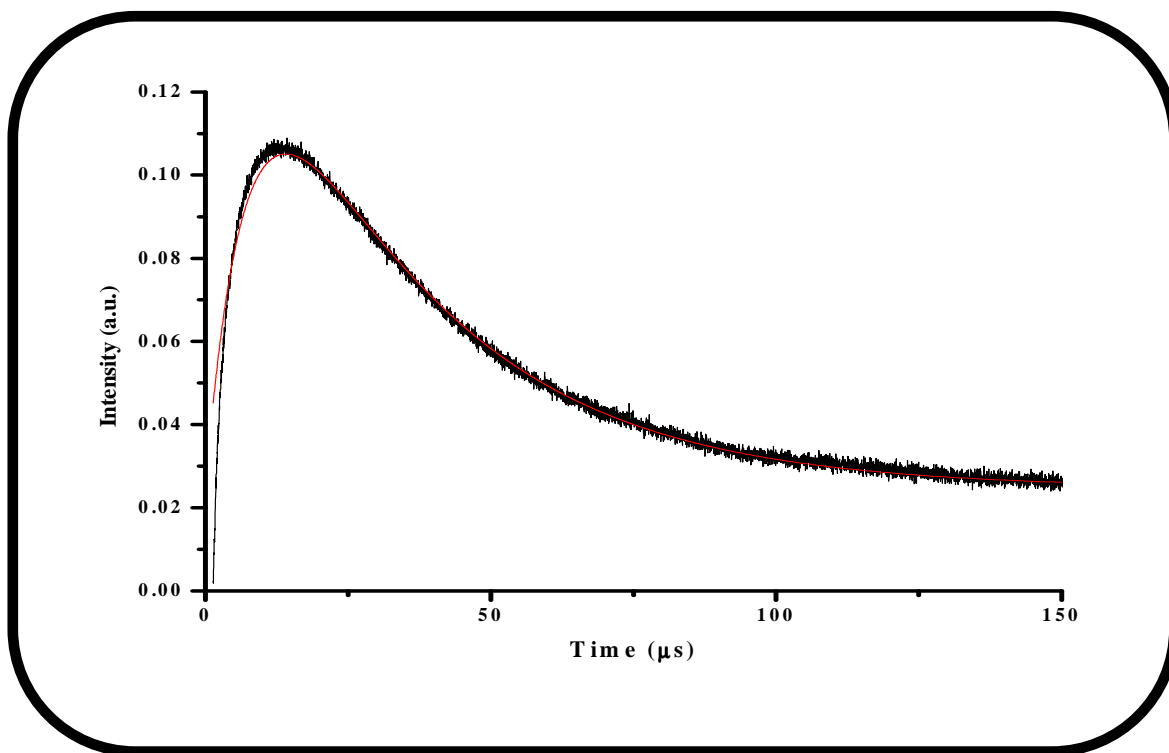


**Figure 5.21:**  $^1\text{O}_2$  decay curve for ZnttbIPc (**31**) in DMF-water (4:1 v/v).

from which energy is readily transferred to ground state molecular oxygen with high efficiency. The  $\Phi_{\Delta}$  value for the ZnPc(**31**)-QD-linked was not determined since the signal was very weak, most likely due to low concentrations of **31** in the linked complex.

### 5.3 Conclusions

Linked and adsorbed or mixed MPc-SWCNT and MPc-QD conjugates have successfully been synthesized using the two low symmetry derivatives reported in this work and the carboxylic acid and ethylamine functionalized SWCNT and MPA capped CdTe QDs. Various spectroscopic techniques have been used to characterize the conjugates. Fluorescence spectra pertaining to the low symmetry Pc derivatives are quenched extensively in the presence of SWCNT, suggesting a rapid electron transfer mediated

process from the electron donating Pcs to the electron accepting nanotubes. Fluorescence spectra gave evidence of FRET in both the mixed and linked MPc-QD conjugates. Interaction of the MPcs with nanoparticles led to improved photophysicochemical properties, particularly in cases where the nanoparticles (SWCNT and QDs) have been attached to the MPcs by a covalent chemical bond. This is expressed more significantly with the use of ZnttbIPc which in the linked MPc-QD conjugate gave the largest FRET efficiency, hence showing that linking enhances FRET.

These results show that the use of low symmetry derivatives to form linked MPc-SWCNT and MPc-QD conjugates may be useful agents for application in PDT or bimodal PDT-PHT.

## **6. General Conclusions and Future Prospects**

**This chapter summarizes the results obtained for the studies conducted and reported in this thesis and future prospects.**

## 6.1 General Conclusions

The synthesis and spectroscopic characterization of numerous symmetrical zinc, cadmium and mercury tetra-substituted MPc complexes have been reported in this work. The introduction of heavy central metal ions such as Cd and Hg presents interesting spectroscopic phenomena, such as symmetry loss and oxidation as a function of the solvent properties and the site of substitution i.e.  $\alpha$  vs  $\beta$ . Novel, low-symmetry zinc derivatives are also presented and spectral characterization was explained with respect to their unique molecular structures. The nanoparticles used gave spectroscopic information typical of such complexes.

Thorough examination of the photophysical and photochemical properties of the synthesized MPc complexes have been obtained and tend to show variations with changes in the central metal ion, solvent and position and type of substituents. HgPc complexes showed enhanced triplet quantum yields ( $\Phi_T$ ), singlet oxygen quantum yields ( $\Phi_\Delta$ ) relative to the smaller metal ions containing corresponding derivatives, particularly in DMSO. This emphasizes the need to give adequate consideration to the solvents employed for such determinations. This is additionally expressed by the photodegradation quantum yields ( $\Phi_{Pd}$ ) obtained. These were predominantly affected by poorly coordinating or chlorinated solvents, in which the oxidative process becomes more accessible. Phototransformation of aryloxy substituted CdPcs was observed during photolysis and has been attributed to the structural framework.

The spectroscopic behaviour of the low-symmetry complexes reported as a result of interactions with single walled carbon nanotubes or quantum dot nanoparticles has also been investigated. The absorption spectra for the MPc-SWCNT and MPc-QD conjugates



were for the most part similar to the pristine MPc complexes, varying only by minuscule shifts or slight broadening in the Q band region. However, distinct spectroscopic differences exist for conjugates that have distinct covalent bonds between the MPcs and nanoparticles and those simply formed by adsorption.

Extensive quenching of Pc fluorescence in the presence of carbon nanotubes suggests photoinduced electron transfer from the electron donating Pcs to electron accepting nanotubes. Photoinduced energy transfer emerged as the dominant form of interaction for MPc-QD conjugates, evident from quenching of the fluorescence emission of the highly photoluminescent QDs coupled with sensitized emission for the MPcs. The involvement of surface states exerts an influence on the fluorescence quantum yields and lifetimes ( $\tau_F$ ) that were determined.

The photophysical and photochemical properties were enhanced as a result of interactions of MPcs with nanoparticles. MPc-SWCNT conjugates may be exploited for combinational PDT-PHT while the MPc-QD conjugates may be used for imaging, due to the fluorescent nature of QDs while the Pc portion serves as a useful photosensitizer, for example in PDT.

### **6.2 Future Prospects**

Due to the high photophysical properties determined for the Cd and HgPc complexes, photocatalysis studies may find that these molecules are of use in industrial catalysis operations.

The low symmetry MPc-nanoparticle conjugates need to be investigated further. Femtosecond laser flash photolysis will give more insight with respect to the

photoinduced electron transfer process for the MPc-SWCNT conjugates. Electrochemical characterization may also prove useful. Spectroscopic studies of the low symmetry MPcs in the presence of a variation of QD, particularly those considered to exhibit low toxicity can be explored. The development of MPc-nanoparticle conjugates characterized by low toxicity, intense red absorption and excellent photophysical and photochemical properties may advance ongoing research for the treatment of cancers.

---

## References

1. G.L. Hornyak, J. Dutta, H.F. Tibbals, A.K. Rao, in *Introduction to Nanoscience*, CRC Press, Taylor and Francis Group, Boca Raton, (2008).
2. B. Rogers, S. Pennathur, J. Adams, in *Nanotechnology: Understanding small systems*, CRC Press, Taylor and Francis Group, Boca Raton, (2008).
3. S. Iijima, *Nature* **354** (1991) 56.
4. S. Iijima, T. Ichihashi, *Nature* **363** (1993) 603.
5. M. Ouyang, J.-L. Huang, C.M. Lieber, *Acc. Chem. Res.* **35** (2002) 1018.
6. N. Nakashima, *Int. J. Nanoscience* **4** (2005) 119.
7. C.A. Dyke, J.M. Tour, *J. Phys. Chem. A* **108** (2004) 11151.
8. R.H. Baughman, A.A. Zakhidov, W.A. de Heer, *Science* **297** (2002) 787.
9. S. Niyogi, M.A. Hammon, H. Hu, B. Zhao, P. Bhowmik, R. Sen, M.E. Itkis, R.C. Haddon, *Acc. Chem. Res.* **35** (2002) 1105.
10. A. Hirsch, *Angew. Chem. Int. Ed.* **41** (2002) 1853.
11. H. Dai, *Acc. Chem. Res.* **35** (2002) 1035.
12. R. Andrews, D. Jacques, A.M. Rao, T. Rantell, F. Derbyshire, *Appl. Phys. Lett.* **75** (1999) 1329.
13. A. Bachtold, P. Hadley, T. Nakanishi, C. Dekker, *Science* **294** (2001) 1317.
14. P.C. Collins, M.S. Arnold, P. Avouris, *Science* **292** (2001) 706.
15. A.C. Dillon, K.M. Jones, T.A. Bekkendahl, C.H. Kiang, D.S. Bethune, M.J. Heben, *Nature* **386** (1997) 377.
16. M. Zhang, T. Murakami, K. Ajima, K. Tsuchida, A.S.D. Sandanayaka, O. Ito, S. Iijima, M. Yudasaka, *PNAS* **105** (2008) 14773.

17. R.P. Feazell, N. Nakayama-Ratchford, H. Dai, S.J. Lippard, *J. Am. Chem. Soc.* **129** (2007) 8438.
18. W. Yang, P. Thordarson, J.J. Gooding, S.P. Ringer, F. Braet, *Nanotechnology* **18** (2007) 412001.
19. A. Bianco, K. Kostarelos, C.D. Partidos, M. Prato, *Chem. Commun.* (2005) 571.
20. P. Moroz, S.K. Jones, B.N. Gray, *Int. J. Hyperthermia* **18** (2002) 267.
21. R.C. Haddon, *Acc. Chem. Res.* **35** (2002) 997.
22. Y.-P. Sun, K. Fu, Y. Lin, W. Huang, *Acc. Chem. Res.* **35** (2002) 1096.
23. B.K. Price, J.M. Tour, *J. Am. Chem. Soc.* **128** (2006) 12899.
24. X. Wang, Y. Liu, W. Qiu, D. Zhou, *J. Mater. Chem.* **12** (2002) 1636.
25. H. Murakami, T. Nomura, N. Nakashima, *Chem. Phys. Lett.* **465** (2008) 73.
26. R.J. Chen, Y.G. Zhan, D.W. Wang, H.J. Dai, *J. Am. Chem. Soc.* **123** (2001) 3838.
27. A. Ma, J. Lu, S. Yang, K.M. Ng, *J. Cluster Science* **17** (2006) 599.
28. J.L. Bahr, J.Y. Dmitry, V. Kosynkin, M.J. Bronikowski, R.E. Smalley, J.M. Tour, *J. Am. Chem. Soc.* **123** (2001) 6536.
29. D.J. Nelson, H. Rhoads, C. Brammer, *J. Phys. Chem. C* **111** (2007) 17872.
30. S.M. Bachilo, M.S. Strano, C. Kittrell, R.H. Hauge, R.E. Smalley, R.B. Weisman, *Science* **298** (2002) 2361.
31. M.S. Dresselhaus, G. Dresselhaus, A. Jorio, *J. Phys. Chem. C* **111** (2007) 17887.
32. F. Hennrich, R. Kupke, S. Lebedkin, K. Arnold, R. Fisher, D. Resasco, M. Kappes, *J. Phys. Chem. B* **109** (2005) 10567.
33. B. Ballesteros, G. de la Torre, C. Ehli, G.M. Aminur Rahman, F. Agullo-Rueda, D.M. Guldi, T. Torres, *J. Am. Chem. Soc.* **129** (2007) 5061.

- 
34. C.A. Dyke, J.M. Tour, *J. Am. Chem. Soc.* **125** (2003) 1156.
  35. J.L. Bahr, J.M. Tour, *J. Mater. Chem.* **12** (2002) 1952.
  36. E.P. Dillon, C.A. Crouse, A.R. Barron, *ACS Nano* **2** (2008) 156.
  37. J. Kastner, T. Pichler, H. Kuzmany, S. Curran, W. Blau, D.N. Weldon, M. Delamesiere, S. Draper, H. Zandbergen, *Chem. Phys. Lett.* **221** (1994) 53.
  38. W.C.W. Chan, D.J. Maxwell, X.H. Gao, R.E. Bailey, M.Y. Han, S.M. Nie, *Curr. Opin. Biotechnol.* **13** (2002) 40.
  39. T. Jamieson, R. Bakhshi, D. Petrova, R. Pocock, M. Imani, A.M. Seifalian, *Biomaterials* **28** (2007) 4717.
  40. T.J. Bukowski, *Critical Reviews in Solid State and Materials Sciences* **27** (2002) 119.
  41. P. Juzenas, W. Chen, Y.-P. Sun, M.A.V.N. Coelho, R. Generalova, N. Generalova, I.L. Christensen, *Adv. Drug Deliv. Rev.* **60** (2008) 1600.
  42. C. Seydel, *Science* **300** (2003) 80.
  43. X.H. Gao, S.M. Nie, *J. Phys. Chem. B* **107** (2007) 575.
  44. N.Y. Morgan, S. English, W. Chen, V. Chernomordik, A. Russo, P.D. Smith, A. Gandjbakhche, *Acad. Radiol.* **12** (2005) 313.
  45. D.K. Chatterjee, L.S. Fong, Y. Zhang, *Adv. Drug. Deliv. Rev.* **60** (2008) 1627.
  46. A.C.S. Samia, X.B. Chen, C. Burda, *J. Am. Chem. Soc.* **125** (2003) 15736.
  47. A.C.S. Samia, S. Dayal, C. Burda, *Photochem. Photobiol.* **82** (2006) 617.
  48. R. Bakalova, H. Ohba, Z. Zhelev, M. Ishikawa, Y. Baba, *Nat. Biotechnol.* **22** (2004) 1360.
  49. W. Chen, J. Zhang, *J. Nanosci. Nanotechnology* **6** (2006) 1159.

- 
50. Y.N. Konan-Kouakou, R. Boch, R. Gurny, E. Allemann, *J. Control Release* **103** (2005) 83.
  51. S. Santra, K.M. Wang, R. Tapeç, W.H. Tan, *J. Biomed. Opt.* **6** (2001) 160.
  52. M. Hines, P. Guyot-Sionnest, *J. Phys. Chem. B* **100** (1996) 468.
  53. R. Rosetti, L. Brus, *J. Phys. Chem.* **86** (1982) 4470.
  54. C.B. Murray, D.J. Norris, M.G. Bawendi, *J. Am. Chem. Soc.* **115** (1993) 8706.
  55. Z.A. Peng, X. Peng, *J. Am. Chem. Soc.* **123** (2001) 183.
  56. L. Qu, X. Peng, *J. Am. Chem. Soc.* **124** (2002) 2049.
  57. M. Bruchez, M. Moronne, P. Gin, S. Weiss, A.P. Alivisatos, *Science* **281** (1998) 2013.
  58. H. Mattoussi, J.M. Matouro, E.R. Goldman, G.P. Anderson, V.C. Sundar, F.V. Mikulec, M.G. Bawendi, *J. Am. Chem. Soc.* **122** (2000) 12142.
  59. D.V. Talapin, A.L. Rogach, I. Mekis, S. Haubold, A. Kornowski, M. Haase, H. Weller, *Coll. Surf. A* **202** (2002) 145.
  60. N. Gaponik, D.V. Talapin, A.L. Rogach, K. Hoppe, E.V. Shevchenko, A. Kornowski, A. Evchmüller, H. Weller, *J. Phys. Chem. B* **106** (2002) 7177.
  61. D. Gerion, F. Pinaud, S.C. Williams, W.J. Parak, D. Zanchet, S. Weiss, A.P. Alvisatos, *J. Phys. Chem. B* **105** (2001) 8861.
  62. S. Hohng, T. Ha, *J. Am. Chem. Soc.* **126** (2004) 21.
  63. I.L. Medintz, H.T. Uyeda, E.R. Goldman, H. Mattoussi, *Nat. Mater.* **4** (2005) 435.
  64. M.Y. Gao, Kirstein, H. Mohwald, A.L. Rogach, A. Kornokowski, A. Eychmüller, H. Weller, *J. Phys. Chem. B* **102** (1998) 8360.

- 
65. P. Zhong, Y. Yu, J. Wu, Y. Lai, B. Chen, Z. Long, C. Liang, *Talanta* **70** (2006) 902.
  66. H. Zhang, Z. Zhou, M.Y. Gao, *J. Phys. Chem. B* **107** (2003) 8.
  67. D.L. Klayman, T.S. Griffin, *J. Am. Chem. Soc.* **95** (1973) 197.
  68. Z. Tang, N.A. Kotov, M. Gierseg, *Science* **297** (2002) 237.
  69. X.G. Peng, J. Wickham, A.P. Alivisatos, *J. Am. Chem. Soc.* **120** (1998) 5343.
  70. F. Aldeek, L. Balan, J. Lamber, R. Schneider, *Nanotechnology* **19** (2008) 475401.
  71. W.W. Yu, Y.A. Wang, X. Peng, *Chem. Mater.* **15** (2003) 4300.
  72. J.A. Hollingsworth, V.I. Klimov, in *Semiconductor and Metal Nanocrystals: Synthesis and Electronic and Optical Properties*, V.I. Klimov (Ed.), Marcel Dekker, New York, 2004, p1-64.
  73. M.G. Bawendi, W.L. Wilson, L. Rothberg, P.J. Carroll, T.M. Jedju, M.L. Steigerwald, L.E. Brus, *Phys. Rev. Lett.* **65** (1990) 1623.
  74. A.I.L. Efros, M. Rosen, *Phys. Rev. Lett.* **78** (1997) 1110.
  75. R.W. Kelsall, I.W. Hamley, M. Geoghegan, in *Nanoscale Science and Technology*, John Wiley and Sons, Ltd., London (2005).
  76. Z.-L. Yang, H.-Z. Chen, L. Cao, H.-Y. Li, M. Wang, *Materials and Science Engineering B* **106** (2004) 73.
  77. L. Li, H. Qian, N. Fang, J. Ren, *J. Luminescence* **116** (2006) 59.
  78. A.L. Patterson, *Phys. Rev.* **56** (1939) 978.
  79. R.P. Linstead, *J. Chem. Soc.* (1934) 1016.
  80. G.T. Byrne, R.P. Linstead, A.R. Lowe, *J. Chem. Soc.* (1934) 1017.
  81. R.P. Linstead, A.R. Lowe, *J. Chem. Soc.* (1934) 1022.

- 
82. C.E. Dent, R.P. Linstead, A.R. Lowe, *J. Chem. Soc.* (1934) 1033.
  83. *Phthalocyanines: Properties and applications*, C.C. Leznoff, A.B.P. Lever (Eds.), VCH Publishers, New York, **Vols. 1-4** (1989, 1993, 1993, 1996).
  84. *The Porphyrin Handbook: Applications of Phthalocyanines*, K. M. Kadish, K.M. Smith and R. Guilard (Eds.), The Porphyrin Handbook, **Vol. 19**, Academic Press, New York, (2003).
  85. P. Gregory, *J. Porphyrins Phthalocyanines* **4** (2000) 432.
  86. J.E. Kuder, *Imag. Sci.* **32** (1988) 51.
  87. D. Wöhrle, D. Meissner, *Adv. Mater.* **3** (1991) 129.
  88. G. de la Torre, P. Vásquez, F. Agulló-López, T. Torres, *Chem. Rev.* **104** (2004) 3723.
  89. D. Dini, M. Hanack, *J. Porphyrins Phthalocyanines* **8** (2004) 915.
  90. R. Rella, A. Serra, P. Siciliano, A. Tepore, L. Troisi, L. Valli, *Thin Solid Films*, **284-285** (1996) 870.
  91. F. Armund, H. Ferez, S. Fouriaux, O. Araspin, J.-P. Pradeau, C.G. Claessens, E.M. Maya, P. Vásquez, T. Torres, *Synthetic Metals* **102** (1999) 1476.
  92. Z. Bao, A.J. Lovinger, A. Dodabalapur, *Appl. Phys. Lett.* **69** (1996) 3066.
  93. A.W. Snow, W.R. Barger, M. Klusty, H. Wohltjen, N.L. Jarvis, *Langmuir* **2** (1986) 513.
  94. J.S. Guillaud, J.P. Germain, *Coord. Chem. Rev.* **180** (1998) 1433.
  95. A.J. Duro, G. de la Torre, J. Barber, J.L. Serano, T. Torres, *Chem. Mater.* **8** (1996) 1061.



- 
96. G.J. Clarkson, N.B. McKeown, K.E. Treacher, *J. Chem. Soc. Perkin Trans. 1* (1995) 1817.
97. K. Hanabusa, H. Shirai, in *Phthalocyanines: Properties and Applications*, C.C. Leznoff, A.B.P. Lever (Eds.), VCH Publications, New York, **Vol.2** (1993) Chapter 4.
98. I. Rosenthal, *Photochem. Photobiol.* **53** (1991) 859.
99. J.D. Spikes, *J. Photochem. Photobiol. B* **6** (1990) 259.
100. S.G. Brown, C.J. Tralau, P.D. Coleridge-Smith, D.T. Akdemir, T.J. Wieman, *Br. J. Cancer* **54** (1986) 43.
101. R. Bonnett, in *Chemical Aspects of Photodynamic Therapy*, D. Phillips (Ed.), Gordon and Breach Science, Canada, (2000).
102. D. Wöhrle, O. Suvorova, R. Gerdes, O. Bartels, L. Lapok, N. Baziakina, S. Makarov, A. Slodek, *J. Porphyrins Phthalocyanines* **8** (2004) 1020.
103. G. Mele, R.D. Sole, G. Vasapollo, E. García-López, L. Palmisano, M. Schiavello, *J. Catalysis* **217** (2003) 334.
104. N. Sehlotho, T. Nyokong, *J. Mol. Catal. A: Chem.* **209** (2004) 51.
105. M.P. de la Filippis, D. Dei, L. Fantetti, G. Roncucci, *Tetrahedron Lett.* **41** (2000) 9143.
106. D. Phillips, *Science Progress* **77** (1993) 295.
107. N. Brasseur, R. Langlois, C. La Madeleine, R. Ouellet, J.E. van Lier, *Photochem. Photobiol.* **69** (1999) 345.
108. S.A. Mikhalenko, E.A. Luk'yanets, *Zh. Obshch. Khim.* **39** (1969) 2129.
109. A. Shaabani, *J. Chem. Res. (S)* (1988) 672.

- 
110. A. Kempa, J. Dobrowolski, *Can. J. Chem.* **66** (1988) 2553.
111. D. Wöhrle, G. Schnurpfeil, G. Knothe, *Dyes Pigments* **18** (1992) 91.
112. A. Tomoda, S. Saito, S. Ogawa, S. Shiraishi, *Chem. Lett.* (1980) 1277.
113. P.A. Barrett, D.A. Frye, R.P. Linstead, *J. Chem. Soc.* (1938) 1157.
114. N.M. Bigelow, M.A. Perkins, in *Phthalocyanine Pigments*, H.A. Lubs (Ed.), Reinhold Press, New York, (1955) p577-606.
115. C.C. Leznoff, in *Phthalocyanines: Properties and Applications*, C.C. Leznoff, A.B.P. Lever (Eds.), VCH Publishers, New York, **Vol. 1** (1989) Chapter 1.
116. M. Hanack, H. Heckmann, R. Polley, in *Houben-Weyl: Methods of Organic Synthesis*, M. Hanack (Ed.), Thieme, Stuttgart, Supplementary Vol. E9d (1997) p717.
117. J.G. Young, W. Onyebuagu, *J. Org. Chem.* **55** (1990) 2155.
118. C.C. Leznoff, M. Hu, C.R. McArthur, Y. Qin, J.E. van Lier, *Can. J. Chem.* **72** (1994) 1990.
119. G. Schmid, M. Sommerauer, M. Hanack, *Angew. Chem. Int. Ed. Engl.* **32** (1993) 1422.
120. M. Sommerauer, C. Rager, M. Hanack, *J. Am. Chem. Soc.* **118** (1996) 10085.
121. M. Hanack, D. Meng, A. Beck, M. Sommerauer, L.R. Subramanian, *J. Chem. Soc. Chem. Commun.* (1953) 58.
122. D.A. Li, M.A. Ratner, T.J. Marks, *J. Am. Chem. Soc.* **110** (1988) 1707.
123. G.G. Roberts, M.C. Petty, S. Baker, M.T. Fowler, N.J. Thomas, *Thin Solid Films* **132** (1985) 113.
124. M.J. Cook, R. Hersans, J. McMurdo, D.A. Russell, *J. Mater. Chem.* **6** (1996) 149.

- 
125. B.A. Henderson, T.J. Dougherty, *Photochem. Photobiol.* **55** (1992) 145.
126. D. Wöhrle, M. Shopova, S. Müller, A.D. Milev, V.N. Mantareva, K.K. Kraster, *J. Photochem. Photobiol. B* **21** (1993) 155.
127. N.B. McKeown, I. Chambrier, M.J. Cook, *J. Chem. Soc. Perkin Trans. 1* (1990) 1169.
128. N. Kobayashi, T. Ashida, T. Osa, *Chem. Lett.* (1992) 2031.
129. S. Rodríguez-Morgade, M. Hanack, *Chem. Eur. J.* **3** (1997) 1042.
130. C.C. Leznoff, T.W. Hall, *Tetrahedron Lett.* **23** (1982) 3023.
131. D. Wöhrle, G. Krawczyk, *Polym. Bull.* **15** (1986) 193.
132. N. Kobayashi, R. Kondo, S.-I. Nakajima, T. Osa, *J. Am. Chem. Soc.* **112** (1990) 9640.
133. M.S. Rodríguez-Morgade, G. de la Torre, T. Torres, in *The Porphyrin Handbook*, K.M. Kadish, K.M. Smith, R. Guilard (Eds.), Academic Press, Elsevier Science, **Vol. 15** (2003) Chapter 99.
134. G. Schmid, M. Sommerauer, M. Geyer, in *Phthalocyanines: Properties and Applications*, C.C. Leznoff, A.B.P. Lever (Eds.), VCH Publishers, New York, **Vol. 4** (1996) Chapter 1.
135. C.F. van Nostrum, R.J.M. Nolte, *Chem. Commun.* (1996) 2385.
136. M. Brewis, G.J. Clarkson, A.M. Holder, N.B. McKeown, *Chem. Commun.* (1998) 1979.
137. S.V. Kudrevich, H. Ali, J.E. van Lier, *J. Chem. Soc. Perkin Trans. 1* (1994) 2767.
138. H. Kliesch, A. Weitemeyer, S. Müller, D. Wöhrle, *Liebigs Ann.* (1995) 1269.

- 
139. Y. Liu, D. Zhu, T. Wada, A. Yamada, H. Sasabe, *J. Heterocyclic Chem.* **31** (1994) 1017.
140. G. de la Torre, T. Torres, *J. Porphyrins Phthalocyanines* **1** (1997) 221.
141. T. Torres, G. de la Torre, J. García-Ruiz, *Eur. J. Org. Chem.* (1999) 2323.
142. H. Tomada, S. Saito, S. Shiraishi, *Chem. Lett.* **12** (1983) 313.
143. P.A. Barrett, C.E. Dent, R.P. Linstead, *J. Chem. Soc.* (1936) 1719.
144. P.A. Barrett, D.A. Frye, R.P. Linstead, *J. Chem. Soc.* (1938) 1157.
145. A. Ogunsipe, J.-Y. Chen, T. Nyokong, *New. J. Chem.* **28** (2004) 822.
146. A. Ogunsipe, T. Nyokong, *J. Mol. Struct.* **689** (2004) 89.
147. S. Gaspard, *J. Chem. Soc. Perkin Trans. 2* (1989) 383.
148. I. Chambrier, D.L. Hughes, J.C. Swarts, B. Isare, M.J. Cook, *Chem. Commun.* (2006) 3504.
149. I. Chambrier, J.C. Swarts, D.L. Hughes, M.J. Cook, *J. Porphyrins Phthalocyanines* **13** (2009) 176.
150. K.P. Srivastava, A. Kumar, *Asian J. Chem.* **19** (2007) 361.
151. P. Clare, F. Gockling, *Inorg. Chim. Acta* **14** (1975) L12.
152. H. Kropf, *Angew. Chem. Int. Ed. Engl.* **11** (1972) 239.
153. S. Gaspard, P. Maillard, *Tetrahedron* **43** (1987) 1083.
154. S. Moeno, T. Nyokong, *J. Photochem. Photobiol. A: Chem.* 201 (2009) 228.
155. W.M. Sharman, J.E. van Lier, *Bionconjugate Chem.* **16** (2005) 1166.
156. P. Margaron, R. Langlois, J.E. van Lier, S. Gaspard, *J. Photochem. Photobiol. B: Biol.* **14** (1992) 187.

- 
157. S. Campidelli, B. Ballesteros, A. Filoramo, D. Díaz Díaz, G. de la Torre, T. Torres, G.M. Aminur Rahman, C. Ehli, D. Kiessling, F. Werner, V. Sgobba, D.M. Guldi, C. Cioffi, M. Prato, J.-P. Bourgoïn, *J. Am. Chem. Soc.* **130** (2008) 11503.
158. S. Dayal, R. Krolicki, Y. Lou, X. Qiu, J.C. Berlin, M.E. Kenney, C. Burda, *Appl. Phys. B* **84** (2006) 309.
159. S. Dayal, J. Li, Y.-S. Li, H. Wu, A.C.S. Samia, M.E. Kenney, C. Burda, *Photochem. Photobiol.* **84** (2007) 243.
160. S. Dayal, Y. Lou, A.C.S. Samia, J.C. Berlin, M.E. Kenney, C. Burda, *J. Am. Chem. Soc.* **128** (2006) 13974.
161. S. Dayal, C. Burda, *Photochem. Photobiol. Sci.* **7** (2008) 605.
162. S. Dayal, C. Burda, *J. Am. Chem. Soc.* **130** (2008) 2890.
163. S. Dayal, C. Burda, *J. Am. Chem. Soc.* **129** (2007) 7977.
164. M. Idowu, J.-Y. Chen, T. Nyokong, *New. J. Chem.* **32** (2008) 290.
165. S. Moeno, T. Nyokong, *Polyhedron* **27** (2008) 1953.
166. J. Britton, E. Antunes, T. Nyokong *Inorg. Chem. Commun.* **12** (2009) 828.
167. M.J. Stillman, A.J. Thomson, *J. Chem. Soc. Faraday Trans. II* **70** (1974) 790.
168. A.B.P. Lever, *Adv. Inorg. Radiochem.* **7** (1965) 27.
169. J.R. Darwent, P. Douglas, A. Harriman, G. Porter, M.C. Richoux, *Chem. Rev.* **44** (1982) 83.
170. M. Gouterman, in *The Porphyrins, Part A. Physical Chemistry*, D. Dolphin (Ed.), Academic Press, New York, Vol. 3 (1978) p1-165.
171. J. Mack, M.J. Stillman, *J. Am. Chem. Soc.* **116** (1994) 1292.
172. T. Nyokong, Z. Gasyna, M.J. Stillman, *Inorg. Chem.* **26** (1987) 1087.

- 
173. K. Kasuga, N. Matura, K. Inoue, M. Handa, T. Sugimori, K. Isa, M. Nakata, *Chem. Lett.* (2002) 352.
174. G.A. Kumar, J. Thomas, N.V. Umnikrishnan, V.P.N. Nampouri, C.P.G. Vallabhan, *J. Porphyrins Phthalocyanines* **5** (2001) 456.
175. M.S. Fischer, D.H. Templeton, A. Zalkin, M. Calvin, *J. Am. Chem. Soc.* **93** (1971) 2622.
176. M.J. Stillman, T. Nyokong, in *Phthalocyanines: Properties and Applications*, C.C. Leznoff, A.B.P. Lever (Eds.) **Vol. 1** (1989) Chapter 3, p139-247.
177. T. Kobayashi, T. Ashida, N. Uyeda, E. Surro, M. Kakuda, *Bull. Chem. Soc. Jpn.* **44** (1971) 2095.
178. K. Ukei, *Acta. Cryst.* **B29** (1973) 2290.
179. C. Reichardt, in *Solvents and Solvent Effects in Organic Chemistry*, H.F. Ebel (Ed.), VCH, Germany, (1988) p285-338.
180. W.-F. Law, R.C.W. Liu, J. Jiang, D.K.P. Ng, *Inorg. Chim. Acta* **256** (1997) 147.
181. N. Kobayashi, H. Konami, in *Phthalocyanines: Properties and Applications*, C.C. Leznoff, A.B.P. Lever (Eds.), VCH Publisher, New York, **Vol. 4** (1999) Chapter 9.
182. J. Grodkowski, J.H. Chambers Jr., P. Neta, *J. Phys. Chem.* **88** (1984) 5332.
183. P. Tau, T. Nyokong, *Dalton. Trans.* (2006) 4482.
184. N. Kobayashi, H. Ogata, N. Nonaka, E.A. Luk'yanets, *Chem. Eur. J.* **9** (2003) 5123.
185. N. Kobayashi, N. Sasaki, Y. Higashi, T. Osa, *J. Inorg. Chem.* **34** (1995) 1636.
186. A.R. Monahan, J.A. Brado, F.A. DeLuca, *J. Phys. Chem.* **76** (1972) 446.

- 
187. W.A. Nevin, W. Liu, S. Greenberg, M.R. Hempstead, S.M. Maruccio, M.M. Melnik, C.C. Leznoff, A.B.P. Lever, *Inorg. Chem.* **26** (1987) 291.
188. E. Schnabel, H. Nöther, H. Kuhn, in *Chemistry of Natural and Synthetic Colouring Matters*, T.S. Gore, B.S. Joshi, S.V. Sunthankar, B.D. Tilak (Eds.), Academic Press, New York, (1962) p561-572.
189. K. Bernauer, S. Fallab, *Fasciculus VII XLV* (1962) 2487.
190. A. Skorobogaty, T.D. Smith, G. Dougherty, J.R. Pilbrow, *J. Chem. Soc.* (1985) 651.
191. M. Kasha, *Radiation. Res.* **20** (1963) 55.
192. M. Kasha, H.R. Rawls, M. Ashraf El-Bayoumi, *Pure Appl. Chem.* **11** (1965) 371.
193. X.-Y. Li, D.K.P. Ng, *Tetrahedron Lett.* **42** (2001) 305.
194. Z.A. Schelly, R.D. Farina, E.M. Eyring, *J. Phys. Chem.* **74** (1970) 617.
195. Z.A. Schelly, D.J. Howard, P. Hemmes, E.M. Eyring, *J. Phys. Chem.* **74** (1974) 3040.
196. H. Abramczyk, I. Szymczyk, G. Waliszewska, A. Lebioda, *J. Phys. Chem.* **108** (2004) 264.
197. R.D. George, A.W. Snow, J.S. Shirk, W.R. Barger, *J. Porphyrins Phthalocyanines* **2** (1998) 1.
198. H. Ogata, R. Higashi, N. Kobayashi, *J. Porphyrins Phthalocyanines* **7** (2003) 551.
199. A.W. Snow, in *The Porphyrin Handbook*, K.M. Kadish, K.M. Smith, R. Guilard, (Eds.), Elsevier Science, New York, **Vol. 17** (2003) Chapter 109.
200. M.J. Stillman, in *Phthalocyanines: Properties and Applications*, C.C. Leznoff, A.B.P. Lever, (Eds.), VCH Publications, New York, **Vol. 3** (1993) Chapter 5.

- 
201. J. Mack, M.J. Stillman, in *The Porphyrin Handbook*, K.M. Kadish, K.M. Smith, R. Guilard, (Eds.), Elsevier Science, New York, **Vol. 16** (2003) Chapter 103.
202. P.N. Schatz, A.J. McCaffery, W. Suetaka, G.N. Henning, A.B. Ritchie, P.J. Stephens, *J. Chem. Phys.* **45** (1966) 722.
203. G.N. Henning, A.J. McCaffery, P.N. Schatz, P.J. Stephens, *J. Chem. Phys.* **48** (1968) 5656.
204. S.B. Piepho, P.N. Schatz, in *Group Theory in Spectroscopy with Applications to Magnetic Circular Dichroism*, Wiley, New York, (1983).
205. P.J. Stephens, *Adv. Chem. Phys.* **35** (1976) 197.
206. J. Mack, M.J. Stillman, N. Kobayashi, *Coord. Chem. Rev.* **251** (2007) 429.
207. J. Michl, *J. Am. Chem. Soc.* **100** (1978) 6801.
208. J. Michl, *Pure Appl. Chem.* **52** (1980) 1549.
209. J. Mack, M.J. Stillman, *Coord. Chem. Rev.* **219-221** (2001) 993.
210. N. Kobayashi, K. Nakai, *Chem. Commun.* (2007) 4077.
211. W.T. Simpson, *J. Chem. Phys.* **17** (1949) 1218.
212. A.J. McHugh, M. Gouterman, C. Weiss, *Theoret. Chim. Acta* **24** (1972) 346.
213. A.M. Schaffer, M. Gouterman, E.R. Davidson, *Theoret. Chim. Acta* **30** (1973) 9.
214. A.M. Schaffer, M. Gouterman, *Theoret. Chim. Acta.* **25** (1972) 62.
215. J. Michl, *J. Am. Chem. Soc.* **100** (1978) 6801.
216. *Density-Functional Theory of Atoms and Molecules*, R.G. Parr, W. Wang (Eds.), Oxford University Press, Oxford, (1989).
217. E.K.U. Gross, J.F. Dobson, M. Petersilka, in *Topics in Current Chemistry*, R.F. Nalewajski (Ed.), Springer, Berlin, **Vol. 181** (1996) p81.



- 
218. R. Van Leeuwen, *Int. J. Mod. Phys. B* **15** (2001) 1969.
219. J. Mack, Y. Asano, N. Kobayashi, M.J. Stillman, *J. Am. Chem. Soc.* **127** (2005) 17697.
220. J. Mack, M. Bunya, D. Lansky, D.P. Goldberg, N. Kobayashi, *Heterocycles* **76** (2008) 1369.
221. *Gaussian 03, Revision C.02*, M.J. Frisch, G.W. Trucks, H.B. Schlegel, G.E. Scuseria, M.A. Robb, J.R. Cheeseman, J.A. Montgomery Jr., T. Vreven, K.N. Kudin, J.C. Burant, J.M. Millam, S.S. Iyengar, J. Tomasi, V. Barone, B. Mennucci, M. Cossi, G. Scalmani, N. Rega, G.A. Petersson, H. Nakatsuji, M. Hada, M. Ehara, K. Toyota, R. Fukuda, J. Hasegawa, M. Ishida, T. Nakajima, Y. Honda, O. Kitao, H. Nakai, M. Klene, X. Li, J.E. Knox, H.P. Hratchian, J.B. Cross, V. Bakken, C. Adamo, J. Jaramillo, R. Gomperts, R.E. Stratmann, O. Yazyev, A.J. Austin, R. Cammi, C. Pomelli, J.W. Ochterski, P.Y. Ayala, K. Morokuma, G.A. Voth, P. Salvador, J.J. Dannenberg, V.G. Zakrzewski, S. Dapprich, A.D. Daniels, M.C. Strain, O. Farkas, D.K. Malick, A.D. Rabuck, K. Raghavachari, J.B. Foresman, J.V. Ortiz, Q. Cui, A.G. Baboul, S. Clifford, J. Cioslowski, B.B. Stefanov, G. Liu, A. Liashenko, P. Piskorz, I. Komaromi, R.L. Martin, D.J. Fox, T. Keith, M.A. Al-Laham, C.Y. Peng, A. Nanayakkara, M. Challacombe, P.M.W. Gill, B. Johnson, W. Chen, M.W. Wong, C. Gonzalez, J.A. Pople, Gaussian, Inc., Wallingford CT (2004).
222. Y. Ikeda, H. Konami, M. Hatano, K. Mochizuki, *Chem. Lett.* (1992) 763.
223. A. Jablonski, *Z. Phys.* **94** (1935) 38.

- 
224. P.W. Atkins, in *Physical Chemistry*, P.W. Atkins (Ed.), Oxford University Press, Oxford, 6<sup>th</sup> Edition, (1998) Chapter 17.
225. K. Ishii, N. Kobayashi, in *The Porphyrin Handbook*, K.M. Kadish, K.M. Smith, R. Guilard, (Eds.), Elsevier Science, New York, **Vol. 16** (2003) Chapter 102.
226. A. Ogunsipe, D. Maree, T. Nyokong, *J. Mol. Struct.* **650** (2003) 131.
227. S. Fery-Forgues, D. Lavabre, *J. Chem. Educ.* **76** (1999) 1260.
228. J. Fu, X.Y. Li, D.K.P. Ng, C. Wu, *Langmuir* **18** (2002) 3843.
229. T.W.J. Gadella Jr, R.M. Clegg, T.M. Jovin, *Biomaging* **2** (1994) 139.
230. X.F. Wang, T. Uchida, S. Minami, *Appl. Spectrosc.* **3** (1989) 840.
231. H.C. Gerritsen, R. Sanders, A. Draaijer, *Proc. SPIE* **2329** (1994) 260.
232. X.F. Wang, T. Uchida, M. Maeshima, S. Minami, *Appl. Spectrosc.* **45** (1991) 560.
233. A.D. Scully, A.J. MacRobert, S. Botchway, P. O'Neill, A.W. Parker, R.B. Ostler, D. Phillips, *J. Fluoresc.* **6** (1996) 119.
234. G.J. Brakenhoff, M. Müller, R.I. Ghauharali, K. Visscher, *Proc. SPIE* **2412** (1995) 115.
235. A.G. Ryder, S. Power, T.J. Glynn, J.J. Morrison, *Proc. SPIE* **4529** (2001) 102.
236. S.E. Maree, D. Phillips, T. Nyokong, *J. Porphyrins Phthalocyanines* **6** (2002) 17.
237. J.C. Swarts, M.D. Maree, *J. Porphyrins Phthalocyanines* **11** (2007) 613.
238. H. Du, R.A. Fuh, J. Li, L.A. Cockan, J.S. Lindsey, *Photochem. Photobiol.* **68** (1998) 141.
239. S.J. Strickler, R.A. Berg, *J. Phys. Chem.* **37** (1962) 814.
240. T. Shen, Z.-L. Yuan, H.-J. Xu, *Dyes Pigments* **11** (1989) 77.
241. J. Kossanyi, D. Chahraoui, *Int. J. Photoenergy* **2** (2000) 9.

- 
242. P. Kubat, J. Mosinger, *J. Photochem. Photobiol. A: Chem.* **96** (1993) 93.
243. H. Ohtani, T. Kobayashi, T. Ohno, S. Kato, T. Tanno, A. Yamada, *J. Phys. Chem.* **88** (1984) 4431.
244. P.S. Vincett, E.M. Voigt, K.E. Rieckhoff, *J. Chem. Phys.* **55** (1971) 4131.
245. D.S. Lawrence, D.G. Whitten, *Photochem. Photobiol.* **64** (1996) 923.
246. X.-F. Zhang, H.-J. Xu, *J. Chem. Soc. Faraday Trans.* **89** (1993) 3347.
247. T. Förster, *Discuss. Faraday Soc.* **27** (1959) 7.
248. J.R. Lakowicz, in *Principles of Fluorescence Spectroscopy*, Kluwer Academic, New York, 2<sup>nd</sup> Ed. (1999).
249. J. Turro, in *Modern Molecular Photochemistry*, The Benjamin/Cummings Publishing Co., Inc., New York (1978).
250. L. Stryer, *Annu. Rev. Biochem.* **47** (1978) 819.
251. J.S. Hsiao, B.P. Krueger, R.W. Wagner, T.E. Johnson, J.K. Delaney, D.C. Mauzerall, G.R. Fleming, J.S. Lindsey, D.F. Bocian, R.J. Donohoe, *J. Am. Chem. Soc.* **118** (1996) 11181.
252. P. Jacques, A.M. Braun, *Helv. Chim. Acta.* **64** (1981) 1800.
253. A. Boguta, D. Wrobel, T.J. Hoffmann, P. Mazurkiewicz, *Cryst. Res. Technol.* **38** (2003) 267.
254. E.S. Dodsworth, A.B.P. Lever, P. Seymour, C.C. Leznoff, *J. Phys. Chem.* **89** (1985) 5698.
255. L. Oddos-Marcel, F. Madeore, A. Bock, D. Neher, A. Ferencz, H. Rengel, G. Wegner, C. Kryschi, H.P. Trommsdorff, *J. Phys. Chem.* **100** (1996) 11850.

- 
256. N. Kobayasi, M. Togashi, T. Osa, K. Ishii, S. Yamauchi, H. Hino, *J. Am. Chem. Soc.* **118** (1996) 1073.
257. N. Kobayashi, T. Ashid, K. Hirota, T. Osa, *Chem. Lett.* (1992) 1567.
258. N. Kobayashi, T. Ishizaki, K. Ishii, H. Konami, *J. Am. Chem. Soc.* **121** (1999) 9096.
259. N.A. Kuznetsova, N. Gretsova, E. Kalmykova, E. Makarova, S. Dashkevich, V. Negrimovskii, O. Kaliya, E. Luk'yanets, *Russ. J. Gen. Chem.* **70** (2000) 133.
260. A. Beeby, S. Fitzgerald, C.F. Stanley, *J. Chem. Soc. Perkin Trans. 2* (2001) 1978.
261. M. Durmus, T. Nyokong, *Spectrochim. Acta Part A* **69** (2008) 1170.
262. J.M. Mates, F.M. Sanchez-Jimenez, *Int. J. Biochem. Cell Biol.* **32** (2000) 157.
263. U. Bandyopadhyay, D. Das, R. Banerjee, *Curr. Sci.* **77** (1999) 658.
264. H. Wiseman, B. Halliwell, *Biochem. J.* **313** (1996) 17.
265. K. Lang, D. Wagnerová, J. Brodliva, *J. Photochem. Photobiol. A: Chem.* **(72)** (1993) 9.
266. H. Li, T.F. Guarr, *J. Chem. Soc. Chem. Commun.* (1989) 833.
267. N.A. Kuznetsova, N. Gretsova, O. Yuzhakova, V. Negrimovsky, O. Kaliya, E. Luk'yanets, *Russ. J. Gen. Chem.* **71** (2001) 36.
268. A. Ogunsipe, *Photophysical and photochemical studies of non-transition metal phthalocyanine derivatives*, Ph.D. Thesis, (2004).
269. M. Niedre, M.S. Patterson, B.C. Wilson, *Photochem. Photobiol.* **75** (2003) 382.
270. M.S. Patterson, S.J.Madsen, R. Wilson, *J. Photochem. Photobiol. B: Biol.* **5** (1990) 69.
271. J.W. Verhoeven, *Pure. Appl. Chem.* **68** (1996) 2223.

272. A.K. Sobbi, D. Wöhrle, D. Schlettwein, *J. Chem. Soc. Perkin Trans. 2* (1993) 481.
273. W. Spiller, H. Kliesch, D. Wöhrle, S. Hackbarth, B. Roder, G. Schnurpfeil, *J. Porphyrins Phthalocyanines 2* (1998) 145.
274. M.J. Cook, I. Chambrier, S.J. Cracknell, D.A. Mayes, D.A. Russell, *Photochem. Photobiol.* **62** (1995) 542.
275. H. Xu, T. Shen, O. Zhou, S. Shen, J. Liu, L. Li, S. Zhou, X. Zhang, Q. Yu, Z. Bi, X. Xias, *J. Photochem. Photobiol. A: Chem.* **65** (1992) 267.
276. S.E. Maree, T. Nyokong, *J. Porphyrins Phthalocyanines 5* (2001) 782.
277. M.D. Maree, D. Phillips, T. Nyokong, *J. Photochem. Photobiol. A: Chem.* **140** (2001) 117.
278. N.A. Kuznetsova, V.V. Okunchikov, V.M. Derkacheva, O.L. Kaliya, E.A. Luk'yanets, *J. Porphyrins Phthalocyanines 9* (2005) 393.
279. G. Winter, H. Heckmann, P. Haisch, W. Eberhardt, M. Hanack, L. Lüer, H.-J. Egelhaaf, D. Oelkrug, *J. Am. Chem. Soc.* **120** (1998) 11663.
280. I. Seotsanyana-Mokhosi, N. Kuznetsova, T. Nyokong, *J. Photochem. Photobiol. A: Chem.* **140** (2001) 215.
281. D.D. Perrin, W.L.F. Armarego, in *Purification of Laboratory Chemicals*, 2<sup>nd</sup> Ed., Pergamon Press, Oxford, (1989).
282. R.F. Kubin, A.N. Fletcher, *J. Luminescence 27* (1982) 455.
283. T.H. Tran-Thi, C. Desforge, C. Thiec, *J. Phys. Chem.* **93** (1989) 1226.
284. S.M. Bishop, A. Beeby, A.W. Parker, M.S.C. Foley, D. Phillips, *J. Photochem. Photobiol. A: Chem.* **90** (1995) 39.

- 
285. L. Kaestner, M. Cesson, K. Kassab, T. Christensen, P.D. Edminson, M.J. Cook, I. Chambrier, G. Jori, *Photochem. Photobiol. Sci.* **2** (2003) 131.
286. W.W. Yu, L. Qu, W. Guo, X. Peng, *Chem. Mater.* **15** (2003) 2854.
287. R.D. George, A.W. Snow, *J. Heterocyclic Chem.* **32** (1995) 495.
288. V.N. Nemykin, V.M. Mytsyk, S.V. Volkov, N. Kobayashi, *J. Porphyrins Phthalocyanines* **4** (2000) 551.
289. K. Kasuga, M. Tsutsui, *Coord. Chem. Rev.* **32** (1980) 67.
290. J. Metz, O. Schneider, M. Hanack, *Inorg. Chem.* **23** (1984) 1065.
291. N. Sehlotho, M. Durmus, V. Ahsen, T. Nyokong, *Inorg. Chem. Commun.* **11** (2008) 479.
292. D. Tasis, N. Tagmatarchis, V. Georgakilas, M. Pratos, *Chem. Eur. J.* **9** (2003) 4000.
293. H. Murakami, G. Nakamura, T. Nomura, T. Miyamoto, N. Nakashima, *J. Porphyrins Phthalocyanines* **11** (2007) 418.
294. D.L. Pavia, G.M. Lampman, G.S. Kriz, in *Introduction to Spectroscopy*, 3<sup>rd</sup> Ed. Brooks Cole, New York, (2000) p73.
295. M.D. Ellison, P.J. Gasda, *J. Phys Chem. C* **112** (2008) 738.
296. N.B. McKeown, in *The Porphyrin Handbook*, K.M. Kadish, K.M. Smith, R. Guilard (Eds.), Academic Press, New York, **Vol. 15** (2003) Chapter 98.
297. T.M. Keller, T.R. Price, J.R. Griffith, *Synthesis* **74** (1980) 613.
298. W.M. Sharman, J.E. van Lier, in *The Porphyrin Handbook*, K.M. Kadish, K.M. Smith, R. Guilard (Eds.), Academic Press, New York, **Vol. 15** (2003) Chapter 97.
299. P. Tau, T. Nyokong, *Polyhedron* **25** (2006) 1802.

- 
300. M. Durmus, T. Nyokong, *Tetrahedron* **63** (2007) 1385.
301. W. Eberhardt, M. Hanack, *Synthesis* **1** (1995) 95.
302. K. Ban, K. Nishizawa, K. Ohta, H. Shirai, *J. Mater. Chem.* **10** (2000) 1083.
303. O.W. Kolling, *Anal. Chem.* **54** (1982) 260.
304. V. Gutmann, *Electrochim. Acta* **21** (1976) 661.
305. A.G. Gurek, O. Bekaroglu, *J. Chem. Soc. Dalton Trans.* (1994) 1419.
306. T.H. Tran-Thi, *Coord. Chem. Rev.* **160** (1997) 53.
307. J.E. Huheey, in *Inorganic Chemistry: Principles of Structure and Applications*, C.C. Leznoff, A.B.P. Lever (Eds.), VCH Publishers, New York, **Vol. 1** (1989) Chapter 3.
308. I. Chambrier, G.F. White, M.J. Cook, *Chem. Eur. J.* **13** (2007) 7608.
309. N. Kobayashi, J. Mack, K. Ishii, M.J. Stillman, *Inorg. Chem.* **41** (2002) 5350.
310. A.L. Maclean, G.J. Foran, B.J. Kennedy, P. Turner, T.W. Hambley, *Aust. J. Chem.* **49** (1996) 1273.
311. K. Kasuga, N. Matsuura, K. Inone, M. Handa, T. Sugimori, K. Isa, M. Nakata, *Chem. Lett.* (2002) 352.
312. N. Kobayashi, T. Fukuda, K. Ueno, H. Ogino, *J. Am. Chem. Soc.* **123** (2001) 10740.
313. C.C. Leznoff, C.R. McArthur, Y. Qin, *Can. J. Chem.* **71** (1995) 1319.
314. M. Geyer, F. Plenzig, J. Rauschnabel, M. Hanack, B. del Rey, A. Sastre, T. Torres, *Synthesis* **9** (1996) 1139.
315. S. Dabak, A. Gul, O. Bekaroglu, *Chem. Ber.* **127** (1994) 2009.
316. A. Weitemeyer, H. Kliesch, D. Wöhrle, *J. Org. Chem.* **60** (1995) 4900.

- 
317. C.C. Leznoff, P. Snirskaya, B. Khouw, R.L. Cerny, P. Seymour, A.B.P. Lever, *J. Org. Chem.* **56** (1991) 82.
318. M. Tian, T. Wada, H. Kimura-Suda, H. Sasebe, *J. Mater. Chem.* **7** (1997) 861.
319. E. Maya, C. García-Frutos, P. Vásquez, T. Torres, *J. Org. Chem.* **65** (2000) 2733.
320. C. Piechochi, J. Simon, *J. Chem. Soc. Chem. Commun.* (1985) 259.
321. J.V. Bakboord, M.J. Cook, E. Hamuryudan, *J. Porphyrins Phthalocyanines* **4** (2000) 510.
322. J. Chen, N. Chen, J. Huang, J. Wang, M. Huang, *Inorg. Chem. Commun.* **9** (2006) 313.
323. A. Hirth, A.K. Sobbi, D. Wöhrle, *J. Porphyrins Phthalocyanines* **1** (1997) 275.
324. J. Mack, M.J. Stillman, *J. Phys. Chem.* **99** (1995) 7935.
325. C. Bullen, P. Mulvaney, *Langmuir* **22** (2006) 3007.
326. A. Mandal, N. Tamai, *J. Phys. Chem. C* **112** (2008) 8244.
327. T. Förster, G. Hoffmann, *Z. Phys. Chem.* **75** (1971) 63.
328. M. Lunz, A. Louise Bradley, *J. Phys. Chem. C* **113** (2009) 3084.
329. J. Zhang, X. Wang, M. Xiao, *Opt. Lett.* **27** (2002) 1253.
330. M.G. Bawendi, P.J. Carroll, W.L. Wilson, L.E. Bruce, *J. Chem. Phys.* **96** (1992) 946.
331. X. Wang, L. Qu, J. Zhang, X. Peng, M. Xiao, *Nano Lett.* **3** (2003) 1103.
332. E.Z. Chong, D.R. Matthews, H.D. Summers, K.L. Njoh, R.J. Errington, P.J. Smith, *J. Biomedicine and Biotechnology* **54169** (2007) 1.
333. A. Javier, D. Magana, T. Jennings, G.F. Strouse, *Appl. Phys. Lett.* **83** (2003) 1423.
334. T.H. Huang, K.E. Rieckhoff, E.M. Voight, *J. Chem. Phys.* **77** (1982) 3424.



- 
335. T.H. Huang, K.E. Rieckhoff, E.M. Voight, *J. Phys. Chem.* **85** (1981) 3322.
336. D. Wöhrle, V. Schmidt, *J. Chem. Soc. Dalton Trans.* (1988) 549.
337. M.E. Frink, D.K. Geiger, G.J. Ferraudi, *J. Phys. Chem.* **90** (1986) 1924.
338. N. Nensala, T. Nyokong, *J. Mol. Catal. A: Chem.* **164** (2000) 69.
339. K. Ozoemena, N. Kuznetsova, T. Nyokong, *J. Mol. Catal. A: Chem.* **176** (2001) 29.
340. N. Sehlotho, T. Nyokong, *J. Mol. Catal. A: Chem.* **219** (2004) 201.
341. Z. Yang, H. Pu, J. Yuan, D. Wan, Y. Liu, *Chem. Phys. Lett.* **465** (2008) 73.
342. B. Ballesteros, S. Campidelli, G. de la Torre, C. Ehli, D.M. Guldi, M. Prato, T. Torres, *Chem. Commun.* (2007) 2950.
343. H. Murakami, T. Nomura, N. Nakashima, *Chem. Phys. Lett.* **378** (2003) 481.
344. A. Gouloumis, S. Liu, P. Vasquez, L. Echegoyen, T. Torres, *Chem. Commun.* (2001) 399.
345. H-B. Xu, H-Z. Chen, M-M. Shi, R. Bai, M. Wang, *Mater. Chem. Phys.* **94** (2005) 342.
346. E. Katz, *J. Electroanal. Chem.* **365** (1999) 157.
347. W. Freyer, S. Mueller, K. Teuchner, *J. Photochem. Photobiol. A: Chem.* **163** (2004) 231.
348. W.C.W. Chan, S. Nie, *Science* **281** (1998) 2016.
349. A.R. Cortan, R. Hull, R.L. Opila, M.G. Bawendi, M.L. Steigerwald, R.J. Carroll, L.E. Brus, *J. Am. Chem. Soc.* **112** (1990) 1327.
350. Y.J. Hu, Y. Liu, R.M. Zhao, J.X. Dong, S.S. Qu, *J. Photochem. Photobiol. A: Chem.* **179** (2006) 324.
351. J. Ma, J.-Y. Chen, M. Idowu, T. Nyokong, *J. Phys. Chem. B.* **112** (2008) 4465.